MECHANISMS AND PROCESSES UNDERLYING THE REVERSIBILITY OF HYPOCONTRACTILITY-INDUCED DILATED CARDIOMYOPATHY

Isabella M. Reichardt

A dissertation

submitted in partial fulfillment for the

requirements for the degree of

DOCTOR OF PHILOSOPHY

University of Washington

2025

Reading Committee:

Jennifer Davis, Chair

Farid Moussavi-Harami

Michael Regnier

Program Authorized to Offer Degree:

Bioengineering

ABSTRACT

MECHANISMS AND PROCESSES UNDERLYING THE REVERSIBILITY OF HYPOCONTRACTILITY-INDUCED DILATED CARDIOMYOPATHY

Isabella M. Reichardt

Chair of the Supervisory Committee:

Jen Davis

Bioengineering, Lab Medicine & Pathology

Dilated cardiomyopathy (DCM) is a progressive heart disease driven by inherited mutations that impair cardiomyocyte contractility, ultimately leading to systolic dysfunction, dilation, and fibrosis. Current therapies, such as angiotensin inhibitors, β-blockers, and left ventricular assist devices (LVADs), are largely palliative and do not address the primary defect in myocyte force generation. Myosin activators have emerged as a promising new class of small molecules that can directly augment contractility at the myofilament level; however, despite encouraging preclinical data, clinical trials have yielded only modest functional improvements for patients. This gap highlights a longstanding assumption in the field that correcting the cardiomyocyte defect alone should be sufficient to reverse disease. Given that DCM often progresses over years to decades before diagnosis, it remains unclear whether targeted myocyte therapies can reverse established remodeling. This dissertation interrogates this assumption by defining how

cardiomyocyte hypocontractility shapes fibroblasts behavior, ECM mechanics, and ultimately, the capacity of the heart to recover. Using transgenic mouse models and engineered heart tissues, we first demonstrate that fibroblasts act as early mechanosensitive rheostats that detect impaired myocyte tension and initiate changes in the ECM. Hypocontractile cardiomyocytes triggered the emergence of a hyperproliferative fibroblast state and increased myocardial stiffness well before the emergence of overt fibrosis. Importantly, conditional deletion of p38 in fibroblasts prevented fibroblast proliferation, ECM remodeling, and myocyte eccentric hypertrophy, demonstrating that interrupting fibroblast signaling halts DCM progression even when the myocyte defect persists. Next, we examined whether restoring myocyte contractility after disease onset is sufficient for recovery. While genetic suppression of the sarcomeric mutation fully restored cardiomyocyte structure, function, and chromatin accessibility, it did not reverse ECM stiffness or reduce fibroblast number. Persistent fibrosis and fibroblast survival limited whole-organ functional recovery. Full phenotypic reversal was achieved when myocyte correction was paired with an inhibitor of ECM crosslinking, revealing that non-myocyte adaptations impose a durable barrier to reverse remodeling. Finally, developmental studies demonstrated that transient myocyte correction during the postnatal period delayed DCM onset and attenuated remodeling, underscoring the importance of injury timing in determining recovery potential. Together, this body of work demonstrates that: 1) fibroblasts and fibrosis are central drivers of DCM progression, 2) adaptations within these compartments are far less amenable to reversal than cardiomyocyte dysfunction, and 3) early-life myocyte hypocontractility shapes the long-term severity of DCM, suggesting that pathological fibroblast and ECM states may be installed during the postnatal window. More broadly, this work can be used to help design new combinational

therapeutic strategies and contextualize the performance of emerging myosin activators as they begin clinical trials for efficacy.

ACKNOWLEDGMENTS

This dissertation is a product of a decade of encouragement, patience, and guidance from so many people. It's impossible to thank everyone who's played a part in getting me here, but I want to start with an email exchange from high school, when I wasn't even sure I belonged in this field. I wrote to Dr. Julie Phillippi:

> ***Me:*** The last question I will unload on you today is sort of self-esteem related. Are most of the people who are involved in biomedical research prodigies? I've just been increasingly worried if this is the sort of thing I can do. I'm good at math and science and I'll be taking AP Calculus next year, but that's not really anything special. I don't know—what I really want to know is, can someone just decide to go into bioengineering in college and be successful?
>
> ***Dr. Phillippi:*** Regarding your last question… I routinely ask myself if this is something I can do! I struggle with it as well because the nature of academic research can be very competitive if you let it. No, I don't think most people are prodigies. Don't get me wrong, there are some scary smart and brilliant people in this field… But yes, I question my ability weekly if not daily. Yet, I am doing it—one day at a time and chugging along. This field takes resiliency and patience. Bottom line: if you feel creative and curious, are patient and diligent, persistent, like collaboration, always wanting to learn something new, and are assertive—this could be a good field for you.

After obtaining a bachelor's degree and PhD in Bioengineering, I could not agree more with her assessment. To anyone reading this who might be questioning yourself, I want you to know that doubt is universal, resilience is essential, and success is built one day at a time. Thank you, Julie, for being my first mentor, helping me navigate academia, reading endless program applications and research proposals, and always being someone I could lean on.

To my undergraduate research advisor, Dr. Sean Palecek: thank you for taking in a freshman who only knew that she thought stem cells sounded cool. You encouraged my excitement for research, and your lab really laid the foundation for my scientific career. To my PhD advisor, Dr. Jen Davis: thank you for guiding me through this six-year journey. You always challenged me to be a better scientist and helped me grow into the researcher I am today. Truly, all of the work in this dissertation wouldn't exist without your vision and drive to do excellent science. To Drs. Mike Regnier and Farid Moussavi-Harami, thank you for going above and beyond as committee members. You both always encouraged me, showed such enthusiasm for my project, and helped me navigate that highs and lows of the PhD.

Thank you to all of the research mentors I have had over the years—I literally would not know how to pipette without you! To my first research mentor, Kaitlin Dunn, I will never forget the first time I saw stem cell derived myocytes beating in a dish. You opened my eyes to the world of research and made me want to pursue a PhD. To my summer research mentors at Promega, Julia Gilden and Peter Hofsteen, thank you for making industry research feel approachable (and fun). Julia, you're the only reason I applied for the NSF GRFP, and I'm so grateful to you for your encouragement. And to Darrian Bugg—thank you for helping me conquer my fear of scruffing a mouse, and more importantly, for guiding me towards being an independent scientist while always being willing to act as a sounding board.

To my labmates and friends in the Davis and Regnier labs—Logan Bailey, Ross Bretherton, Sasha Smolgovsky, Elaheh Karbassi, Silvia Marchiano, Ambika Gunaje, Amy Gifford, Dessiree Ortac, Charlie Thel, and Likitha Nimmagadda—thank you for making the lab a fun place to come to work every day! A PhD can be an isolating experience, especially during a pandemic, but I never felt alone when I had all of you to lean on. I'd especially like to acknowledge Sasha, who helped immensely with experimentation and the mouse colony during the last few months of my PhD. This dissertation wouldn't have been possible without you! I would also like to give a special thank you to Kalen Robeson, Abby Nagle, Kerry Kao, Thomas Vincent, and Sonette Steczina, who cheered me on, let me vent about failed experiments, and were always willing to go on a quick coffee break. Our friendship is one of the things I cherish most out of everything I gained from this program. To my undergraduate trainees, Ellie Plaster and Rachelle Soriano, thank you for your invaluable contributions to this project. I know you will go on to do brilliant things in medical and graduate school.

Thank you to my family, who have always been my number one supporters. When I look at the skills that have helped me most as a researcher, it is easy to see that my parents really laid the foundation for my success. From my dad patiently helping me through tricky math problems and my mom acting as editor and chief for all of my essays, I learned how to think critically, problem solve, and communicate clearly, all of which are essential skills in science. I would also like to thank my mom for being such a strong role model. She always fought for me, especially when a teacher once told me engineering wasn't a realistic goal "for a girl". To my sister Claire, thank you for always being one phone call away. You're a budding scientist in your own right, and I'm so excited to see what you'll accomplish.

Finally, to all of my friends, thank you for keeping me grounded, reminding me there's life outside the lab, and making Seattle feel like home. Nicole Wothe, Connor Jenkins, Kaitlin Hall, Thalia Cronin, and Clara Garcia—you've made these years brighter, sillier, and so much more fun than I ever could have imagined.

DEDICATION

This thesis is dedicated to all of the mice that were sacrificed during my PhD to deepen our knowledge of cardiovascular plasticity and disease reversal.

Table of Contents

List of Tables

List of Figures

List of Supplemental Figures

Chapter 1: Introduction and Significance

1.1 Prevalence and pathophysiology of familial dilated cardiomyopathy

Dilated cardiomyopathy is a disease characterized by systolic dysfunction and left ventricle (LV) dilation, with a reported incidence of 118.33 per 100,000 people between 2017–2019 (*1*, *2*). DCM can be classified as acquired (due to ischemia, toxic exposure, infections, and pregnancy) or idiopathic, where there is no clear cause for disease (*3*). Approximately 46% of DCM cases are idiopathic, with a higher prevalence among adults over 65 years, males, and African Americans (*1*). However, the true prevalence of idiopathic DCM is likely underreported, with some estimates suggesting it affects up to 1:250 people (*4*).

The genetic basis for dilated cardiomyopathy was not appreciated until the mid 1980's, when several family-based studies reported that 20-50% of idiopathic DCM cases are familial (*5*). Since then, Next Generation Sequencing has identified over 30 causal mutations in genes across the cardiomyocyte:

1) **Sarcomere:** Mutations in contractile proteins account for approximately 30% of idiopathic DCM cases. Truncating mutations in titin (*TTN*) are particularly significant, with 25% of familial DCM cases involving *TTN* mutations (*6*). Other mutations include cardiac actin (*ACTC1*), myosin-binding protein C (*MYBPC3*), myosin heavy chains (*MYH6, MYH7*), myosin light chains (*MYL2, MYL3*), tropomyosin (*TPM1*), cardiac troponin C (*TNNC1*), troponin I (*TNNI3*), and troponin T (*TNNT2*).
2) **Sarcoplasmic reticulum:** Mutations in genes regulating intracellular Ca^{2+} and excitation-contraction coupling, such as ryanodine receptor (*RYR2*) and phospholamban (*PLN*), have been identified (*4*, *7*).

3) **Desmosome:** Desmosomal protein mutations, which cause arrhythmogenic right ventricular cardiomyopathy, have recently been identified in causing DCM, as well (*8*). These include desmocollin-2 (*DSC2*), desmoglein-2 (*DSG2*), desmoplakin (*DSP*), junction plakoglobin (*JUP*), and plakophilin-2 (*PKP2*).
4) **Nucleus:** Mutations in nuclear envelope proteins, such as lamin A/C (*LMNA*) and thymopoietin (*TMPO*), have been identified in DCM. Interestingly, *LMNA* mutations were identified in 33% of familial DCM cases involving an atrioventricular block, suggesting *LMNA* mutations are particularly enriched in patients experiencing conduction abnormalities (*9*)
5) **Membrane and extracellular proteins:** Mutations in extracellular proteins and membrane proteins, like desmin (*DES*), dystrophin (*DMD*), and laminin (*LAMA4*), have also been identified in causing DCM (*4*, *7*).

While many hoped that uncovering the genetic basis for DCM might enable more targeted clinical approaches, there are significant limitations to using genotype to guide patient care. Familial DCM has substantial phenotypic diversity; even patients carrying the same mutation can differ dramatically in disease presentation, severity, and penetrance. For example, in one family carrying a *TTN* truncating mutation, a girl presented with clinical DCM at 3 months of age whereas her mother and grandfather presented in early adulthood at 23 and 36 years of age, respectively (*10*). This heterogeneity is exacerbated when evaluating patients with differing genotypes and backgrounds, such as age, sex, or treatment history (*11*). Evidence from one large family study underscores this complexity. In a cohort of 211 families with DCM, 22% of relatives were found to have clinically detectable disease. Among otherwise healthy relatives, 10% carried pathogenic or likely pathogenic variants, and of these, 42% developed clinically

evident DCM within five years of follow up (*12*). These findings highlight both the incomplete penetrance of DCM mutations and the unpredictable timeframe of disease onset across patients.

One explanation for this heterogeneity is that the heart undergoes compensatory remodeling to counteract the genetic mutations (*13*). During this compensatory phase, patients may be genotype-positive with no clinical signs of disease. It is only when compensation fails and the heart pathologically remodels that DCM becomes clinically detectable (*14*, *15*) (**Figure 1.1**). Within this framework, the interplay between the severity of the genetic mutation and a patient's clinical background likely determines how long the heart can sustain the compensatory remodeling phase before progressing to heart failure. This model also reflects a broader assumption in the field that compensatory remodeling is reversible and restricted to the cardiomyocyte, whereas pathological remodeling is irreversible and propagates to other cellular niches (*16*). However, how the myocardium compensates, which cell types contribute, and the extent to which these processes are reversible have not been systematically explored in DCM.

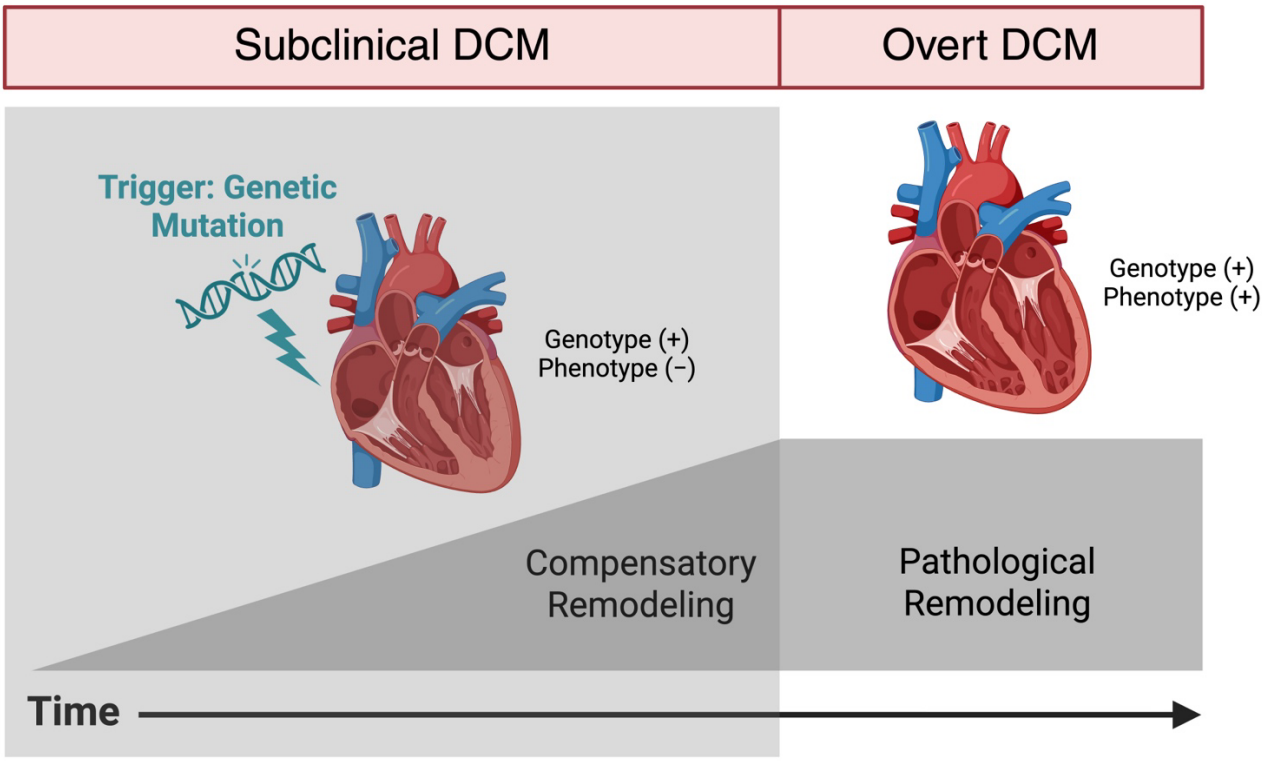

Figure 1.1: Compensatory remodeling masks the disease phenotype in inherited DCM. *Although genetic mutations underlie inherited dilated cardiomyopathy (DCM), patients often experience a period of compensatory remodeling where they are genotype positive but phenotype negative, ultimately masking the pathology of disease. Once the disease progresses to pathological remodeling, the patient will become symptomatic. This is often the stage at which patients are diagnosed and treated for DCM. (Figure made with BioRender).*

These uncertainties make it difficult to determine the best time to intervene. In principle, treating during the compensatory phase, before irreversible remodeling has occurred, would be ideal. However, in practice, early intervention is complicated by the fact that many genotype-positive individuals may never develop disease and that mutations in the same gene can give rise to hypertrophic cardiomyopathy (HCM), a diametric disease to DCM characterized by

hypercontraction, LV hypertrophy, and diastolic dysfunction (*17*). Despite advances in identifying the genetic basis of DCM, genotype alone cannot reliably guide care or new therapeutic design. To determine why mutations in the same gene can lead to divergent remodeling outcomes, it is necessary to define the mechanistic basis of dilated and hypertrophic cardiomyopathies.

1.2 Determining the mechanistic basis of dilated and hypertrophic cardiomyopathies

Although DCM and HCM arise from mutations in many of the same sarcomeric genes, the way these variants alter contraction in the cardiomyocyte is quite different. Early observations showed HCM-causing mutants generally sensitize the myofilament to Ca^{2+}, prolonging contraction and delaying calcium reuptake into the sarcoplasmic reticulum. Conversely, DCM mutations desensitize the myofilament to Ca^{2+}, accelerating relaxation and requiring higher cytosolic calcium for equivalent force generation (*18*). Despite these well-characterized biophysical differences, neither myocyte shorting nor calcium-transient amplitude reliably predicts whether remodeling will be hypertrophic or dilated (*18*). Some in the field have proposed that sarcomere mutations cause inefficient ATP utilization and that energetic deficits underly remodeling in cardiomyopathies (*19*), although this may still be a secondary consequence of altered force generation at the myofilament.

To develop a more comprehensive framework for understanding the molecular basis of dilated and hypertrophic remodeling, Davis et. al established a tension index (TI) model to predict cardiac growth. This model integrated myocyte-generated tension over time and accurately predicted both the severity and direction of cardiac remodeling. Multiple DCM and HCM murine models and induced pluripotent stem cell (iPSC)-derived cardiomyocytes (CM)

from patients with cardiomyopathies were used to build and validate this model. Mutations that decreased the overall TI, by reducing maximal force generation or shortening relaxation time, produced dilated remodeling, whereas those that increased the TI led to hypertrophic growth (**Figure 1.2**) (*18*). Ca^{2+} amplitude, decay, and integrated area were not predictive of any growth outcomes (*18*). Collectively, these findings suggest that cardiomyocytes sense and respond to both the duration and magnitude of mechanical tension, rather than to changes in calcium cycling alone.

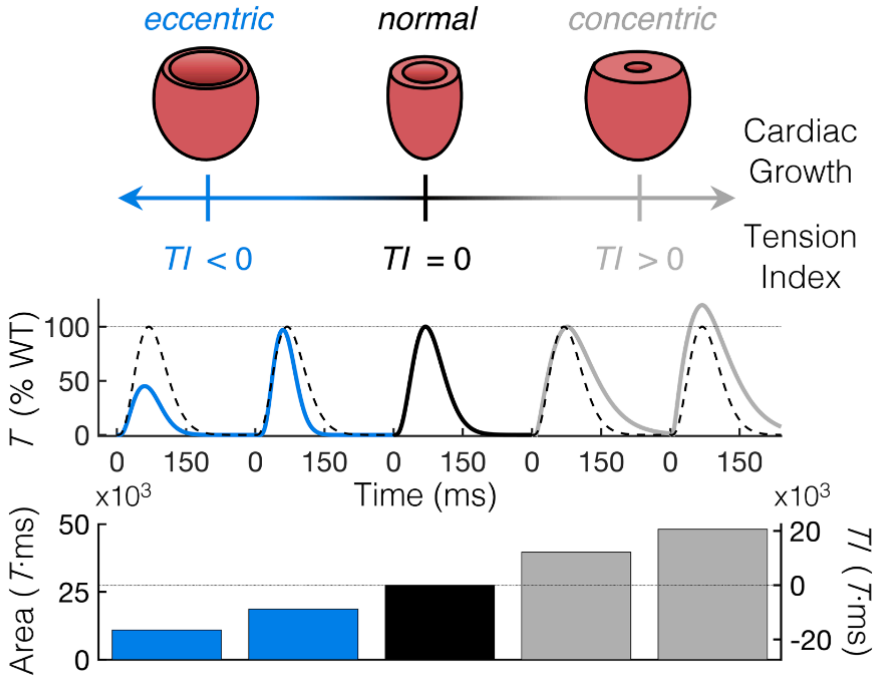

Figure 1.2: The tension index underlies cardiac growth in familial cardiomyopathies. *The tension index (TI) is the integral of twitch tension over time in a cardiomyocyte. Davis et al. postulated that if an inherited mutation decreases the TI of a tissue, either by decreasing maximal force or increasing relaxation time, that this would lead to eccentric remodeling (i.e., dilated cardiomyopathy). Conversely, if an inherited mutation increased the TI, by increasing max force or slowing relaxation time, it would lead to concentric remodeling (i.e., hypertrophic cardiomyopathy). Figure from* (*20*).

A follow up study by Powers et al. found that normalizing the TI prevented maladaptive dilated remodeling. In this study, mice with a DCM-causing mutation (D230N) were crossed with mice harboring an HCM-causing mutation (L48Q) to generate double transgenic (DTG) mice. The opposing effects of the mutations, with D230N decreasing the TI and L48Q increasing it, produced an overall normalized TI relative to controls. This normalization prevented DTG mice from developing the dilation and systolic dysfunction observed in the D230N-only littermates (*20*). These findings underscore the predictive and therapeutic potential of the TI model, suggesting that balancing mechanical tension could serve as a strategy to prevent pathological remodeling in both DCM and HCM. However, a key limitation of this study is that DTG mice possess both mutations from birth, leaving it unclear whether normalizing the TI in established disease can reverse remodeling once it has occurred.

Although the tension index model provides a unifying framework for determining how sarcomeric mutations direct cardiac growth, it primarily describes remodeling intrinsic to the myocyte. How changes in myocyte contractility influence non-myocyte populations, particularly fibroblasts, and how these interactions contribute to disease progression remain poorly understood. Moreover, whether restoring myocyte mechanical homeostasis is sufficient to reverse established remodeling, or if persistent alterations in the fibroblast and extracellular matrix compartments form a barrier to recovery, is not known. Addressing these questions is critical for defining the mechanisms that distinguish reversible from irreversible remodeling in dilated cardiomyopathy.

1.3 Current treatments for DCM are insufficient

Despite major advances in understanding the genetic and cellular mechanisms underlying DCM, current therapeutic strategies remain largely palliative. Existing treatments primarily focus on halting disease progression and prolonging survival. Clinically, DCM patients are managed similarly to those with heart failure with reduced ejection fraction (HFrEF). Short term pharmacological treatments include angiotensin-converting enzyme (ACE) inhibitors and β-blockers, whereas severe cases often require surgical interventions, such as implantation of left ventricular assist devices (LVADs) and heart transplants (*17*).

While pharmacologic and mechanical treatments can induce LV reverse remodeling in DCM, characterized by improved cardiac function and decreased dilation, these effects are often transient and vary greatly among patients (*21–24*). Treatment with ACE inhibitors and β-blockers led to complete reverse remodeling in ~15% of the DCM patient cohort; however, one-third of patients redeveloped DCM over time (*21*). Pediatric patients with DCM are particularly unresponsive to ACE inhibitors and β-blockers (*25*). Mechanical unloading with LVADs in adult DCM patients improved systolic function and reduced dilation in the short term, but cardiac function declined months after device implantation (*22*). The inability of these treatments to reverse the DCM phenotype may stem from their palliative nature, focusing on preventing further adverse remodeling rather than correcting the underlying mechanical defect in myocyte force generation (*17*, *18*, *26*).

1.4 Targeted myocyte treatments and challenges

Given that one-size-fits-all treatments have been ineffective in reversing DCM, the field has worked to develop more targeted therapies to improve force generation in the myocyte.

Notably, many of these "targeted" treatments for DCM are also being investigated to improve systolic function in HFrEF patients, who have various underlying causes for disease. The following section summarizes therapeutics that are under investigation for treating DCM, but an important caveat is that much of the human clinical data has been performed in general HFrEF patients.

1.4.1 Inotropes

Early attempts to create targeted therapies for DCM focused on positive inotropes, which either elevate cytosolic Ca^{2+} or sensitize the myofilament to Ca^{2+} ions. Despite several promising candidates, including levosimendan, pimobenden, bepridil, and MCI-154, many failed to demonstrate clinical efficacy or exhibited pro-arrhythmogenic risks (*27*). Genetically engineered mice with increased myofilament Ca^{2+} sensitivity also showed an elevated risk for ventricular tachycardia (*28*), suggesting that all Ca^{2+} sensitizers have the potential to cause arrythmias in patients.

1.4.2 Myosin Activators

To circumvent the off-target effects of increased cytosolic calcium, recent drug development has focused on therapies that directly modulate tension at the myofilament. Omecamtiv Mecarbil (OM) and Danicamtiv are two such drugs that have shown promise for treating heart failure by enhancing force generation without altering calcium transients, suggesting that they could bypass many of the pitfalls associated with positive inotropes (*29*, *30*). Given the primary defect in DCM is tension generation at the myofilament, myosin activators have the potential to address the root cause of disease.

Initially, OM was thought to increase force generation by increasing phosphate (Pi) release (*30*). However, follow up studies revealed that OM also decreases myosin motility (*31*) and slows the power stroke (*32*), prolonging the time myosin remains bound to actin. While these characteristics are more in line with a myosin inhibitor, it appears force generation is increased through enhanced thin filament cooperativity (*33*) and disruption of the super-relaxed state (SRX) of myosin (*34*). Taken together, these studies demonstrate that OM is not a true myosin activator but increases force primarily through thin filament activation and SRX destabilization.

In vitro mechanics assays have demonstrated that OM can improve Ca^{2+} sensitivity of the myofilament in mice with a DCM-causing mutation in tropomyosin (E54K)(*35*). Despite this, phase II and III clinical trials using OM to treat HFrEF patients have had modest results. Phase II clinical trials with OM on HFrEF patients demonstrated safety of the drug with no evidence for increased rates of adverse events, like hypotension, myocardial infarction, or arrhythmias (COSMIC-HF, NCT01786512). Efficacy of OM also showed promise with increased stroke volume and decreased end-diastolic dimension and B-type natriuretic peptide (BNP) (*36*). In phase III clinical trials in HFrEF patients, OM modestly but significantly reduced heart failure events or cardiovascular death from 39.1% in the placebo group to 37% in the OM group (GALACTIC-HF, NCT02929329) (*37*). A greater treatment effect was noted in patients with severe heart failure (*37*, *38*). Similar to the COSMIC Phase II trial, OM treatment decreased BNP levels and had no effect on incidence of ischemic events and arrhythmias (*37*). Notably, recent meta analyses of heart failure trials has demonstrated there is no correlation between reduced BNP concentrations and mortality (*39*, *40*) and a smaller Phase III clinical trial showed that OM

did not alter exercise capacity in chronic HFrEF patients (METEORIC-HF, NCT03759392) (*41*), calling into question whether OM meaningfully reverses disease in patients.

Danicamtiv is a new promising myosin activator that is believed to work by increasing myofibril Ca^{2+} sensitivity and ATPase activity. Danicamtiv treatment in a murine DCM model increased the TI of the myocardium and substantially improve LVEF, although notably max force and LVEF never recovered fully to wildtype levels (*42*). Danicamtiv has shown promise in Phase I and II clinical trials. In dogs with heart failure, Danicamtiv improved LV stroke volume. In HFrEF patients, Danicamtiv improved global longitudinal and circumferential strain but did have an increase in mild adverse events (NCT03447990) (*43*). A phase II clinical trial evaluating Danicamtiv in patients with familial DCM carrying *MYH7* and *TTN* mutations was completed in early 2024 and identified no new safety concerns. However, preliminary efficacy data demonstrated limited clinical improvement, with 12 weeks of Danicamtiv treatment resulting in a 1.77-2.44% increase in EF and 0.17-2.09% drop in LV end diastolic dimension (NCT04572893) (*44*)

1.4.3 Troponin Activators

Troponin activators, such as CK-136 (formerly AMG 594) and TA1, have recently emerged as a new class of inotropes that selectively sensitizes the thin filament to Ca^{2+} without increasing overall Ca^{2+} transients, similarly circumventing the negative consequences of excess Ca^{2+} from treatment with inotropes (*45*). However, these molecules are still in phase I and pre-clinical trials, so their clinical efficacy is still unknown.

Despite the increasing mechanistic specificity of myocyte-targeted therapeutics, their clinical impact in treating HFrEF and familial DCM has been modest. Together, these studies

highlight a central limitation of current strategies: restoring myocyte contractility alone does not guarantee robust recovery of the whole heart. Although DCM begins within the myocyte, hypocontraction likely affects the myocardium as an integrated tissue, and myocyte correction may be constrained by persistent remodeling in non-myocyte compartments. Understanding how fibroblasts and the extracellular matrix respond to and interact with corrected myocytes will be essential for identifying the barriers that prevent full functional reversal of disease.

1.5 Myocyte-fibroblast crosstalk in cardiac remodeling

Considering that the myocardium functions as a multicellular syncytium, adaptations in non-myocytes may limit the reversibility of DCM. Crosstalk between cardiomyocytes and fibroblasts is essential for coordinating tissue remodeling during both development and disease progression (*46*). These interactions occur through multiple modes of communication, including paracrine signaling, electrical coupling, and feedback through the ECM.

1.5.1 Paracrine signaling between myocytes and fibroblasts

Among paracrine factors, transforming growth factor β (TGFβ) is one of the most extensively studied mediators of myocyte-fibroblast communication. TGFβ is widely recognized as a master regulator of fibroblast activation, promoting proliferation, differentiation into contractile myofibroblasts, and enhanced ECM deposition (*47*). In response to cardiac stress, myocytes upregulate and secrete TGFβ (*48*, *49*). Fibroblast-specific deletion of the TGFβ receptors Tgfbr1 and Tgfbr1 in a murine model of transaortic constriction (TAC) reduced interstitial fibrosis, attenuated myocyte hypertrophy, and improved systolic function (*50*), demonstrating that fibroblast responsiveness to TGFβ directly feeds back on myocyte hypertrophy and dysfunction. Conversely, TGFβ signaling also contributes to hypertrophic

growth within myocytes themselves (*51*), and cardiomyocyte-specific deletion of Tgfbr2 mitigates both hypertrophy and fibrosis following TAC (*24*). Together, these findings highlight the reciprocal role of TGFβ in coordinating myocyte and fibroblast responses to stress and underscores how intercellular signaling can perpetuate maladaptive remodeling.

Cytokines expressed by myocytes and fibroblasts are also common paracrine signals used for crosstalk in disease. Interleukin 6 (IL-6) has been thoroughly studied in the context of myocardial infarction (MI). In the short term, IL-6 is cardioprotective and prevents myocytes from apoptosing due to oxidative stress, but chronic IL-6 decreases myocyte contractility and induces maladaptive hypertrophy (*52*). *In vitro* co-culture experiments suggest that angiotensin II (AngII) secreted by fibroblasts prompts IL-6 secretion by cardiomyocytes, which in turn causes myocyte hypertrophy and fibroblast proliferation (*53*) Interleukin 33 (IL-33), which is primarily expressed by cardiac fibroblasts, was found to be cardioprotective. Deletion of the receptor for IL-33, ST2, worsened hypertrophy, systolic dysfunction, and fibrosis due to TAC. Moreover, recombinant IL-33 treatment prevented myocyte hypertrophy and lessened the fibrotic response in WT but not ST2 knockout mice (*54*).

1.5.2 Electrical coupling between myocytes and fibroblasts

Fibroblasts and cardiomyocytes can electrically couple through gap junctions. While cardiomyocytes predominantly connect to one another via connexin-43 (Cx43), fibroblasts primarily express of connexin-45 (Cx45) (*55*). Fibroblast-myocyte junctions exhibit intermediate conductance compared to myocyte-myocyte and fibroblast-fibroblast pairs, suggesting they may form Cx43:Cx45 hemichannels (*56*). Functional coupling between cardiomyocytes and fibroblasts has been demonstrated using dye transfer assays in the rabbit sinoatrial node (*57*).

However, most evidence for fibroblast-myocyte gap junctions is derived from *in vitro* studies, where connexin expression is often upregulated, or from immunostaining data showing co-localization of junctional proteins, which is not functionally relevant (*58*). The extent to which such coupling occurs *in vivo* under physiological conditions remains uncertain. Notably, fibroblasts upregulate Cx45 expression during long term recovery from MI (*59*), and it has been proposed that these cells may help passively conduct electrical signals across fibrotic regions of the myocardium (*58*).

1.5.3 Mechanical cross talk through the ECM

Perhaps one of the most critical signaling axes between fibroblasts and cardiomyocytes is through the extracellular matrix. Fibroblasts build and remodel the ECM throughout development and disease, and this dynamic network in turn transmits both mechanical and biochemical cues to the cardiomyocyte (*60*). At the tissue level, the ECM integrates and distributes contractile forces across the myocardium, and its stiffness directly impacts the amount of work cardiomyocytes can generate. Contractile work is maximized when the elastic moduli of the cardiomyocyte and its surrounding ECM are matched (*61*). If the ECM is too compliant, cardiomyocyte tension generation deforms the matrix rather than transmitting the forces intercellularly; conversely, if ECM is too stiff, contraction becomes largely isometric and cardiomyocytes experience intracellular strain (*61*). In the diseased heart, fibrosis is the primary determinant of elevated ventricular wall stiffness (*14*), which can increase up to three-fold relative to healthy tissue (*62*). Multiple studies have demonstrated a linear relationship between substrate stiffness and myocyte tension (*63*), suggesting that cardiomyocytes actively tune their contractile output in an attempt to maintain equilibrium between intracellular and extracellular

tension. Likewise, atomic-force microscopy (AFM) experiments have shown that fibroblasts adjust their internal stiffness to match that of their substrate (*64*).

Conversely, fibroblasts can increase the stiffness of the ECM in several ways. Collagen accumulation in the myocardium is strongly correlated with increased ventricular stiffness (*14*) and is a hallmark of DCM (*65*). One of the earliest compositional changes identified in DCM was a shift in the collagen I:III ratio. While ECM from healthy hearts was enriched in the more compliant collagen isoform, collagen III, DCM hearts had increased collagen I deposition, which is known to be more rigid (*66*). Proteomic characterization of the cardiac ECM has revealed that such compositional remodeling extends well beyond collagens I and III. In a murine model of heart failure with preserved ejection fraction (HFpEF), changes across more than 100 ECM proteins were shown to increase LV stiffness, even in the absence of overt increases in total ECM (*67*). Structural modifications of existing ECM proteins can further contribute to stiffening. For example, enhanced crosslinking of fibrillar collagens by lysyl oxidase (LOX) increases matrix rigidity, and LOX expression is elevated in failing DCM hearts (*68*). Changes in crosslinking can also affect collagen fibril organization and diameter, altering the nano-scale architecture of the matrix (*66*). Taken together, these studies indicate that ECM remodeling in DCM likely occurs across multiple structural scales, with each contributing to the progressive stiffening of the heart.

It is clear that there is tight mechanical regulation between the fibroblasts, ECM, and cardiomyocytes in the heart. However, the mechanisms coordinating this mechanical homeostasis remain poorly defined in DCM. While fibrosis has largely been regarded as a secondary, late-stage consequence to myocyte hypocontractility, it is unclear whether changes in the ECM are passively reflecting or actively enforcing the altered mechanical loading of the

heart. The extent to which cellular and extracellular stiffness can be reversed is also unknown, especially considering the half-life of collagen is estimated to be 117 years in cartilage and 15 years in the skin (*69*). Moreover, if ECM remodeling is irreversible, it is possible that biochemical or mechanical cues in the matrix may act as a positive feedback loop, keeping fibroblasts and myocytes dysregulated in spite of a targeted treatment.

1.6 Fibroblast state space, anti-fibrotic therapies, and ECM reversibility

Until recently fibroblast biology in the heart was largely defined using ischemic models (*70*). Recent work suggests that fibroblasts have a range of physiological responses depending on the size of the disease or injury stimulus, and that non-ischemic heart diseases, like DCM, are very different from MI. The following section reviews the current understanding of fibroblast activation states and the potential for fibrotic regression, both in DCM and other forms of heart disease, and discusses the therapeutic potential of antifibrotic strategies for reversing fibrosis and improving cardiac function.

Excerpts from the following review have been provided for this section.

Controlling cardiac fibrosis through fibroblast state space modulation

Cell Signal. 2021 Mar:79:109888. doi: 10.1016/j.cellsig.2020.109888. Epub 2020 Dec 16.

Isabella M. Reichardt[a*], Kalen Z. Robeson[a*], Michael Regnier[a,c,d], and Jennifer Davis[a,b,c,d]

These authors contributed equally to this work

[a] *Department of Bioengineering, University of Washington, Seattle, WA 98105, United States*

[b] *Department of Pathology, University of Washington, 850 Republican, #343, Seattle, WA 98109, United States*

[c] *Institute for Stem Cell & Regenerative Medicine, University of Washington, Seattle, WA 98109, United States*

[d] *Center for Cardiovascular Biology, University of Washington, Seattle, WA 98109, United States*

1.6.1 The Landscape Model of Cellular State Space

Previously, fibroblast cell states were defined rigidly, as quiescent un-activated fibroblasts, activated proliferating fibroblasts, or matrix-secreting myofibroblasts (*70*). Convention dictated that in response to a severe cardiac injury, cardiac fibroblasts would first proliferate and then transdifferentiate into myofibroblasts, a cell type that is critical for generating collagen-rich scar tissue and preventing cardiac rupture. As our understanding of heart disease and progressive cardiac remodeling has evolved, the cardiac fibroblast has emerged as a key target for heart failure therapeutics. Furthermore, recent genomic studies have greatly expanded the known complexity of cardiac fibroblast phenotypes, underscoring that the linear transdifferentiation model is insufficient to describe fibroblast fate (*70–74*). To evolve the field's understanding of injury-induced cardiac fibrosis, the complexity of the linear fibroblast transdifferentiation paradigm must be expanded. By improving the understanding of the dynamics of fibroblast state space, new therapeutic targets for treating maladaptive fibrotic remodeling may be identified.

What is cellular state space? Cell state transitions such as development, growth, maturation, senescence, and transdifferentiation are critical in both normal physiology and disease. These cell transformations are driven by shifts in genetic profile, which can be described

with a “state space” model. Classically, state space is a mathematical concept whereby dynamic systems can be described using a set of variables that comprise every possible state of the system. In the context of cell biology, this can be illustrated as a hilly landscape traversed by cells as they differentiate or transition between states (*75*, *76*). A marble analogy is often used to think about cells moving dynamically through this landscape, where peaks and valleys represent unstable and stable cell states, respectively. The position on the landscape (x/y-dimension) is determined by a compressed set of multidimensional gene expression variables—essentially representing the relative similarity of cell states. The overall height (z-dimension) of the landscape represents the activation energy required to transition between stable cell states (Figure 1). Mathematical modeling has shown that this idea of state space landscape is grounded in mathematical theory (*77*). In the heart, cardiac injuries deliver strong pro-fibrotic signals to cardiac fibroblasts. However, how signals modulate the cellular state of fibroblasts and the relationship of these state changes to matrix organization, quantity, and composition is still poorly understood.

Fibroblast cell state dynamics can inform overall matrix dynamics in the heart. Ideally, after cardiac injury, therapeutic targeting would be able to tune the heart’s fibrotic response to maintain structural integrity in the short term, preventing cardiac rupture, but reduce or abrogate cardiac fibrosis and maladaptive remodeling in the long term (*78*). There is growing evidence to suggest that tactically controlling fibroblast state via their state space landscape effectively modulates the heart’s fibrotic response, and hence has therapeutic potential (*79–82*). For example, if a therapeutic could reduce the activation energy for a myofibroblast to transition to a state with lower matrix secretion, pathologic fibrotic remodeling could be lessened. However, this goal requires identification of cardiac fibroblast state trajectories during injury, repair, and

recovery, along with the regulators of those state transitions. Determining how modifying fibroblast state transitions, either through pathway inhibition, activation, or reprogramming, impacts fibroblast population dynamics will be vital towards understanding how therapeutic state modulation alters the physiological role of fibroblasts in the heart.

Epigenetic and transcriptional analyses by high-throughput genome sequencing technologies like RNAseq, ATACseq, and CHIPseq may be used to molecularly define the state space occupied by cardiac fibroblasts. These new techniques enable unbiased and global snapshots of cellular state space transitions. Since transcript sequencing at the single cell level captures a snapshot of cells scattered along the differentiation or transdifferentiation trajectory; nuanced or ephemeral cell populations can be identified. This can be achieved using pseudotime analysis to understand how cells are moving through state space; however, pseudotime is best corroborated by serial sampling (*83*) and RNA labeling (*84*) to allow for more definitive analysis of how cells move through transcriptional space. This sort of analysis is exemplified in the field of hematopoietic progenitor differentiation (*85*, *86*), which showed that the differentiation of hemopoietic progenitors into either erythroid or myeloid lineages required destabilizing the progenitor state (*86*) and movement through metastable intermediate substates during the differentiation process (*85*). Since state destabilization seems to be critical for state transition, cardiac fibroblasts may undergo similar cell state destabilizations to form fibrosis-producing myofibroblasts in the heart after injury. Approaching fibroblast transdifferentiation through the lens of multidimensional state space is critical to developing the next generation of therapeutic approaches for cardiac fibrosis.

1.6.2 Cardiac fibroblast states

While it was previously believed that cardiac myofibroblasts originated from several different sources, such as resident endothelial cells or circulating immune cells (*87–92*), genetic lineage tracing studies have shown that the majority (>95%) of activated myofibroblasts in the heart are derived from resident cardiac fibroblasts expressing Transcription Factor 21 (Tcf21) and Platelet-derived Growth Factor Receptor α (Pdgfrα) (*93–97*). In the uninjured myocardium, quiescent Tcf21 and Pdgfrα These developmental studies provide new insight into how hypocontraction during the postnatal period shapes the trajectory of dilated cardiomyopathy in adulthood. Transiently suppressing the pathogenic mutation during development substantially delayed the onset of myocyte dysfunction and adverse remodeling. While these mice ultimately developed DCM, the delayed phenotype suggests that pathogenic processes initiated during early myocardial maturation exacerbate disease severity later in life. This finding aligns with the broader conclusion of this dissertation, which is that timing and duration of transgene expression critically influence both the severity of disease and the extent to which the myocardium can recover.

We initially hypothesized that fibroblasts from the Postn^{+} lineage might be a key driver of the early fibroblast expansion in I61Q hearts, and that suppression of the mutant cTnC during development would halt this proliferation and was the mechanism behind the delayed onset. Although preliminary histological data suggested increased PDGFRα^{+} fibroblasts in Postn-rich regions, lineage tracing revealed that Postn^{+} fibroblasts themselves were not hyperproliferative in DCM. In fact, their proportional contribution to the total fibroblast pool appeared to decline, suggesting that other fibroblast subsets may be responsible for the expansion observed in this model. Given that POSTN can initiate fibroblast proliferation (*291*). This data together could

potentially indicate fibroblast proliferate in response to encountering POSTN in the matrix rather originating from the Postn+ lineage. To further support that the Postn^{+} population is not the primary effector, development p38 MAPK deletion did not prevent dysfunction, dilation, or hypertrophy. This suggests that the Postn^{+} developmental fibroblast subset is not the primary driver of early fibroblast expansion or disease initiation in this model, and that inhibiting this pathway during development is not protective.

Overall, these results emphasize that the developmental period is a critical window for shaping long-term cardiac outcomes. However, not all cell populations that are highly active during this window are necessarily culpable in disease initiation, underscoring the need for precise identification of pathogenic drivers before pursuing early-life interventions.

These developmental studies provide new insight into how hypocontraction during the postnatal period shapes the trajectory of dilated cardiomyopathy in adulthood. Transiently suppressing the pathogenic mutation during development substantially delayed the onset of myocyte dysfunction and adverse remodeling. While these mice ultimately developed DCM, the delayed phenotype suggests that pathogenic processes initiated during early myocardial maturation exacerbate disease severity later in life. This finding aligns with the broader conclusion of this dissertation, which is that timing and duration of transgene expression critically influence both the severity of disease and the extent to which the myocardium can recover.

We initially hypothesized that fibroblasts from the Postn^{+} lineage might be a key driver of the early fibroblast expansion in I61Q hearts, and that suppression of the mutant cTnC during development would halt this proliferation and was the mechanism behind the delayed onset. Although preliminary histological data suggested increased PDGFRα^{+} fibroblasts in Postn-rich

regions, lineage tracing revealed that Postn^{+} fibroblasts themselves were not hyperproliferative in DCM. In fact, their proportional contribution to the total fibroblast pool appeared to decline, suggesting that other fibroblast subsets may be responsible for the expansion observed in this model. Given that POSTN can initiate fibroblast proliferation (*291*). This data together could potentially indicate fibroblast proliferate in response to encountering POSTN in the matrix rather originating from the Postn+ lineage. To further support that the Postn^{+} population is not the primary effector, development p38 MAPK deletion did not prevent dysfunction, dilation, or hypertrophy. This suggests that the Postn^{+} developmental fibroblast subset is not the primary driver of early fibroblast expansion or disease initiation in this model, and that inhibiting this pathway during development is not protective.

Overall, these results emphasize that the developmental period is a critical window for shaping long-term cardiac outcomes. However, not all cell populations that are highly active during this window are necessarily culpable in disease initiation, underscoring the need for precise identification of pathogenic drivers before pursuing early-life interventions.

expressing fibroblasts make up ~15% of the non-myocyte cardiac cell population, whereas activated fibroblasts and myofibroblasts are extremely rare or non-existent (*97*). This changes with injury or disease, as quiescent fibroblast progenitors begin transitioning to new states (*70*). Fibroblast state transitions have been most characterized in the myocardial infarction (MI) model where within two days of injury, a subset of cardiac fibroblasts become proliferative and activated. These cells are marked by expression of the matricellular protein Periostin (Postn) (*79*, *96*, *98*) and minor to moderate expression of alpha smooth muscle actin (*Acta2 or* αSMA) (*79*, *96*, *98*), which gives these cells new contractile function. Importantly, Postn deletion blocks the formation of myofibroblasts (*82*), indicating that in addition to labeling the myofibroblast

state it also regulates this transition. In the days following injury, these activated fibroblasts mature into fully activated myofibroblasts, which boost secretion of matrix proteins and alter the composition of the extracellular matrix (ECM) to form a rigid scar (*99*, *100*). More mature myofibroblasts are identified by their strong expression of collagens I and III, αSMA, and a splice variant of fibronectin, Fibronectin Containing Extra Domain A (Fn-EDA) (*79*, *95*, *96*, *98*, *101*). These cells also exhibit reduced expression of Tcf21 and Pdgfrα (*79*, *102*).

Recent studies demonstrate that fibroblast cell state is more complex than previously thought, suggesting that a dynamic state space model may more accurately depict fibroblast transdifferentiation then the traditional linear model (**Figure 1.3**). This is supported by recent findings regarding myofibroblast cell fate after injury resolution. Contrary to older studies, newer data has identified that most myofibroblasts don't undergo apoptosis after injury resolution (*103*, *104*), but rather transition to a new state or regress back towards quiescence depending on the type of injury (*71*, *79*). For example, around 14 days after myocardial infarction (MI) myofibroblasts appear to transition to a matrifibrocyte state that is molecularly defined by the expression of chondrocyte and osteogenic genes (*71*). These matrifibrocytes are derived from myofibroblasts of the *Postn* lineage and are found in mature scars using the markers chondroadherin (Chad), cartilage oligomeric matrix protein (Comp), and CAP-Gly Domain Containing Linker Protein 2 (Clip2) (Figure 1). This subtype of cardiac fibroblast is postulated to chronically maintain the infarct scar. In contrast, *Postn*-traced myofibroblasts reverted to a less activated state after only two weeks of recovery from chronic stimulation of the heart via Angiotensin II (AngII) and phenylephrine (PE) (*79*). These data raise questions about what is a "deactivated" myofibroblast, and how similar is this state to its original quiescent fibroblast progenitor. Another possible myofibroblast state transition is senescence. Research in cancer

biology identified that senescent myofibroblasts often secrete enzymes that proteolytically degrade the extracellular matrix (*105*). This state has also been identified in the heart and may be essential for reversing cardiac fibrosis during the heart's recovery from injury (*106*). The disappearance of myofibroblasts over time via transdifferentiation, deactivation, and senescence suggests that the myofibroblast state is transient and likely unstable (*71*, *73*). Using a state space model, this could be described by positioning myofibroblasts in a very shallow "valley", indicating that this state requires minimal activation energy to move into a more stable state (**Figure 1.3**). In the heart, myofibroblasts might transition back to the progenitor state or move towards a more mature fibroblast injury phenotype, such as the matrifibrocyte. Although this hypothesis has not been directly examined, it also opens up questions regarding where these cellular states reside in multidimensional molecular state space and how different fibroblast states can impact cardiac structure and function. The impact of redefining fibroblast transdifferentiation as a multidimensional state space model provides a more complex and comprehensive cellular and molecular road map that will be crucial for developing new targeted antifibrotic therapeutics.

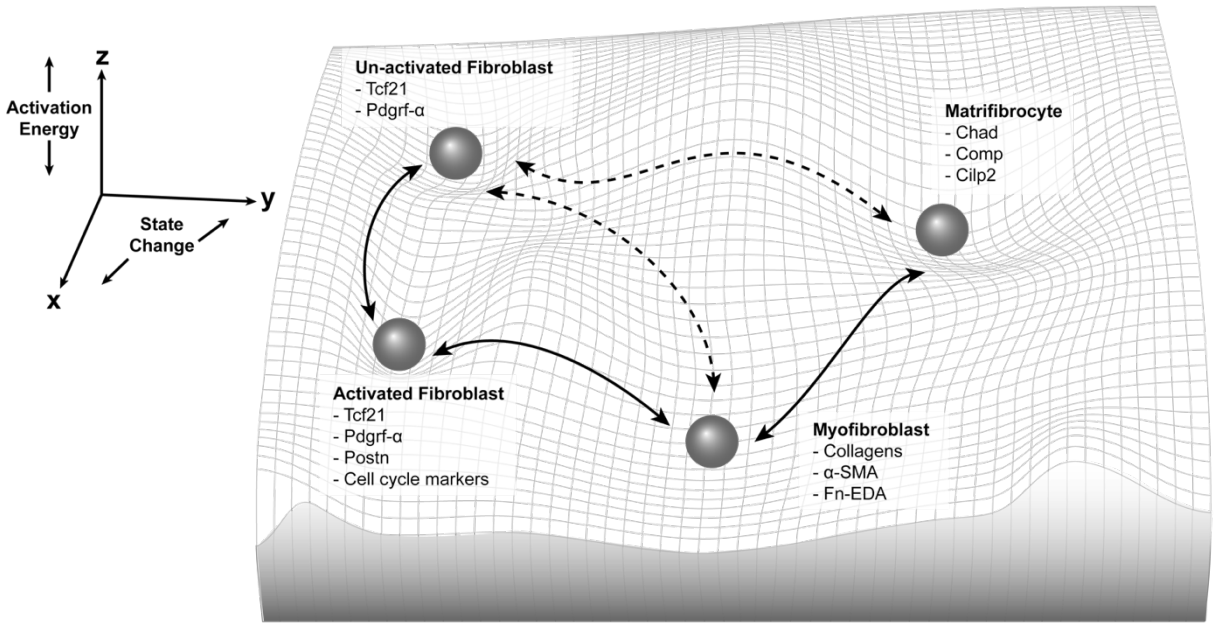

Figure 1.3: Cardiac Fibroblast Movement in Cell State Space. *Cardiac fibroblasts have long been thought to exist on a linear continuum between an inactivated state and a fibrotic matrix secreting myofibroblast state. This figure depicts a more complete picture of cardiac fibroblast "state space." State transition may be reversible indicated by the bidirectional arrow heads, new fibroblasts cell states may exist (e.g. matrifibrocytes), and transdifferentiation directly between these states might be possible indicated by dotted lines. Importantly the third dimension of state space "activation energy" is critical to understanding this concept. For example, the myofibroblast state could be unstable and not in a deep valley, indicating that a small amount of activation energy could induce a state change. In contrast, a more permanent cell state, like a cardiomyocyte, would have a much deeper valley to represent low likelihood of state transition. Known gene expression markers of the fibroblast states shown are listed, however it is important to note that a position in multidimensional state space is far more complex than a small number of marker genes.*

1.3 Cardiac fibroblast & myofibroblast heterogeneity

Single cell RNA sequencing (scRNAseq) techniques have broadened the understanding of fibroblast cell state and provided evidence for a more nuanced fibroblast heterogeneity in both healthy and injured hearts. The general population of resident fibroblasts activate, proliferate, and increase their matrix production as described previously, but the molecular heterogeneity present in these populations suggests they consist of a diverse group of substates. However, these new clusters of molecularly distinct fibroblasts have not yet been functionally validated by other techniques. Three studies recently investigated the diversity of non-myocytes in murine hearts. Skelly *et al.* were one of the first groups to identify new cardiac fibroblast states by performing scRNAseq on cells isolated from uninjured hearts. A new fibrocyte population of cells was identified, expressing transcriptional markers of both fibroblasts (collagen type I alpha 1 chain (Col1a1), Pdgfrα, and Tcf21) and immune cells (high affinity immunoglobulin gamma Fc receptor I (Fcrg1), cluster of differentiation 14 (Cd14), and protein tyrosine phosphatase receptor type C (Ptprc)). However, the functional role of these cells in the heart at baseline or in injury was not investigated. Quiescent fibroblasts were also shown to produce growth factors for the maintenance of other cardiac cells, including neurons, endothelial cells, and mural cells, highlighting that cardiac fibroblasts play a larger role in cardiac homeostasis beyond matrix secretion (*74*). These findings demonstrate cardiac fibroblast state is heterogenous and suggest these unique fibroblast clusters may have different functional roles.

Farbehi *et al*. expanded on this work, identifying new quiescent and activated fibroblast substates in response to MI. The quiescent fibroblast population segregated into two major groups marked by relative expression of the surface marker spinocerebellar ataxia 1 (Sca1). Fibroblasts with strong expression of Sca1 had higher expression of cell adhesion genes, whereas fibroblasts with low Sca1 expression had high expression of signal transduction genes. This

would suggest that the quiescent fibroblasts have separate subpopulations involved in cell adhesion and signal transduction. Farbehi *et al.* also used lineage tracing to isolate and selectively sequence Pdgfrα expressing cells. By deep sequencing a fraction of the cells, they identified novel myofibroblast subtypes expressing both profibrotic and antifibrotic signatures. They also showed the canonical changes in the proportions of cells falling into each of these subtypes three to seven days post injury. In line with the established fibroblast state paradigm, activated and cycling fibroblasts peaked 3 days post infarction and myofibroblasts peaked 7 days post infarction (*72*), which is consistent with state change timelines established by other approaches (*71*). Two novel fibroblast states were also identified. One was a transitory fibroblast state, which cell trajectory analysis placed as an intermediate substate between Sca1-low and the second novel state defined by Wnt inhibitory factor 1 (Wif1) expression. These cells expressed antifibrotic paracrine signaling and were present at all time points, persisting for at least 7 days after infarction. This fibrosis inhibition cell state opposes all the activating fibroblasts in the heart by expressing inhibitors of wingless-related integration site (WNT), cellular communication network factor 2 (Ccn2) and transforming growth factor beta (TGFβ) signaling and seems to be important for the timing of heart repair (*72*). Farbehi *et al*. also reanalyzed the data from *Skelly et al.* and were able to find all of the same baseline cell populations identified in their work.

Most recently, McLellan *et al.* completed a scRNAseq study looking at the fibroblast populations present after an AngII infusion model. This study also found the Wif1 expressing cell population identified by Farbehi *et al*. Surprisingly, no αSMA expressing myofibroblast population was detected. Instead they identified two fibroblast subpopulations expressing the matricellular proteins Cilp and thrombospondin 4 (Thbs4) (*73*). Pseudotime analysis showed that

Thbs4 expressing cells arose from Cilp cells. The Cilp and Thbs4 expressing fibroblasts also expressed markers similar to the matrifibrocyte (Comp, secreted frizzled related protein 2 (Sfrp2), and cellular communication network factor 5 (Ccn5)) indicating that these markers could be important for post-injury fibroblast states. Additionally, Cilp expressing fibroblasts expressed higher levels of matrix remodeling proteins. None of these groups expressed αSMA or had the molecular components of canonical myofibroblasts (*70*). However, these cells did express Postn and seemed to be responsible for extracellular matrix production in this AngII infusion injury model. This suggests that different injury models may elicit a variety of fibroblast states in order to modulate the composition and quantity of extracellular matrix (**Figure 1.4A**). Notably, there are two types of fibrosis: replacement and reactive. Replacement fibrosis occurs when there is significant cardiomyocyte death, such as with MI, ischemia reperfusion (I/R), or cryoablation. The fibrotic response generated from these injuries is vital for preventing ventricular rupture after massive myocyte loss. In contrast, reactive fibrosis usually results in fibrosis that accumulates in the interstitial space. In animal models, reactive fibrosis is observed in models of pressure overload or treatment with a cocktail of AngII and PE (*107*). To date it is unclear whether the same cellular and molecular mechanisms underlie these different types of fibrosis. Thus, the results of these scRNAseq studies begin to elucidate the different substates that fibroblasts might occupy in response to different injuries. Moreover, robust time course and genetic perturbation studies will be needed in order to ascertain if the substates identified represent novel cell states with discernable functions or are transition states and represent cells undergoing transdifferentiation.

These scRNAseq studies have also determined that intercellular communication between fibroblasts and other non-myocytes is critical for proper heart function (*72–74*). By mapping

expression of ligands and cognate receptors, these scRNAseq studies have started to elucidate these interactions. Skelly *et al*. found that fibroblasts are the most promiscuous cell type in the heart, with fibroblasts expressing ligands that target the other cardiac cell types and promote survival of specific cardiac cell populations. *In vitro* coculture experiments showed that fibroblast signaling is necessary but not sufficient for cardiac macrophage and endothelial cell growth (*74*). McLellen *et al*. corroborated these results with their scRNAseq data set, showing that fibroblast signaling is crucial in the uninjured heart. Their analysis of ligand/receptor networks post AngII-induced hypertrophy showed an increase in communication signals between all cell types and an upregulation of signaling pathways associated with amino acid synthesis and collagen fibral organization. Downregulated signaling pathways in this study were enriched for inflammation and leukocyte/monocyte trafficking, indicating a suppression of the inflammatory response. In addition to direct signaling with other cell types, cardiac fibroblasts' regulation of matrix structure and composition is an important signaling modality for other cell types in the heart. It has been shown that matrix composition—specifically the presence of the extracellular heparan sulfate proteoglycan agrin—can promote cardiomyocyte proliferation even in adult mammals (*108*). Finally, fibroblasts can also interact with other cardiac cells through mechanotransduction. Coculture of macrophages and fibroblasts on a fibrillar collagen matrix showed that macrophages are attracted by the dynamic contraction of activated fibroblasts (*109*). This could mean that αSMA positive contracting fibroblasts play a role in initiating the immune response post injury. Future work will need to continue elucidating the important role that fibroblasts play in intercellular signaling, both at baseline and in response to injury. The role cardiac fibroblasts play in signaling is at a nascent level of understanding. More in-depth reviews of communication between cardiac fibroblasts and other cell types can be found here (*110*, *111*).

Collectively, these scRNAseq studies demonstrate the limitations of the historic view of injury-induced fibroblast to myofibroblast transdifferentiation, underscoring the need for this paradigm to be expanded to include fibroblast and myofibroblast population heterogeneity, intermediate substates, and transient cell states. Each of these states have distinct patterns of gene expression and, presumably, different responsibilities within the injured myocardium, yet most of these studies lack true functional validation. This highlights a barrier in the field: integrating high dimensional data from transcriptome sequencing with protein expression and measurements of fibroblast structure and function. It is important to note that these scRNAseq experiments were carried out in mice—with the exception of McLellen *et al.,* where findings were corroborated with human bulk RNAseq data (*73*). Therefore, while it seems likely that the human fibroblast cell state landscape resembles that of the mouse fibroblast, the human fibroblast landscape still remains poorly characterized.

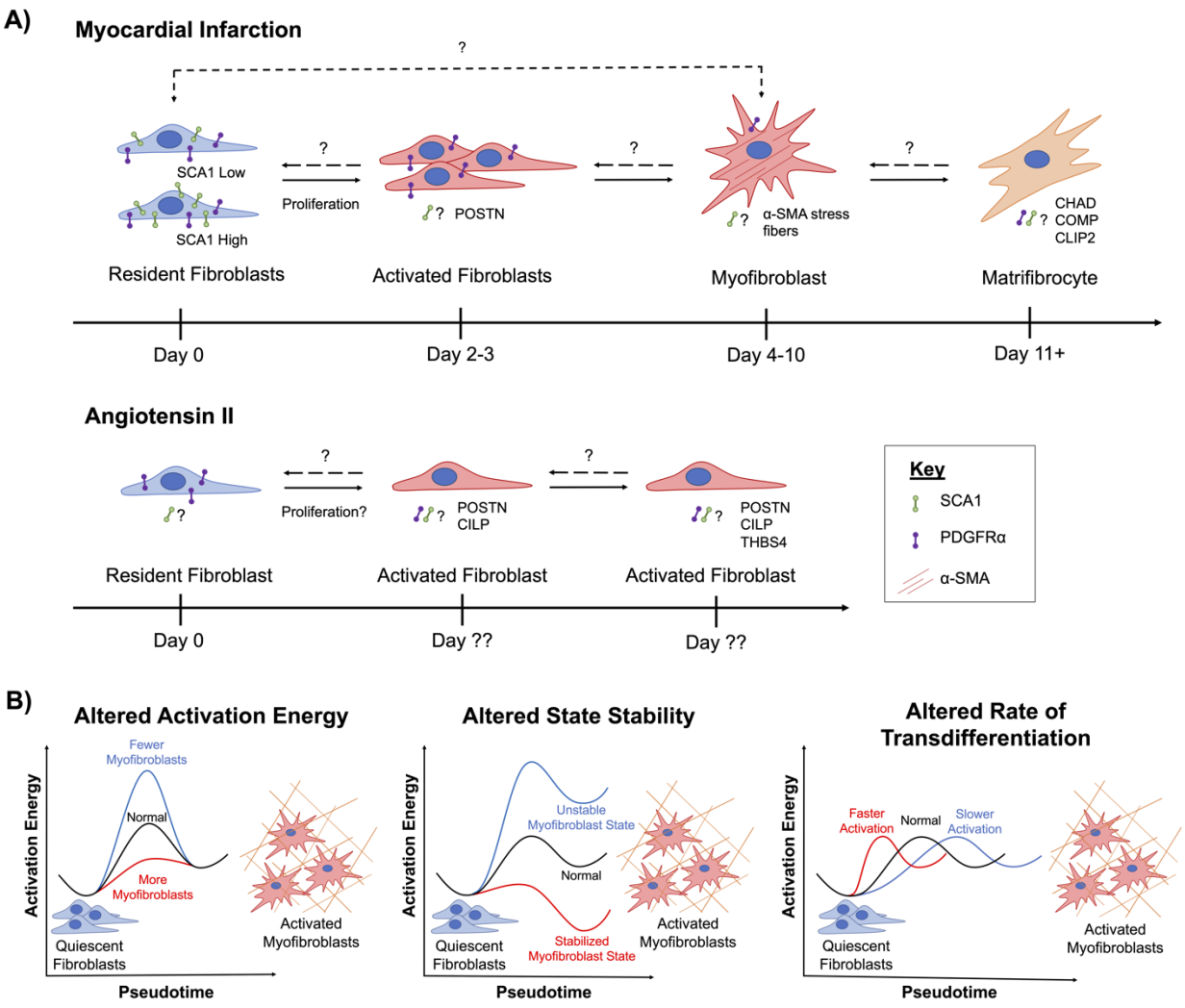

Figure 1.4: Models of Cardiac Fibroblast State Transitions. ***A)*** *Differential Fibroblast Injury Response in Myocardial Infarction and Angiotensin-Infusion Injury Models. Recent RNAseq studies suggest that fibroblasts state transitions vary based on the injury stimulus. This figure summarizes what is known about fibroblast transdifferentiation in response to myocardial infarction and angiotensin II infusion, but also illustrates unknowns regarding: the proliferation phase in an Angiotensin model, the genotype (SCA1 high or low) of resident fibroblast population that transitions to a myofibroblast identity, and SCA1 expression as fibroblast undergo state transitions.* ***B)*** *State Space Modulation of Myofibroblast Identity. Perturbing genes in the fibrotic pathway can alter the fibroblast state space landscape, changing*

the number of α-SMA expressing myofibroblasts. Illustrations represent several hypothetical outcomes from fibroblast state space modulation.

Robust lineage reporters for quiescent fibroblasts and myofibroblasts have dramatically moved forward the field of cardiac fibroblast biology. (*79*, *93*). The next step forward is to use new single cell analysis tools to tease apart the genomic complexity behind any given lineage reporter. This will allow cardiac fibroblasts substates to be placed relative to each other in multidimensional state space (**Figure 1.3**). Lineage reporters permanently label a cell based on the expression of a single gene. While they are important for tracking a cells history, these cells can only be labeled once, limiting the identification of various molecular states a single cell might occupy throughout its differentiation trajectory. Therefore, development of a multi-lineage reporter may be useful for fully teasing apart fibroblast state dynamics. For now, scRNAseq experiments on isolated lineage-traced cells can begin to elucidate some of the complexities that underlie each cardiac fibroblast lineage (*72*, *73*).

1.6.3 Modulating Fibroblast Cell State to Alter Myocardial Fibrosis

Many factors must converge to drive cell state transitions. Injuries in the heart often involve several stimuli, such as ischemia, inflammation, or cell death, which overwhelmingly push cardiac fibroblasts towards activated states. Enhancing or inhibiting key genes can reshape the state space landscape, making it more or less likely to achieve a fibrotic fibroblast state. Therefore, these pathways can be leveraged to shift cardiac fibroblasts into more desirable cell states, mitigating fibrosis and halting maladaptive cardiac remodeling. The following section summarizes *in vivo* studies defining fundamental regulators of cardiac fibroblast state and how they have been therapeutically targeted to improve cardiac fibrosis and dysfunction.

1.1.1.1 TGFβ Pathway

TGFβ is a master regulator of the fibrotic response. The TGFβ receptor has two subunits: the type I and type II TGFβ receptors (Tgfbr1/2). In the canonical signaling pathway, binding of TGFβ to Tgfbr1/2 results in phosphorylation of the transcription factors Smad2 and Smad3. Once phosphorylated, these proteins complex with Smad4 in the cytoplasm, translocate to the nucleus, and promote a profibrotic genetic profile (*112*). Modulating the expression of these proteins alters fibroblast cell state and, by extension, fibrosis in the heart due to injury.

In ischemic injuries, Smad3 expression is important for proper cardiac myofibroblast function, but does not appear to be a driver of the myofibroblast state. Knockdown of Smad3 increased αSMA expressing myofibroblast density and proliferation, but resulted in reduced (*113*) or disorganized collagen deposition (*114*). Deletion in both the whole heart and Postn-expressing fibroblasts resulted in increased myofibroblast number (*113*, *114*), suggesting that Smad3 is not involved in initiation or maintenance of the myofibroblast state. However, myofibroblast morphology and alignment in the infarct area was impaired, and isolated fibroblasts exhibited decreases in collagen I and III (*114*), indicating that Smad3 is essential for mounting a proper fibrotic response to ischemic injuries. The mechanism behind the proliferative myofibroblast phenotype seen in these knockouts is unknown; it could be a direct effect of Smad3 deletion or secondary due to poor collagen deposition. In pressure overload models, Smad3 is also a critical regulator of myofibroblast function and state, with both global and fibroblast-specific Smad3 knockdown resulting in decreased interstitial fibrosis (*112*, *115*). Smad2 knockout did not reduce fibrosis, suggesting Smad3 is the major driver of the fibrotic response in the canonical pathway. Deletion of Smad2 and Smad3 together (Smad2/3) decreased ECM gene expression, fibroblast proliferation, and αSMA positive myofibroblast number after

transverse aortic constriction (TAC) (*112*). These results suggest that Smad2/3 are important for fibroblast function, expansion, and induction of the αSMA positive myofibroblast state in pressure overload systems. The transcription factor Scleraxis has been identified as a key downstream effector of the Smad3-induced myofibroblast phenotype, with Scleraxis knockdown inhibiting the myofibroblast state (*116*, *117*). While not studied in a disease context, decreased expression of Scleraxis may underlie the lack of myofibroblasts in Smad3 null mice. The opposing proliferative response of fibroblasts in ischemic and pressure overload models has not been studied. One possible explanation is the relative magnitudes of each injury: redundant fibrotic signaling pathways may take over in ischemic injuries to prevent ventricular rupture. This reiterates that fibroblasts likely have different cell states for responding to different injury stimuli. Notably, deletion of Smad2/3 did not confer any functional benefits. However, upstream knockdown of Tgfbr1/2 in fibroblasts decreased interstitial fibrosis, abrogated systolic and diastolic function, and improved cardiac hypertrophy (*112*). While fibroblast specific effects were not investigated in this model, TGFβ signaling appears to affect heart function and hypertrophy through Smad2/3-independent pathways.

TGFβ signaling is not restricted to just fibroblasts. In pressure overloaded hearts, phosphorylated Smad3 has been found in the nuclei of cardiomyocytes and vascular cells, as well. Myocyte-specific deletion of Tgfbr2 reduced both pathological hypertrophic remodeling and interstitial fibrosis (*118*). These data suggest that in pressure overload, myocyte TGFβ signaling also plays a role in defining fibroblast state, although exact fibroblast effects were not studied. In contrast, myocyte specific deletion of Smad2/3 in TAC mice did not reduce reactive fibrosis, indicating that the myocyte effect on fibroblast state may occur through secondary or non-canonical pathways (*112*). For example, cardiomyocyte specific Smad4 knockout in

uninjured mice changed sarcomere calcium sensitivity, causing these mice to develop a fibrotic, dilated cardiomyopathy (DCM) phenotype. This underscores how changes in myocyte health and function can alter fibroblast state.

1.1.1.2 p38 Mitogen Activated Protein Kinase (MAPK)

TGFβ can activate both canonical and non-canonical fibrosis signaling pathways. When the TGFβ ligand binds to its receptors, the MAPK pathways are also activated, including the p38 mitogen-activated protein kinase (p38), extracellular signal-regulated kinase (ERK), and c-Jun-N-terminal kinase (JNK) (*112*). While little work has been done *in vivo* with ERK and JNK in the context of cardiac fibrosis or fibroblasts, p38 has been identified as a major regulator of the fibrotic response in the heart (*100*). In fact, increasing evidence is demonstrating that these non-canonical pathways may play a significant role in mediating fibroblast state and the fibrotic response to injury (*100*, *119*).

p38 is a crucial regulator of the myofibroblast state. In ischemic injuries, targeted genetic deletion of the p38α isoform from both Tcf21 and Postn-expressing fibroblasts drastically decreased reparative fibrosis, leading to massive mortality due to ventricular rupture (*82*). In contrast to Smad3 deletion in ischemic injuries (*113*, *114*), knockdown of p38α in both fibroblast cell states grossly decreased the number of αSMA expressing myofibroblasts in the infarct and border zones (*82*). These results were replicated in an AngII/PE reactive fibrosis model. In a gain of function experiment, p38 was activated by creating a transgenic mouse where the p38 regulator, mitogen activated kinase kinase 6 (MKK6), was made constitutively active. This model resulted in increased cardiac fibrosis and number of αSMA positive myofibroblasts at baseline and in response to I/R and AngII/PE-induced injuries. These data suggest that p38α is a

potent activator of the myofibroblast state, essential for both mounting and sustaining the matrix secreting αSMA positive myofibroblast phenotype (*82*). In the context of state space, it is possible that p38 deletion increases the activation energy required for myofibroblast transdifferentiation, whereas p38 overexpression decreases this activation energy, accounting for the respective changes in myofibroblast number (**Figure 1.4B**).

In addition to TGFβ-driven signaling, recent work suggests that p38 incorporates spatial cues in its determination of fibroblast state (*120*). Integration of fibroblast lineage tracing and matrix alignment analyses revealed that Postn and αSMA expressing myofibroblasts are most commonly found in the border zone of MI hearts, where the ECM is most aligned. The center of the scar, often characterized by disordered collagen organization (*121*) exhibited lower myofibroblast density. Myofibroblast morphology correlated with matrix alignment: myofibroblasts found in the aligned border zone were highly elongated, while those found in the disorganized scar were more circular. These results were recapitulated *in vitro* by culturing isolated adult cardiac fibroblasts on biomimetic nanofabricated devices with random or aligned patterns. Fibroblasts cultured on the aligned patterns showed increased myofibroblast transdifferentiation and expression of matrix proteins than those cultured on random patterns. TGFβ failed to exacerbate the myofibroblast phenotype on aligned patterns, potentially suggesting that chemical and mechanical cues converge onto a single pathway to induce myofibroblast transdifferentiation. Deletion of p38 abrogated pattern-induced αSMA positive myofibroblast transdifferentiation (*120*). Moreover, alignment initiated p38-mediated stabilization of the yes-associated protein (YAP), a pathway that is highly studied in the context of cancer (*122*). Transduction of a constitutively active nuclear YAP was sufficient to activate

the myofibroblast cell state. These data suggest that p38 integrates both spatial and chemical cues to mediate fibroblast cell state (*123*).

1.1.1.3 Serum Response Factor (SRF), Transient Receptor Potential Channels (TRPC), and YAP

Multiple pathways have been found to converge or intersect with the p38 pathway, including the myocardin-related transcription factors-serum response factor (MRTF-SRF) axis, transient receptor potential cation channel subfamily C member 6 (TRPC6), and YAP. The transcription factor SRF is essential for vascular smooth muscle cell (SMC) differentiation (*124*) and has been implicated in inducing the contractile, SMC-like genetic profile in myofibroblasts. SRF binds to a promotor sequence known as the serum response element (also known as the CArG box) with the help of mechanosensitive transcription co-factors, such as MRTF-A and MRTF-B. The activity of these co-factors is highly dependent on actin dynamics, and is therefore regulated by Rho GTPases (*125*). This signaling axis is known to activate due to injury, changes in mechanical forces and cell shape, or with TGFβ signaling (reviewed in (*126*)), highlighting its connection to the Smad and p38 pathways.

MRTF-A and TRPC6 are downstream effectors important for induction of the myofibroblast state. Global deletion of MRTF-A post-MI decreased fibrosis, non-myocyte proliferation, and overall number of αSMA positive fibroblasts, indicating that MRTF-A is necessary for the αSMA positive myofibroblast phenotype (*125*). Transient receptor potential canonical family member 6 (TRPC6) has been identified as an essential target of SRF through the p38 pathway (*119*). Previously linked to pathological hypertrophic remodeling, TRPC6 upregulation is known to activate calcineurin and nuclear factor of activated T cells (NFAT) (*127*). Global knockout of TRPC6 in MI mice caused higher incidence of ventricular rupture,

decreased function, and reduced collagen deposition. Mechanistic studies *in vitro* with isolated cardiac fibroblasts demonstrated that TRPC6 expression is directly upregulated by SRF and can be inhibited with p38 inhibitors. Moreover, TRPC6 overexpression was a potent activator of myofibroblasts, and TRPC6 knockout abrogated TGFβ-mediated myofibroblast transdifferentiation (*119*). Together these data demonstrate that TRPC6 is a crucial downstream effector of p38-dependent transitions of fibroblasts into fibrosis-producing myofibroblasts.

YAP inhibition is essential for fibroblast specification during development and maintenance of the quiescent fibroblast cell state in adults. YAP is a transcriptional coactivator in the Hippo pathway that is negatively regulated by the kinases Lats1 and Lats 2 (Lats1/2) (*122*). Deletion of Lats1/2 from the developing mouse heart prohibited epicardial differentiation into mature cardiac fibroblasts (*80*). Deletion of Lats1/2 in adult cardiac fibroblasts destabilized the quiescent fibroblast state, causing spontaneous myofibroblast transdifferentiation (**Figure 1.4B**). Lats1/2 knockout mice had gross increases in fibrosis, both at baseline and with MI injury (*122*). These data suggest that Lats1/2-dependent YAP inhibition is crucial for maintaining the quiescent fibroblast state. YAP signaling intersects with both p38 and SRF pathways. MRTF-A mRNA and protein levels have been shown to directly correlate with YAP expression. In MI, deletion of YAP from Tcf21 and Col1a1-expressing fibroblasts decreased collagen deposition, fibroblast proliferation, and αSMA positive fibroblast activation. Similar decreases in fibrosis were seen in AngII/PE-treated mice with loss of YAP function in Tcf21 fibroblasts. MRTF-A levels were also attenuated in the YAP knockouts, suggesting that YAP is required for MRTF-A activity (*128*). These results demonstrate the importance of YAP/MRTF-A signaling in the myofibroblast state transition in response to ischemic and chronic injuries. In the p38 pathway, YAP appears to be a crucial component for transduction of mechanical signals via focal

adhesions (*123*, *129*). Notably, knockdown of YAP in fibroblasts did not increased mortality due to ischemic injury (*128*), indicating that other fibrotic signaling pathways may be responsible for the reparative fibrosis response, although this may also be an artifact of increased myocyte survival. In contrast, myocyte specific deletion of YAP resulted in dramatically increased fibrosis and mortality post-MI (*130*) and neonatal deletion of YAP in cardiomyocytes impaired regeneration (*131*). The differential effects of YAP signaling in myocytes and fibroblasts again highlights how myocyte health can affect fibroblast cell state, but also underscores the level of specificity required to target this pathway therapeutically.

Collectively, these studies demonstrate that manipulating the expression of key proteins in the fibrotic cascade can alter fibroblast state space dynamics, resulting in altered global fibrosis. However, how state space is altered is still a major unknown for the field. This section reviewed how pathway manipulations can alter myofibroblast density in the myocardium. Based on this data, there appear to be at least three potential mechanisms for state space modulation: (1) a change in the activation energy required to reach a myofibroblast state, (2) a change in quiescent or activated fibroblast state stability, or (3) a change in the rate of myofibroblast transdifferentiation. With respect to the first mechanism, altered activation energy by p38 inhibition or enhanced activity likely alters the activation energy required to achieve a myofibroblast state. Because p38 inhibition results in dramatically fewer myofibroblasts in response to injury (*100*), it's postulated that loss of p38 function increased the activation energy needed to achieve a myofibroblast state. In contrast, p38 activation by MKK6 resulted in spontaneous myofibroblast transdifferentiation without an injury stimulus (*100*), suggesting that this perturbation to p38 signaling lowered the activation energy, making the myofibroblast transition easier (**Figure 1.4B**). For the second mechanism (altered stability), we postulate that

YAP regulates fibroblast and myofibroblast state stability because models with increased YAP activity (via Lats1/2 knockdown) caused a mass activation of myofibroblasts in both uninjured and infarcted mouse hearts (*122*). Conversely, YAP inhibition decreased myofibroblast transdifferentiation (*128*). Hence a reasonable hypothesis is that YAP inhibition stabilizes the quiescent fibroblast state while YAP activity stabilizes the myofibroblast state. (**Figure 1.4B**). With respect to the third mechanistic model (altered rates of transdifferentiation), there is minimal evidence to support this mechanism in the cardiac literature, but dermal wound closure which is mediated by myofibroblasts occurred much slower in TRPC6 knockout mice (*119*). This suggest that modulations of some molecular regulators only slow down or speed up the transition to a myofibroblast state, without entirely inhibiting transdifferentiation (Figure 2b). However, the mechanisms for these changes in state space landscape are hypothetical and of course could include some combination of the mechanisms proposed here. Moreover, these mechanisms are simplified to only the conversion of resident fibroblasts to myofibroblasts, and a more robust analysis may need to examine the state transitions in between. For example, Scleraxis and Pdgfrα have been implicated in forming and maintaining resident cardiac fibroblasts (*102*, *116*). This suggests that there are key regulators to every fibroblast state and demonstrates that the complexity of fibroblast state space transcends myofibroblast transdifferentiation. To truly begin elucidating how these regulators control state space, rigorous scRNAseq experimentation must be incorporated into pathway manipulation studies, although these experiments may be cost prohibitive. Adoption of analyses from the reprogramming field may be beneficial; for example, free energy calculations may be helpful for determining relative state stabilities (*132*). RNA velocity and pseudotime calculations may be useful for characterizing state transitions and differentiation rates (*72*, *73*). Other experiments, analyses,

and calculations may yet need to be developed to be able to make robust state space determinations. For example, the field currently lacks methods for integrating multiomic transcriptional and proteomic changes. While scRNAseq will begin to uncover information about state space, these data must be validated with protein-based and physiologic assays. Ultimately, a better understanding of the regulators of the various fibroblast states, and how their modulation affects global cardiac fibrosis, will enable therapeutic targeting of specific states to inhibit maladaptive cardiac remodeling.

1.6.4 Antifibrotic Therapeutics

Targeted genetic manipulation is essential for identifying the cell-specific role of a given signaling pathway, and these data can be leveraged to develop antifibrotic therapies for patients. In some cases, improvements in fibrosis do not always beget improvements in function. This could be because the myocytes are damaged to a point of no return, where lessened fibrosis cannot improve function. Alternatively, systems with less fibrosis could also have a fundamentally different type of fibrosis, with different biochemical composition, architecture, or organization resulting in an overall stiffer heart despite fibrotic attenuation. Hence alterations in the quantity of fibrosis may not be the proper index for evaluating the impact of a given therapeutic. To complicate matters further, human clinical trials don't typically use fibrosis as an endpoint, despite advancements in non-invasive assessments of fibrosis by magnetic resonance imaging (MRI) with late gadolinium enhancement (*133*, *134*). Instead, studies often rely on functional metrics as endpoints, even when testing antifibrotics. This makes it especially hard to determine how a given treatment is directly altering human cardiac fibrosis, let alone fibroblast state space. Therefore, the following section and Table 1 summarizes pre-clinical and clinical

data from inhibiting two regulators, p38 and YAP, that show promise for altering global fibrosis and function through cardiac fibroblast state modulation. In addition, this section reviews fibroblast reprogramming approaches as a therapeutic.

1.1.1.4 p38 Inhibitors

p38 inhibitors are a promising class of drugs for reducing fibrosis and improving heart function. However, timing of p38-targeted therapeutics is crucial. In mouse models, early p38α deletion in Tcf21 expressing fibroblasts post-MI resulted in more dramatic decreases in fibrosis, improvements in function, and increases in mortality rates, compared to deletion from activating Postn positive fibroblasts (*135*). This suggests p38 inhibition could be a double-edged sword: if administered too early, they may cause ventricular rupture, but if given too late, fibrosis and dysfunction may not be adequately attenuated. In a DCM hamster model, chronic administration of the p38 inhibitors SB203580 or FR167653 improved systolic function and decreased fibrosis (*136*). Rats given the p38 inhibitor RWJ-67657 7 days after MI demonstrated decreased remote fibrosis and αSMA protein expression, but only moderate improvements in function (*137*). Pirfenidone is a small molecule drug that has recently been approved to treat lung fibrosis. While pirfenidone has several proposed mechanisms of action, it has also been implicated in targeting TGFβ signaling and inhibiting p38 phosphorylation (*138*). In rodents, pirfenidone has decreased cardiac fibrosis in response to MI (*139*), pressure overload (*138*, *140*), and AngII-induced injuries (*141*). While pirfenidone was able to halt fibrosis progression in a chronic pressure overload model, it was not able to reverse existing fibrotic remodeling, highlighting the importance of preventative treatment (*138*). In humans, a couple of anti-inflammatory p38 inhibitors have started clinical trials. Despite promising phase II clinical data (NCT00910962)

(*142*), a large phase III clinical trial testing the effects of Losmapimod, a competitive inhibitor of p38, failed to improve adverse outcomes after MI (NCT02145468) (*143*). Array BioPharma, a subsidiary of Pfizer, recently started a phase III clinical trial to investigate the effects of the anti-inflammatory and p38-inhibitor ARRY-371797 on DCM patients with mutations in the laminin A/C gene (NCT03439514), but this study will not be completed until 2024. This trial is supported by preclinical data in a mouse model with this laminin mutation, where treatment with ARRY-371797 decreased dilation and systolic dysfunction (*144*). *[Note: This trial was terminated early following a mid-trial analysis that indicated ARRY-371797 was unlikely to produce meaningful clinical benefits for patients* (*145*)*].*

1.1.1.5 YAP Inhibitors

The YAP pathway has been identified as a key target for reducing cancer resistance to chemotherapies. Therefore, YAP inhibitors have been investigated thoroughly in this context (reviewed in (*146*)). However, given recent data proposing YAP as a potent activator of the fibrotic cascade (*122*, *128*), it may be helpful to review promising YAP inhibitors that could be applied to cardiac fibrosis. Verteporfin, a drug widely studied for treating macular degeneration, was recently found to have YAP inhibition properties. In the kidney, verteporfin treatment of mice with unilateral ureteral obstruction decreased interstitial fibrosis, αSMA expressing myofibroblast number, and Smad2/3 nuclearization (*147*, *148*). In human isolated lung fibroblasts, a high-throughput screen of >13000 small molecules identified statins as potent YAP inhibitors, potentially explaining why patients with interstitial lung disease had better outcomes on statins. Simvastatin decreased established lung fibrosis in the bleomycin mouse model in a Lats1/2 independent manner (*149*). Inhibition of the dopamine receptor D1 (DRD1), which

couples to G-protein receptors, via dihydrexidine (DHX) disrupted YAP signaling in isolated fibroblasts and reduced lung and liver fibrosis in bleomycin and bile duct ligation models, respectively. DHX was also found to inhibit YAP nuclearization in isolated cardiac fibroblasts, although its use has not been tested in an *in vivo* cardiac fibrosis model (*150*). Given that these YAP inhibitors have shown promise in other fibrotic systems, they may be useful for combatting cardiac fibrosis, as well.

Paper/ Clinical Trial	**Therapeutic(s)**	**Species**	**Injury Model**	**Result**
Kyoi et al., 2006 (*136*)	SB203580* FR167653*	Hamster	Dilated Cardiomyopathy	Decreased cardiac fibrosis, myocyte death, dilation, and hypertrophy.
See et al., 2004 (*137*)	RWJ-67657*	Rat	Myocardial Infarction	Improved systolic function; decreased dilation, αSMA protein expression, and collagen I deposition; enhanced myocyte hypertrophy.
Yamagami et al., 2015 (*138*)	Pirfenidone*	Mouse	Pressure Overload	Improved systolic function; decreased dilation and interstitial fibrosis.
Nguyen et al., 2010 (*139*)	Pirfenidone*	Rat	Myocardial Infarction	Improved systolic function; decreased fibrosis; decreased frequency of ventricular tachycardia; decreased fibrosis in the

				infarct zone, border zone, and non-infarct area of the heart.
Wang et al., 2013 (*140*)	Pirfenidone*	Mouse	Pressure Overload	Decreased mortality and cardiac fibrosis.
Yamazaki et al., 2012 (*141*)	Pirfenidone*	Mouse	Angiotensin II	Decreased hypertrophy and cardiac interstitial and perivascular fibrosis.
Newby et al., 2014 (*142*) NCT00910962	Losmapimod*	Human Phase II	Myocardial Infarction	535 patients: no increase in adverse cardiac reactions; decreased B-type natriuretic peptide concentrations after 12 weeks.
O'Donoghue et al., 2016 (*143*) NCT02145468	Losmapimod*	Human Phase III	Myocardial Infarction	3503 patients: no improvements in frequency of adverse cardiac events (e.g. sudden cardiac death, recurrent MI).
Muchir et al., 2012 (*144*)	ARRY-371797*	Mouse	Dilated Cardiomyopathy	Improved fractional shortening; decreased dilation and αSMA gene expression; no change in Col1a1 and Col1a2 gene expression.
[Garcia-Pavia et al., 2024 (*145*)] NCT03439514	ARRY-371797*	Human Phase III	Dilated Cardiomyopathy	Ongoing- set to be completed in 2024. [Note: Terminated early due to futility, no safety concerns]

Liang et al., 2017 (*147*)	Verteporfin[#]	Mouse	Unilateral Ureteral Obstruction	Decreased renal interstitial fibrosis and number of αSMA expressing myofibroblasts.
Szeto et al., 2016 (*148*)	Verteporfin[#]	Mouse	Unilateral Ureteral Obstruction	Decreased renal interstitial fibrosis, number of αSMA expressing myofibroblasts, and Smad2/3 nuclearization.
Santos et al., 2020 (*149*)	Simvastatin[#]	Mouse	Bleomycin-induced Pulmonary Fibrosis	Decreased pulmonary interstitial fibrosis and collagen deposition.
Haak et al., 2019 (*150*)	Dihydrexidine[#]	Mouse	Bleomycin-induced Pulmonary Fibrosis Bile duct ligation	Decreased pulmonary fibrosis and αSMA fluorescent intensity. Decreased hepatic fibrosis and αSMA fluorescent intensity.

Table 1.1 Summary of pre-clinical and clinical studies on P38 and YAP inhibitors. *The p38 inhibitors summarized here are all from studies within cardiac systems, whereas the YAP inhibitors are from a mix of renal, hepatic, and pulmonary systems. *p38 inhibitor; # YAP inhibitor*

Conclusion of *Controlling Cardiac Fibrosis Through Fibroblast State Space Modulation* by Isabella M Reichardt*, Kalen Z. Robeson*, Michael Regnier, and Jennifer Davis. *Cell Signal.* 2021 Mar:79:109888. doi: 10.1016/j.cellsig.2020.109888. ***equal contribution**

1.6.5 Reversibility of ECM remodeling.

Given the mixed results of fibroblast- and antifibrotic-targeted interventions reviewed above, the following section revisits the concept of fibrotic regression in DCM and related cardiac diseases, with a focus on its relevance to disease reversibility. Mechanical unloading via LVAD in heart failure patients failed to reduce collagen quantity in the myocardium; although collagen expression in fibroblasts was greatly decreased, potentially suggesting a halt in further collagen deposition (*151*). Similarly, removing cardiac pressure overload from mice initiated some collagen degradation but failed to fully regress collagen deposition (*152*). However, pharmacological treatment of mice with diastolic dysfunction demonstrated the reversibility of hidden fibrosis (*67*). This was corroborated by a separate study in removal of cardiac pressure overload normalized Col3:Col1 ratios, with Col3 regaining dominance over the recovery period (*23*). These studies suggest that myocardial ECM content may be reversible even if overall quantity is not.

The irreversible nature of cardiac fibrosis, in spite of mechanical unloading or removal the disease trigger, remains a major source of confusion for the field. Recently, one approach for removing fibrosis from the heart is to engineer chimeric antigen receptor (CAR) T cells to ablate activated fibroblasts expressing fibroblast activated protein (FAP) (*153*). However, these studies often administer the CAR-T cells before substantial fibrosis has been laid down, which would indicate prevention of fibrosis, not reversal. This approach also reflects a broader assumption that fibroblasts are actively maintaining fibrosis in the heart, and that ablation of these fibroblasts will naturally result in fibrotic regression. However, early collagen turnover studies indicate that ~70% of collagen is metabolically inert with an apparent half-life of 1000 years, while the remaining 30% had a half-life on the order of 100s of days (*154*). While fibrotic regression has

been shown in the liver (*155*), 92% of proteins found in the muscle have a longer half-life than those found in the liver (*156*). Considering the heart is less regenerative than the liver, it is possible that fibrosis is more long-lived in the heart. If there are natural mechanisms for fibrotic regression in the heart, the cell types involved and processes for breaking down and reabsorbing the ECM has not been well characterized.

1.7 Epigenetic remodeling and reversibility

1.7.1 Reversibility of epigenetic remodeling.

While genetic mutations are the inciting stimulus in inherited DCM, there is growing appreciation for the role of epigenetic remodeling plays in driving the disease phenotype. Many types of epigenetic changes have been observed in DCM, including DNA methylation, histone modification, chromatin remodeling, and variant noncoding RNA expression (*157*). As DCM progresses into heart failure, DNA methylation patterns in myocytes regress back to a fetal state, causing re-expression of developmental isoforms of sarcomeric proteins (*158*). Interestingly, mechanical unloading using LVADs in DCM patients only partially reversed maladaptive epigenetic remodeling, despite improvements in cardiac dilation, function, and hypertrophy. Expression of some histone methylation markers were normalized with LVAD treatment, while others were permanently dysregulated (*22*). Moreover, transcriptional dysregulation has been shown to persist in murine heart failure models, even after total reverse remodeling with improved dilation and ejection fraction (*159*). These studies highlight the role of epigenetic remodeling in DCM progression and suggest that the epigenome retains permanent markers of mechanical remodeling.

1.7.2 Epigenetic memories of mechanical stimuli.

Recent *in vivo* studies suggest that cells retain mechanical "memories" in their epigenome that influence how these cells respond to future mechanical stimuli (*160–162*). Human mesenchymal stem cells (hMSC) were mechanically dosed using a novel hydrogel culture platform that allows for precise control over hydrogel stiffness over time. Longer mechanical dosing on stiff substrates caused irreversible histone acetylation, opening chromatin availability and biasing future hMSC fate determinations even after the cells were removed from the stiff mechanical microenvironment. Interestingly, this histone acetylation was reversible in cells that experienced shorter bouts of mechanical dosing on the stiff substrate (*161*, *162*). *In vivo*, mechanical dosing with cardiac pressure overload caused re-activation of the quiescent fibroblast population. Interestingly, chromatin regions proximal to genes involved in controlling cardiac hypertrophy and fibrosis were highly dynamic, with reversible accessibility across injury and treatment; however, there were other regions in the genome that were persistently dysregulated by cardiac injury (*163*). These data suggest that the epigenome can store memories of mechanical remodeling, altering cell fate and response to injury; although, the concept of mechanical memories has not yet been examined in a terminally differentiated cell type, like cardiomyocytes.

1.8 Summary

The following dissertation addresses several major gaps in the field surrounding hypocontractility-induced DCM. Although the tension-index model provides a framework for describing how sarcomeric mutations drive myocyte-intrinsic remodeling, how myocyte dysfunction propagates to non-myocyte populations, particularly fibroblasts, remains poorly

defined. Chapter 2 examines how the myocardium compensates for impaired myocyte tension generation, with a specific focus on fibroblast behavior and ECM remodeling. Despite long-standing assumptions that compensatory remodeling is reversible whereas pathological remodeling is permanent, these concepts have not been rigorously evaluated in DCM. Moreover, it is unknown whether restoring myocyte mechanical homeostasis is sufficient to reverse disease progression, or whether persistent remodeling within fibroblasts and the ECM forms a barrier to recovery. Chapter 3 investigates the time-dependent reversibility of adaptations across cardiomyocytes, fibroblasts, and the ECM following suppression of the disease-inciting mutation. Finally, it is unclear how early in life the disease trajectory of DCM is established, specifically, whether dysfunction during postnatal maturation installs long-lasting pathological states that later shape disease severity. Chapter 4 explores how developmental myocyte correction influences long-term myocardial structure and function. Together, these studies define how fibroblast remodeling contributes to DCM progression, how much of this secondary remodeling is reversible, and how early-life mechanical cues may set the stage for DCM pathogenesis.

Chapter 2: Fibroblast proliferation drives ECM remodeling and disease progression in DCM

While ECM remodeling is recognized as a major biomarker for poor outcomes, it is still largely described as secondary to myocyte dysfunction in DCM. Cardiac fibroblasts are the primary cell responsible for ECM deposition and remodeling in the heart. Canonical understanding of the fibroblast has largely been defined in myocardial infarction models, but recent studies suggest that diseases with interstitial fibrosis, as is the case with DCM, notably lack myofibroblasts and instead exhibit their own unique pro-fibrotic fibroblast cell states (*47*, *163*, *164*). Given fibroblasts are highly mechanically sensitive and physically couple to myocytes via the ECM (*165*), it is likely that these shifts in fibroblast cell state occur early on in DCM disease progression. The following section examines how fibroblasts 1) shift their cell state over the course of DCM, 2) contribute to disease progression, and 3) can be targeted to prevent elements of the DCM phenotype.

Excerpts from the following paper have been provided for this chapter.

Prevention of Hypocontractility-Induced Proliferative Fibroblast States Alleviates Dilated Cardiomyopathy

Science. 2025 Sep. DOI: 10.1126/science.adv9157

Ross C. Bretherton[1-3*], Isabella M. Reichardt[1-3*], Kristin A. Zabrecky[2-4], Abigail Nagle[1-3], Logan R.J. Bailey[2,3,5], Darrian Bugg[2,3,5], Sasha Smolgovsky[2,3,5], Amy L. Gifford[2,3,5], Timothy S.

McMillen[1,6], Alex J. Goldstein[2,5], Kristina B. Kooiker[2,3,7], Galina V. Flint[1], Amy Martinson[2,3,5], Jagdambika Gunaje[2,3,5], Franziska Koser[8], Elizabeth Plaster[2,3,5], Wolfgang A. Linke,[8] Michael Regnier,[1-3,9] Farid Moussavi-Harami[2,3,5,7,9], Nathan J. Sniadecki[1-3,5,9,10], Cole A. DeForest[1,2,11-14], Jennifer Davis[1-3,5,9#]

**** These authors contributed equally to this work***

[1] Department of Bioengineering, University of Washington; Seattle, WA 98105 USA

[2] Institute for Stem Cell and Regenerative Medicine, University of Washington; Seattle, WA 98109 USA

[3] Center for Cardiovascular Biology, University of Washington; Seattle, WA 98109 USA

[4] Department of Comparative Medicine, University of Washington; Seattle, WA 98109 USA

[5] Department of Lab Medicine and Pathology, University of Washington; Seattle, WA 98109 USA

[6] Department of Anesthesiology, University of Washington; Seattle, WA 98109 USA

[7] Division of Cardiology, University of Washington; Seattle, WA 98109 USA

[8] Institute of Physiology II, University of Münster; Münster DE

[9] Center for Translational Muscle Research, University of Washington; Seattle, WA 98109 USA

[10] Department of Mechanical Engineering, University of Washington; Seattle, WA 98105 USA

[11] Department of Chemical Engineering, University of Washington; Seattle, WA 98105 USA

[12] Department of Chemistry, University of Washington; Seattle, WA 98105 USA

[13] Molecular Engineering & Sciences Institute, University of Washington; Seattle, WA 98105 USA.

[14] Institute for Protein Design, University of Washington; Seattle, WA 98105 USA.

#Corresponding Author: Jennifer Davis

2.1 Summary

Introduction. Dilated cardiomyopathy (DCM), a major cause of heart failure, often stems from inherited sarcomeric mutations that cause cardiomyocyte hypocontractility. While therapeutics aimed at restoring cardiomyocyte function are showing positive clinical effects, they often fall short of fully reversing the DCM phenotype. One likely obstacle is fibrosis, a deposition of excess extracellular matrix (ECM), which strongly predicts disease severity and remains largely intractable in preclinical models.

Rationale. Since fibroblasts orchestrate the production and remodeling of the heart's ECM, we reasoned that these cells regulate the severity of DCM phenotypes by sensing altered mechanical signals from hypocontractile cardiomyocytes and adapting the material properties of the extracellular environment to maintain the heart's preferred mechanical state. We examined this hypothesis using transgenic mice and engineered heart tissues in which cardiomyocytes expressed a DCM-linked sarcomeric variant causal for hypocontractility.

Results. Genetically inducing cardiomyocyte hypocontractility increased myocardial and ECM stiffness before the onset of eccentric hypertrophy, which is a defining feature of DCM. Although we observed upregulation of titin isoforms and post-translational modifications that stiffen cardiomyocytes, small effect sizes prompted investigation of fibroblast and ECM contributions. During this early phase of DCM, hyperproliferative-mechanosensitive fibroblast states formed and caused the fibroblast population to double. Yet, classic markers of cardiac fibrosis such as increased collagen content, crosslinking, and maturity were absent. Consistent with these findings, fibroblasts showed no signs of activation. Instead, increased fibroblast density compacted myocardial tissues and structurally stiffened the ECM by enhancing collagen fibril packing and collagen fiber alignment. To determine how hypocontractile cardiomyocytes

drive fibroblast expansion, we analyzed cardiomyocyte-fibroblast crosstalk using single-nucleus RNA sequencing. Ligand-receptor pair analysis identified ECM-receptor interactions as dominant routes for cardiomyocyte-fibroblast communication. Indeed, naïve cardiac fibroblasts proliferated when embedded in hydrogels containing ECM peptides from our DCM mouse model. Further screening revealed that collagen types 4 and 6, which were upregulated in cardiac fibroblasts from DCM mice, promoted proliferation. A coculture assay engineered to measure mechanosensations at ECM focal adhesions with a genetically encoded FRET-based tension sensor identified heightened tension sensations in cardiac fibroblasts cultured on hypocontractile cardiomyocytes in relaxed but not activated conditions when compared to wildtype, indicating cardiac fibroblast differentially sense passive mechanical properties of cardiomyocytes. Mechanotransduction analysis identified TGFβ, YAP, and p38 signaling as key pathways driving fibroblast proliferation. Since p38 regulates both TGFβ and YAP signaling in cardiac fibroblasts, we examined whether disabling this pathway could blunt DCM disease progression and severity. Conditional deletion of p38 in cardiac fibroblasts prevented their proliferation and completely blocked ECM remodeling and eccentric cardiomyocyte growth. Despite persistent expression of the hypocontractility-linked sarcomeric variant, fibroblast-specific p38 deletion substantially improved both myocardial and cardiomyocyte function.

Conclusion. These findings revealed that p38-mediated fibroblast responses to myocyte hypocontractility are essential regulators of DCM disease severity and progression owing to their function as biomechanical rheostats that detect impaired myocyte mechanics and adaptively remodel the material properties of the extracellular environment. This marks a potential untapped cellular target for therapeutically intervening with non-ischemic DCM.

2.2 Introduction

Dilated cardiomyopathy (DCM) is a leading cause of heart failure worldwide, which arises from a cadre of insults including inherited mutations in contractile or structural proteins expressed in cardiomyocytes (*18*, *20*, *166*). The clinical hallmarks of DCM are reduced systolic function, myocardial thinning, left ventricular chamber dilation, and fibrosis. Despite a robust prevalence of DCM in the population, there are limited treatment options and, as of yet, no cure (*4*, *7*, *166*, *167*). Potential pharmaceuticals for DCM such as myosin modulators have underperformed at fully correcting the DCM phenotype, especially established fibrosis in mice and clinical trials, thus tempering their therapeutic value (*20*, *37*, *168*). This absence of fully effective treatments may be due to a decades long struggle with mechanistically linking the primary contractile defect to variable DCM phenotypes (*16*).

Common to most severe DCM phenotypes is fibrosis, which often precedes and exacerbates cardiac structural remodeling (*65*, *169*, *170*). Remodeling of the heart's extracellular matrix (ECM), such as during the fibrotic response to stress, is primarily regulated by resident fibroblasts of the *Tcf21* and *Pdgfra* lineages (*93*, *96*, *171*, *172*). While cardiac fibroblasts can be activated chemically to secrete fibrotic ECM, these cells are also highly sensitive to mechanical signals including substrate stiffness, alignment, and stretch (*173*). Fibroblasts are posited to function within mechanical feedback loops by structurally and biochemically tuning the extracellular environment's material properties to maintain a tissue's preferred mechanical state (*174*). Given fibroblasts are physically coupled to cardiomyocytes via the ECM (*165*), it was hypothesized that in DCM driven by myocyte hypocontractility cardiac fibroblasts act as tissue-scale mechanical rheostats that sense impaired myocyte force generation and then adaptively remodel the extracellular environment to maintain mechanical homeostasis. We further propose

that these adaptive fibroblast responses are essential secondary drivers of DCM phenotype and disease severity.

2.3 Results

2.3.1 Hypocontractile sarcomeres induce myocardial stiffening from fibrillar collagen reorganization prior to initiating dilated modes of myocyte growth.

Sarcomeric hypocontractility was modeled in mice by expressing an experimentally-derived I61Q variant of cardiac troponin C (cTnC) specifically in cardiomyocytes using a doxycycline-repressible α-myosin heavy chain promoter (**Supplemental Figure 2.1A** (*18*)). The I61Q mutation lowers cTnC's Ca^{2+} binding affinity and hence reduces force production on a beat-to-beat basis (*175*, *176*). This change is apparent by echocardiography, which showed reduced ejection fraction in the hearts of I61Q transgenic mice by 2 months of age relative to the control (CON) group, which consisted of non-transgenic and tetracycline transactivator (tTA) transgenic littermates ((**Supplemental Figure 2.1B**). These 2 genotypes were merged into a single control group, because previous studies showed no effects of the tTA transgene (*18*). The time frame of dilated remodeling was defined by morphologic measurements of isolated CON and I61Q myocytes in the presence of a myosin inhibitor blebbistatin, which ensures the cellular dimensions represent structural changes rather than sarcomere elongation from I61Q cTnC-dependent desensitization of the myofilaments to Ca^{2+} (*18*). At 2 months of age I61Q myocytes had normal lengths and length:width ratios when compared to CON indicating a lack of structural remodeling (**Figure 2.1A-B**). However, by 4 months I61Q myocytes were longer and had greater length:width ratios- a structural hallmark of eccentric hypertrophy and DCM (**Figure 2.1A-B** (*177*, *178*)). Consistent with this progressive increase in I61Q myocyte length from serial

sarcomere addition (*179*), heart weight to body weight ratios were similar to CON at 2 months of age but significantly increased by 4 (**Figure 2.1C**, $p<0.001$). By contrast, diastolic chamber dimensions as measured by echocardiography were increased at both ages (**Figure 2.1D**). This discrepancy between myocyte and organ level dilation in I61Q mice could stem from altered diastolic tone driven by Ca^{2+} desensitized myofilaments that lower crossbridge attachment at diastolic [Ca^{2+}]. This hypothesis was examined by measuring sarcomere lengths in isolated myocytes from 2-month-old I61Q and CON mice at diastolic [Ca^{2+}] (*18*). As expected I61Q myocytes had longer resting sarcomere lengths (**Figure 2.1E**). Organ level dilation could also be caused by myocardial stiffness, considering genotype positive cardiomyopathy patients can have stiffer hearts prior to the onset of structural remodeling (*16*, *180*, *181*). Indeed, a hemodynamic index of cardiac stiffness, end diastolic pressure-volume relationship (EDPVR), was elevated in 2-month-old I61Q mice and worsened with age (**Figure 2.1F**). To determine if myocardial or ECM stiffness caused heightened EDPVR in I61Q mice, the passive mechanical properties of intact and decellularized hearts were measured using a Langendorff working heart preparation that lacked electrical stimulation (**Supplemental Figure 2.1C-D**). Here, intact hearts from I61Q transgenic and CON mice were subjected to retrograde perfusion with Krebs-Henseleit buffer containing blebbistatin to negate any stiffness from attached crossbridges, and then a balloon was inserted into the left ventricle for volumetric inflation of the chamber in a stepwise manner (**Figure 2.1G & Supplemental Figure 2.1C**). The balloon pressure was recorded during each inflation step, which exhibited a maximal pressure required to achieve the initial volume change followed by a gradual decrease in pressure due to viscoelastic relaxation (**Figure 2.1G**). Following intact measurements, hearts were decellularized and the assay repeated to measure passive mechanical properties of the ECM in the same preparation. Both intact and

decellularized preparations from I61Q mice required higher maximal pressures per inflation, indicating both the myocardium and ECM are stiffer relative to CON (**Figure 2.1H-I, Supplemental Figure 2.1C-D**).

Titin isoforms and post-translational modifications were surveyed by Western blot given their regulation of myocyte passive stiffness in the physiologic range (*182*). The stiffer N2B isoform was upregulated in I61Q hearts (**Figure 2.1J, Supplemental Figure 2.1E**), whereas post translational modifications of titin that enhance myocyte compliance were reduced as shown by the lack of phosphorylation at serine residues in the N2B unique sequence (S267P) and PEVK region (S26P) when compared to CON (**Figure 2.1K-L, Supplemental Figure 2.1E** (*183*, *184*)). While titin composition was altered in I61Q cardiomyocytes, the modest effect size prompted examination of the ECM's biochemical composition, quantity, and organization to determine additional causes of stiffness in I61Q hearts (*175*). Label-free data-independent acquisition (DIA) mass spectrometry (MS) of decellularized cardiac ECM from I61Q cTnC transgenic and CON mice was performed (**Fig. 2.1M & Supplemental Figure 2.2A-P**) and recovered ~72% of core collagens, ECM glycoproteins, and proteoglycans (*185*). The relative abundance of primary ECM constituents was largely unchanged between genotypes (~6% of the matrisome, **Figure 2.1M & Supplemental Figure 2.2A**). Only 22 core matrisome proteins were differentially expressed between CON and I61Q mice including several laminin subtypes and type 6 collagen (**Figure 2.1M**)- an established biomarker of heart failure not yet linked to ECM stiffening (*185–187*). Closer examination of collagen abundance with less stringent p-values ($p<0.05$) showed several fibrillar collagens starting to increase in I61Q cardiac ECM but only network forming collagens 6a and 8a were statistically different (**Supplemental Figure 2.2B**). This matches histologic analysis of fibrosis by picrosirius red staining, in which no differences were detected

between groups at this age (**Figure 2.1N-O**). By 4 months, I61Q transgenics began accruing interstitial cardiac fibrosis concomitant with the structural lengthening of myocytes (**Figure 2.1A-C & N-O**). The MS data were also used to detect covalent and non-covalent crosslinking of fibrillar collagens as a mechanism for ECM stiffness. Of the few glycation sites identified, none were different between genotypes (**Supplemental Figure 2.2C-E**). By contrast, we found that a smaller proportion of I61Q fibrillar collagens had hydroxylated proline and lysine residues, with the biggest decrease being reduced abundance of hydroxylated lysines in COL1A1 (**Supplemental Figure 2.2F-I**). Reduced proline and lysine hydroxylation on fibrillar collagens is typically associated with ECM instability and immaturity (*188–190*), and collagen birefringence imaging showed a greater proportion of collagen fibers were immature in I61Q versus control ECM (**Supplemental Figure 2.2Q**). No differences in ECM crosslinking enzyme abundance were detected (**Supplemental Figure 2.2J-P**), suggesting crosslinking wasn't responsible for stiffer ECM in I61Q mice. Multiscale reorganization of collagen fibers was also explored as a causal mechanism for ECM stiffness (*191*). Second harmonic generation (SHG) microscopy and imaging of decellularized I61Q and CON hearts below the epicardial surface identified increased collagen fiber alignment in the circumferential-longitudinal plane (**Figure 2.1P-S**), which is consistent with findings linking collagen fiber alignment to heightened anisotropic strength and stiffness (*192*, *193*). There was no significant difference in collagen fiber length between controls and I61Q ECM preparations (**Figure 2.1R**), indicating the observed topographical changes were not simply a product of collagen elongation. Because smaller collagen fibril diameter and increased packing also enhance ECM strength and passive stiffness (*194–196*), transmission electron microscopy (TEM) was used to examine collagen fiber ultrastructure. Indeed, I61Q collagen fibrils had smaller diameters and cross-sectional areas

with a greater packing density relative to controls (**Figure 2.1T-V & Supplemental Figure 2.2R**). The proteoglycan decorin, which restrains collagen fibril diameter and creates denser networks similar to these findings (*197*, *198*), was more abundant in I61Q ECM (**Figure 2.1W**). These data suggest the structural organization of fibrillar collagen rather than quantity, composition, or crosslinking underlies the passive ECM stiffness in I61Q hearts.

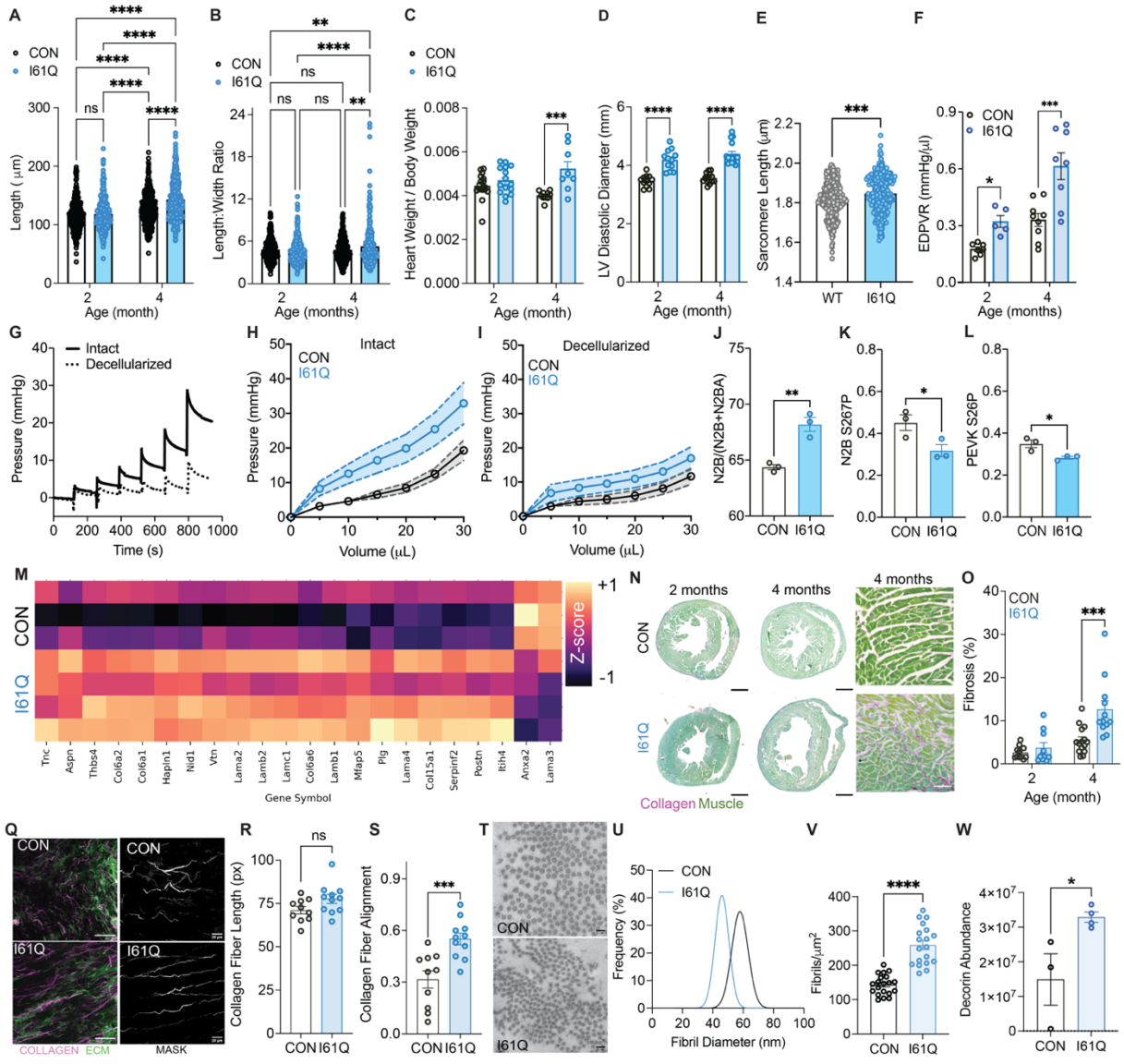

Figure 2.1: Cardiomyocyte hypocontractility stiffens and aligns the myocardium prior to eccentric hypertrophic remodeling and fibrosis. ***A)*** *Quantification of isolated cardiomyocyte length and* ***B)*** *length:width ratio in relaxed conditions from the described genotypes (CON n=399/402 (2/4 month), I61Q n=357/399 (2/4 month). Quantification of* ***C)*** *heart weight (HW) body weight (BW) ratios by gravimetrics and* ***D)*** *left ventricular diastolic chamber diameter by echocardiography at 2 (I61Q n=12, CON n=12) and 4 (I61Q n=16, CON n=15) months of age.* ***E)*** *Quantification of diastolic sarcomere length in intact cardiomyocytes from I61Q and CON hearts (CON n=399/402 (2/4 month), I61Q n=357/399 (2/4 month)).* ***F)*** *Quantification of end diastolic pressure-volume relationship (EDPVR) by invasive hemodynamics (CON n=5/9 (2/4 month), I61Q n=5/8 (2/4 month)).* ***G)*** *Representative developed pressure traces from stepwise inflation of a balloon inside a blebbistatin-treated intact (dark line) and decellularized (straight line) heart.* ***H)*** *Pressure-volume curves of intact and* ***I)*** *decellularized mouse hearts at 2 months (n=7 both genotypes). Quantification of titin* ***J)*** *isoforms N2B and N2BA,* ***K)*** *N2B S267P phosphorylation site, and* ***L)*** *serine PEVK region S267 phosphorylation by Coomassie staining and Western blot (n=3 both genotypes). N2B isoform is expressed relative to the total titin (N2B + N2BA) and phosphospecific antibodies were normalized to the titin stain on the Coomassie gel.* ***M)*** *Heatmap of significant differentially expressed matrisome proteins color coded by z-score identified by MS in 2 month old decellularized ECM (CON n=3, I61Q n=4).* ***N)*** *Representative images and* ***O)*** *quantification of fibrosis in cardiac sections stained with picrosirius red-fast green (PSR/FG, scale bar=1mm (left & middle panel), scale bar=50μm (right panel)).* ***Q)*** *Representative two-photon max intensity projection images of SHG (left panel, scale bar=100μm) and masking of the collagen fibers (scale bar=20μm) in decellularized hearts in which Z-stacks were taken starting 10 micron below the epicardial surface. Fibrillar collagen (magenta) and ECM autofluorescence (green). CurveAlign quantification of collagen fiber* ***R)*** *length and* ***S)*** *alignment from 2-month-old I61Q (n=10) hearts and CON controls (n=11).* ***T)*** *Representative TEM images of collagen fibrils in 2-month-old I61Q and CON hearts. Quantification of* ***U)*** *fibril diameter and* ***V)*** *density from TEM images (n=20 ROIs/mouse, 3 mice per genotype).* ***W)***

Quantification of decorin abundance identified by MS. 4 biological replicates per genotype were used for isolated myocyte experiments ***(A,B,&E)****. Data are mean ± SEM, ns=not significant, **p<0.01,***p<0.005, ****p<0.001 by 2-way ANOVA with Holm-Sidak's multiple comparisons test (****A-D, F, O****) or two-tailed unpaired t-test (****E,J-L, R-S, V-W****).*

2.3.2 Hyperproliferative fibroblasts promote early cardiac stiffening and collagen reorganization.

Typically tissue stiffness initiates cardiac fibroblast activation and transition to a myofibroblast state- a cellular process required for fibrotic ECM production (*47*, *70*). Activated myofibroblasts were measured in myocardial sections from 2-month-old I61Q cTnC and CON mice by quantifying the number of cells that were positive for both the myofibroblast marker smooth muscle α-actin (αSMA) and quiescent fibroblast marker platelet-derived growth factor receptor α (PDGFRα). No fibroblast-to-myofibroblast conversion was evident even after the onset of fibrosis in I61Q hearts (**Figure 2.2A-B**). The competence of I61Q cardiac fibroblasts to activate was also examined in vitro by stimulating them with recombinant TGFβ1 and calculating the percentage of the population that had formed αSMA-positive stress fibers (*167*). This assay revealed no differences between genotypes at baseline or in response to TGFβ1, suggesting cardiac fibroblasts from I61Q transgenics are capable of differentiating into myofibroblasts and possess equal sensitivity to activating ligands as CON (**Supplemental Figure 2.3A-B**). Previous single cell RNAseq studies have demonstrated that αSMA positive fibroblasts comprise only a small fraction of the activated myofibroblast population, whereas periostin (*Postn*) expression marks all activated myofibroblast states (*199*). To determine if I61Q fibroblasts are canonically activating but not transitioning to mature αSMA^{+} states, *Postn* lineage

tracing was performed in I61Q transgenic and CON mice using a Cre-regulated dual color fluorescent reporter and tamoxifen (TAM) inducible *Postn*-Cre-driver (*Postn*^{iCre}*-mT/mG,* (*135*, *171*, *200*)). *Postn* lineage tracing detected small pockets of activated *Postn*$^{+}$ cells in the interstitium and adventitia of I61Q hearts but only at 8 months of age, which matches the start of decompensation (**Figure 2.2A (right panels), 2C, Supplemental Figure 2.3C-D**) (*20*). These results suggest [1] the typical fibrotic process of myofibroblast formation only occurs in hypocontractility-induced DCM once the heart is failing, and [2] fibroblast activation to an intermediate or fully matured myofibroblast state is not essential for ECM and myocardial stiffening.

To determine the basis for this myofibroblast-independent cardiac stiffening, single nuclei RNAseq (snRNAseq) of 2-month-old CON and I61Q hearts were analyzed for the emergence of atypical fibroblast states (**Figure 2.2D**). Five fibroblast substates were identified by hierarchical clustering of differentially expressed genes with each cluster expressing *Col1a1* and *Col1a2* at varying levels (**Figure 2.2D-F**). Cluster 1 and 3 fibroblasts were rare in controls but expanded in I61Q hearts (**Figure 2.2D-E, Supplemental Figure 2.3E)**. These clusters were defined by transcripts involved in mechanotransduction (ECM-receptor, focal adhesion, and adherens junctions) and cell cycle/chromatin segregation, respectively (**Figure 2.2G, Table S1**). Independent bulk RNAseq analysis of PDGFRα purified cardiac fibroblasts validated these findings with greater sequencing depth. Here 363 upregulated genes and 449 downregulated genes were identified in I61Q fibroblasts (**Data S1, Figure 2.2H, Supplemental Figure 2.3F**). Genes with the largest change in expression included a variety of cell cycle regulators such as cyclin genes (*Ccnb1*, *Ccnb2*, *Ccnd1*, *Ccne2*, *Ccnf*), cyclin dependent kinase 1 (*Cdk1*), marker of proliferation Ki67 (*Mki67*), and aurora kinase (*Aurka*) (**Figure 2.2H, Supplemental Figure**

2.3F, Data S1). To assess whether altered levels of cell cycle markers led to heightened proliferation and expansion of I61Q fibroblasts, cardiac sections from postnatal day 14 (p14), 1 and 2 month old mice were stained for the fibroblast marker PDGFRα and cell cycle marker phospho-histone H3 (pHH3, **Figure 2.2I-M**), which demonstrated that fibroblasts in I61Q myocardial sections had heightened proliferation signals beginning at 2-months when CON fibroblasts are quiescent (*46*). In accordance with heightened cell cycle activity PDGFRα^{+} fibroblast density doubled and remained at this level in I61Q hearts throughout the course of disease despite a decline in cell cycle activity at 4 months of age (**Fig 2.2I-J, Supplemental Figure 2.3G),** suggesting steady-state was reached with regards to fibroblast expansion. To determine if immune cell activation was associated with cardiac fibroblast proliferation, myocardial sections were analyzed at the 2-month timepoint for cardiac-infiltrating CD11b^{+} myeloid and CD4^{+} T cells, which have known pro-fibrotic roles in other etiologies of heart failure. These histologic methods showed CON and I61Q hearts had similar immune profiles, suggesting crosstalk with immune cells wasn't driving proliferation (**Supplemental Figure 2.3H-K**). This I61Q cTnC-dependent expansion of the fibroblast population coincided with upregulated *Col1a1*, *1a2*, and *3a1* transcripts and downregulation of key ECM degrading enzymes like metalloproteinases (*Mmp* and *Adamts*) and cathepsins (*Cts*), which together should have promoted fibrotic tissue deposition (**Supplemental Figure 2.3L-Q**). As this was not observed in I61Q hearts (**Figure 2.1M-O, Supplemental Figure 2.2B**), we reasoned that post-transcriptional fibrillar collagen immaturity (**Supplemental Figure 2.2F-I, Q**) restrained the fibrotic response despite the expanded fibroblast population.

While fibrillar collagen deposition is a common fibroblast-dependent mechanism underlying tissue stiffening, increased cell density and cumulative traction forces exerted by the

expanded fibroblast population in I61Q could also contribute myocardial stiffening and circumferential ECM alignment, as observed with progressive volume overload linked to DCM (*201*). Indeed, hyperproliferative I61Q fibroblasts compacted the surrounding ECM to a greater extent than those from CON hearts following encapsulation in free-floating collagen gels (**Figure 2.2N-O**). To test whether proliferation was essential to gel compaction, a small-molecule cyclin-dependent kinase inhibitor (CDKi) dinaciclib was delivered in the culture media. CDKi treatment reduced proliferation of cardiac fibroblasts from both genotypes to similarly low levels and blocked genotype-dependent gel compaction (**Figure 2.2N-P**), demonstrating increased fibroblast numbers rather than greater cell contraction caused compaction. To further confirm that gel compaction was due to proliferation rather than ECM degradation, a set of cell-laden collagen gels were also treated with marimastat, a broad-spectrum inhibitor of matrix metalloproteinases, which had no effect on I61Q fibroblast proliferation or gel compaction for either fibroblast genotype (**Supplemental Figure 2.3R-T**). Similar to the collagen gels, fibrin tissues seeded with cardiac fibroblasts from I61Q transgenic hearts had increased compaction and generated more passive tension than those seeded with CON cardiac fibroblasts as measured by polydimethylsiloxane (PDMS) post deflection (**Figure 2.2Q-S).** Concomitant with the heightened passive tension, I61Q fibroblasts were more aligned within the tissues, suggesting fibroblast proliferation contributes to myocardial stiffness and alignment (**Figure 2.2T**).

Stiffening of cardiomyocytes and altered preload from I61Q-dependent hypocontractility could also produce the traction needed to align and lengthen collagen fibers. To study the acute effects of I61Q cTnC on tissue alignment and stiffening in the absence of hemodynamic load, naïve neonatal rat cardiomyocytes were seeded into engineered heart tissues (EHTs) mounted on

PDMS posts and adenovirally transduced with FLAG-tagged I61Q cTnC (AdI61Q) or wildtype cTnC (AdWT) as a control. After 2 weeks of culture, AdI61Q EHTs functionally phenocopied the I61Q transgenic mice (*20*), including reduced twitch force and hypocontractility (**Figure 2.2U-V**). Notably absent from the I61Q EHT phenotype was any difference in passive tension generation or tissue alignment (**Figure 2.2W-X**), which differs from tissues engineered with cardiac fibroblasts from I61Q transgenic mice (**Figure 2.2Q-T**)**.** Taken together these experiments demonstrate that in the absence of fibroblast-generated passive tension and/or hemodynamic loading, I61Q cTnC expression by the cardiomyocyte alone is insufficient to align and stiffen myocardial tissues in vitro.

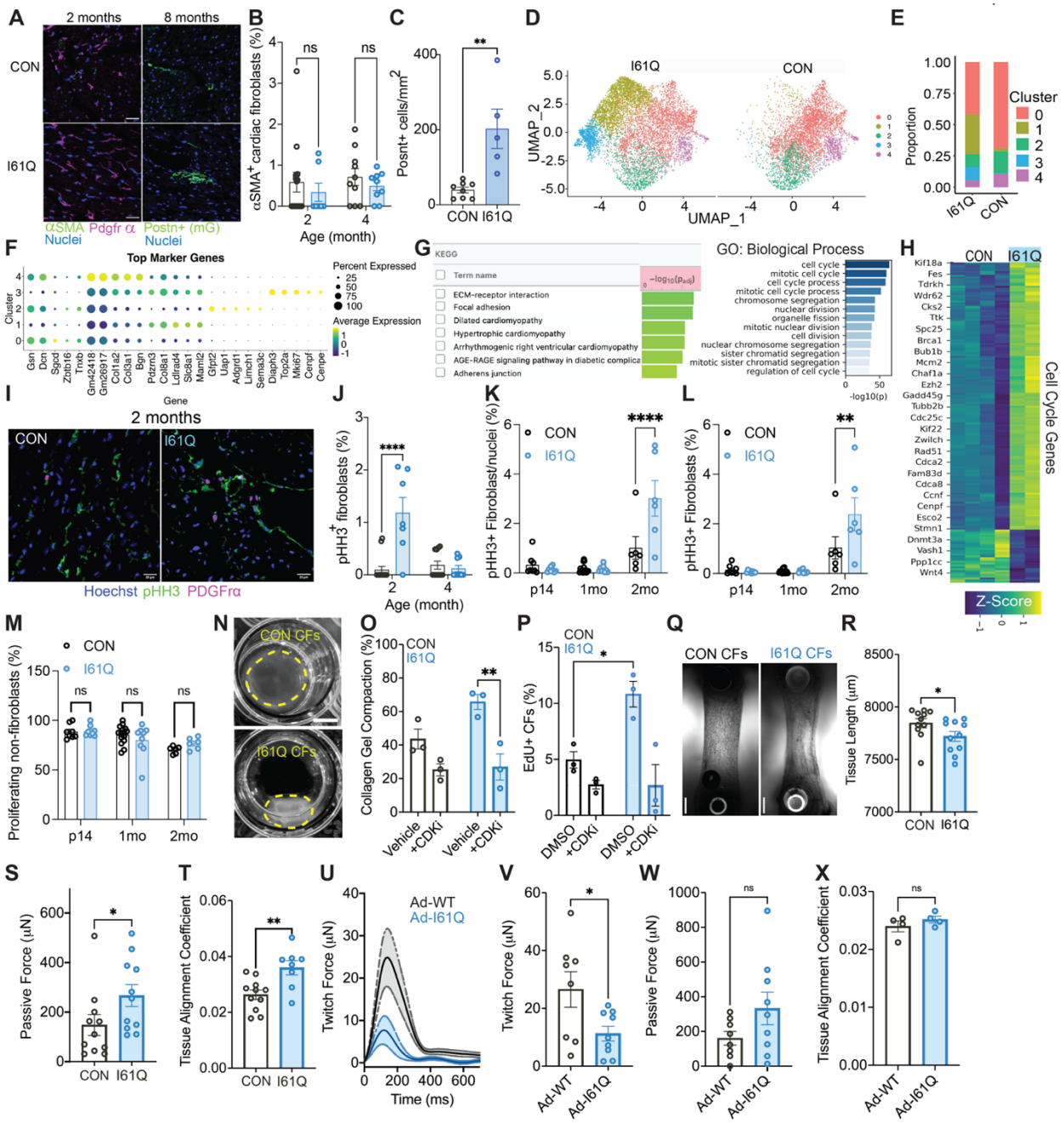

Figure 2.2: Hyperproliferative fibroblast states that fail to activate drive fibrosis-independent tissue stiffening in I61Q hearts. A) *Representative images of (Left) 2-month-old CON and I61Q cardiac sections stained for smooth muscle α-actin (αSMA) and platelet-derived growth factor receptor α (PDGFRα) and (Right) Postn lineage traced cell density in 8-month-old cardiac sections.* ***B)*** *Quantification of immunofluorescent imaging for the percentage of fibroblasts (PDGFRα^{+}) expressing*

αSMA (2-month n=14 CON, n=7 I61Q, 4 month n=10 CON, n=9 I61Q). ***C)*** *Quantification of Postn^{+} cell density in I61Q (n=5) and CON (n=8) hearts at 8 months of age. (D) UMAP dimensionality reduction plot for all sequenced cardiac fibroblast nuclei from 2-month-old I61Q and CON hearts. Each color represents distinct fibroblast clusters (states) based on differential gene expression.* ***E)*** *Proportion analysis showing genotype dependent changes in the percentage of the cardiac fibroblast population residing in each of the defined cell clusters (states).* ***F)*** *Dot plot of the top 5 significantly expressed genes that define each fibroblast cluster.* ***G)*** *Significant Kegg pathways and gene ontology biological processes (GO:BP) identified by differentially regulated genes in fibroblast clusters 1 and 3 that are unique to the I61Q genotype.* ***H)*** *Heatmap showing expression levels of cell cycle genes.* ***I)*** *Representative images (scale bar=20 μm) and quantification of immunofluorescent staining for:* ***J)*** *phospho-histone H3 (pHH3) and PDGFRα,* ***K)*** *pHH3+, PDGFRα+ cells per total nuclei (Hoechst), and* ***L)*** *pHH3+,PDGFRα+ cells as a percentage of the total number of PDGFRα+ cells in I61Q and CON cardiac sections.* ***M)*** *Quantification of pHH3+ non fibroblasts in I61Q (n=8 (p14), 9 (1 month), 6 (2 month)) and CON (n=8 (p14), 15 (1 month), 6 (2 month)) cardiac sections.* ***N)*** *Representative images (scale bar=5 mm) and* ***O)*** *quantification of the compaction of free-floating collagen gels seeded with cardiac fibroblasts (CFs) isolated from I61Q and CON hearts ± cell cycle inhibitor (CDKi) (n=5 per genotype).* ***P)*** *Quantification of cardiac fibroblast proliferation by EdU incorporation ± cell cycle inhibitor (CDKi).* ***Q)*** *Representative images of cardiac fibroblast-seeded fibrin tissues mounted between PDMS posts (scale bar=1 mm). Quantification of* ***R)*** *length and* ***S)*** *passive force production by tissues seeded with cardiac fibroblasts from 2-month-old I61Q cTnC transgenic or CON mice (n=11 per genotype).* ***T)*** *Quantification of cellular and ECM alignment in fibrin tissues seeded cardiac fibroblasts derived from I61Q cTnC transgenic and CON hearts by wheat germ staining (n=11 CON, n=8 I61Q).* ***U)*** *Average twitch forces generated by engineered heart tissues (EHTs) 2 weeks after cardiomyocytes were adenovirally transduced with either control (AdWT, n=8) or I61Q mutant cTnC (AdI61Q, n=6). Quantification of (V) twitch force,* ***W)*** *passive tension, and (X) tissue alignment by wheatgerm staining in EHTs. Data are mean ± SEM, ns=not*

*significant, *p<0.05,**p<0.01,***p<0.005,****p<0.001 by 2-way ANOVA with Holm-Sidak's multiple comparisons test (B,J-M,O-P) or two-tailed unpaired t-test (C, R-T,V-X). All scale bars = 50μm unless otherwise noted.*

2.3.3 Sarcomere hypocontractility-induced ECM interactions and diastolic tension promote fibroblast proliferation.

Cellular crosstalk that might drive the hyperproliferative phenotype of I61Q cardiac fibroblasts was interrogated by performing ligand-receptor analysis of myocyte and fibroblast clusters identified by snRNAseq (**Figure 2.2D, 2.3A**). Seventeen ligand-receptor pairs of varying strengths were identified where receptors were expressed by fibroblasts and ligands expressed by myocytes (**Figure 2.3A**). Ligand-receptor analysis of immune cell-fibroblast and endothelial cell-fibroblast pairs showed minimal overlap with myocyte-fibroblast interactions except for *Ccn1*/*Sdc4* and *Adam9*/*Itgb1* (**Figure 2.3A & Supplemental Figure 2.4A-B**), suggesting myocyte-fibroblast communicate via discrete signals. Of those myocyte-fibroblast interactions 6 were strongly altered in I61Q hearts (**Figure 2.3A**). Most of these communication pathways involved ECM-receptor pairs that included *Col4a5/Ddr1, Col4a2/Ddr1, Col4a3/Itga11+Itgb1, Col4a3/Itga1+Itgb1*, and *Adam9/Itga3+Itgb1* (**Figure 2.3A**). To examine if these ECM interactions induced fibroblast proliferation in equivalent mechanical environments cardiac fibroblasts were encapsulated in poly(ethylene glycol) (PEG)-based hydrogels (~2 kPa storage modulus) that were covalently decorated with pepsin-digested ECM from CON or I61Q hearts and functionalized with 4-azidobutyric acid N-hydroxysuccinimide ester (*193*, *194*). CON ECM hydrogels lowered I61Q cardiac fibroblast proliferation to CON levels, whereas hydrogels containing I61Q ECM maintained the heightened proliferation of I61Q fibroblasts but also

increased CON cell cycle activity to I61Q levels (**Figure 2.3B**). To isolate which ECM ligands drive proliferation 36 combinations of ECM proteins contained in soft (~10 kPa) polyacrylamide gels were screened with naïve CON cardiac fibroblasts. Here type 4 and 6 collagen caused the greatest increase in proliferation relative to other ECM substrates (**Figure 2.3C**). COL6A was enriched in I61Q ECM proteomics (**Figure 2.1M, Supplemental Figure 2.2B**) and *Col4a* was identified as a ligand-receptor pair exclusively in I61Q hearts (**Figure 2.3A**), suggesting matrix signals are advancing the DCM phenotype. Since some modestly enriched secreted factor-receptor pairs were identified in I61Q hearts (**Figure 2.3A**), additional experiments were performed to rule out myocyte secreted factors as causal for the I61Q fibroblast phenotype. Here, naive CON cardiac fibroblasts cultured in conditioned media from 2- or 4-month-old CON or I61Q myocytes showed no difference in the number of proliferating fibroblasts with any of the treated or control conditions (**Supplemental Figure 2.4C**). Similarly, collagen gels seeded with CON cardiac fibroblasts and treated with conditioned media from 2-month-old CON or I61Q myocytes had slightly enhanced collagen gel compaction, but no genotype-dependent differences (**Supplemental Figure 2.4D**). These data support ECM-ligand interactions rather than myocyte secreted factors as drivers of fibroblast expansion in I61Q hearts.

Since these findings pinpoint ECM-receptor interactions, a coculture assay was developed to determine if cardiac fibroblast focal adhesions sense different mechanical signals in an I61Q versus CON cardiomyocyte environment. For this assay CON cardiac fibroblasts were genetically modified with a FRET-based vinculin tension sensor and sparsely seeded on top of neonatal myocyte monolayers that were adenovirally transduced with either I61Q or wildtype cTnC (**Figure 2.3D**). Fibroblast focal adhesion FRET efficiency was measured as a surrogate for force when the myocytes were under fully relaxed (+blebbistatin), diastolic (pCa 6.0), or

submaximally activated (pCa 5.2) conditions (**Figure 2.3E-G**). Fibroblasts sensed heightened focal adhesion tension in the I61Q myocyte environment when the cardiomyocytes were either completely relaxed (**Figure 2.3E**) or in diastolic Ca^{2+} conditions (**Figure 2.3F**). Surprisingly, focal adhesions tension sensations were similar between genotypes in submaximally activated conditions despite the presence of I61Q-expressing myocytes (**Figure 2.3G**), indicating cardiac fibroblast focal adhesions differentially sense passive tension in I61Q myocytes that results from hypocontractility and stiffer titin isoforms rather than the forces generated during active contraction. This elevated passive tension sensation is consistent with [1] upregulated ECM-receptor/focal adhesion genes in fibroblast states unique to I61Q hearts (clusters 1 & 3, **Figure 2.2D, 2.2G**, **Table S1**) and [2] larger and more elongated focal adhesions identified in cardiac fibroblasts from I61Q transgenics (**Figure 2.3H-J**). As proof of principle that increased diastolic tension induces cardiac fibroblast proliferation, engineered heart tissues (EHTs) were generated with CON cardiac fibroblasts and neonatal myocytes adenovirally transduced with wildtype or I61Q cTnC and subjected to chronic preload in culture (**Supplemental Figure 2.4E-F** (*202*, *203*)). While preload increased the percentage of actively proliferating fibroblasts independent of genotype, I61Q cTnC expression had stronger effects (**Figure 2.3K**). The interaction between I61Q cTnC expression and preload also increased tissue and collagen alignment (**Figure 2.3L**), which more accurately modeled the I61Q transgenic phenotype than unloaded I61Q EHTs (**Figure 2.2X**).

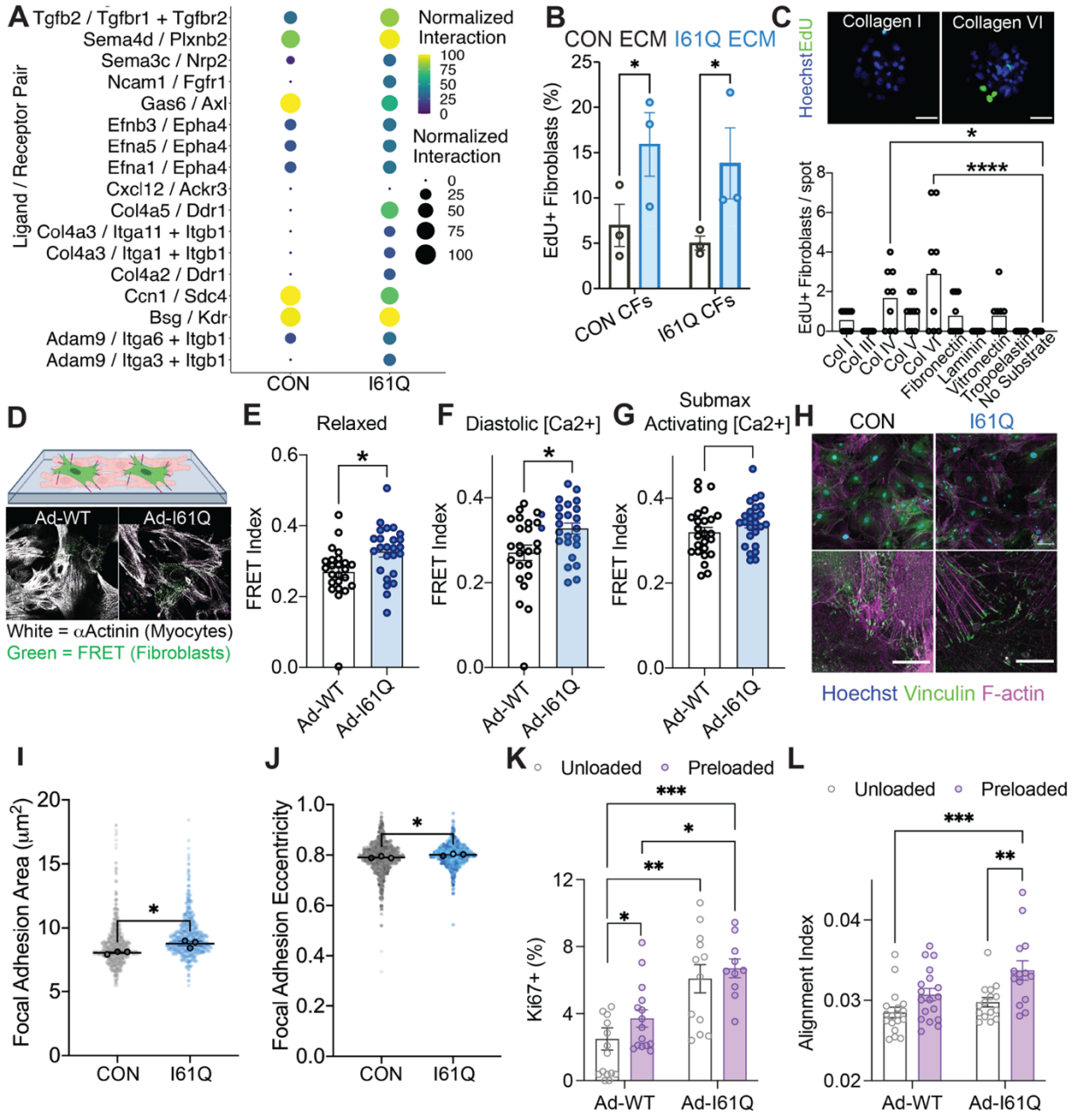

Figure 2.3: Diastolic mechanosensations at fibroblast focal adhesions are accentuated by ECM-receptor interactions that trigger proliferation. *A) Ligand-receptor analysis of myocyte-fibroblast interactions predicted from snRNAseq of 2-month-old CON and I61Q hearts where the ligand is expressed in myocytes and receptor is expressed in fibroblasts.* ***B)*** *Proliferation by EdU assay of CON and I61Q fibroblasts seeded within PEG gels decorated with ECM peptides from CON and I61Q hearts.*

(C, Top) *Representative images of cardiac fibroblasts seeded onto the ECM screening array stained for EdU to mark proliferating cells and* ***(C, Bottom)*** *quantification of EdU+ fibroblast counts on ECM-coated microspots.* ***D)*** *Schematic of cocultures with cardiomyocyte monolayers adenovirally transduced with either CON or I61Q cTnC that were sparsely overlaid cardiac fibroblasts genetically encoded with a FRET-tension sensor in the focal adhesion protein vinculin. Quantification of the average FRET efficiency (correlates with tension) at fibroblast focal adhesions in* ***E)*** *relaxed (+blebbistatin),* ***F)*** *diastolic [Ca^{2+}], and* ***G)*** *submaximal activating conditions (n=25 fibroblasts per group).* ***H)*** *Representative images (scale 100 μm, inset scale 30μm) of CON and I61Q cardiac fibroblasts stained for vinculin and filamentous actin (F-actin)and quantified for focal adhesion* ***I)*** *area* ***J)*** *eccentricity (n=681 CON & n=622 I61Q fibroblasts from 3 different mice per genotype). Quantification of* ***K)*** *the percentage of proliferating cardiac fibroblast as measured by Ki67 positivity (n=15 unloaded-WT, n=15 preloaded-WT, n=15 unloaded-I61Q, n=15 preloaded-I61Q) and* ***L)*** *collagen alignment (n=18 unloaded-WT, n=18 preloaded-WT, n=15 unloaded-I61Q, n=14 preloaded-I61Q) in unloaded or chronically preloaded EHTs generated with cardiomyocytes adenovirally transduced with WT or I61Q cTnC. *p<0.05,**p<0.01,***p<0.005 by either 2-way ANOVA or one-way ANOVA with Holm-Sidak's multiple comparisons test (B-C, K-L), or two-tailed unpaired t-test (E-G, I-J).*

2.3.4 Genetically disabling p38-mediated cardiac fibroblast responsiveness reduces DCM severity.

While several mechanotransduction pathways exist within fibroblasts, including those mediated by focal adhesions, ligand-receptor pair analysis of snRNAseq data also predicted stronger TGFβ signaling via *Tgfβr1* overexpression in I61Q cardiac fibroblasts (**Supplemental Figure 2.5A-B**). Since the response of I61Q cardiac fibroblasts to TGFβ in culture was similar to CON (**Supplemental Figure 2.3A-B**) other mechanotransduction pathways that could underlie

cardiac fibroblast expansion in I61Q mice were examined. YAP, a well-established index of mechanotransduction and regulator of proliferation (*204–206*), had higher activity in I61Q cardiac fibroblasts as identified by nuclear translocation assay (**Supplemental Figure 2.5C**). Our previous findings demonstrated that in cardiac fibroblasts both TGFβ signaling and strain-dependent increases in YAP-TEAD mechanotransduction require p38 activity (*82*, *123*). In accordance with these findings, p38 activity was increased in cardiac fibroblasts from 2-month-old I61Q transgenics as measured by western blot and p38 nuclear translocation assays (**Supplemental Figure 2.5D-F**). Given these data conditional p38 deletion in cardiac fibroblasts (p38 KO) was used to determine if p38 was essential for fibroblast expansion in response to I61Q-cTnC and ultimately the DCM phenotype. So, I61Q cTnC transgenics were crossed with cardiac fibroblast-specific p38 KOs, giving rise to four experimental genotypes (**Figure 2.4A**): controls (CON), p38 KO, I61Q, and I61Q plus fibroblast-specific p38 KO (p38 KO I61Q). All experimental weanlings received one week of TAM by intraperitoneal injection followed by 10 weeks of TAM chow (**Figure 2.4B**), which elicits ~85% recombination efficiency and nearly complete loss of p38 by 2 weeks in *Tcf21*$^{+}$ fibroblasts (*207*). snRNAseq of whole heart nuclei demonstrated that cardiac fibroblast-specific p38 deletion reduced the proportion of fibroblasts that transition to states 1 and 3, which were unique to mice expressing I61Q cTnC and defined by the upregulation of transcripts involved in cell cycle activity and mechanotransduction (**Figure 2.4C-D, 2.2G)** I61Q and CON UMAPs are also shown in **Figure 2.2D**, **Supplemental Figure 2.5G-J**). p38 deletion also lowered the expression of *Col1a1*, *Col1a2*, and *Col3a1* (**Supplemental Figure 2.3L-N**) and restored several myocyte-fibroblast crosstalk pathways to control levels (**Supplemental Figure 2.5A-B**). Myocardial sections immunostained with PDGFRα and pHH3 antibodies validated the snRNAseq findings, as p38 KO-I61Q myocardium

had reduced numbers of actively proliferating PDGFRα^{+},pHH3^{+} fibroblasts when compared to I61Q alone (**Figure 2.4E**). Concomitant with lower cell cycle activity PDGFRα^{+} fibroblast density was reduced in p38 KO-I61Q mice (**Figure 2.4F**). Deeper bioinformatic analysis of cell cycle regulatory signals that were overexpressed in I61Q but downregulated in p38KO-I61Q fibroblasts identified early growth response gene 1 (*Egr1*), which is a transcription factor downstream of integrin receptor signaling involved in proliferation, fibrosis, and pro-regeneration fibroblast senescence (*208–210*). RT-qPCR confirmed *Egr1* is upregulated in I61Q cardiac fibroblasts (**Supplemental Figure 2.5K**). EGR1 was also found in the nuclei of PDGFRα^{+} fibroblasts in I61Q myocardium but was non-existent in age matched CON and p38 KO-I61Q cardiac sections (**Fig. 4G**). To determine if *Egr1* is sufficient to induce cardiac fibroblast proliferation, 2-month-old CON and I61Q cardiac fibroblasts were retrovirally transduced with human *EGR1* and the percentage of proliferating fibroblasts quantified by EdU positivity (**Supplemental Figure 2.5L & 2.4H**). *EGR1* overexpression increased CON fibroblast proliferation to the same level as I61Q fibroblasts transduced with dsRed (control), whereas *EGR1* overexpression had no additive effects on proliferation in I61Q fibroblasts (**Figure 2.4H**). The addition of a p38 inhibitor (SB203580, 10 μmol/L) reduced proliferation in both CON and I61Q cardiac fibroblasts treated with dsRed virus, but *EGR1* overexpression in tandem with p38 inhibition restored proliferation to normal I61Q levels (**Figure 2.4H**). These data demonstrate that *Egr1* initiates fibroblast proliferation and acts downstream of p38.

4-month-old myocardial sections stained with picrosirius red-fast green showed that fibroblast-specific p38 deficiency in I61Q transgenics (p38 KO-I61Q) blocked interstitial fibrosis at this later timepoint (**Figure 2.4I-J, Supplemental Figure 2.5M**). Analysis of collagen fiber alignment by SHG imaging of decellularized hearts demonstrated that in most of the p38 KO-

I61Q cohort collagen fibers were less aligned and more like controls (**Figure 2.4K**). To confirm that alterations in cardiac fibroblast proliferation and matrix phenotype were due to p38-dependent changes in fibroblast function rather than altered primary sarcomere contractile defects from I61Q cTnC, Ca^{2+}-activated force generation was measured in demembranated trabecula from all of the experimental genotypes. As represented by a marked rightward shift in the isometric cardiac muscle force–Ca^{2+} relationship (**Figure 2.4L**), the I61Q cTnC transgene-dependent decrease in force generation at half-maximal Ca^{2+} concentrations (pCa_{50}) was retained in p38 KO-I61Q cardiac muscle when compared to CON and p38 KO (**Figure 2.4L-M**), demonstrating fibroblast-specific p38 deficiency fails to correct the desensitization of the myofilaments to Ca^{2+} in I61Q mice. Unexpectedly, intact cardiac muscle from p38 KO-I61Q generated higher twitch forces with improved contractility when compared to I61Q (**Figure 2.4N, Supplemental Figure 2.6A-B**). Functional rescue of the I61Q cTnC phenotype was also observed at the whole heart level by echocardiography in which p38 KO-I61Q mice had a significant recovery in ejection fraction (**Figure 2.4O**, $p<0.05$). Invasive hemodynamics further confirmed that p38 KO-I61Q mice improved systolic function relative to I61Q transgenics, as cardiac stroke work, ESPVR, and stroke volume were all restored to control levels (**Figure 2.4P-Q, Supplemental Figure 2.6C-E**). We've ascribed this restoration of twitch force and pressure development in p38 KO-I61Q hearts to reduced fibroblast numbers that should prevent early myocardial stiffening (**Figure 2.4F & I-J**), although Starling effects from the increased preload in p38 KO-I61Q cannot be ruled out as a factor (**Figure 2.4P**). This is in contrast to I61Q mice that operate at much higher end diastolic volume but with reduced stroke volume indicating I61Q hearts are stretched beyond their preload reserve (**Figure 2.4P, Supplemental Figure 2.6D**).

To determine how disabling p38 in cardiac fibroblasts could correct myocyte contractile function, single myocyte contraction and Ca^{2+} kinetics were assayed. Unloaded shortening amplitude was reduced in I61Q cardiomyocytes but completely rescued in the p38 KO-I61Q group (**Figure 2.4R**). This rescue was likely driven by increased Ca^{2+} transient amplitudes measured in p38 KO-I61Q cardiomyocytes that were higher relative to all other genotypes (**Figure 2.4S**). To determine if fibroblast-specific p38 deletion also corrected myocardial remodeling of the heart, echocardiography was used to measure diastolic chamber dimensions. Here, p38 KO-I61Q diastolic chamber dimensions were increased at 4 months of age similar to mice expressing just I61Q cTnC (**Figure 2.4T**), which we ascribed to I61Q-dependent reduction in diastolic tone (**Figure 2.1E**) rather than bona fide eccentric hypertrophy from serial sarcomere addition (*24*). Indeed, assessments of cardiomyocyte morphology in relaxed conditions (+blebbistatin) indicated p38 KO-I61Q cardiomyocytes had significantly reduced cell lengths and areas when compared to I61Q (**Figure 2.4U-V**, $p<0.001$). These data collectively demonstrate disabling p38-mediated fibroblast responsiveness to sarcomere hypocontractility alleviates much of the adaptive remodeling and reduces the severity of the DCM phenotype.

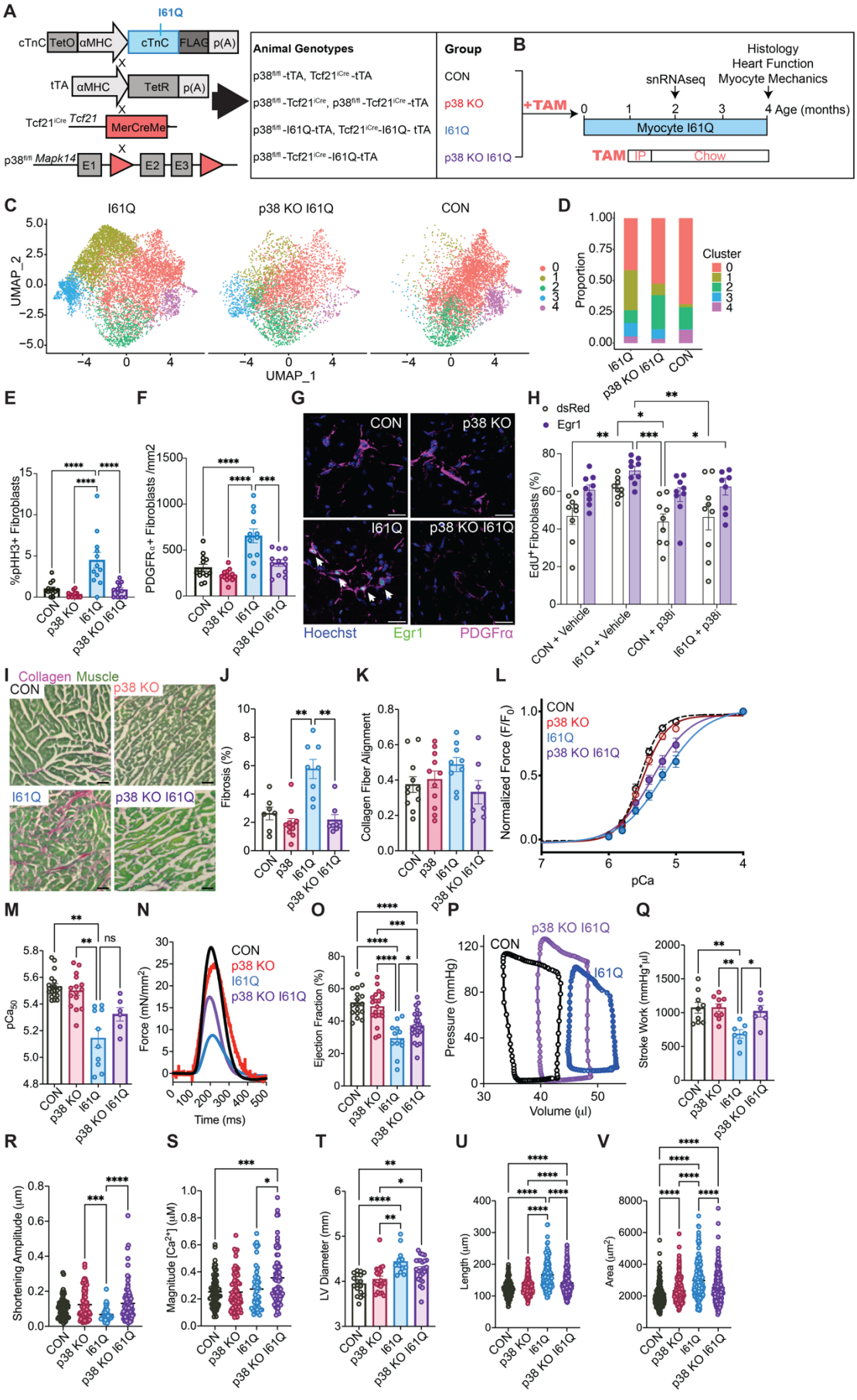
A
I61Q
cTnC TetO αMHC cTnC FLAG p(A)
tTA αMHC TetR p(A)
Tcf21iCre Tcf21 MerCreMer
p38f/f Mapk14 E1 E2 E3
Animal Genotypes
p38f/f -tTA, Tcf21iCre -tTA
p38f/f -Tcf21iCre, p38f/f -Tcf21iCre -tTA
p38f/f -I61Q-tTA, Tcf21iCre-I61Q- tTA
p38f/f -Tcf21iCre -I61Q-tTA
Group
CON
p38 KO
I61Q
p38 KO I61Q
B
Histology
Heart Function
Myocyte Mechanics
snRNAseq
+TAM
0 1 2 3 4 Age (months)
Myocyte I61Q
TAM IP Chow
C
I61Q
p38 KO I61Q
CON
UMAP_2
UMAP_1
Cluster
D
Proportion
Cluster
I61Q
p38 KO I61Q
CON
E
%pHH3+ Fibroblasts
CON
p38 KO
I61Q
p38 KO I61Q
F
PDGFRα+ Fibroblasts /mm2
G
CON
p38 KO
I61Q
p38 KO I61Q
Hoechst
Egr1
PDGFRα
H
dsRed
Egr1
EdU+ Fibroblasts (%)
CON + Vehicle
I61Q + Vehicle
CON + p38i
I61Q + p38i
I
Collagen Muscle
CON
p38 KO
I61Q
p38 KO I61Q
J
Fibrosis (%)
K
Collagen Fiber Alignment
L
CON
p38 KO
I61Q
p38 KO I61Q
Normalized Force (F/F0)
pCa
M
pCa50
N
CON
p38 KO
I61Q
p38 KO I61Q
Force (mN/mm2)
Time (ms)
O
Ejection Fraction (%)
P
p38 KO I61Q
CON
I61Q
Pressure (mmHg)
Volume (μl)
Q
Stroke Work (mmHg*μl)
R
Shortening Amplitude (μm)
S
Magnitude [Ca2+] (μM)
T
LV Diameter (mm)
U
Length (μm)
V
Area (μm2)

Figure 2.4: Fibroblast-specific p38 deficiency corrects cardiac dilation and systolic dysfunction in I61Q cTnC transgenic mice. ***A)*** *Schematic showing the generation of I61Q cTnC transgenic mice with tamoxifen inducible fibroblast-specific p38 deletion and the experimental genotypes derived from the described breeding scheme. Here, I61Q cTnC and tTA transgene were bred with a mouse line containing conditional p38a loss of function ($p38^{fl/fl}$) and a tamoxifen-inducible Cre recombinase knocked into the Tcf21 locus ($Tcf21^{iCre}$).* ***B)*** *Experimental design schematic showing the I61Q mutant cTnC is expressed just after birth (~ postnatal day 2), mice were allowed to develop normally for 1 month, and then tamoxifen was administered to induce fibroblast-specific p38 excision. Experimental endpoints were at 2- and 4-months of age.* ***C)*** *UMAP dimensionality reduction plot and* ***D)*** *proportion analysis for all sequenced cardiac fibroblast nuclei from 2-month-old I61Q, p38-I61Q, and CON hearts. Each color represents distinct fibroblast clusters (states) based on differential gene expression. *UMAPs for I61Q and CON were also shown in figure 2 for clarity but all 3 groups were sequenced simultaneously as part of the same experiment. Quantification of* ***E)*** *fibroblast proliferation and* ***F)*** *fibroblast density by immunofluorescent staining for pH3 and PDGFRα in 2-month-old myocardial sections (CON n=13, p38KO n=13, I61Q n=12, p38KO-I61Q n=12).* ***G)*** *Representative images of Egr1 (green) and PDGFRα (magenta) in myocardial sections. White arrows indicate $Egr1^{+}$ nuclei (Hoescht stain, CON n=8, p38KO n=8, I61Q n=7, p38KO-I61Q n=7, scale bar=100mm).* ***H)*** *Quantification of the percentage of proliferating (EdU^{+}) CON or I61Q cardiac fibroblasts ± dsRed (control) or human Egr1 retroviral vectors ± p38 inhibitor as determined by positivity.* ***I)*** *Representative PSR/FG stained myocardial sections and* ***J)*** *quantification of collagen (red) (CON n=7, p38KO n=11, I61Q n=8, p38KO-I61Q n=8).* ***K)*** *Quantification of collagen fiber alignment from decellularized CON (n=11), p38KO (n=11), I61Q (n=9), and p38KO-I61Q (n=7) hearts.* ***L)*** *Representative relationship between normalized tension and Ca^{2+} concentration (pCa) and* ***M)*** *Ca^{2+} sensitivity of tension generation (pCa_{50}) in membrane permeabilized trabeculae of CON (n=19), p38KO (n=15), I61Q (n=10), and p38KO-I61Q (n=6) mice.* ***(N)*** *Mean twitch forces from intact trabeculae of 4-month-old CON (n=5), p38KO (n=5), I61Q (n=5),*

and p38KO-I61Q (n=4) mice. ***O)*** *Quantification of left ventricular ejection fraction measured by echocardiography from CON (n=17), p38KO (n=20), I61Q (n=12), and p38KO-I61Q (n=23) mice.* ***P)*** *Representative pressure-volume loops and* ***Q)*** *quantification of stroke work by from invasive hemodynamic measurements at 4 months (CON n=9, p38KO n=9, I61Q n=7, p38KO-I61Q n=6).* ***R)*** *Quantification of unloaded sarcomere shortening amplitude (CON n=85, p38KO n=87, I61Q n=45, p38KO-I61Q n=85 cardiomyocytes) and* ***S)*** *Ca^{2+} transient amplitude (CON n=75, p38KO n=81, I61Q n=54, p38KO-I61Q n=66) in isolated intact cardiomyocytes from the described genotypes.* ***T)*** *Quantification of left ventricular diastolic diameter at 4 months of age by echocardiography (n same as* ***O****).* ***U)*** *Quantification of isolated cardiomyocyte length and* ***V)*** *area from the described genotypes (CON n=250, p38KO n=250, I61Q n=199, p38KO-I61Q n=200). For isolated myocyte experiments (****R,S,U,&V****) the following biological replicates per genotype were used: CON n=4, p38KO n=5, I61Q n=4, p38KO-I61Q n=5. Data are mean ± SEM, ns=not significant, *p<0.05,**p<0.01, ,***p<0.005,****p<0.001 by 2-way ANOVA with Holm-Sidak's multiple comparisons test.*

2.4 Conclusions and Future Work

2.4.1 Conclusions

This study explored the function of fibroblasts as mechanical rheostats within the heart capable of adaptively remodeling the ECM to preserve cardiac function and mechanical homeostasis in response to a DCM-linked sarcomeric variant that causes myocyte hypocontractility. These data suggest fibroblast function is one of a myriad of nested mechanical homeostatic feedback loops guiding organ structure-function in which cells exhibit dynamic reciprocity with their extracellular mechanical environment (*211–214*). In DCM, fibroblasts are well-equipped to respond to the contractile insufficiencies of cardiomyocytes, as they are necessarily mechanosensitive to fulfill their role of maintaining tissue integrity (*215*). It is likely

that reduced cardiomyocyte tension leads to strain overload as hemodynamic loads on the myocardial wall increase throughout development and disease progression (*216*). Here, both cardiomyocytes and fibroblasts adapted to the pathogenic cTnC variant to preserve the heart's mechanical integrity and systolic function, where cardiomyocytes altered their morphology and tuned excitation-contraction coupling mechanisms. Both cardiomyocyte adaptations appear to be highly reversible should the inciting disease stimulus be therapeutically blocked or removed. By contrast, cardiac fibroblasts proliferated in response to the I61Q-dependent loss of myocyte tension generation, which is likely a permanent modification given cardiac fibroblasts are resistant to cell death and lack regulatory mechanisms for restricting cell number (*217–219*). Hence, the tissue alignment, compaction, and stiffness resulting from fibroblast proliferation may also prove irreversible without a fibroblast-specific therapy that blocks their response to sarcomere hypocontractility (*120*, *207*), which was achieved in this study by targeted genetic deletion of p38. This result is supported by a recent report that developmental ablation of cardiac fibroblasts softens myocardial tissue (*219*). Our finding that the material properties of DCM myocardium are shaped in part by cardiac fibroblast population growth rather than the fibrotic process of fibroblast to myofibroblast transition is critically important to the treatment of non-ischemic DCM (*173*), given activated myofibroblast states are transient, and unlike changes in fibroblast number, these state transitions could reverse in response to myocyte-specific therapeutics for DCM (*217*). Promising therapeutic strategies for DCM like myosin activators may not correct fibroblast proliferation, which could explain their modest effects on tissue stiffening (*36*, *168*). It is therefore unlikely that correcting myocyte tension generation alone could reduce fibroblast numbers in the DCM heart unless given at the earliest stage of the disease process. Finally, this study challenges the paradigm that ECM remodeling is secondary to

eccentric hypertrophy of the myocyte and instead supports an essential role for fibroblasts and the extracellular environment in shaping cardiac form and function in DCM (*220*), indicating effective therapeutics for this disease will need to address collective cell behaviors rather than singularly restore myocyte function.

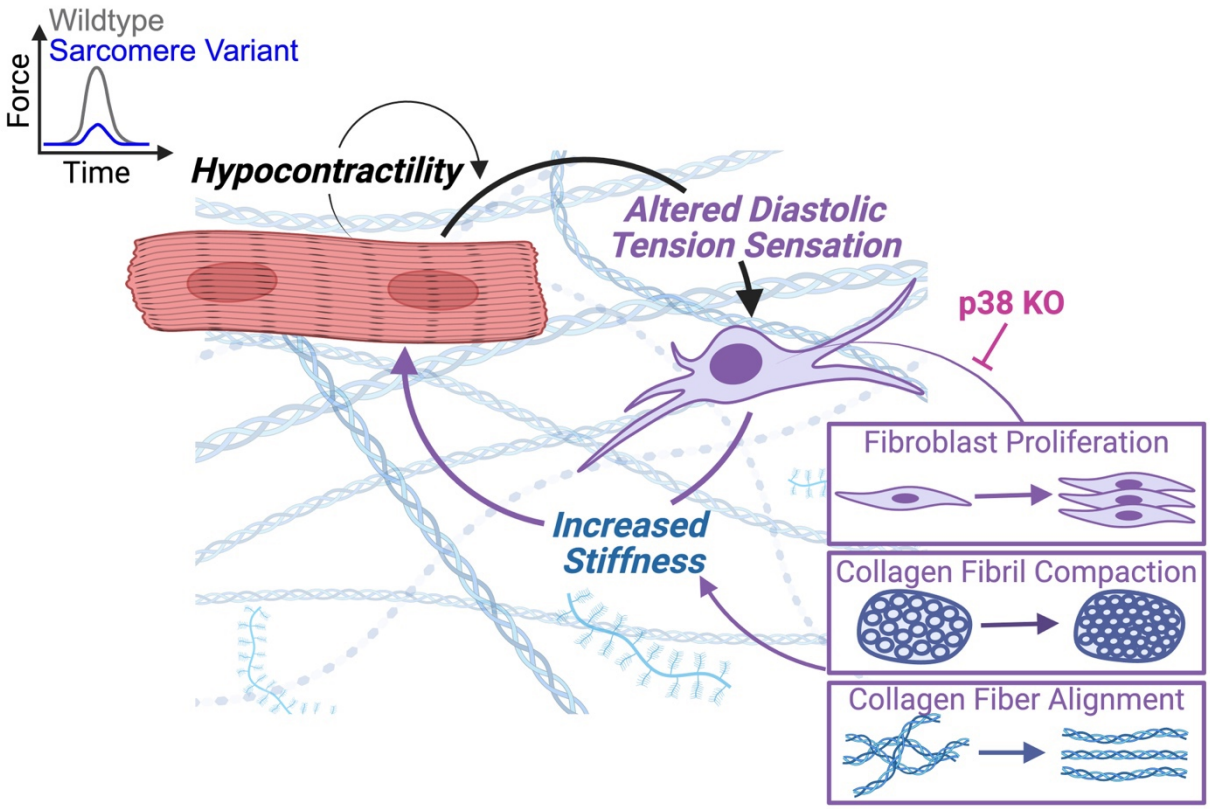

Figure 2.5: Cardiac fibroblast p38 deficiency blocks cardiomyocyte hypocontractility-induced myocardial stiffening by structurally reorganizing collagen in a DCM model. *In DCM mice generated by the transgenic expression of a sarcomeric variant that causes cardiomyocyte hypocontractility, we identified p38-mediated fibroblast responses that expand the fibroblast population, remodel fibrillar collagen architecture, and stiffen the myocardium prior to morphological remodeling of cardiomyocytes as essential determinants of DCM disease severity. Figure generated using BioRender.com.*

2.4.2 Summary and future work

This study helped establish the role fibroblasts play in the development and progression of DCM. Furthermore, it showed that fibrotic remodeling is not merely a secondary effect of myocyte dysfunction, but rather a major element of a multicellular negative feedback loop whereby myocyte dysfunction and hypertrophy drives fibroblast proliferation and ECM remodeling, which in turn worsens myocyte and whole organ remodeling (**Figure 2.5**).

2.5 Methods

Mice

All animal experiments were approved by the University of Washington Institutional Animal Care and Use Committee. I61Q mice were generated as previously described, by mating to a tetracycline transactivator (tTA) line on the FVB/NJ genetic background (*18*). These I61Q tTA mice were further bred onto a line containing LoxP-targeted Mapk14 ($p38^{fl/fl}$) mice and a tamoxifen regulated Cre recombinase that was knocked into the Tcf21 locus (Tcf21iCre) to generate I61Q cTnC-$p38^{fl/fl}$-$Tcf21^{iCre}$ mice (p38 I61Q), which were on mixed genetic background (*207*). Tamoxifen was administered to mice by intraperitoneal injection for 5 consecutive days (400mg/kg body weight in peanut oil), followed by tamoxifen citrate chow ad libitum until a 2- or 4-month experimental endpoint. Echocardiography was performed on a Vevo2100 or Vevo3100 under inhalation isoflurane at heart rates exceeding 350bpm. Invasive hemodynamics on isoflurane-anesthetized mice was performed under heart rates of 420-500bpm using a high-fidelity pressure-volume catheter (1.2F, Transonic) inserted into the left ventricle via the right carotid artery. All mouse studies are performed with cohorts from multiple inbred pairs with randomized interventions and littermates as controls. To avoid bias, genotypes and

experimental groups remain blinded until data are analyzed. Biological replicates are equally comprised of animals/cells from both sexes.

Histology

Fixed cardiac tissues were either processed into paraffin and sectioned (I61Q colony) or cryosectioned in OCT for histologic assessment. Picrosirius red-fast green stained slides were imaged across 6 fields of view at 20x magnification per heart and segmented for collagen content using the color thresholding tool in ImageJ. Whole-heart cross-section images were generated from slide scans obtained by a Hamamtsu Nanozoomer digital pathology system. For fibroblast proliferation and activation, slides were stained with antibodies for SMA (Sigma A2547, 1:500), phospho-histone H3 (abcam, 1:200), and PDGFR (1:100 abcam) overnight in staining buffer (1X PBS, 1% BSA, 1% fish skin gelatin), then stained using Alexa Fluor-conjugated secondaries (1:1000 Thermo Fisher) and Hoechst (1:2000 Thermo Fisher) for 90 minutes in staining buffer at room temperature. Stained slides were imaged on a Leica Stellaris 5 confocal microscope under 20x magnification. For quantification, images from six representative regions of interest were obtained at 2x scanner zoom and counted manually blinded to mouse genotype using FIJI (*221*).

Cardiac Perfusion Decellularization

Freshly harvested hearts were retrograde perfused with a 1% sodium dodecyl sulfate (SDS) solution for 12 hours to decellularize, followed by 1% Triton-X 100 for 1 hour to remove SDS, then rinsed by perfusion with deionized water for 1 hour. Hearts were then transferred to 15mL deionized water, which was refreshed daily for 5 days to ensure complete removal of detergent.

Multiphoton ECM imaging and structural analysis

Hearts were perfused with 1% agarose and mounted on a 100mm petri dish with the left ventricular free wall facing up, then imaged in whole mount on an Olympus FV1000MP microscope using 860nm excitation from a Mai-Tai HP laser (Spectra Physics, 59% power) and a Violet/Green emission filter cube. Z-stacks consisting of 20 images with 1.5-micron step within the left ventricular free wall starting 10 micron below the epicardial surface were condensed into maximum intensity projections using ImageJ, then the SHG channel (violet) was quantified for fiber alignment and length using CurveAlign 4.0 beta in CT-FIRE fiber mode *(222, 223)*.

Transmission Electron Microscopy (TEM)

To examine changes in individual collagen fiber architecture, hearts from CON and I61Q mice were excised and 2mm tissues were cut out of the myocardium and prepped for electron microscopy. Samples were immediately fixed in 4% Glutaraldehyde in 0.1M sodium cacodylate buffer, then stored overnight at 4C. The tissues were washed 5 x 5 minutes in buffer at room temperature and post fixed in buffered 2% osmium tetroxide on ice for 1 hour. The tissues were subsequently washed 5 times in ddH20, then en bloc stained in 1% Uranyl Actetate, (aqueous), overnight at 4C. The next day the tissue is washed 5 for 5 minutes in ddH2O then dehydrated in ice cold 30%, 50%, 70%, and 95% ETOH. Samples were then allowed to come to room temperature. This was followed by 2 changes of 100% ETOH and two changes of propylene oxide. The tissue was then infiltrated in a 1:1 mixture of propylene oxide : Epon Araldite resin, for 2 hours followed by two changes of fresh Epon Araldite, 2 hours each change, then placed in flat embedding molds and polymerized in a 60 degree C overnight. Thin sections of 80nm were

cut on a Leica EM UC7, post stained with Reynolds Lead Citrate, and imaged on a JEOL 1230 at 80KV. Individual fibrils were segmented using Cellkpose-SAM (*224*) and fibril density, diameter, and cross-sectional area was quantified using FIJI. Analysis was performed on 20 images from each genotype.

Cardiac muscle and ECM mechanics

For passive mechanics studies, a Langendorff balloon was inserted into the left ventricle and the heart was perfused with Krebs-Henseleit buffer containing blebbistatin (25μM, Toronto Research Chemicals). The balloon was inflated in 5 microliter steps to 35 μL with 2 minutes of stress relaxation time between each step. This regimen was performed once to precondition the tissue, and then repeated in duplicate for measurements of developed pressure. Following passive muscle measurements, the heart was decellularized as above with the balloon remaining inserted in the left ventricle and the mechanical testing regimen was repeated for the ECM alone. Pressure traces were acquired using LabView and exported to Excel for analysis of developed pressure and curve slope.

ECM Proteomics

Hearts were perfusion decellularized above, and digested in solution as previously described (*211*). Briefly, samples were first denatured for 2hrs at 37 °C in urea (8M, Fisher) and dithiothreitol (10mM, Thermo Fisher), continuously agitated. Following 30 minutes of alkylation with iodoacetamide (25mM, supplier), samples were then diluted with ammonium bicarbonate (100mM, pH=8.0, Sigma Aldrich), and 2μL PNGase F (500 U/μL, New England Biolabs) was added to deglycosylate the samples over a 2 hour incubation at 37 °C. Samples were then digested by adding 2μL LysC (500ng/μL, Pierce) for 2 hours then 6μL trypsin (100ng/μL New

England Biolabs) overnight, both at 37 °C. Trypsin (4μL) was added the next day for 2 hours of additional digestion at 37 °C, then inactivated through addition of 50% trifluoracetic acid (Sigma Aldrich) before samples were clarified through centrifugation (16,000 x g, 5 minutes) and cleaned for liquid chromatography on an MCX column (Waters). For proteomics by data independent acquisition (DIA) mass spectrometry, samples were analyzed at the Nathan Shock Center for Aging proteomics core on a Q Exactive HF Hybrid Quadrupole-Orbitrap Mass Spectrometer (Thermo Fisher) with a Nanoacquity HPLC (Waters). Total ion currents were normalized between samples using the PowerTransformer function of the scikit-learn package in Python (*225*), then differential expression between groups was tested by one-way ANOVA. Figures were generated using Seaborn and matplotlib (*226*).

Cardiac fibroblast isolation and culture

Primary cardiac fibroblasts were isolated as described previously (*227*). Fibroblasts for RT-PCR and Western blot analyses were negatively sorted on Cd11b microbeads and positively sorted for anti-feeder microbeads through LS columns on a QuadroMACS magnet (Miltenyi Biotec). Fibroblasts for RNASeq, proliferation assays, and engineered tissues were plated on 60mm tissue culture dishes and expanded to the first passage in Dulbecco's Modified Eagle Medium (DMEM) with 20% fetal bovine serum (FBS) and 1X penicillin/streptomycin solution. Cells in culture were passaged with 0.25% trypsin-EDTA and seeded onto 24-well iBidi μ-plates at a density of 1000 cells/cm^2 for *in vitro* proliferation studies. The FBS concentration in the media was dropped to 2% upon seeding, and EdU (10μM, Thermo Fisher), dinaciclib (5μM, ApexBio), or ilomastat (10μM, MedChemExpress) were added where indicated. After 24 hours cells were fixed in 4% paraformaldehyde and stained using a Click-It EdU proliferation kit

(Thermo Fisher) per manufacturer's instructions. To screen ECM components, 250,000 WT cardiac fibroblasts were seeded onto an ECM Select Array Kit Ultra-36 (Advanced Biomatrix) and cultured for 24 hours in EdU-containing media as above. Collagen gel compaction was assayed as previously described (*214*), with fibroblasts seeded into 1% collagen type I (Advanced Biomatrix) hydrogels at a density of 80,000 cells/mL in a 24-well plate for 24hrs in DMEM with 2% FBS.

PEG-ECM hydrogels

4-armed PEG_{20kDa}-BCN, NHS-Azide, and the MMP-degradable crosslinking peptide N_3-RGPQGIWGQLPETGGRK(N_3)-NH_2 were all synthesized as previously described (*228*, *229*). To generate soluble ECM peptides 4 hearts per genotype were pooled, snap frozen and homogenized by mortar and pestle under liquid nitrogen, lyophilized to a powder, then resuspended at 10mg/mL in a pepsin solution (1mg/mL in 0.1M hydrochloric acid) for 48 hours at room temperature, stirred. Digested ECM was neutralized with the addition of NaOH and re-lyophilized. Digested ECM was resuspended at 25mg/mL in PBS. To azide-functionalize ECM, 2μL of NHS-Azide (60mM in DMSO) was added to 118μL of ECM solution and reacted for 1 hour on ice. Primary cardiac fibroblasts were encapsulated at 10 million cells/mL in gels comprised of 3mM PEG-BCN, 6mM crosslink, 1mM N_3-GRGDS, and 5mg/mL azide-modified ECM, which were then cultured in DMEM containing 10% FBS and 10μM EdU for 24 hours prior to fixation. Gels were then blocked in PBS containing 0.1M sodium azide to quench any remaining BCN groups in the polymer network and stained as above.

RNA Sequencing and Analysis

Fibroblasts cultured to 80% confluency were lysed in Trizol (Thermo Fisher) and total RNA was extracted using a Direct-zol RNA Microprep kit, including DNAse treatment (Zymo Research). For RNAseq, RNA integrity was verified using RNA Screentape on a 2200 Tapestation (Agilent) and samples with high RNA integrity (RINe ≥ 7) were submitted to BGI Genomics for RNA sequencing (PE100). Resultant FASTQ files were aligned to the mm10 reference genome using RNA-STAR (*230*), assigned to genes using featurecounts (*231*), and gene transcript counts tested for differential expression using DESeq2 (*232*). Differentially expressed genes were tested for pathway enrichment using G:Profiler (*233*), and heatmaps were generated in python using the Seaborn package (M. Waskom, Seaborn (2020)). RT-PCR was performed as previously described using the Superscript III First-Strand Synthesis System (Thermo Fisher), iTaq universal SYBR Green Supermix (Bio-Rad) and the primers in **Table S2** (*199*).

Single nuclei RNA sequencing (snRNAseq) of whole hearts

Whole heart samples were prepared using the sci-RNA-seq3 combinatorial indexing method as described previously with the following modifications (*234*, *235*). Two hearts from each group were snap frozen in liquid nitrogen. Nuclei were isolated from frozen tissues by grinding the frozen tissue with a mortar and pestle, lysing the powdered tissue in hypotonic lysis buffer B, and dissociating the tissue in a gentleMACS M tube run on the "Protein 001" program followed by 50 strokes in a Dounce homogenizer with a type A/loose pestle. Lysates were subsequently filtered through a 40 μm filter and centrifuged at 500xg for 5 minutes at 4°C. The nuclear pellet was then resuspended in 0.3 M sucrose, phosphate buffered saline (PBS), Triton X-100 $MgCl_2$ (SPBSTM) buffer (*234*, *235*), which was filtered through a 20μm filter. The nuclei

were subsequently fixed in methanol/DSP for 5 minutes at room temperature. Fixed nuclei were rehydrated with 0.3 M SPBSTM, centrifuged at 500xg for 5 minutes at 4°C, and resuspended in 0.3 M SPBSTM. Sequencing was performed at the Northwest Genomics Center on a Novaseq 6000 flow cell. Cleaned reads were aligned to the reference genome (GRCm38/mm10) using STAR (*230*). Doublets were identified using scrublet and subsequently filtered out (*236*). Further analysis and quality filtering was performed using the Seurat package in R (*237*). Nuclei were filtered out if they contained fewer than 200 UMI, over the top 1% quantile of UMI, or over 5% mitochondrial reads. Overall, 41,014 singlets across all cell types were sequenced with a mean UMI of 687. Clustering was then performed following the standard approach, with cell types manually identified by canonical marker genes. For fibroblast subcluster analysis, fibroblast reads were then normalized using the SCTransform function with the "glmGamPoi" method. Mitochondrial mapping rate was regressed out using the vars.to.regress argument. Principal component analysis was performed on the scaled data, and then cells were clustered on the first 5 principal components using the FindNeighbors function and the FindClusters function with resolution 0.3. To visualize the data, non-linear dimensional reduction via Uniform Manifold Approximation and Projection (UMAP) was used to project cells in 2D space on the basis of the first 5 principal components. 5 fibroblast clusters were identified, and cluster markers were identified using FindAllMarkers. The data have been deposited at Gene Expression Omnibus (GEO) repository and have been assigned the GEO accession number: GSE294563. GSM8911388-GSM8911399 were the accession numbers assigned to each of the individual data files.

For ligand-receptor pair analysis the ICELLNET package was used following the standard workflow described in the package vignette (*238*). To ensure cell-type specificity in the

communication analysis, each cell type within a pair was specifically subsetted based on identity from the larger global Seurat object and combined into a new object containing only the 2 specified cell types for analysis. The ICELLNET analysis was subsequently performed to identify outgoing and incoming signals with respect to the fibroblasts between fibroblast-cardiomyocyte, fibroblast-endothelial, fibroblast-immune cell, and fibroblast-fibroblast intercellular communication networks. The intercellular interaction scores generated by the ICELLNET analysis were subsequently normalized to wild-type values and averaged by genotype for plotting. The process was repeated for each cell type pairing.

Western Blotting

Magnetically sorted fibroblast pellets were lysed in 120 μL of Laemmli Buffer with DTT, of which 30 μL was loaded onto a 10% acrylamide gel for sodium dodecyl sulfate polyacrylamide gel electrophoresis (SDS-PAGE) and wet transfer to a polyvinylidene fluoride membrane for immunodetection. Membranes were blocked and immunostained in tris-buffered saline (20 mM Tris, 150 mM NaCl, pH 7.6) containing 0.1% Tween 20 and 5% nonfat powdered milk. Primary antibodies for phospho-p38 MAPK (Cell Signaling 9211, 1:1000), total p38 MAPK (Cell Signaling 9212, 1:1000), and GAPDH (Fitzgerald 10R-2932, 1:10,000) were incubated overnight at 4°C under gentle agitation. Rabbit or mouse primary antibodies were detected using a horseradish peroxidase-conjugated anti-rabbit IgG (Sigma AP307P, 1:4000) or anti-mouse IgG (Sigma AP308P, 1:4000) secondary antibody for 90 minutes at room temperature, then developed using SuperSignal West Pico PLUS (Thermo Fisher) chemiluminescence substrate. The titin N2B isoform was expressed relative to the total titin, meaning the sum of the isoforms N2B and N2BA. This was measured on a Coomassie-stained

titin gel. For the phosphospecific antibodies, the titin signal on the western blot was normalized to the corresponding signal on the Coomassie-stained stained blotting membrane, to account for differences in loading. The antibodies and protocols used were derived in the Linke lab (*183*).

Mouse cardiomyocyte isolation and cell culture

For functional measurements, mouse ventricular cardiomyocytes were freshly isolated by Langendorff perfusion with Liberase TM (0.225 mg/mL, Roche) in Krebs-Henseleit buffer (135 mM NaCl, 4.7 mM KCl, 0.6 mM KH2PO4, 0.6 mM Na2HPO4, 1.2 mM MgSO4, 20 mM HEPES, 10 M BDM, and 30 mM taurine) as previously described (*239*). Ventricular cardiomyocytes were mechanically dispersed and filtered through a 200 m nylon mesh then allowed to sediment for 5-10 minutes. Sedimentation was repeated three times using increasing [Ca2+] from 0.125 to 0.25 to 0.5 mmol/L. Cardiomyocytes were plated on laminin-coated coverslips in Tyrode's solution (137 mM NaCl, 5.4 mM KCl, 0.5 mM MgCl2, 1.2 mM CaCl2 2H2O, 10 mM HEPES, and 5 mM Glucose, pH 7.4) for 1 hour at 37 °C prior to functional measurements. For myocyte morphology measurements, cardiomyocytes were similarly isolated and plated with buffers containing 25 M blebbistatin and subsequently fixed with 4% PFA at room temperature for 15 minutes.

Measurements of cardiomyocyte contractility and calcium transients

Sarcomere measurements were obtained from isolated cardiomyocytes using the IonOptixTM SarcLen Sarcomere Length Acquisition Module with a MyoCam-S3 digital camera (Ionoptix Co.) attached to an Olympus uWD 40 inverted microscope. For these measurements cardiomyocytes were bathed in 1.2 mM Ca2+ Tyrode's solution and kept at 37 °C. To jumpstart pacing, cardiomyocytes were stimulated with frequencies varying from 0.5, 1.0, and 1.5 Hz at 10

V for a minimum of 10 contractions at each frequency. Sarcomere lengths were then measured in real time at a frequency of 1 Hz and averaged across 10-15 contraction cycles. Separate coverslips were treated with 1 M Fura-2–acetoxymethyl ester to measure calcium transients. Blinded analysis was performed using the IonWizard software. Statistical analyses were performed on individual myocyte measurements (n 20 cardiomyocytes/mouse; n=3-4). Significance was determined using Student's t-test. For myocyte geometry quantification approximately 50 cells per mouse were manually traced using FIJI.

Rat cardiomyocyte isolation and EHT experiments

Freshly isolated neonatal rat cardiomyocytes and fibroblasts were seeded into 100 μL fibrin EHTs containing 1 million cells per tissue between a pair of flexible and rigid PDMS posts that were 12 mm in length and 1.5 mm in diameter within a 24-well plate, as previously described (*240*). EHTs were polymerized for 85 minutes, then demolded and immersed in plating media [4:1 DMEM:Medium 199 (M199), 10% horse serum, 5% FBS, 100 U/mL penicillin streptomycin (pen-strep)] containing AdGFP or AdI61Q at a multiplicity of infection of 200. After 24 hours, EHTs were switched to maintenance medium consisting of 1:1 DMEM:M199 containing 5% FBS, 100 U/mL pen-strep, 5 g/L 6-aminocaproic acid, 1X insulin-transferrin-selenium, and 0.1% chemically defined lipid concentrate, which was thenceforth swapped every other day until the 14-day experimental endpoint. EHTs were then bathed in Tyrode's buffer equilibrated to 37 °C for contractile analysis as previously described (*240*).. Briefly, EHTs were paced at 1 Hz by a custom 24-well plate pacing apparatus with carbon electrodes biphasically stimulated (5V/cm, 10ms duration) with a medical stimulator (Astro Med Grass Stimulator, Model S88X) while imaged. Brightfield videos of PDMS post deflection during EHT contraction

were taken at 66.67 frames per second on a Nikon TEi epi-fluorescent microscope under 2x magnification. Deflection of the flexible post relative to the rigid post was tracked using a custom MATLAB script in order to calculate passive force, twitch force, and the area under the twitch curve (tension index). Following functional measurements, EHTs were fixed in ice-cold 4% PFA for 1 hour and stained with anti-FLAG (Sigma, 1:1000), Alexa Fluor 568-conjugated wheat germ agglutinin (Thermo Fisher 1:1000), and Hoechst 33342 (Thermo Fisher, 1:1000). For alignment, 8 ROIs per wheat-germ stained EHT were confocally imaged in whole mount at 20x magnification on a Leica Stellaris 5 confocal microscope and analyzed using the Directionality plugin in FIJI. Alignment coefficient was calculated as the amount divided by the dispersion of directionality.

Intact and skinned muscle mechanics

Hearts were quickly removed via thoracotomy and rinsed in oxygenated modified Krebs buffer containing 118.5 mM NaCl, 5 mM KCl, 1.2 mM MgSO4, 2 mM NaH2PO4, 25 mM NaHCO3, 1.8 mM CaCl2, and 10 mM glucose. Hearts were then perfused and dissected in oxygenated modified Krebs with 0.1 mM CaCl2 and 20 mM 2,3-butanedione 2-monoxime (BDM) to limit contraction and damage during tissue dissection.

For demembranated tissue mechanics, dissected hearts were permeabilized in a glycerol relaxing solution containing 100 mM KCl, 10 mM MOPS, 5 mM K2EGTA, 9 mM MgCl2 and 5 mM Na2ATP (pH 7.0), 1% (by vol) Triton X-100, 1% protease inhibitor (Sigma P8340), and 50% (by vol) glycerol at 4°C overnight then stored in fresh solution without Triton X-100 for storage at - 20°C. Briefly, right ventricular trabeculae were dissected and mounted between a force transducer and motor, and sarcomere length (SL) was set to ~2.3 m, as previously

described.(5) Experiments were conducted in a physiological solution (15°C, pH 7.0) containing a range of pCa (= –log[Ca2+]) from 9.0 to 4.0. Force and ktr (rate of tension redevelopment) were collected at each pCa and analyzed with custom using LabView software.

For intact twitch measurements unbranched, intact trabeculae were dissected from the right ventricular wall and mounted between a force transducer (Cambridge Technology, Inc., model 400A) and a rigid post, as previously described. The tissue was then submerged in a custom experimental chamber that was continuously perfused with oxygenated modified Krebs buffer (1.8 mM CaCl2) at 33°C. After a ~20min equilibration and washout at 0.5 Hz pacing, optimal length was set to ~2.3 m SL and tissue was paced at 1 Hz. 30 second traces were recorded on custom LabView software and were analyzed with custom code written using MATLAB software (Mathworks).

Acknowledgements

We acknowledge the support of the proteomics and bioinformatics core of the Diabetes Research Center NIDDK (DK017047), the Vision Research Core at UW (P30EY001730), the Brotman Baty Advanced Technology Lab (BAT-Lab) at UW, D. Hailey and the Garvey Imaging core at the UW Institute for Stem Cell and Regenerative Medicine (ISCRM), and B. Johnson and the UW Histology and Imaging Core. We thank R. Tian for use of critical instrumentation, S. Mohran for insightful discussion, and E. Olszewski and other members of the Davis lab for their insights and experimental assistance.

Funding

We acknowledge funding from ISCRM (fellowship to R.C.B.), the German Research Foundation (Li 690/14-1 to W.A.L.), the National Science Foundation (DGE 1762114 to R.C.B.

and I.M.R.), and the National Institutes of Health (FHL 165834A to I.M.R.; P30 AR074990 to N.J.S. and M.R.; R01 HL149734 and R01 HL146868 to N.J.S.; RM1 GM131981 to M.R.; R01 HL.157169 to F.M.-H.; R35 GM138036 to C.A.D.; R01 HL142624, HL141187, and HL162229 to J.D.).

2.6 Supplemental Figures

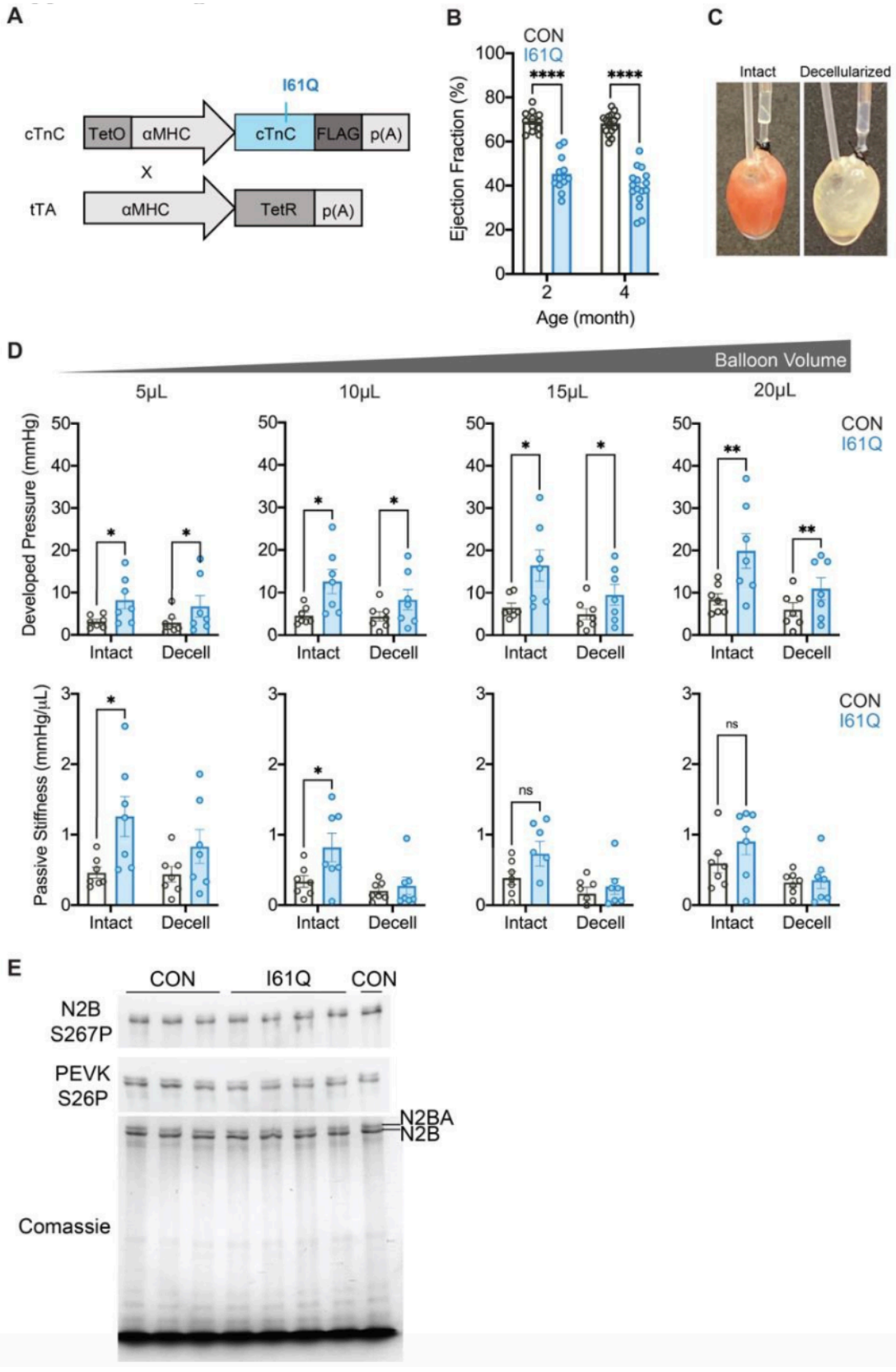

Supplemental Figure 2.1: I61Q cTnC transgenic hearts are hypocontractile and less compliant. A) *Schematic of the genetic crosses used to generate I61Q cTnC transgenic mice. Mice with cardiomyocyte-specific expression of a FLAG-tagged I61Q mutant cTnC transgene driven by a tetracycline regulated α-myosin heavy chain (αMHC) promoter were crossed with tetracycline transactivator (tTA) mice which elicits constitutive expression of the I61Q mutant cTnC transgene.* ***B)*** *Quantification of left ventricular ejection fraction by echocardiography at 2 (I61Q n=12, CON n=12) and 4 (I61Q n=16, CON n=15) months of age.* ***C)*** *Representative images of an intact (left) and decellularized (right) heart in a modified Langendorff working heart preparation for passive mechanical measurements.* ***D)*** *Developed balloon pressure (top) and passive stiffness measured as the slope of the pressure volume curve varying balloon volume (bottom). n=7 both genotypes. ns = nonsignificant, *p<0.05,**p<0.01 by 2-way ANOVA with Holm-Sidak's multiple comparisons test.* ***E)*** *Titin Western blots detected with phosphorylation site-specific antibodies (Top) and Coomassie stained gel (Bottom) of 2 month old I61Q and CON cardiac lysates.*

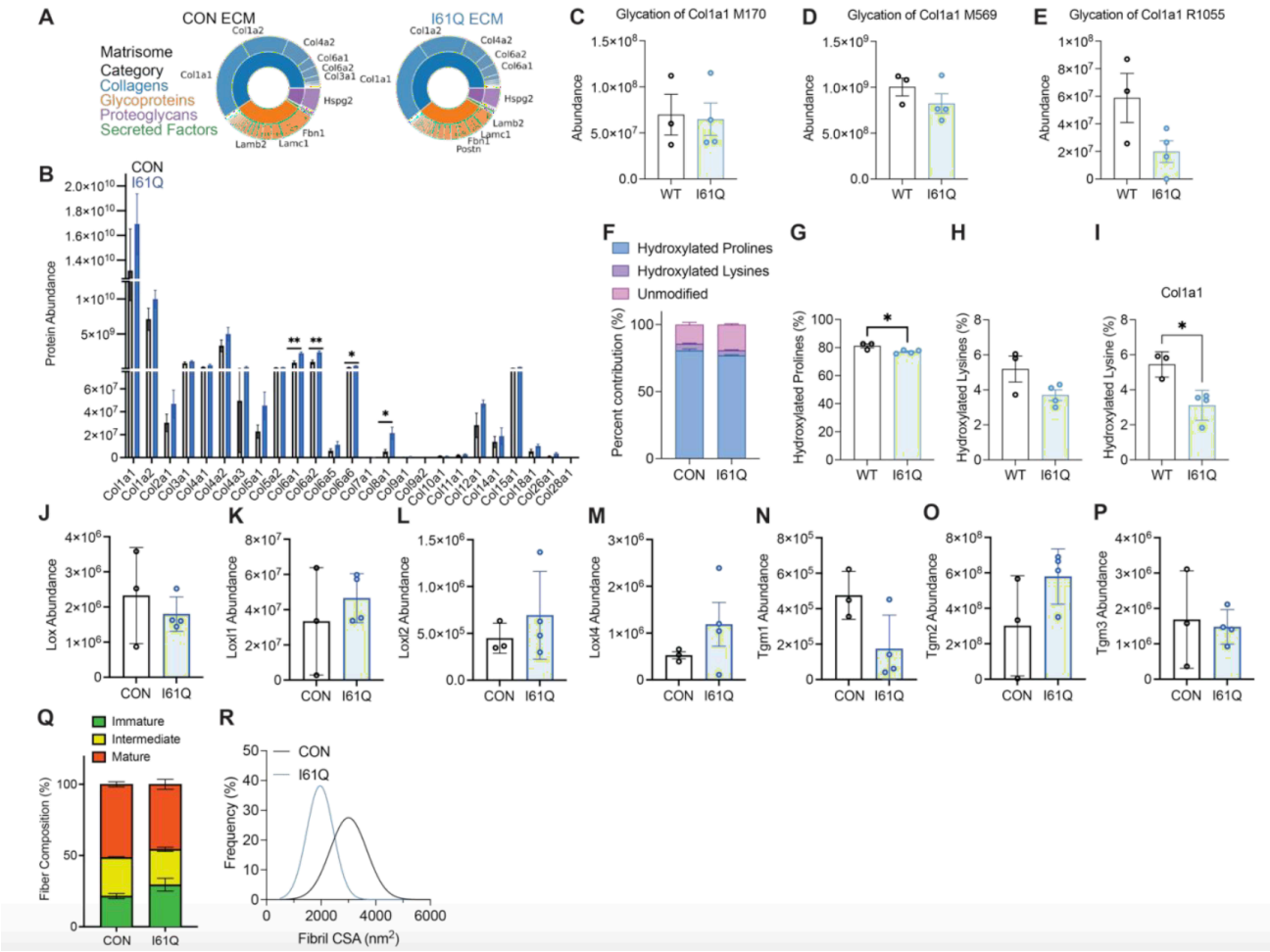

Supplemental Figure 2.2: Determinants of increased ECM stiffness in 2 month old I61Q transgenic hearts. ***A)*** *Pie charts showing the relative abundance of matrisomal proteins (colored by category) detected by mass spectrometry (MS) of decellularized cardiac ECM from control and I61Q mice (CON n=3, I61Q n=4). The top 10 most abundant proteins are labeled.* ***B)*** *Abundance of all collagen subtypes detected by MS. Quantification of Col1a1 glycation at residue* ***C)*** *M170,* ***D)*** *M569, AND* ***C)*** *R1055.* ***F)*** *Quantification of the percentage of total fibrillar collagen that is unmodified (pink), hydroxylated at lysine residues (purple), or hydroxylated at proline residues (blue). Quantification of the percentage of all fibrillar collagen with hydroxylated* ***G)*** *prolines and* ***H)*** *lysines.* ***I)*** *Quantification of the percentage of hydroxylated lysines in Col1a1. The abundance of* ***J)*** *lysyl oxidase,* ***K)*** *lysyl oxidase 1,* ***L)*** *lysyl oxidase 2,*

***M**) lysyl oxidase 4, **N**) transglutaminase 1, **O**) transglutaminase 2, and **P**) transglutaminase 3 detected by MS. **Q**) Percent composition of green (very immature), yellow (immature), and orange-red (mature) birefringent fibers detected by polarized light microscopy of picrosirius red-fast green stained myocardial sections from 2 month old CON and I61Q mice (Con n = 9, I61Q n = 10). **R**) TEM analysis of the distribution of collagen fibril cross- sectional area (CSA) between genotypes (n=20 ROIs/mouse, 3 mice per genotype). *p<0.05 two-tailed unpaired t- test.*

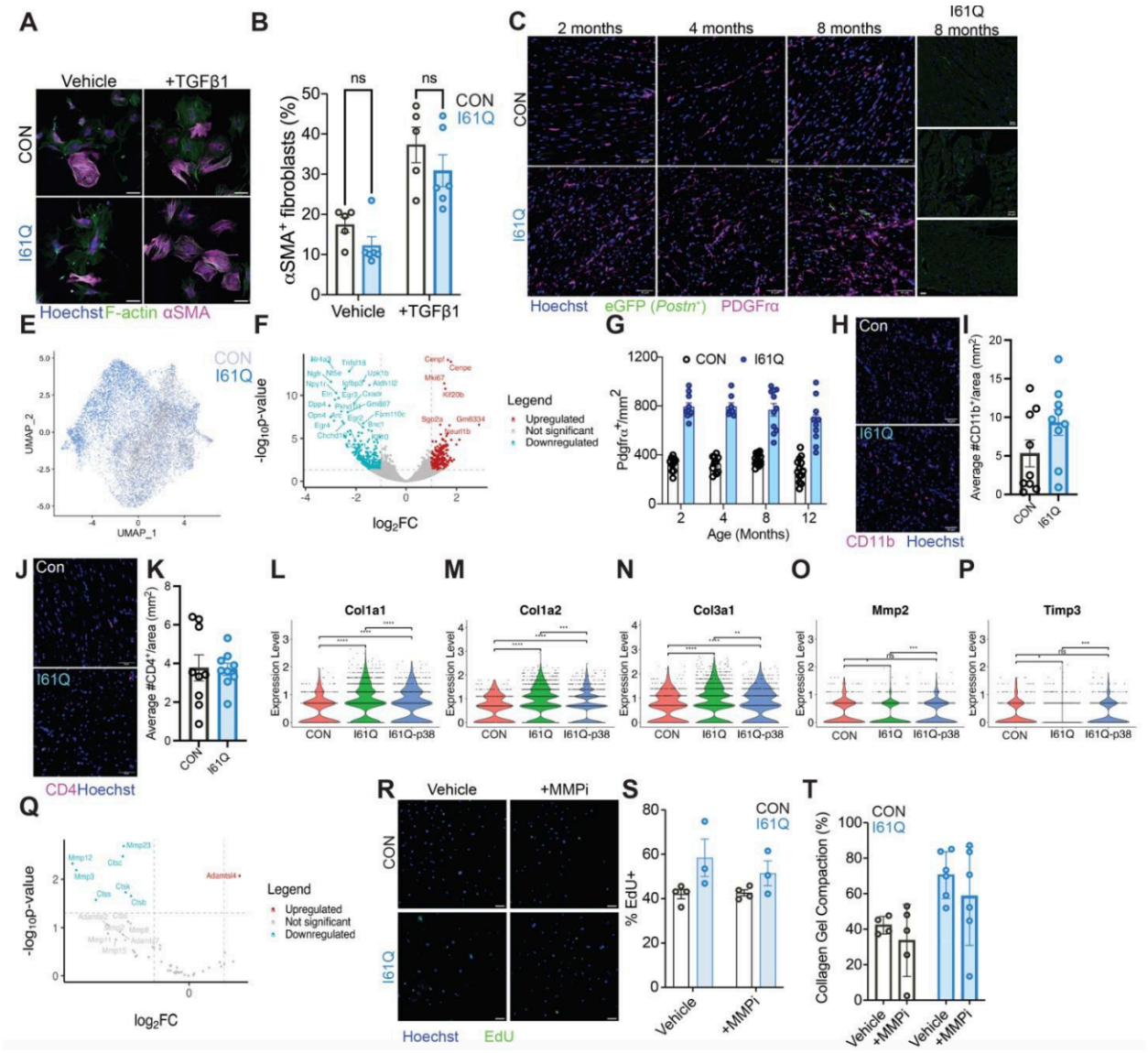

Supplemental Figure 2.3: I61Q fibroblasts are competent to activate but fail to transition to a myofibroblast state in vivo. ***A)*** *Representative images (scale 50μm) and* ***B)*** *quantification of TGFβ-induced fibroblast-to-myocyte conversion by αSMA immunocytochemistry (CON n=5, I61Q n=6 biological replicates).* ***C)*** *Representative myocardial sections from tamoxifen-labeled Postn$^{mT/mG}$ I61Q TTA hearts and CON controls (left & middle columns, scale bar = 40μm, right column scale bar = 20μm).* ***E)*** *UMAP dimensionality reduction plot for all sequenced cardiac fibroblast nuclei from 2 month old I61Q and CON hearts in which each nuclei is colored by genotype.* ***F)*** *Volcano plot of differentially*

expressed genes in bulk RNAseq analysis of cardiac fibroblasts isolated from 2 month old I61Q and CON hearts. ***(G)*** *Quantification of PDGFRα^{+} fibroblast density in cardiac sections from CON (n=11/10/15/13 : 2/4/8/12 months of age) and I61Q (n=10/8/11/10 : 2/4/8/12 months of age) mice at various timepoints. Representative images and quantification of cardiac infiltrating* ***(H, J)*** *CD11b+ and* ***(J,K)*** *CD4+ cells in 2 month old I61Q (n=9) and CON (n=9) hearts. Violin plots showing the distribution of* ***L****) Col1a1,* ***M****) Col1a2,* ***N****) Col3a1,* ***O****) Mmp2,* ***P****) Timp3 expression levels in the cardiac fibroblast population segregated by genotype.* ***Q****) Volcano plot of differentially expressed genes that encode key ECM proteases like matrix metalloproteinases (Mmps), cathepsins (Cts) and a distintegrin and metalloproteinase with thrombospondin motifs (ADAMTS).* ***R****) Representative EdU-stained immunofluorescent images (scale 50μm) and* ***S****) quantification of CON and I61Q fibroblasts treated with vehicle or ilomastat (MMPi), (CON n=4, I61Q n=3 biological replicates).* ***T****) Collagen gel compaction after 24 hours of treatment with either vehicle control or ilomastat (CON n=4 vehicle / 5 MMPi, I61Q n=6 vehicle/6 MMPi biological replicates). ns = nonsignificant, *p<0.05,**p<0.01,***p<0.005 by either 2-way ANOVA (****B,S,T****) or one-way ANOVA (****L-P****) with Holm-Sidak's multiple comparisons test, or two-tailed unpaired t-test (****I,K****).*

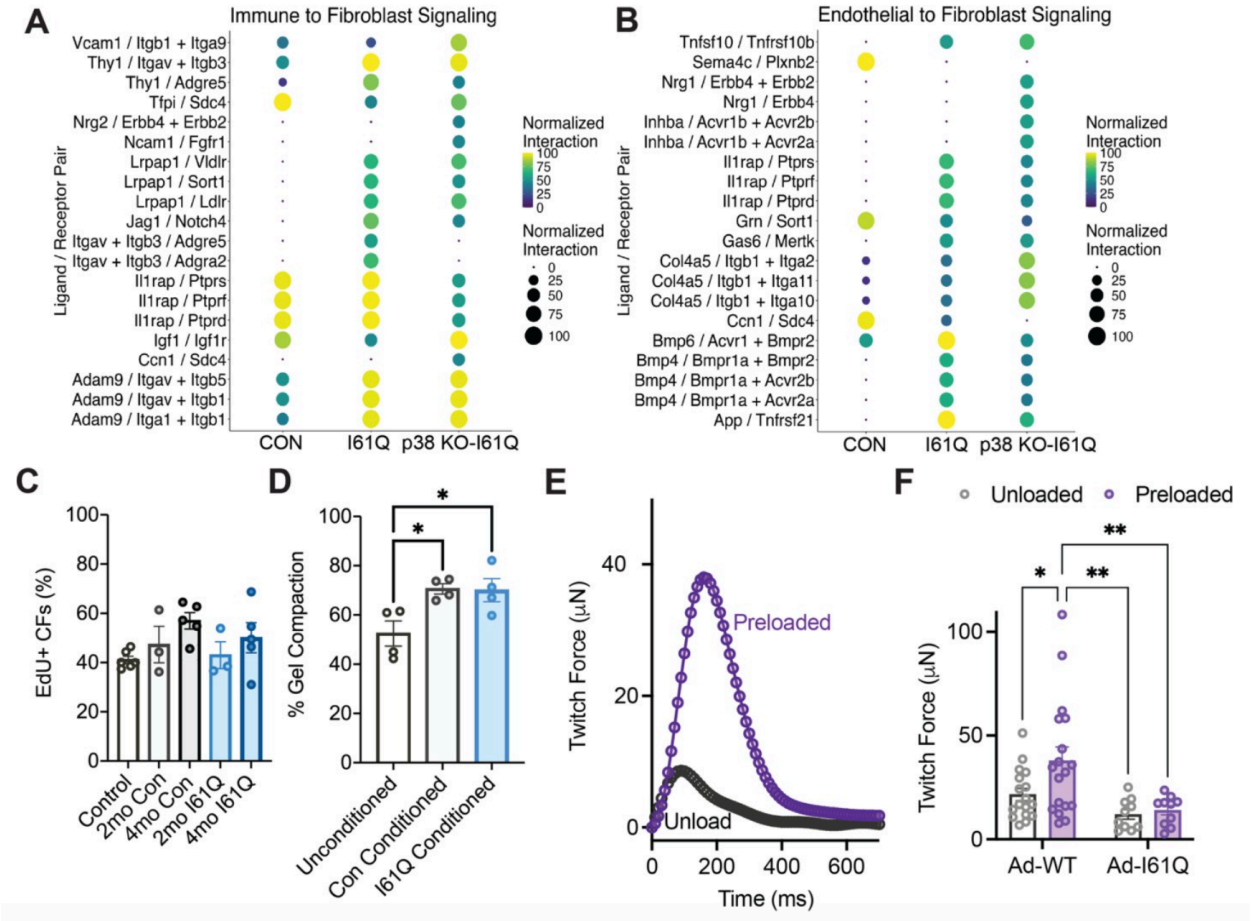

Supplemental Figure 2.4: Mechanical and chemical crosstalk associated with cardiac fibroblast proliferation. *Ligand-receptor analysis of* ***A)*** *immune cell-fibroblast and* ***B)*** *endothelial cell-fibroblast interactions predicted from snRNAseq of 2 month old CON and I61Q hearts where the ligand is expressed by immune or endothelial cells and the receptor is expressed by fibroblasts.* ***C)*** *EdU staining of CON cardiac fibroblasts treated with conditioned media from 2 and 4- month-old cardiomyocytes indicated that secreted factors from I61Q myocytes do not induce fibroblast proliferation over CON (Control n=6, 2 mo Con n=3, 4 mo Con n=5, 2 mo I61Q n=3, 4 mo I61Q n=5 biological replicates).* ***D)*** *Conditioned media from 2-month cardiomyocytes of both genotypes slightly enhanced collagen gel compaction by fibroblasts, but no genotype-dependent effects were observed (Unconditioned n=4, Con Conditioned n=4, I61Q Conditioned n=4 biological replicates).* ***E)*** *Representative twitch from WT EHTs*

under normal or chronic preload and ***F)*** *quantification of twitch force amplitude (n=18 unloaded-WT, n=18 preloaded-WT, n=15 unloaded-I61Q, n=14 preloaded-I61Q). *p<0.05,**p<0.01 by 1 or 2-way ANOVA with Holm-Sidak's multiple comparisons test.*

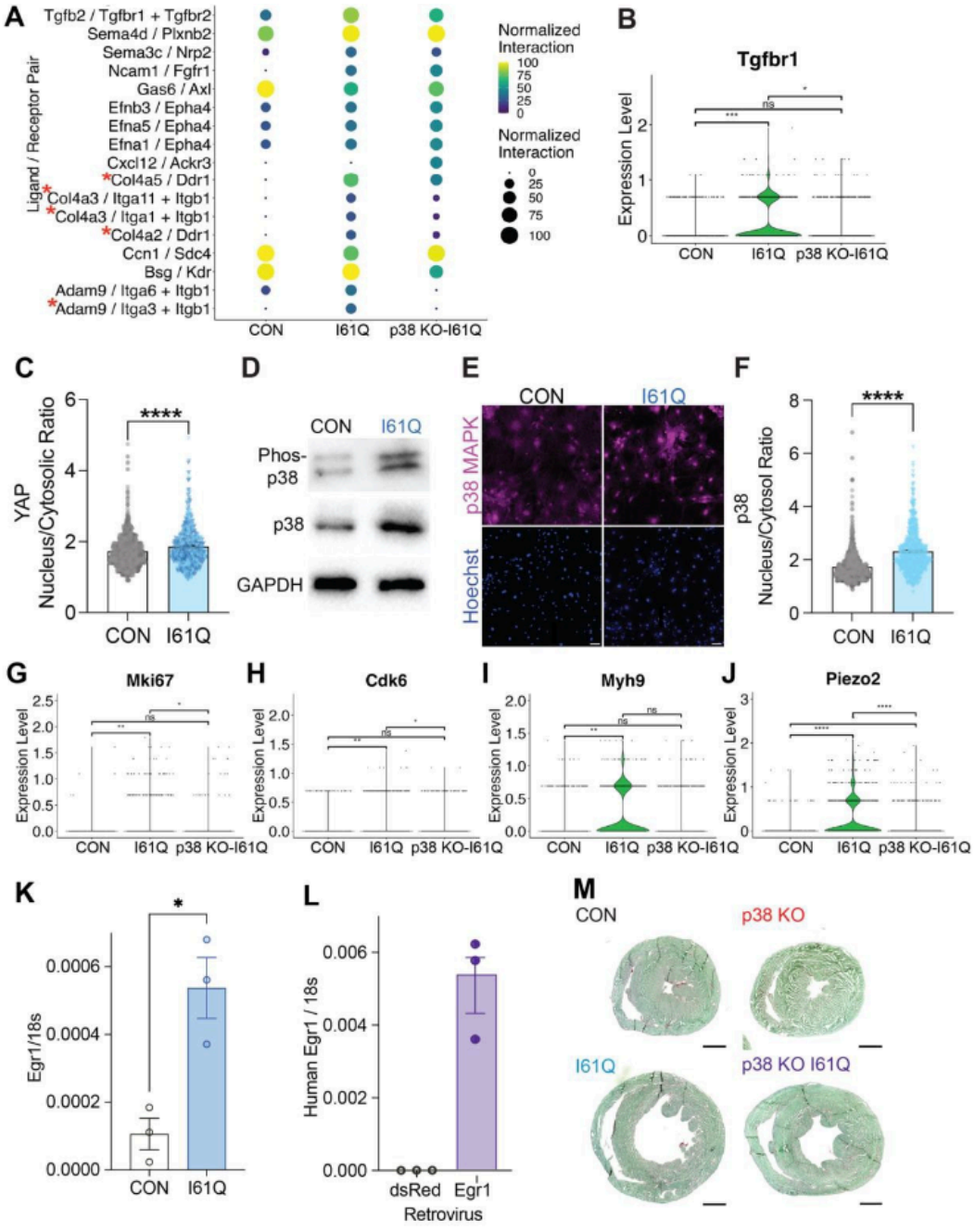

Supplemental Figure 2.5: Mechanotransduction signals and Egr1 gene expression are increased in cardiac fibroblasts from I61Q mice. ***A)*** *Ligand-receptor analysis of myocyte-fibroblast interactions predicted from snRNAseq where the ligand is expressed in myocytes and receptor is expressed in fibroblasts. Red * = ligand-receptor interactions that weakened in the p38-I61Q mice when compared to I61Q mice.* ***B)*** *Violin plot showing the distribution of Tgfbr1 expression levels in cardiac fibroblast nuclei segregated by genotype.* ***C)*** *Quantification of YAP nuclear translocation in I61Q and CON cardiac fibroblasts, indicating YAP activity (n=3 biological replicates per genotype).* ***D)*** *Quantification of p38 abundance and phosphorylation by Western blot on lysates from purified cardiac fibroblasts isolated from I61Q cTnC transgenic and CON hearts.* ***E)*** *Representative images from cardiac fibroblast immunostaining for p38 MAPK (scale 50μm) and* ***F)*** *quantification of p38 nuclear localization in I61Q and CON cardiac fibroblasts, indicating p38 activity (n=3 biological replicates per genotype). ****p<0.001 by unpaired t-test on n=3 biological replicates. Violin plots showing the distribution of* ***G)*** *Mki67,* ***H)*** *Cdk6,* ***I)*** *MyH9, and* ***J)*** *Piezo2 expression levels in cardiac fibroblast nuclei segregated by genotype.* ***K)*** *RT-qPCR of murine Egr1 expression in cardiac fibroblasts isolated from CON and I61Q hearts. *p<0.05 by unpaired t-test on n=3 biological replicates.* ***L)*** *RT-qPCR of human Egr1 in CON cardiac fibroblasts retrovirally transduced with either dsRed (control) or Egr1.* ***M)*** *Representative cardiac cross-sections from 4-month-old mice stained with PSR/FG. (CON n=7, p38 KO n=11, I61Q n=8, p38 KO I61Q n=8).*

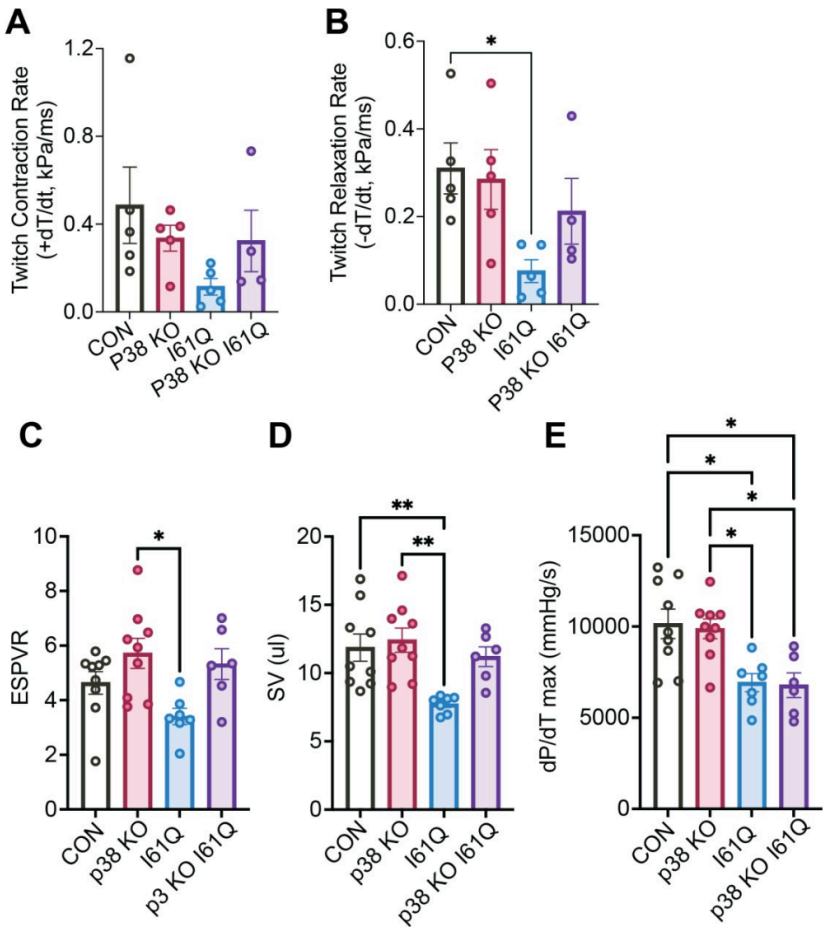

Supplemental Figure 2.6: Metrics of cardiomyocyte and whole heart systolic function and contractility. *Quantification of mean twitch* ***A)*** *contraction and* ***B)*** *relaxation rates in intact trabeculae of 4-month-old CON (n=5), p38 KO (n=5), I61Q (n=5), and p38 KO I61Q (n=4) mice. Quantification of* ***C)*** *end systolic pressure-volume relationship (ESPVR),* ***D)*** *stroke volume (SV), and* ***E)*** *rate of systolic pressure development (dP/dT max) as measured by invasive hemodynamics. CON (n=9), p38 KO (n=9), I61Q (n=6), and p38 KO I61Q (n=6) mice *p<0.05,**p<0.01 by one- way ANOVA with Holm-Sidak's multiple comparisons test.*

Functional Clustering	GENE SYMBOL	GENE NAME	avg_log2FC	p_val_adj
Cell Division	Fbxl7	F-box and leucine-rich repeat protein 7(Fbxl7)	0.78453824	1.0698E-13
	Hjurp	Holliday junction recognition protein(Hjurp)	3.12941851	4.3353E-55
	Stag1	STAG1 cohesin complex component(Stag1)	0.89730275	1
	Tpx2	TPX2, microtubule-associated(Tpx2)	7.14696931	3.385E-201
	Aspm	abnormal spindle microtubule assembly(Aspm)	8.02939971	7.62E-226
	Anln	anillin, actin binding protein(Anln)	6.62340735	3.109E-173
	Mki67	antigen identified by monoclonal antibody Ki 67(Mki67)	6.90094133	0
	Cenpe	centromere protein E(Cenpe)	7.36756845	3.012E-257
	Cdk14	cyclin dependent kinase 14(Cdk14)	1.3670676	2.7079E-08
	Ckap5	cytoskeleton associated protein 5(Ckap5)	2.68151031	1.8849E-30
	Epb41l2	erythrocyte membrane protein band 4.1 like 2(Epb41l2)	0.66447001	1
	Foxn3	forkhead box N3(Foxn3)	0.57610164	1
	Kif11	kinesin family member 11(Kif11)	9.17799621	1.893E-241
	Kif20b	kinesin family member 20B(Kif20b)	6.62340735	1.037E-195
	Knl1	kinetochore scaffold 1(Knl1)	7.64894245	4.338E-238
	Nedd9	neural precursor cell expressed, developmentally down-regulated gene 9(Nedd9)	0.98413379	1.0118E-12
	Pard3	par-3 family cell polarity regulator(Pard3)	0.53053778	1
	Prkce	protein kinase C, epsilon(Prkce)	1.23373465	0.00253223
	Prc1	protein regulator of cytokinesis 1(Prc1)	7.32384707	9.935E-223
	Smc4	structural maintenance of chromosomes 4(Smc4)	3.22244504	4.5068E-72
	Ttc28	tetratricopeptide repeat domain 28(Ttc28)	0.5785221	0.39539178
Chromosome Segregation	Hjurp	Holliday junction recognition protein(Hjurp)	3.12941851	4.3353E-55
	Stag1	STAG1 cohesin complex component(Stag1)	0.89730275	1
	Mki67	antigen identified by monoclonal antibody Ki 67(Mki67)	6.90094133	0
	Cenpe	centromere protein E(Cenpe)	7.36756845	3.012E-257
	Cenpf	centromere protein F(Cenpf)	6.43076228	2.882E-265
	Cenpp	centromere protein P(Cenpp)	3.74408884	1.5412E-94
	Diaph3	diaphanous related formin 3(Diaph3)	6.49057167	0
	Knl1	kinetochore scaffold 1(Knl1)	7.64894245	4.338E-238
	Top2a	topoisomerase (DNA) II alpha(Top2a)	7.6531547	0
Mechanotransduction cell-matrix adhesion ECM-receptor interaction cell-cell adhesion adherens junction integrin signaling actin focal adhesion cytoskeleton	Itgb1	integrin beta 1 (fibronectin receptor beta)(Itgb1)	0.83893886	0.03262762
	Itgb5	integrin beta 5(Itgb5)	1.02771347	2.9834E-15
	Itgbl1	integrin, beta-like 1(Itgbl1)	1.29018872	1.8659E-50
	Svep1	sushi, von Willebrand factor type A, EGF and pentraxin domain containing 1(Svep1)	1.03858811	1.2048E-26
	Fat1	FAT atypical cadherin 1(Fat1)	1.4739828	4.0007E-08
	Lpp	LIM domain containing preferred translocation partner in lipoma(Lpp)	0.45759207	0.00423184
	Dlg1	discs large MAGUK scaffold protein 1(Dlg1)	1.22900962	4.0239E-05
	Myh9	myosin, heavy polypeptide 9, non-muscle(Myh9)	1.78344777	1.4507E-12
	Pard3	par-3 family cell polarity regulator(Pard3)	0.53053778	1
	Diaph3	diaphanous related formin 3(Diaph3)	6.49057167	0
	Ccn2	cellular communication network factor 2(Ccn2)	0.63414517	1
	Dst	dystonin(Dst)	0.33220504	0.38990052
	Fn1	fibronectin 1(Fn1)	1.17643586	0.00264442
	Col1a1	collagen, type I, alpha 1(Col1a1)	0.57703769	4.79E-297
	Col1a2	collagen, type I, alpha 2(Col1a2)	0.46872606	0.44179418
	Col5a2	collagen, type V, alpha 2(Col5a2)	0.93818073	3.2562E-07
	Col8a1	collagen, type VIII, alpha 1(Col8a1)	0.78928321	1.4571E-12
	Eln	elastin(Eln)	0.41137917	1
	Ltbp2	latent transforming growth factor beta binding protein 2(Ltbp2)	1.35572888	5.3215E-08
	Vcan	versican(Vcan)	0.50034194	0.28000086
	Emp1	epithelial membrane protein 1(Emp1)	0.58238009	1
	Igf1r	insulin-like growth factor I receptor(Igf1r)	0.62809905	1
	Prkca	protein kinase C, alpha(Prkca)	1.24958112	4.2648E-17
	Tead1	TEA domain family member 1(Tead1)	1.36667752	6.6506E-09
	Rock2	Rho-associated coiled-coil containing protein kinase 2(Rock2)	0.92794531	0.02960884

Supplemental Table 2.1: Transcriptional features defining fibroblast states 1 and 3 that are enriched in I61Q mice.

Conclusion of *Prevention of Hypocontractility-Induced Proliferative Fibroblast States Alleviates Dilated Cardiomyopathy* by Ross C. Bretherton[*], Isabella M. Reichardt[*], Kristin A. Zabrecky, Abigail Nagle, Logan R.J. Bailey, Darrian Bugg, Sasha Smolgovsky, Amy L. Gifford, Timothy S. McMillen, Alex J. Goldstein, Kristina B. Kooiker, Galina V. Flint, Amy Martinson, Jagdambika Gunaje, Franziska Koser, Elizabeth Plaster, Wolfgang A. Linke, Michael Regnier, Farid Moussavi-Harami, Nathan J. Sniadecki, Cole A. DeForest, Jennifer Davis *Science. Science.* 2025 Sep. DOI: 10.1126/science.adv9157. ***equal contribution**

Chapter 3: Persistent tissue stiffness prevents full reversal of hypocontractility-induced dilated cardiomyopathy

Building on findings from the previous chapter, which demonstrated that fibroblast proliferation and extracellular matrix (ECM) remodeling actively contribute to disease progression in DCM, this chapter explores how this secondary remodeling impacts the reversibility of the disease. While early interventions targeting either myocytes (*241*) or fibroblasts (*242*) can prevent the development of the full DCM phenotype, it remains unclear whether the heart retains sufficient plasticity to recover once significant structural and transcriptional remodeling has occurred.

In particular, this chapter examines the effectiveness of a precise myocyte-targeted genetic correction strategy in reversing established DCM. It asks whether restoring myocyte contractility is sufficient to reverse downstream consequences of disease, including fibroblast expansion, ECM stiffening, and functional decline, or whether these features become refractory to correction over time. Together, these studies aim to define the limits of myocardial reversibility and to identify which features of dilated remodeling are responsive to therapeutic intervention, and which may require separate, cell type-specific targeting.

The following people have contributed to the work in this chapter:

Isabella M. Reichardt[1-3], Abigail Nagle[1-3], Kristina B. Kooiker[2,3,6], Elizabeth Plaster[2,3,4], Sasha Smolgovsky[2,3,5], Elaheh Karbassi[2,5], Jagdambika Gunaje[2,3,5], Rachelle Soriano[2,7], Michael Regnier,[1-3,8] Farid Moussavi-Harami[2,3,5,6,8], Darrian Bugg[2,3,5], Jennifer Davis[1-3,5,8]

[1] *Department of Bioengineering, University of Washington; Seattle, WA 98105 USA*

[2] *Institute for Stem Cell and Regenerative Medicine, University of Washington; Seattle, WA 98109 USA*

[3] *Center for Cardiovascular Biology, University of Washington; Seattle, WA 98109 USA*

[4] *Department of Public Health, University of Washington; Seattle, WA 98109 USA*

[5] *Department of Lab Medicine and Pathology, University of Washington; Seattle, WA 98109 USA*

[6] *Division of Cardiology, University of Washington; Seattle, WA 98109 USA*

[7] *Department of Biochemistry, California State University; Los Angeles, CA USA*

[8] *Center for Translational Muscle Research, University of Washington; Seattle, WA 98109 USA*

3.1 Introduction

Familial dilated cardiomyopathy (DCM) is a common heart disease caused by inherited mutations in the cardiomyocyte that lead to hypocontractility (*20*). Molecular changes in myofilament tension generation ultimately lead to left ventricle (LV) dilation, eccentric hypertrophy, and collagen deposition (*7*, *17*, *18*). Existing treatments, such as ACE inhibitors, β-blockers, or left ventricular assist devices (LVADs), do not address the root cause of the disease and often produce variable and short lived improvements for patients (*21–24*). Recently, myosin activators have emerged as a new class of drug that holds promise for directly augmenting myocyte force production. However, despite promising pre-clinical results (*35*, *42*), these drugs have yielded only modest benefits in clinical trials (*37*, *38*, *243*). Considering that DCM is a progressive disease that often causes decades of compensatory remodeling before it is diagnosed and treated (*16*), the inability to develop effective therapies is likely related to the field's poor understanding of myocyte plasticity and disease reversibility in the context of familial DCM (*244*). While early interventions targeting either myocytes (*20*) or fibroblasts (*242*) can prevent

the onset of DCM, it remains unclear whether the heart retains sufficient plasticity to recover once significant pathological remodeling has occurred. Indeed, *in vivo* murine studies have demonstrated that short-term cardiac hypertrophy is fully reversible, whereas chronic hypertrophy can only be moderately improved (*245*). Reverse remodeling has been characterized in acquired cardiac diseases, such as heart failure (*23*, *151*), and there is increasing evidence suggesting that maladaptive genomic and extracellular matrix (ECM) signals may persist despite functional improvements (*22*, *151*, *152*, *159*, *246*). Given that aberrant chromatin (*158*, *247*) and ECM remodeling (*242*) underlie the progression of DCM, we hypothesized that permanent changes in the myocyte, matrix, and chromatin landscape may limit the reversal of DCM.

3.2 Results

3.2.1 Repressing the inciting sarcomeric mutation partially reverses the DCM phenotype

Familial DCM was modeled in mice using a doxycycline-repressible, experimentally-derived point mutation (I61Q) in cardiac troponin C (cTnC). The I61Q cTnC variant decreases Ca^{2+} binding affinity (*175*, *176*), which induces hypocontractility and eccentric remodeling when expressed in cardiomyocytes (*18*). While previous studies characterized the pathological effects of the I61Q variant in the heart (*18*, *242*), this study uniquely leveraged the repressible nature of this model to assess whether genetic correction of a sarcomeric variant can reverse established cardiac dysfunction and remodeling. In whole heart lysates from I61Q transgenic mice on standard chow, approximately 50% of endogenous cTnC was replaced with the FLAG-tagged I61Q variant. Administration of doxycycline chow (DOX) abrogated I61Q cTnC expression and reduced FLAG expression 50-fold (**Figure 3.1A)**. Skinned trabeculae isolated from I61Q mice showed a rightward shift in the force versus calcium (pCa) relationship relative to control (CON)

littermates (**Figure 3.1B**), which was quantified as a decrease in pCa_{50} (**Figure 3.1B**). Seven days of DOX restored the pCa_{50} of I61Q trabeculae back to CON levels (**Figure 3.1B-C**), indicating the I61Q variant can be functionally suppressed within the timeframe of endogenous cTnC turnover (~5.3 days (*248*)). Therefore, DOX can be used in this model as a treatment mimetic to replace the variant with native cTnC at any time during the DCM disease progression.

To evaluate the heart's capacity to recover from DCM, I61Q mice were aged to an advanced stage of DCM preceding heart failure (6 months) and then given one month of DOX (**Figure 3.1D**). Age matched 7-month-old CON and DCM mice that remained on standard chow acted as controls. Untreated I61Q mice showed robust systolic and diastolic dysfunction (**Figure 3.1E & G**) and LV dilation (**Figure 3.1F**) relative to CON mice by echocardiography. One month of DOX increased the EF of I61Q mice by 54%, but systolic function still remained depressed compared to CON, indicating only partial recovery (**Figure 3.1E**). Pairwise comparisons before and after treatment showed a 7% decrease in ventricle dilation of the I61Q mice treated with DOX ($p < 0.05$, student's t test), but diastolic dimension remained elevated relative to age-matched CON mice (**Figure 3.1F**). Conversely, diastolic dysfunction and increased ventricular mass, as measured by E/A ratio and ventricle weight/body weights, were completely restored to CON values (**Figure 3.1G-H**). These findings suggest that genetic correction in the myocyte is sufficient to reverse some, but not all, of the DCM disease hallmarks. To examine whether additional recovery time would elicit greater reverse remodeling, a second cohort of I61Q mice was given three months of DOX treatment, with age matched 9-month-old mice on standard chow acting as controls (**Figure 3.1D**). Similar to the 1-month treatment, the EF of I61Q mice was improved by 38% but remained depressed compared to CON after 3 months of DOX (**Figure 3.1I**). Diastolic chamber dimension, diastolic dysfunction, and

ventricle hypertrophy were all restored to CON levels (**Figure 3.1J-L**). These findings indicate that prolonged treatment may permit further reversal of chamber dilation but does not enhance functional recovery beyond what was achieved in a one-month treatment window.

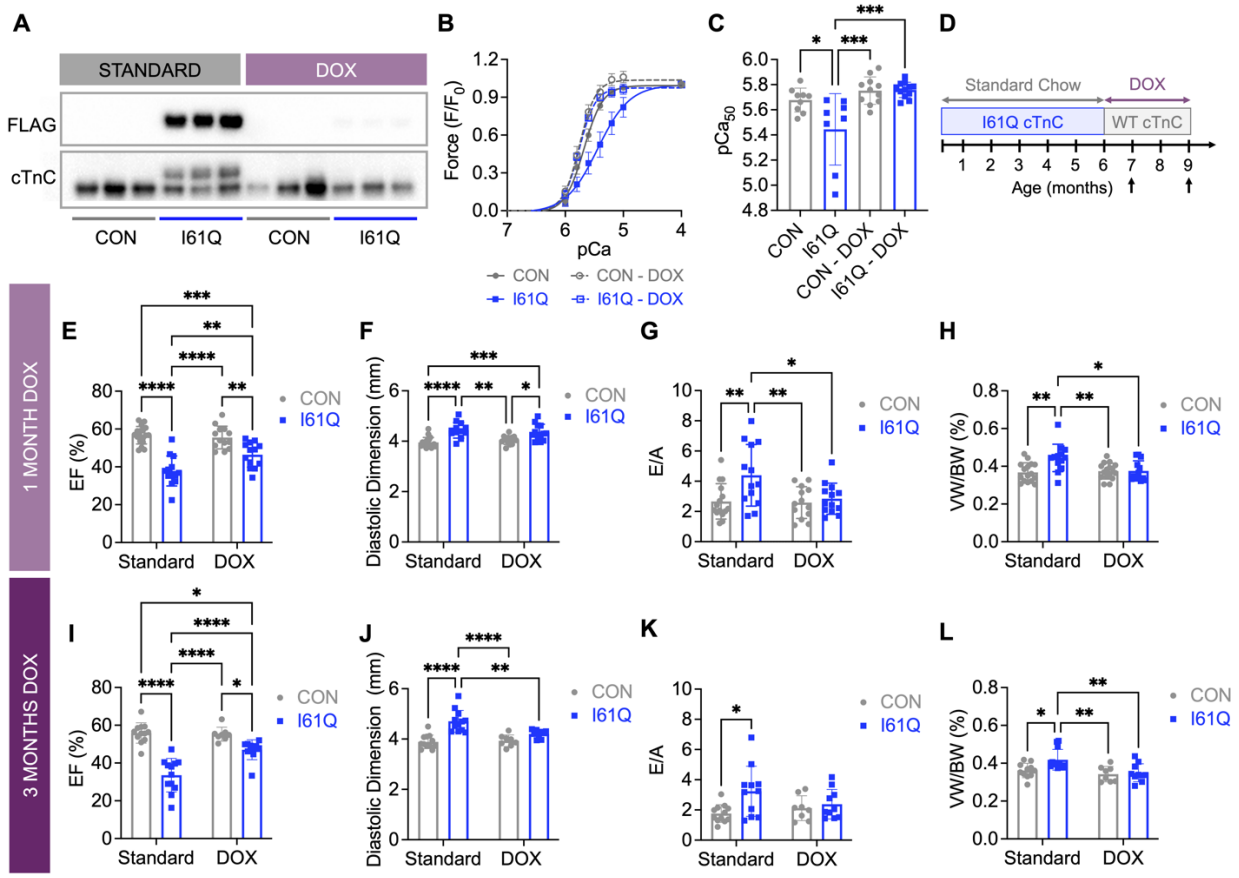

Figure 3.1: Repressing the inciting sarcomeric mutation partially reverses the DCM phenotype. A) *Western blot for cTnC and FLAG after 1 month of DOX chow, demonstrating efficient repression of the I61Q cTnC (N=3 for all groups).* ***B)*** *Force PCA curve and* ***C)*** *pCa_{50} from demembranated CON and I61Q tissues (6 months) +/- 7 days of treatment, demonstrating I61Q cTnC is rapidly cleared from the sarcomere, restoring myofilament Ca^{2+} sensitivity (CON n=9, I61Q n=8, CON DOX n=11, I61Q DOX n=13 trabeculae from N=4 mice per group).* ***D)*** *Schematic of the experimental design, where I61Q mice and their control littermates were aged out to 6 months before beginning treatment with DOX chow for*

*one or three month(s), effectively replacing I61Q cTnC with WT cTnC. Left ventricular **E)** ejection fraction (EF), **F)** diastolic dimension, and **G)** E/A obtained through echocardiography on WT and DCM mice +/- 1 month of DOX (CON N=18, I61Q N=13, CON DOX N=13, and I61Q DOX N=13). **H)** Quantification of ventricle hypertrophy measured by the ratio of ventricle weight (VW) to body weight (BW) (CON N=15, I61Q N=13, CON DOX N=11, and I61Q DOX N=9 mice). Significance was determined using a Two-way ANOVA + Tukey post-hoc. Left ventricular **I)** EF **J)** diastolic dimension, and **K)** E/A obtained through echocardiography on CON and DCM mice +/- 3 months DOX. **L)** Quantification of VW/BW in CON and I61Q mice with 3 months of DOX. (CON N=12, I61Q N=12, CON DOX N=8, and I61Q DOX N=10). All bar graphs are mean ± SD, dots represent biological replicates, and significance was determined using a Two-way ANOVA + Tukey post-hoc: *p<0.05, **p<0.01, ***p<0.005, ****p<0.001.*

By 12 months of age, the I61Q mice have a 65% survival rate due to heart failure (**Supplemental Figure 3.1A**). To determine whether end-stage DCM is still reversible, I61Q mice were aged to 12 months and then given one month of DOX (**Supplemental Figure 3.1B**). 13-month-old I61Q mice on standard chow have severe systolic dysfunction, with an average EF of 20% (**Supplemental Figure 3.1C**). DOX treatment increased the EF of these mice by 111%, although function still remained depressed relative to CON mice (**Supplemental Figure 3.1C**). Surprisingly, I61Q mice that began treatment later in the disease progression experienced a 2-fold greater increase in EF (**Supplemental Figure 3.1D**), suggesting that disease severity does not limit recovery potential. Similarly, DOX treatment partially reduced ventricular dilation (**Supplemental Figure 3.1E**), with a 7% decrease in diastolic dimension (**Supplemental Figure 3.1F**), and diastolic dysfunction (**Supplemental Figure 3.1G**). Ventricular mass was completely reduced to CON levels (**Supplemental Figure 3.1F-G**), suggesting myocyte hypertrophy may

be more plastic than function. These findings indicate that even at a very advanced stage of disease, myocyte correction can yield meaningful improvements in cardiac function and geometry.

3.2.2 Cardiomyocytes recover functionally, structurally, and epigenetically

Chronic cardiomyocyte hypertrophy has been shown to induce irreversible cardiac remodeling, even after removal of the pro-growth stimulus (*245*). Given that familial DCM is a chronic and progressive disease, we hypothesized that permanent changes in the cardiomyocyte may be limiting the functional recovery of the heart. To examine function at the tissue level, intact trabeculae were isolated from CON and I61Q mice at 7 months of age. Trabeculae from I61Q mice on standard chow generated less force than CON, and one month of DOX only partially improved force production (**Figure 3.2A-B**). Myocytes isolated from untreated I61Q mice produced less force (**Figure 3.2C**), contracted slower (**Figure 3.2D**), and relaxed faster (**Figure 3.2E**) than CON, consistent with a decrease in calcium affinity. In contrast to whole organ and tissue scales, myocytes from DOX-treated I61Q hearts functionally recovered but also had enhanced shortening relative to CON (**Figure 3.2C**). Contraction velocity and relaxation time also returned to CON values (**Figure 3.2D-E**). I61Q myocytes presented classic features of eccentric remodeling, including increased cell area, length, and width, which was also fully normalized in the DOX-treated group (**Figure 3.2F-H**). DCM patients who receive LVADs have persistent maladaptive epigenetic changes, despite improvements in myocyte hypertrophy and function (*22*). To examine the genomic plasticity of the cardiomyocyte, we performed multiomic single nucleus assay for transposase-accessible chromatin sequencing (snATACseq) with gene expression on isolated nuclei from whole hearts. CON and I61Q mice were aged to 2 months and

given one month of DOX. A secondary cohort were withdrawn from the DOX chow and harvested at 5 months to examine how turning the I61Q cTnC back on affects gene transcription and the epigenetic landscape (**Figure 3.2I**). 15,352 cardiomyocytes were identified and segregated into 5 clusters based on chromatin accessibility (**Figure 3.2J**). Myocytes from CON and I61Q DOX mice primarily localized to cluster 0, whereas myocytes from I61Q mice on standard chow or whose DOX chow had been withdrawn shifted into cluster 2 (**Figure 3.2K-L**). This pattern supports a clear on/off paradigm in which expression of the I61Q cTnC transgene induces chromatin remodeling that resolves rapidly once the mutation is suppressed. To identify the transcription factors underlying these state transitions, motif enrichment of differentially accessible regions was integrated with differential gene expression, revealing factors that are both upregulated and have accessible binding motifs in clusters 0 and 2. Cluster 2 exhibited enhanced activity of GATA4 and NFATC2, which is consistent with hypertrophic remodeling and reactivation the fetal gene program (*249*). ESRRA activity was diminished in cluster 2, potentially reflecting a loss of maturate gene programs involving myocyte calcium handling, ion transport, and metabolism (*250*). Moreover, cluster 2 also shifted from MEF2D towards MEF2C activity, which aligns with a pro-proliferative gene program (*251*) (**Figure 3.2M**). Together these findings indicate an epigenetic shift towards pathological hypertrophy and developmental reprogramming in I61Q cardiomyocytes that is completely reversible.

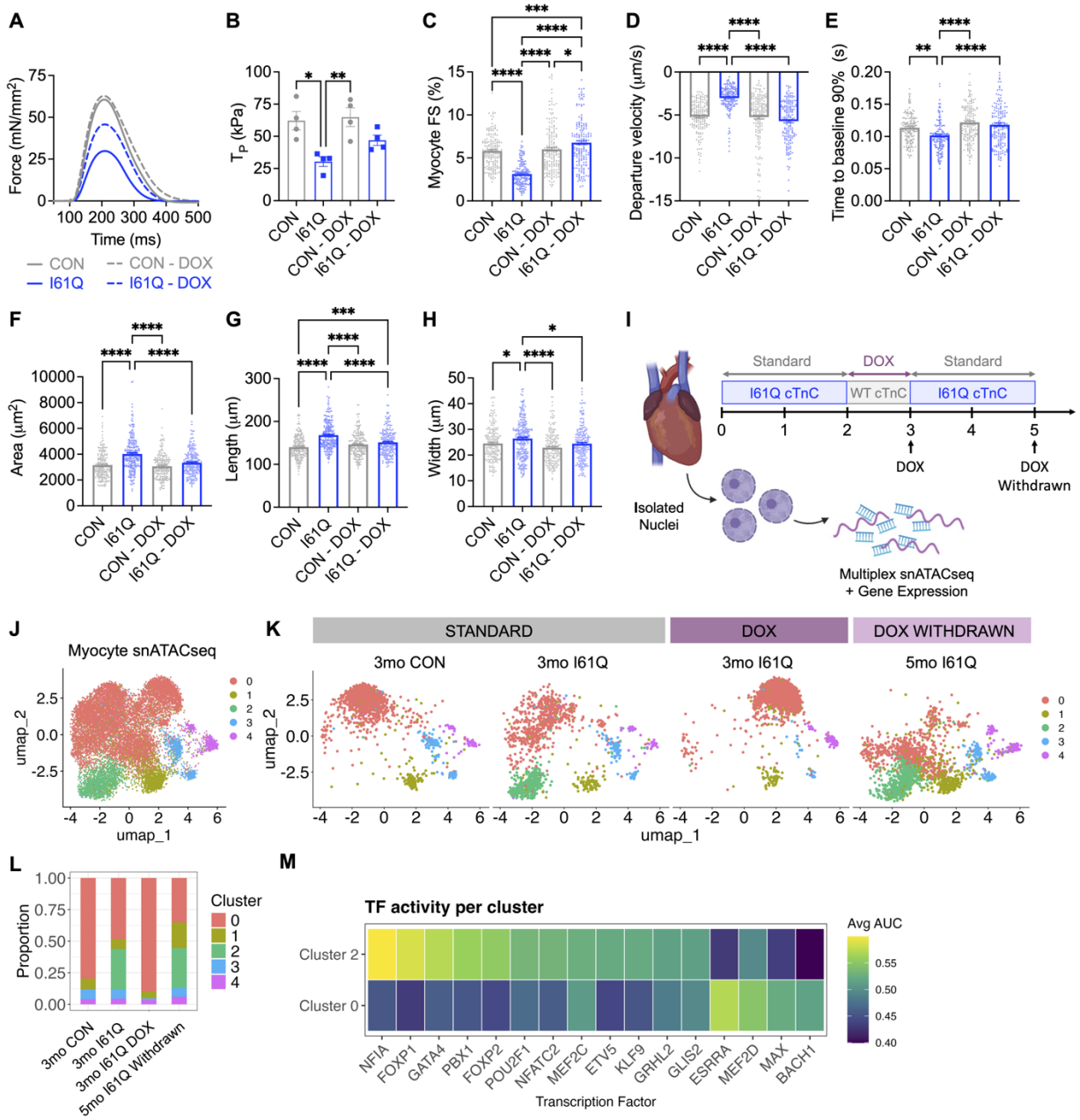

Figure 3.2: Cardiomyocytes recovery functionally, structurally, and epigenetically. ***A)*** *Representative traces and* ***B)*** *quantification of trabecula contraction. (N=4 for all groups).* ***C)*** *Isolated myocyte fractional shortening,* ***D)*** *contraction velocity, and* ***E)*** *time to relaxation (90%). Bar graphs are mean ± standard deviation (SD) and dots represent individual myocytes (N=4 mice for all groups). Significance was determined using a One-way ANOVA with Tukey post hoc on myocytes (CON n=171, I61Q n=160,*

CON DOX n=176, I61Q DOX n=171). ***F)*** *Isolated myocyte area,* ***G)*** *length, and* ***H)*** *width from CON and I61Q mice +/- DOX. Bar graphs represent mean + SEM and significance was determined using a One-way ANOVA with Tukey post-hoc. (CON n=200, I61Q n=250, CON DOX n=200, I61Q DOX n=200 myocytes).* ***I)*** *Experimental schematic showing doxycycline treatment and withdrawal timeline for snATACseq.* ***J)*** *UMAP clustering 15352 myocytes based on open peaks.* ***K)*** *UMAP of clustering based on accessible peaks separated by condition.* ***L)*** *Proportion of cells in each cluster.* ***M)*** *Heatmap showing transcription factor activity of clusters 0 and 2, defined as the integrated AUC score combining RNA expression of each transcription factor with enrichment of its corresponding motif in accessible chromatin. *p<0.05, **p<0.01, ***p<0.005, ****p<0.001.*

3.2.3 Persistent tissue stiffness limits recovery of the heart

We previously demonstrated that I61Q mice have increased passive stiffness due to titin phosphorylation and ECM remodeling (*242*). Considering that the myocyte functionally recovered while the tissue did not, we reasoned that irreversible tissue stiffening could be preventing full recovery of the heart. To determine the reversibility of this stiffening, papillary muscles were isolated and passive stiffness measurements were repeated before and after decellularization of the tissue. The tissues were serially stretched in a Krebs-Henseleit buffer containing blebbistatin to disregard any stiffness contributions from active crossbridge formation (**Figure 3.3A**). Preliminary data from this assay suggests that I61Q papillary muscles have elevated passive stiffness compared to CON in both intact and decellularized preparations. DOX treatment did not appear to reverse the stiffness of either compartment and maybe even worsened the passive ECM stiffness of I61Q mice (**Figure 3.3B-C**). Staining with picrosirius red and fast green (PSR/FG) showed that I61Q mice have increased interstitial fibrosis that does not reverse with one or three months of DOX treatment (**Figure 3.3D-F**). Collagen birefringence was

measured in PSR/FG-stained slides to examine the relative maturity of the fibrosis. Regardless of treatment all I61Q mice exhibited an immature matrix, as seen by majority green-yellow birefringence, and were not different than CON (**Figure 3.3G-I**). To assess whether the collagen is competent to degrade, collagen hybridizing peptide (CHP) staining was used to detect regions of unfolded collagen triple helices (*252*). I61Q mice showed increased CHP incorporation relative to CON mice, which remained elevated with one month of DOX but returned to baseline after 3 months of DOX (**Figure 3.3J-L**). Collectively, this data suggests that the fibrosis caused by hypocontraction in the I61Q model is irreversible despite being relatively immature and competent to degrade, which likely contributes to the persistent passive tissue stiffness.

To determine the extent to which this stiffness affects the reversibility of DCM, I61Q mice were given a combined treatment of DOX and β-aminopropionitrile (BAPN), an inhibitor of the collagen crosslinking enzyme lysyl oxidase (LOX), to correct the myocyte and help alleviate residual stiffness (**Figure 3.3M**) ((*253*)). Compared to mice that had been treated with BAPN alone, I61Q mice treated with DOX and BAPN experienced full recovery of EF (**Figure 3.3N**) and complete reversal of dilation (**Figure 3.3O**), diastolic dysfunction (**Figure 3.3P**), and ventricular hypertrophy (**Figure 3.3Q**). This data suggests that softening the myocardium is necessary to achieve full recovery from DCM, although notably ECM quantity and stiffness still need to be assessed in these mice.

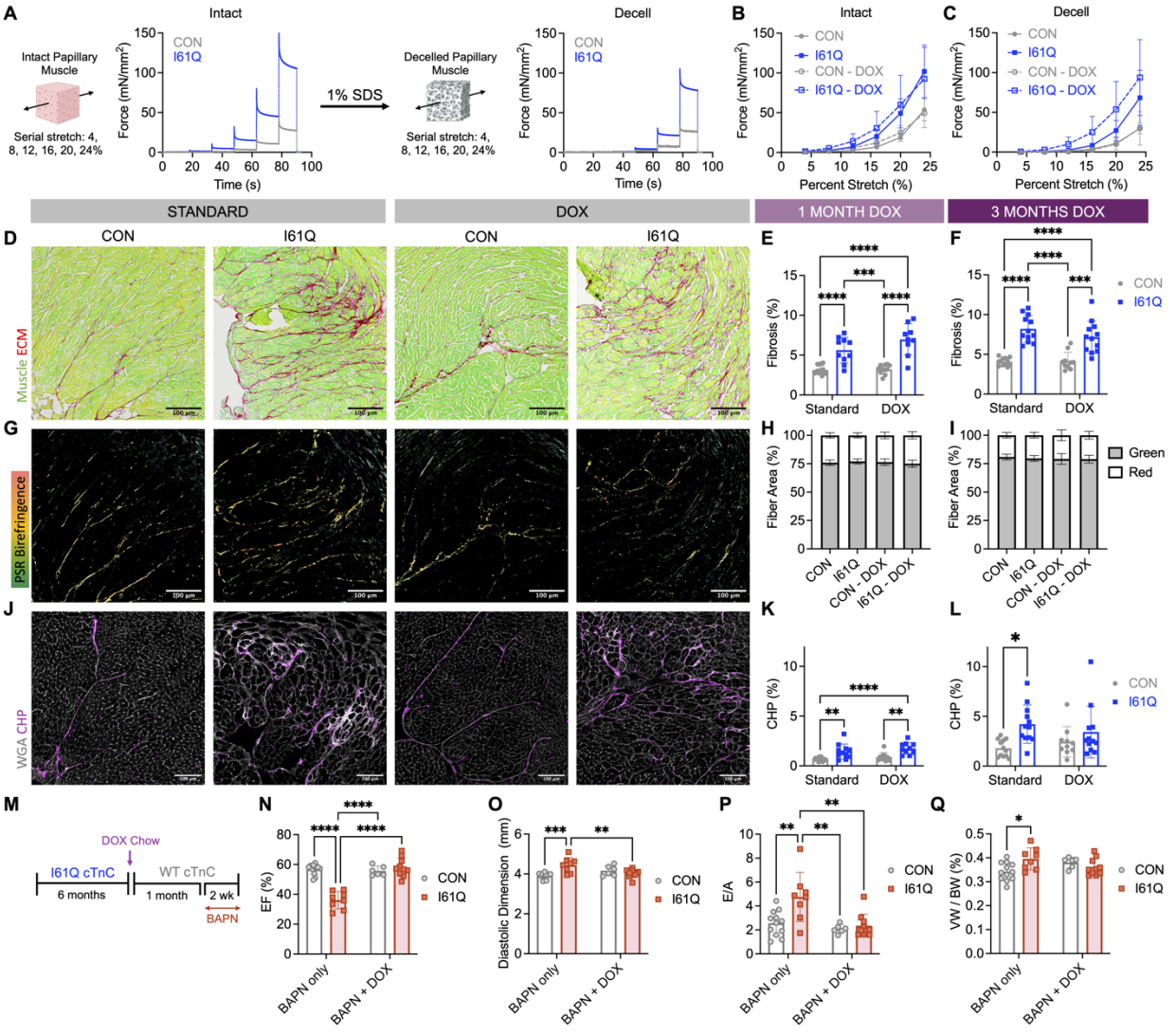

Figure 3.3: Persistent tissue stiffness limits recovery of the heart. ***A)*** *Schematic showing papillary muscle passive stretch testing with representative CON and I61Q traces before and after decellularization.* ***B-C)*** *Passive stiffness for* ***B)*** *intact and* ***C)*** *decellularized papillary muscles (CON N=5, I61Q N=5, CON DOX N=4, I61Q DOX N=4).* ***D)*** *Representative 10× images of cardiac tissue sections stained with picrosirius red / fast green (PSR/FG). Quantification of fibrosis at* ***E)*** *one month and* ***F)*** *three months of DOX chow.* ***G)*** *Representative images of collagen birefringence in PSR/FG-stained myocardial sections. Quantification of birefringence, with green/yellow and red fibers expressed as a percentage of total birefringent fiber area, at* ***H)*** *one month and* ***I)*** *three months of DOX.* ***J)***

Representative 20× images of sections stained with collagen hybridizing peptide (CHP, magenta) to detect denatured collagen, and wheat germ agglutinin (WGA, gray) to label cell membranes. Quantification of CHP area normalized to total tissue area at ***K)*** *one month and* ***L)*** *three months of treatment.* ***M)*** *Experimental timeline for myocyte correction with DOX chow plus global ECM softening with daily β-aminopropionitrile (BAPN) injections.* ***N-P)*** *Echocardiographic analysis of* ***N)*** *EF,* ***O)*** *diastolic dimension, and* ***P)*** *E/A ratio in CON and I61Q mice treated with BAPN only and DOX with BAPN.* ***Q)*** *Ventricular weight to body weight ratio for CON and I61Q mice following BAPN or DOX + BAPN treatment. One-month DOX groups: CON N = 15, I61Q N = 10, CON DOX N = 11, I61Q DOX N = 9 (PSR/FG, birefringence) and CON N = 13, I61Q N = 8, CON DOX = 8, I61Q DOX N = 9 (CHP). Three-month groups: CON N = 12, I61Q N = 12, CON DOX N = 10, I61Q DOX N = 12 (all assays). BAPN only: CON N = 12, I61Q = 8; BAPN + DOX: CON N = 6, I61Q N = 10. All bar graphs are mean ± SD, dots represent biological replicates, and statistical comparisons were made using two-way ANOVA with Tukey post-hoc test. *p<0.05, **p<0.01, ***p<0.001, ****p<0.0001.*

3.2.4 Fibroblast number remains elevated despite transcriptional deactivation

To determine why myocyte correction does not cause fibrotic regression, we examined fibroblast number and activation. Previously, we showed that fibroblast proliferation is the primary mechanism by which ECM is deposited and remodeled in the I61Q model, although lineage tracing studies showed that a small subset of I61Q fibroblasts begin to activate around 8 months (*242*). Interestingly, fibroblast number remained elevated in DOX treated I61Q hearts (**Figure 3.4A–B**). To determine whether these fibroblasts remain transcriptionally active or return to a quiescent state following myocyte correction, single-nucleus RNA sequencing (snRNAseq) was performed on isolated fibroblasts. 211,301 fibroblasts with an average UMI count of 714 were obtained (**Figure 3.4C**). As we saw previously (*242*), fibroblasts from I61Q

mice with and without DOX treatment largely occupied the same quiescent clusters as control fibroblasts (**Figure 3.4D-E**). However, a subset of fibroblasts in untreated DCM hearts shifted into cluster 4 (**Figure 3.4G**). To determine which of these clusters was most involved in ECM production, an ECM score was calculated by examining the relative mRNA expression of all known collagens, glycoproteins, and proteoglycans. Cluster 4 had a higher ECM score than all other fibroblast clusters (**Figure 3.4E-F**). Differential expression analysis revealed this as an activated fibroblast cluster marked by elevated expression of *Postn* and *Cilp*, but lacking *Acta2* (αSMA) (**Figure 3.4G**), which resembles the activated fibroblast state observed in non-ischemic models of heart disease (*164*). Notably, this population was diminished in I61Q mice that had received DOX (**Figure 3.4E & H**), indicating an overall deactivation of fibroblasts following myocyte correction. Consistently, the ECM score of was reduced in fibroblasts from I61Q mice that had been treated with DOX (**Figure 3.4I**). To determine which genes were reversibly upregulated in I61Q fibroblasts, differential gene expression analysis was also performed by genotype and treatment group to extract population level changes across all fibroblast clusters. Many of the reversibly elevated genes included matrix-associated genes such as *Col1a1*, *Col1a2*, *Fbn1*, *Loxl2*, *Postn*, *Sparc*, and *Vcan* (**Figure 3.4J**), and were enriched for GO terms related to ECM production, organization, and crosslinking (**Figure 3.4K**), suggesting reduced ECM synthesis following DOX treatment. In contrast, a smaller set of genes, including *Nfkb1*, *Gab2*, and *Itpr1*, remained persistently elevated despite treatment (**Figure 3.4J**). Gene ontology analysis linked these transcripts to osteoclast differentiation and T cell receptor signaling (**Figure 3.4K**), raising the possibility that fibroblasts in DOX-treated I61Q hearts may be transcriptionally primed for matrix degradation and immune signaling but remain unable to resolve established fibrosis. Fibroblast size was increased in I61Q mice on standard chow but

returned to baseline with DOX treatment (**Figure 3.4L**), lending further support to the deactivation of these cells.

To determine whether reducing fibroblast number could reverse established remodeling, p38 MAPK was genetically deleted in Tcf21-expressing fibroblasts from I61Q cTnC mice using a Tcf21-MerCreMer. Mice were aged to 4 months, the age at which there is significant collagen deposition, before initiating tamoxifen to induce p38 knockout (KO). The mice were then allowed 2 months for recovery (**Supplemental Figure 3.2A**). Although early p38 knockdown in $Tcf21^{+}$ fibroblasts completely abrogated fibroblast proliferation and was protective against DCM progression (*242*), p38 KO after disease onset failed to reduce fibroblast number or fibrosis (**Supplemental Figure 3.2B-C**). Moreover, EF and diastolic function remained impaired, LV dilation was worsened, and myocyte and ventricular hypertrophy remained elevated (**Supplemental Figure 3.2D-H**). These findings indicate that p38 modulation is only able to prevent fibroblast expansion, but not contract the population.

Another approach for reducing fibroblast numbers was to genetically ablate them from I61Q mice using a tamoxifen inducible diptheria toxin (DTA) driven by a Tcf21-MerCreMer. Fibroblasts were ablated at 4 months of age, followed by one month of DOX treatment (**Figure 3.4M**). Preliminary results suggest that fibroblast ablation did not improve outcomes beyond those achieved with DOX alone: EF and diastolic dimension improved only partially (**Figure 3.4N-O**). However, fibroblast number still needs to be quantified in order to determine if enough fibroblasts were ablated with this strategy to see an effect.

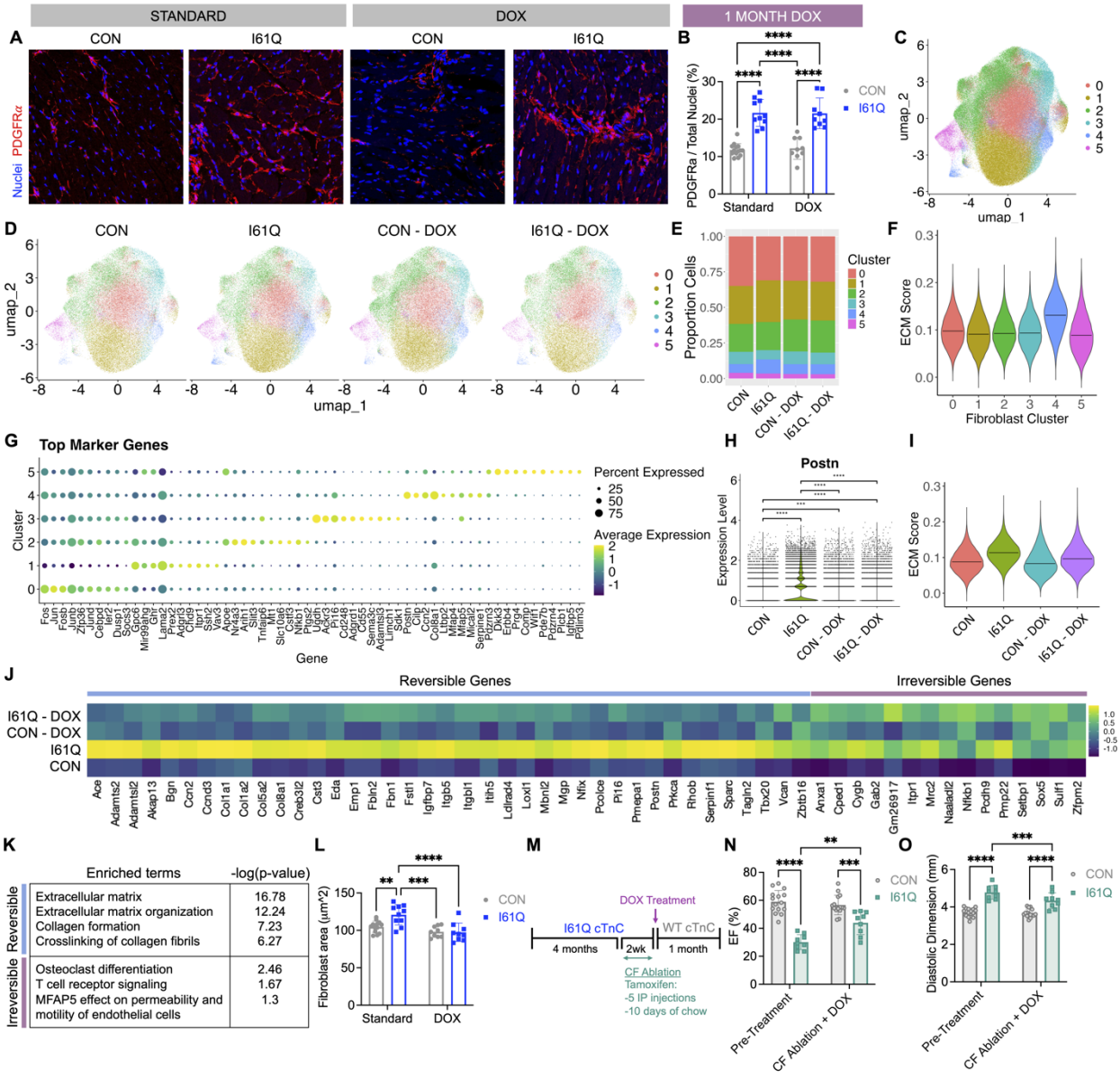

Figure 3.4: Fibroblast number remains elevated despite transcriptional deactivation. ***A)*** *Representative images and* ***B)*** *quantification of PDGFRα+ fibroblast number normalized to total nuclei number.* ***C)*** *UMAP showing fibroblast clustering across all groups and* ***D)*** *separated by experimental group (N=2 for all groups).* ***E)*** *Proportion of cells in each cluster.* ***F)*** *ECM score for relative expression of all known collagens, glycoproteins, and proteoglycans across each fibroblast cluster.* ***G)*** *Top differential markers for each cluster.* ***H)*** *Violin plot of Postn expression across each group.* ***I)*** *ECM score split by group.* ***J)*** *Heatmap showing top differentially expressed genes that were reversibly or irreversibly elevated in I61Q*

fibroblasts with DOX treatment. ***K)*** *Top GO terms for reversible and irreversible gene sets.* ***L)*** *Mean fibroblast area quantified using PDGFRα area per cell.* ***M)*** *Experimental timeline for cardiac fibroblast (CF) ablation combined with DOX treatment.* ***N-O)*** *Echocardiographic analysis of left ventricular ejection fraction (EF) and diastolic dimension in CON and I61Q mice before and after CF ablation plus DOX. All bar graphs are mean ± SD and dots represent biological replicates. Statistical comparisons in B and M were made using two-way ANOVA with Tukey post-hoc test (CON N = 14, I61Q N = 10, CON DOX N = 9, I61Q DOX N = 9) and in O-P Fisher's LSD test was used due to repeated measures (CON N = 15, I61Q N = 9). *p<0.05, **p<0.01, ***p<0.001, ****p<0.0001.*

3.2.5 Cell-intrinsic epigenetic cues may prime I61Q fibroblasts for survival

To determine why cardiac fibroblasts persist despite transcriptional deactivation and injury resolution, we examined potential cell extrinsic and intrinsic survival mechanisms. Signaling from the ECM to the cell, particularly through focal adhesions, has been shown to initiate pro-survival gene programs involving AKT and ERK (*254*). Increased substrate stiffness sustains these gene programs and enhances fibroblast persistence (*254*, *255*). To examine whether the diseased I61Q ECM was providing extrinsic cues to the fibroblasts through their focal adhesions, naive induced pluripotent stem cell-derived fibroblasts (iPSC-FB) with a Clover-mRuby2 FRET tension sensor heterozygously knocked into the vinculin gene (VinTS) were cultured on thin slices of decellularized ECM from 7-month-old CON and I61Q mice given standard or DOX chow. This *in vitro* assay allowed us to measure adhesion forces directly as a result of which ECM the cells were cultured on, negating any potential confounding effects from hemodynamics or other cell types. iPSC-FB cultured on I61Q matrix had decreased matrix-adhesion force relative to those cultured CON ECM (**Figure 3.5A-C**). Interestingly, iPSC-CF cultured on I61Q matrix from DOX-treated mice were stronger relative to CON (**Figure 3.5C**).

The length of the adhesions on the matrix was similarly decreased in iPSC-CF cultured on I61Q matrix and increased on DOX-treated ECM (**Figure 3.5D**). These data mirror the overshoot in isolated myocyte function (**Figure 3.2C**) and suggest that adhesion signaling cues from the matrix are dynamic.

Considering that focal adhesions are mechanically linked to the nucleus via the actin cytoskeleton (*256*) and fibroblasts cultured on stiff substrates retain permanent epigenetic memories (*162*), 8592 fibroblasts were pulled out of the snATACseq dataset (**Figure 3.2I**) to examine whether I61Q fibroblasts retained cell intrinsic cues that primed them for survival despite normalization of adhesion forces. Fibroblasts from I61Q mice shifted into cluster 2, and unlike cardiomyocytes, DOX treatment caused fibroblasts to shift into an entirely new cluster 1 rather than back to CON clusters. I61Q fibroblasts from mice where DOX was withdrawn shifted back into cluster 2 (**Figure 3.5E-F**), highlighting that reintroducing I61Q cTnC causes fibroblasts chromatin accessibility to shift back to a diseased state. Chromatin accessibility analysis revealed that several survival-associated loci, including *Yap1*, *Mapk1*, *Bcl2*, *Akt1*, and *Pdgfra,* were more accessible in I61Q fibroblasts and remained open after DOX treatment (**Figure 3.5G-K**), indicating epigenetic priming for survival. Gene expression analysis from 7-month fibroblasts isolated for snRNAseq (**Figure 3.4C**) showed expression of these genes were also upregulated in I61Q fibroblasts and remained elevated despite DOX treatment, although *Mapk1* and *Bcl2* also appeared upregulated in CON mice treated with DOX (**Figure 3.5L**). Finally, preliminary western blots suggest I61Q fibroblasts have a slight upregulation in BCL2 and total ERK protein relative to CON mice, although phosphorylated ERK was unchanged (**Figure 3.5M-P**). Together, these findings suggest fibroblasts may be primed for survival in I61Q mice, potentially explaining their retention even after the myocytes have been corrected.

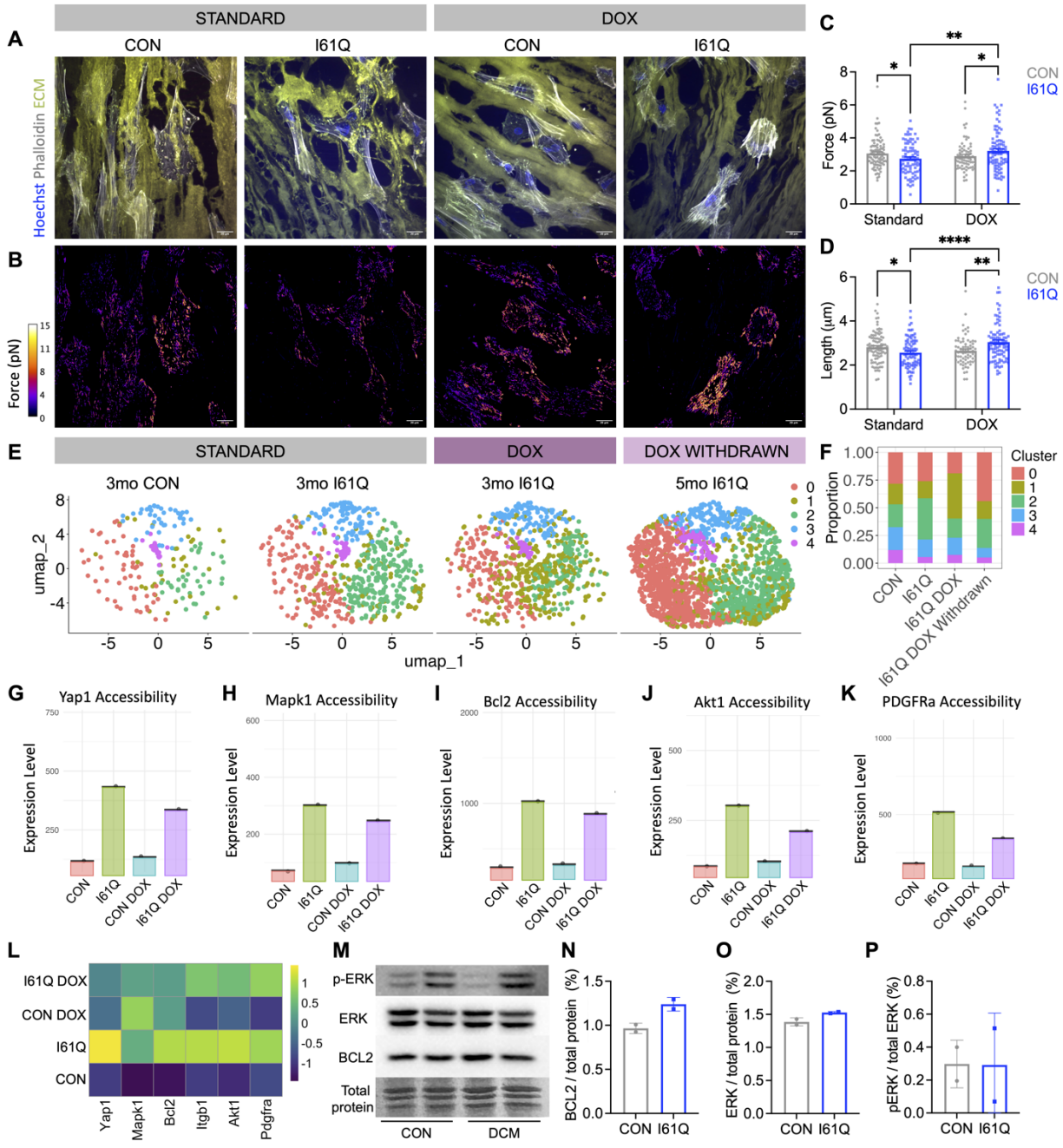

Figure 3.5: Cell-intrinsic epigenetic cues may prime I61Q fibroblasts for survival. A-B) *Representative images of induced pluripotent stem cell-derived fibroblasts (iPSC-CFs) with a Clover-mRuby2 FRET tension sensor knocked into the vinculin locus, cultured on decellularized extracellular matrix from 7-month CON and DCM mice with and without DOX.* ***A)*** *Phalloidin staining (grey) and autoflorescent ECM (green) showing where iPSC-CF overlap with ECM.* ***B)*** *Adhesion force calculated from the FRET*

tension sensor. Quantification of ***C)*** *adhesion force and* ***D)*** *adhesion length in for adhesions overlapping ECM.* ***E)*** *UMAP of fibroblast clustering based on accessible peaks separated by condition.* ***F)*** *Proportion of cells in each cluster.* ***G-K)*** *Peak accessibility for Yap1, Mapk1, Bcl2, Akt1, and Pdgfra across all 3-month conditions.* ***L)*** *Heatmap for Yap1, Mapk1, Bcl2, Akt1, and Pdgfra expression in 7-month fibroblasts.* ***M-P)*** *Western blots and quantification for phosphorylated ERK (p-ERK), total ERK, and BCL2 on freshly isolated CON and I61Q fibroblasts. For N-P, bars represent mean +/- SD and each point represents fibroblasts pooled from N=2 mice (for a total of N=4 mice for each condition). For C-D, bars represent mean +/- SE, where the points represent individual cells (CON n = 91, I61Q n = 80, CON DOX n = 72, I61Q DOX n =93 iPSC-CFs cultured on ECM from N = 3 mice per group) and stats were determined using a Two-way ANOVA with Fisher's LSD test.*

3.3 Discussion

This study set out to define the plasticity of the myocardium in the context of an inherited sarcomeric mutation. Silencing the DCM-inducing mutation produced robust improvements in cardiac function, even at advanced stages of disease. Strikingly, mice with the lowest starting ejection fractions exhibited the greatest recovery, mirroring clinical findings with Omecamtiv Mecarbil, in which patients with more severe heart failure saw larger treatment benefits (GALACTIC-HF, NCT02929329) (*37*). The magnitude of functional improvement observed here far exceeded preliminary efficacy reported for Danicamtiv. In our model, I61Q mice with a starting LVEF of 34.6%±6.1% saw a 38±20.4% (N=10) increase in function after 12 weeks of DOX, whereas patients with gains, respectively, after 12 weeks of Danicamtiv (*44*). Although the baseline LVEF of patients who completed that interval was not reported, the mean starting LVEF for all patients with MYH7 and TTN entering the trial was 35.5±7.1% (N=12) and 30.8±8.2%, respectively (*243*). Given that an acute 10 minute treatment with Danicamtiv

improved the LVEF of I61Q mice by 26.5% (N=11) (*42*), these findings suggest that genetic correction may enable more durable reverse remodeling than pharmacologic myosin activation or that the optimal Danicamtiv dosing regimen for humans has not yet been defined. Long-term studies of Danicamtiv, or other myosin activators, with chronic infusion in animal models could help clarify why clinical trials demonstrated only modest functional improvements. However, such studies may be difficult to perform in mice given Danicamtiv's short half-life (0.22 hours) (*257*).

Surprisingly, cardiomyocytes appeared more plastic and amenable to correction than fibroblasts. Cardiomyocytes not only recovered structurally and functionally in response to genetic correction, but their epigenetic landscape also fully reverted to a healthy state. In contrast, although fibroblasts downregulated ECM-related transcripts, they retained epigenetic signatures consistent with a priming for survival. Unlike fibroblasts in other organs, such as the skin (*258*, *259*) or liver (*260*, *261*), where myofibroblasts undergo senescence and apoptosis once the injury has resolved, cardiac fibroblast numbers remained elevated even after myocyte contractility was normalized. Multiple studies have suggested the heart lacks a mechanism for sensing fibroblast depletion and replenishing fibroblast number (*218*, *219*). Our data suggests the inverse is also true: the heart lacks a mechanism for sensing fibroblast excess and reducing fibroblast number once the injury has resolved. This finding is consistent with MI studies showing that cardiac myofibroblasts deactivate after wound repair but are not cleared from the myocardium (*217*). While fibroblast persistence after MI may be adaptive for maintaining the scar and preventing cardiac rupture, it is unclear whether their persistence in DCM serves any adaptive purpose or instead reflects a maladaptive failure to correct the fibroblast population. Cardiac fibroblasts are known to be relative resistant to apoptosis, in part due to high expression

of anti-apoptosis proteins such as BCL2 and cIAP-2 (*262–264*). We observed a baseline level of BCL2 expression in CON fibroblasts and an increased epigenetic priming for *Bcl2* in I61Q fibroblasts, although it remains unclear whether this transient expression is actively blocking apoptosis or if cardiac fibroblasts simply lack cues for cell death. Considering that *Pdgfra* expression remained high in DOX-treated I61Q fibroblasts (**Figure 3.5K-L**) and that PDGFRα is required for cardiac fibroblast survival (*218*), PDGFRα signaling may underlie the continued survival of cardiac fibroblasts. PDGF signaling is well-known for promoting survival pathways, including PI3K/AKT and MAPK/ERK, particularly in cancer biology and cancer-associated fibroblasts (*265*). Given that tyrosine kinase inhibitors (TKIs) targeting PDGFRα are used clinically to treat gastrointestinal stromal tumors (*266*), future work will explore whether PDGFRα inhibition reduces cardiac fibroblast number and promotes full recovery of the heart. Collectively, these findings challenge a long-standing assumption that cardiac fibroblasts are more plastic than cardiomyocytes due to their ability to proliferate and transdifferentiate (*60*, *267*), and instead suggest that in the absence of cell death, cardiomyocytes retain substantial plasticity whereas fibroblasts remain persistently primed for survival and dysregulation.

Despite full myocyte recovery and robust LVEF improvements at the whole heart level, silencing the sarcomeric mutation failed to fully reverse the DCM phenotype. Persistent tissue stiffness, driven primarily by the ECM, emerged as a major barrier to complete functional recovery. Concomitant with fibroblast survival, we observed persistent interstitial fibrosis in DOX-treated I61Q mice. This result aligns with human (*22*, *151*) and murine studies (*152*, *159*, *245*, *246*) showing that mechanical unloading with LVADs or removal of the disease-inducing stimulus prevents further collagen deposition but fails to reverse established fibrosis, highlighting a critical gap in our understanding of whether cardiac fibrosis can be reversed.

Targeted depletion of activated fibroblasts, via chimeric antigen receptor (CAR) T-cells targeting fibroblast activated protein (FAP), has been proposed as a strategy to promote fibrotic regression (*153*). However, we show that fibroblast proliferation, not activation, is the predominant source of fibrosis in DCM, so FAP may not be a viable target in this context. Moreover, the DTA fibroblast ablation strategy did not confer functional benefits beyond DOX treatment alone, although ablation efficiency and fibrosis still need to be quantified before concluding whether fibroblast clearance can meaningfully reverse cardiac ECM. Importantly, these approaches rest on the assumption that cardiac fibroblasts are actively maintaining fibrosis and their removal will naturally lead to ECM regression. Yet early collagen turnover studies indicate that ~70% of collagen is metabolically inert, with an apparent half-life of 1000 years, while the remaining 30% turns over on the order of hundreds of days (*154*). This intrinsic ECM stability suggests that only a limited fraction of collagen is actually competent to degrade, and thus fibroblast ablation may halt further fibrosis but is unlikely to regress existing matrix. Indeed, we found that fibroblast-specific p38 inhibition did not reduce fibroblast number or interstitial fibrosis, which is consistent with prior studies showing that p38 inhibitors are effective prophylactically but cannot dismantle established fibrosis (*268–270*). Notably, a recent clinical trial testing a p38 inhibitor in DCM patients with *LMNA* mutations was terminated early for futility in improving the 6-minute walk test (*145*), aligning with our observation that late p38 inhibition in fibroblasts fails to yield functional benefit. Together, these data illustrate that correcting myocyte contractile defects alone does not initiate fibrotic regression. Given that fibrosis is a stronger predictor of sudden cardiac death than systolic dysfunction in DCM patients (*65*), it remains uncertain whether a myocyte-directed therapy that restores contractility but leaves fibrosis intact will reduce the arrhythmia burden in these patients.

Dual treatment with DOX and BAPN was the only intervention that fully restored cardiac function. However, the mechanism by which BAPN enables complete recovery remains unclear. Although BAPN can soften the ECM by inhibiting LOX-mediated collagen crosslinking (*271*), these effects have primarily been demonstrated in preemptive or early-injury settings. In a model with established fibrosis, such softening would require meaningful collagen turnover, which, as discussed above, may not occur in the adult heart. Alternatively BAPN has also been shown to blunt angiotensin II/phenylephrine (AngII/PE)-induced increases in blood pressure by reducing vascular stiffness (*272*), raising the possibility that its benefit stems from lowering cardiac load rather than directly altering interstitial fibrosis. Thus, future work will examine the effects of BAPN on myocardial stiffness, fibrosis, and the vasculature to determine how it augments functional recovery.

In conclusion, we demonstrated that sarcomeric correction reverses cardiomyocyte structure, function, and epigenetics, yet full cardiac recovery is ultimately constrained by persistent ECM stiffness and fibroblast survival. These findings establish that while cardiomyocytes are remarkably amenable to repair, fibroblast-driven matrix pathology remains a key barrier to full reversal of DCM. More broadly, this work can be used to help design new combinational therapeutic strategies and contextualize the performance of emerging myosin activators as they begin clinical trials for efficacy.

3.4 Methods

Animal Models

All animal experiments were approved by the University of Washington Institutional Animal Care and Use Committee. I61Q mice were generated as previously described, by mating to a tetracycline transactivator (tTA) line on the FVB/NJ genetic background (*18*, *242*). The CON group consisted of both nontransgenic and tTA transgenic littermates because previous studies showed no effects of the tTA transgene (*18*). To suppress the I61Q-cTnC transgene, doxycycline hyclate chow (625mg/kg Harlan Laboratories, TD.01306) was administered to mice. To knockout p38 in Tcf21-expressing fibroblasts, we used a previously generated cross where I61Q tTA mice were bred onto a line containing LoxP-targeted Mapk14 ($p38^{fl/fl}$) and a tamoxifen regulated Cre recombinase that was knocked into the Tcf21 locus ($Tcf21^{iCre}$) to generate I61Q cTnC-$p38^{fl/fl}$-$Tcf21^{iCre}$ mice (p38 I61Q) (*242*). To initiate knockout, 25mg/kg tamoxifen (Sigma, T5648) was delivered to mice by intraperitoneal (IP) injection in a 95% peanut oil and 5% ethanol solution for 5 consecutive days, followed by tamoxifen citrate chow (400mg/kg Harlan Laboratories, TD.130860) ad libitum for 10 days. To generate a line where Tcf21-expressing fibroblasts could be conditionally ablated, I61Q tTA $Tcf21^{iCre}$ mice were crossed with a line containing a floxxed diptheria toxin knocked into the ROSA26 ($R26^{DTA}$) locus (Jackson Laboratory, Strain #:009669) (*273*). To initiate ablation, mice were given 80mg/kg of tamoxifen via IP injection for 5 days, followed by 10 days of tamoxifen citrate chow. To inhibit lysyl oxidase (LOX) activity, I61Q tTA mice were given IP injections of 500mg/kg 3-aminoproprionitrile fumarate salt (Millipore Sigma, A3134) in sterile PBS for 14 consecutive days as previously described (*217*).

To assess whole heart structure and function, echocardiography was performed on a Vevo 3100 (VisualSonics) using the MX550D probe under gaseous isoflurane with heart rates exceeding 400bp. M-mode measurements were acquired from the short axis view and analysis was performed using VisualSonics Vevo LAB software to acquire values for ejection fraction, chamber dimensions, and LV wall thickness. Tissue doppler and pulse wave measurements were acquired from a four-chamber view and Vevo LAB was used to obtain diastolic parameters. Analysis was performed blinded to genotype and DOX treatment. Statistics were performed in GraphPad Prism.

Intact, skinned, and decellularized muscle mechanics

Intact and skinned mechanics were performed as previously described (*242*). Hearts were rapidly excised via thoracotomy and rinsed in oxygenated modified Krebs buffer (118.5mM NaCl, 5mM KCl, 1.2mM $MgSO_4$, 2mM NaH_2PO_4, 25mM $NaHCO_3$, 1.8mM $CaCl_2$, and 10mM glucose). Hearts were then perfused and dissected in oxygenated modified Krebs with 0.1 mM $CaCl_2$ and 20 mM 2,3-butanedione 2-monoxime (BDM) to limit contraction and damage during tissue dissection.

For demembranated (skinned) tissue mechanics, dissected hearts were permeabilized overnight at 4°C in a glycerol-based relaxing solution (100mM KCl, 10mM MOPS, 5mM K_2EGTA, 9mM $MgCl_2$ and 5mM Na_2ATP, pH 7.0, supplemented with 1% Triton X-100 (by vol), 1% protease inhibitor (Sigma P8340), and 50% glycerol (by vol)). Tissues were then transferred to a fresh solution without Triton X-100 and stored at -20°C. Right ventricular trabeculae were dissected and mounted between a force transducer and motor, and sarcomere length (SL) was set to ~2.3 μm, as previously described (*20*). Measurements were performed in a

physiological solution (15°C, pH 7.0) containing a range of pCa (–log[Ca^{2+}]) from 9.0 to 4.0. Steady-state force and the rate of tension redevelopment (ktr) were recorded at each pCa and analyzed with custom using LabVIEW software.

For intact twitch measurements, unbranched trabeculae were isolated from the right ventricular wall and mounted between a force transducer (Cambridge Technology, Inc., model 400A) and a rigid post, as previously described (*20*). Tissues were immersed in a continuously perfused, oxygenated modified Krebs buffer (1.8 mM $CaCl_2$) at 33°C. After a ~20 min equilibration and washout at 0.5 Hz pacing, SL was adjusted to ~2.3 μm and tissues were paced at 1Hz. 30s traces were recorded on custom LabView software and were analyzed with custom code written using MATLAB software (Mathworks).

To obtain passive stiffness measurements, papillary muscles were isolated and mounted as described for intact twitch experiments. All buffers additionally contained 25μM blebbistatin to inhibit cross-bridge formation. Measurements were performed in a modified Krebs buffer containing 0.1mM Ca^{2+} and 25μM blebbistatin. Tissues were set to a baseline length (L_0) just above slack and subjected to a serial stretch protocol increasing L_0 by 4%, 8%, 12%, 16%, 20%, and 24%, with each step held for 30s. This protocol was repeated at least twice per tissue to ensure mechanical stability. Papillary muscles were then decellularized by rocking overnight at 4°C in 1% sodium dodecyl sulfate (SDS), and passive stiffness measurements were repeated starting from the same L_0. Force was normalized to cross-sectional area to account for size-dependent differences in stiffness. Traces were recorded using custom LabVIEW software and were analyzed using custom R code.

Mouse cardiomyocyte isolation and culture

Mice were heparinized and ventricular myocytes were isolated using Langendorff retrograde perfusion as previously described (*235*, *239*) with Liberase TH (0.055 mg/mL, Sigma 5401151001) in Krebs-Henseleit buffer (113mM NaCl, 4.7mM KCl, 0.6mM KH_2PO_4, 0.6mM Na_2HPO_4, 1.2mM $MgSO_4*7H_2O$, 12µM $NaHCO_3$, 12µM $KHCO_3$, 10.8mM HEPES, 10mM BDM, 5.66mM D-Glucose, pH 7.46) and 25µM blebbistatin (Toronto Research Chemicals AB592500). Digestion was aided by a mechanical dissociation step before being filtered through a 200µm mesh. Myocytes were allowed to sediment for 5-10 minutes and the supernatant was replaced with increasing concentrations of Ca^{2+} from 0.125 to 0.25 to 0.5mM with BDM and blebbistatin. Myocytes were plated onto laminin-coated coverslips (40µg/mL, Thermo Fisher) in a modified DMEM (Fisher Scientific, 10-017-CV) plating medium with 5% FBS, 1% penstrep, 1% L-Glutamine, and 10mM BDM for at least 2 hours prior to fixation or functional measurements. For myocyte morphology measurements, myocytes were relaxed in PBS with 25µM blebbistatin and fixed in 4% PFA.

Cardiomyocyte morphology tracing

For myocyte geometry measurements, plated myocytes were stained with Wheat Germ Agglutinin, Alexa Fluor 488 Conjugate (1:100, Invitrogen W11261). 100 myocytes per animal were manually traced and cell area, length, and width were quantified using Fiji (*221*). Cell measurements were performed blinded to genotype and treatment. Statistical analyses were performed on pooled myocyte measurements in GraphPad Prism.

Measurements of cardiomyocyte contractility

Cardiomyocyte functional measurements were performed as previously described (*242*) with constant perfusion of warm M199 with Earle's salts and L-glutamine (Corning 10-060-CV)

and 10.25mM HEPES (pH 7.46). In brief, measurements were obtained using the IonOptix SarcLen Sarcomere Length Acquisition Module with a MyoCam-S3 digital camera (Ionoptix Co.) attached to an Olympus uWD 40 inverted microscope. To jumpstart pacing, myocytes were stimulated with 0.5, 1.0, and 1.5Hz at 10V for a minimum of 10 contractions at each frequency. Measurements were obtained with 0.5Hz pacing with a minimum of 10 beats per myocyte for 30-50 myocytes/mouse. Blinded analysis was performed using the IonWizard software. Statistical analyses were performed on individual myocyte measurements.

Nuclei isolation from whole ventricles

Nuclei were isolated from whole ventricles using a modified version of the 10X demonstrated protocol "Nuclei Isolation from Complex Tissues for Single Cell Multiome ATAC + Gene Expression Sequencing" (*274*). Ventricles were excised, flash frozen in liquid nitrogen, and stored at -80C. To isolate nuclei, ventricles were lysed in an NP40 Lysis Buffer (10mM Tris-HCl pH 7.4, 10mM NaCl, 3mM $MgCl_2$, 0.25% NP40, 1mM DTT, and 0.1U/µL RNase Inhibitor in nuclease-free water). To assist with lysis, ventricles were put in an M tube (Miltenyi 130-096-335) and mechanically homogenized using a gentleMACS^{TM} Dissociator (Miltenyi 130-093-235) "protein_01.01 protocol" before being dounced 50 times in a Type B "loose" douncer. Tissues were incubated 2 minutes on ice, for a total lysis time of ~5 minutes. Nuclei were passed through a 40um strainer, washed with PBS with 1% BSA and 0.1U/µL RNase inhibitor and resuspended in a 7-AAD Flow Sorting Solution (1X PBS, 0.5% BSA, 0.1U/µL) with 10mg/mL 7-AAD Ready Made Solution (Sigma, SML1633). To remove sarcomere debris from lysed myocytes, nuclei were flow sorted on an Aria III into a PBS solution with 2% BSA (for a final concentration of 1% BSA) at a flow rate of 2-3, until 500k nuclei were collected. To

permeabilize nuclei, the pellet was incubated in 0.1X Lysis Buffer (10mM Tris-HCl pH 7.4, 10mM NaCl, 3mM $MgCl_2$, 1% BSA, 1mM DTTA, 0.1U/µL RNase Inhibitor, 0.01% Tween-20, 0.01% NP40, and 0.001% Digitonin in nuclease-free water) for 2 minutes on ice. Nuclei were washed in Wash Buffer (10mM Tris-HCl pH 7.4, 10mM NaCl, 3mM $MgCl_2$, 1% BSA, 0.1% Tween-20, 1mM DTT, and 0.1U/µL in nuclease-free water) and resuspended in Diluted Nuclei Buffer (1X Nuclei Buffer Kit A, 1mM DTT, 0.1U/µL in nuclease-free water) to a final concentration of 4k nuclei/µL for a targeted nuclei recovery of 10k. Nuclei concentration was determined using the ReadyCount™ Green/Red Viability Stain (Thermo Fisher A49905).

10x Single Cell Multiome ATAC + Gene Expression sequencing and analysis

Library preparation and sequencing were performed with assistance from the Institute for Stem Cell and Regenerative Medicine (ISCRM) Genomics Core. Permeabilized nuclei were loaded onto a Chromium Next GEM Chip J (10x Genomics, 1000230), and single-nucleus droplet partitions were generated using the Chromium Next GEM Single Cell Multiome ATAC + Gex Reagent kit (10X Genomics, 1000285), following the manufacturer's protocol (*275*). Independent ATAC and Gene expression libraries were constructed according to the recommended workflow. Final libraries were sequenced on an Illumina NextSeq 2000 using a NextSeq 2000 P3 kit (Illumina, 20040559).

Raw sequencing output (BCL files) were processed using the 10x Genomics Cloud Analysis platform. BCL files were demultiplexed with Cell Ranger ARC (v2.0.2) to generate FASTQ files for both chromatin accessibility (ATAC) and gene expression (GEX) libraries. Reads were aligned to the Mus musculus mm10 genome using the 10x Genomics ARC reference build refdata-cellaranger-arc-mm10-2020-A-2.0.0. Gene expression was quantified with intronic

reads included (include-introns = true), consistent with Multiome v1 chemistry requirements. For each sample, Cell Ranger ARC (v2.0.2) performed initial quality control, barcode filtering, peak calling, ATAC fragment processing, and UMI counting. After individual library processing, samples were normalized and aggregated using the Cell Ranger ARC aggr pipeline with default depth-normalization parameters. The resulting aggregated feature-barcode matrices for ATAC and GEX modalities were exported for downstream analysis in R using Seurat and Signac (*238*, *276*).

More stringent peak calling was performed using MACS2 (v2.2.8) (*277*) through the Signac CallPeaks wrapper, using default parameters for single-nucleus ATAC-seq. Peaks were filtered to remove nonstandard chromosomes and regions overlapping the ENCODE mm10 blacklist. Fragment counts were re-quantified over the MACS2 peak set using FeatureMatrix, and a new ChromatinAssay was generated and added to the Seurat object for downstream dimensionality-reduction and differential accessibility analyses. Nuclei were filtered out if they had low or excessively high ATAC fragment counts (below 500 or above 100,000), low or excessively high UMI (below 200 or above 2,500), elevated mitochondrial content (above 5%), a nucleosome signal greater than 2, or insufficient TSS enrichment (below 1). Doublets were identified and removed using DoubletFinder (*278*). After quality control, 30,020 nuclei representing all cell types were retained, with a median of 813 UMIs, 5,904 ATAC fragments, and a fraction of reads in peaks (FRiP) score of 0.39 per nucleus. Cell types were identified using RNA-based clustering in Seurat. Gene expression counts were normalized using SCTransform, with the "glmGamPoi" method, regressing out mitochondrial mapping rate using the vars.to.regress argument. Principal component analysis (PCA) was performed on the scaled SCT assay, and downstream analyses were carried out using the first 10 principal components. Nuclei

were clustered using FindNeighbors and FindClusters with a resolution of 0.1, and visualization was performed using UMAP computed from the same PCs. Cell types were manually annotated based on canonical marker genes, identifying myocytes, fibroblasts, endothelial cells, immune cells, pericytes, smooth muscle cells, and epicardial cells. Myocytes and fibroblasts were individually subset and processed for downstream ATAC analysis. The myocyte subset contained 14,533 nuclei (median 1,550 RNA UMIs and 9,652 ATAC fragments per nucleus), whereas the fibroblast subset contained 8,848 nuclei (median 600 RNA UMIs and 4,032 ATAC fragments per nucleus). The ATAC counts were normalized using TF-IDF, and dimensionality reduction was performed using latent semantic indexing (LSI). Shared nearest neighbor graphs and UMAPs were constructed from the informative LSI components, with components 2-30 for myocytes and 2-5 for fibroblasts (reflecting the differences in cell number), and clusters were identified using the smart local local moving (SLM) algorithm with resolutions of 0.1 for myocytes and 0.2 for fibroblasts.

Five myocyte clusters were identified, with cluster 0 representing the predominant CON myocyte population and cluster 2 representing the diseased-associated myocyte state. Transcription factor (TF) activity analysis was performed by integrating gene expression and chromatin accessibility. ATAC peaks were annotated with TF motifs from the JASPAR2020 vertebrate/core database using the mm10 genome (*279*), and motif deviation scores were computed per cell using chromVAR (*280*). In parallel, differential gene expression and differential motif activity between clusters 0 and 2 were quantified using the wilcoxauc implementation in the presto package (*281*) on the SCT (RNA) and chromVAR (motif) assays, respectively, yielding AUC statistics and adjusted p values for each TF. Five fibroblast clusters were identified, but in contrast to the myocytes there was no single cluster that clearly

represented a disease-specific state. To assess gene-level chromatin accessibility across conditions, we computed a gene activity matrix from fibroblast ATAC peaks using Gene Activity and stored it as a pseudoRNA assay. PseudoRNA counts were normalized with LogNormalize in Seurat using the median pseudoRNA UMI count as the scale factor. Normalized gene activity scores were then aggregated to the sample level using AggregateExpression, grouping by fibroblast identity and sample to generate pseudo-bulk accessibility profiles for each experimental condition. These pseudo-bulk profiles were used to visualize accessibility of selected survival genes across conditions using boxplots.

Mouse cardiac fibroblast isolation and purification

Cardiac fibroblasts were isolated and enriched as previously described (*199*). In brief, mice were heparinized, and fibroblasts were isolated by Langendorff perfusion with type II collagenase (2mg/mL, Worthington LS004176) and Liberase TH (0.4mg/mL) in Krebs-Henseleit buffer (113mM NaCl, 4.7mM KCl, 0.6mM KH_2PO_4, 0.6mM Na_2HPO_4, 1.2mM $MgSO_4*7H_2O$, 12µM $NaHCO_3$, 12µM $KHCO_3$, 10.8mM HEPES, 10mM BDM, 5.66mM D-Glucose). After 15 minutes of perfusion, ventricles were mechanically teased apart and put on a rocker in digestion media at 37C until ventricles were fully dissociated (~15 additional minutes). The digestion mixture was filtered through a 70µm filter and washed with DMEM with 20% fetal bovine serum (FBS, Fisher Scientific SH30071.03) and 1% penstrep. To enrich the cell pellet for fibroblasts, fibroblasts were magnetically sorted using a Miltenyi QuadroMACS magnetic cell separation kit. Cells were resuspended in 180µL sorting buffer (1X PBS, 5% BSA, 2mM EDTA, degassed) and 20µL of Cd11b microbeads (Miltenyi 130-049-601) and incubated for 15 minutes at 4C. Samples were washed through the LS columns (Miltenyi 130-042-401) and the flow

through was collected (Cd11b- fraction). The cells were spun down and resuspended in 160µL of sorting buffer with 40µL MEFSK4 (anti-feeder) microbeads (Miltenyi 130-095-531). Cells were again incubated 15 minutes at 4C and washed through the magnetic columns. The flow through was discarded and magnetic columns containing MEFSK4+ fraction were removed and rinsed with sorting buffer. Viability was assessed using trypan blue, with viability of greater than 90% for each sample.

For western blots fibroblasts from two respective preps were pooled for each genotype and condition in order to maximize protein per sample and minimize variability. After isolation, fibroblasts were directly lysed in Laemmli buffer at a ratio of 10k cells/µL of buffer and stored at -80C. For single nucleus RNAseq fibroblast pellets were spun down, supernatant was removed, and cells were snap frozen in liquid nitrogen and stored at -80C.

Fibroblast single nucleus RNA sequencing and analysis

Nuclei were isolated from fibroblasts as previously described (*234*, *242*) with the following modifications. Cells were lysed at room temperature for 5mins with cold hypotonic lysis buffer solution B (6.8mM Na_2HPO_4 dibasic, 4mM $NaH_2PO_4*H_2O$, 1.5mM KH_2PO_4 monobasic, 2.4mM KCl, 2.7 $MgCl_2$, 0.67% Bovine Albumin Fraction V, 0.02% igepal, 0.9% DEPC). Nuclei were passed through a 40um filter and fixed for 5mins in room temperature methanol with 1.25mg/mL DSP. Finally, nuclei were rehydrated in 0.3M SPBSTM (333mM sucrose, 1X DPBS, 0.1% TritonX-100, 3mM $MgCl_2$ made up in nuclease free water) and passed through 20um filter. Nuclei were counted and quality was evaluated using trypan blue. Nuclei were spun down, supernatant was removed, and nuclei were stored at -80C. All spins were performed at 500rcf at 12C for 5mins to prevent crystallization of DEPC.

Sequencing was performed at the Northwest Genomics Core on a Novaseq 6000 flow cell. Cleaned reads were aligned to the reference genome (GRCm38/mm10) using STAR (*234*). Further analysis, filtering, and visualization was performed using the Seurat package in R (*237*) as previously described (*242*). In brief, nuclei were filtered out if they contained fewer than 200 UMI, over the top 1% of UMI, or over 5% mitochondrial reads. Overall, 239,946 nuclei of all cell types were sequenced with median UMI of 716. Clustering was performed following the standard approach, with cell types manually identified by canonical marker genes. 211,301 fibroblasts with an average UMI count of 714 were subset, normalized using the SCTransform function using the "glmGamPoi" method with the percent mitochondrial reads regressed out using the vars.to.regress argument. Principal component analysis was performed on the scaled data, the nuclei were clustered on the first 10 principal components using the FindNeighbors function, and the FindClusters function was performed with a resolution of 0.4. To visualize the data, non-linear dimensional reduction via UMAP was used to project cells in 2D space. 6 fibroblast clusters were identified, and cluster markers were obtained using FindAllMarkers. An ECM Score was obtained as previously described (*282*) using the AddModuleScore function to get a score for relative expression of all known ECM collagens, glycoproteins, and proteoglycans obtained from MatrisomeDB 2.0 (*283*) Genes that were reversibly or irreversibly upregulated with I61Q and DOX treatment were identified using the FindMarkers function between each experimental group. GO terms were obtained using gprofiler2 (*284*).

Western blots

For whole ventricle western blots, ventricles were flash frozen in liquid nitrogen and stored at -80C. To obtain protein pellets, frozen tissue was dissociated using a mortar and pestle

and resuspended directly in concentrated Laemmli buffer (15% Glycerol, 1% SDS, 62.5mM Tris HCl, pH 6.8, 0.05% bromophenol blue, 60mM DTT, and 1x complete protease inhibitor). Lysates were further diluted in Laemmli buffer, incubated for 5mins at 100°C, and sample concentrations were normalized by total protein (Coomassie, Fisher Scientific, 50-212-965) staining following SDS-PAGE electrophoresis. Equal amounts of protein were subsequently loaded in 12% bis-acrylamide gels to allow separation of native cTnC from the FLAG-tagged I61Q-cTnC transgene, which has a slightly higher molecular weight. The gels were transferred to PVDF membranes for immunodetection. Membranes were blocked in 5% milk in tris buffered saline containing 0.1% Tween-20 (TBST), pH 7.6. Primary antibodies were applied overnight at 4°C in blocking buffer: cTnC (1:1000, Abcam ab137130), M2 Flag antibody (1:1000, Sigma F1804). HRP-conjugated secondary antibodies (1:4000, Sigma) were applied the following day for 1 hour at room temperature and blots were developed using SuperSignal West Pico PLUS (Thermo Fisher, PI34580) chemiluminescence substrate.

For fibroblast westerns, samples were boiled at 95C for 5min and 180k fibroblasts worth of lysate was loaded onto a 12% gel and run as described above. Primary antibodies: BCL2 (1:1000, BD Biosciences 610538), p-ERK (1:1000, Cell Signaling 4370T), ERK (1:500, Cell Signaling 4695S).

Histology and immunohistochemistry

Hearts were cut in half on the transverse plane prior to processing and sectioning. Hearts were fixed in 4% PFA overnight, run through a sucrose gradient (PBS + 5%, 10%, 20%, and 30% sucrose), and embedded in optimal cutting temperature (OCT) compound. 5μm sections were used for all histological and immunohistochemical analyses. Prior to Sirius Red/Fast Green

staining (0.1% Direct Red 80, 0.1% Fast Green in Picric Acid) sections were additionally incubated in bouin's solution at 55-60°C for 10mins. This method stains muscle tissue in green and fibrotic scar in red. Images of whole hearts were taken at 10x magnification and quantified using HSB color thresholding in Fiji (Hue categories: fibrotic area 19-220 without pass, total area 141-190 without pass). PDGFRα (1:100 R&D systems) staining was done on independent OCT samples. These methods are previously described from our laboratory (*199*). OCT sections were rinsed in 1X PBS and blocked 1hr (PBS, 1% BSA, 0.5% Triton-X100, 0.1% cold fish skin gelatin). Primary antibodies were incubated overnight in blocking solution at 4°C. AlexaFluor secondary antibodies (1:1000, Invitrogen) were used for 1.5 hours at room temperature to detect the antigen and hoechst (1:2000, Thermo Fisher) was used to visualize nuclei. To obtain myocyte cross-sectional area, OCT sections were stained with Wheat Germ Agglutinin, Alexa Fluor 488 Conjugate (1:100, Invitrogen) for 1 hour at room temperature. To examine collagen turnover, OCT sections were stained with a biotin conjugated collagen hybridizing peptide (CHP, 10μM, 3Helix). The diluted CHP solution was incubated at 80°C for 5mins and incubated 15-90 seconds in an ice slurry to cool the solution down before being applied to the slides and incubated overnight at 4°C. Streptavidin Alexa Fluor 647 conjugate was used as a secondary (1:1000, Thermo Fisher) and Wheat Germ Agglutinin, Alexa Fluor 488 Conjugate was used as a counterstain to obtain total tissue area. Secondaries were incubated for 1hr at room temperature. All samples were mounted using Mowiol 4–88 (Sigma 81381).

Image analysis

To quantify PDGFRα^{+} cells in tissue, whole cross-sections were imaged on an Olympus slide scanner at 20X and segmented using a trained Ilastik pipeline (*285*). Cell counts were

normalized to total number of nuclei to obtain fibroblast number as a percent of all cells. To obtain myocyte cross sectional area (CSA), 50 endocardial and 50 epicardial myocytes were manually traced per mouse in Fiji (*221*). CHP area was quantified using the thresholding function in Fiji. Thresholds were stringently set using positive controls (such as myocardial infarction samples) where there is known collagen turnover to avoid over-thresholding. CHP area was normalized to total tissue area, which was obtained by thresholding WGA.

Analysis of collagen birefringence

Images of whole heart sections PSR/FG sections were taken at 10x magnification with the polarizer rotated to 90 degrees. This produced images with a very black background and bright collagen birefringence. Notably, not all red fibers from PSR/FG staining were birefringent because the samples were not rotated at all angles. Analysis of collagen birefringence was completed using HSB color thresholding in Fiji (Hue categories: Orange/Red/White 23–235 without pass, Yellow/Green 24–82) (*221*). The Yellow-Green hue range was reduced compared to previous methods (*199*) to remove myocyte background in the green spectra. The percent area of each color category was then normalized to the total birefringent fiber area and total tissue area.

Culturing iPSC-CM on decellularized mouse ECM

To generate an induced pluripotent stem cell line with a tension sensor, the Clover-mRuby2 FRET tension sensor was heterozygously knocked into the vinculin gene following the head protein domain in the WTC11 iPS cell line (VinTS iPSCs) (Nagle et al., paper in review at *Biophys J.*). This force sensor contains a linker with 7 GGSGGS repeats, translating to a force range of 2-9 piconewtons in the FRET efficiency range of 45-5%13. The Clover-mRuby2

tension sensor with a (GGSGGS)x7 linker was obtained from the Hoffman lab via Addgene (#111764). The sensor construct was cloned into a donor plasmid containing homology arms on either side of the sensor with 1000bp on either side of residue 883, amplified from WTC11 genomic DNA.

VinTS iPSCs were cultured in mTeSR Plus (Stem Cell Technologies) and passaged after reaching 60-80% confluency. Cells are passaged by 10-minute incubation with versene, followed by centrifugation at 1000 rpm for 3 minutes. Cells are resuspended in mTeSR Plus with 10μM ROCK inhibitor (Y-27632, Selleckchem), and plated onto tissue culture plates that had been incubated at least 30 minutes in a 60X dilution of Matrigel (Corning) into DMEM:F12.

VinTS iPSCs were differentiated into cardiac progenitors as previously described (*286*) On day -2, iPSCs were replated onto Matrigel coated plates in mTeSR with 10uM ROCK inhibitor. On day -1, iPSCs were primed with 1uM CHIR-99021 (Cayman) in mTeSR Plus. On day 0, stem cells were washed with HBSS and fed with a differentiation medium (base medium RPMI-1640 (Gibco), 5μM CHIR-99021, 500μg/mL BSA (Sigma), 213μg/mL ascorbic acid (Sigma) to activate Wnt signaling and induce mesoderm fate. On day 2, Wnt signaling was inhibited to induce cardiac fate by feeding cells with 2μM Wnt-C59 (SelleckChem) in RBA medium. On day 4, cells were fed RBA medium only. Cardiac progenitors were further specified into epicardial cells and finally differentiated into fibroblasts according to the Whitehead protocol (*287*). At day 6, cardiac progenitors were replated at 60k cells/well to a pre-coated 0.1% gelatin 12-well plate and fed Advanced DMEM/F12 (Gibco) with 100μg/ml ascorbic acid, 1.3X Glutamax (Gibco) (LaSR medium), and 10uM Y-27632. On days 7 and 8, cells were fed LaSR + 3μM CHIR-9902. On days 9-11, cells were fed with LaSR only. On day 12, epicardial cells were replated at 650k cells/well to a precoated 0.1% gelatin 6 well plate and fed LaSR with 10μM Y-

27632 to begin fibroblast specification. Cells were fed daily out to day 33 with LaSR with 10ng/mL bFGF (R&D Systems).

To generate coverslips with dECM, CON and I61Q hearts were pinned and decellularized on plates coated in Sylgard™ 184 (Electron Microscopy Services). Tissues were rocked at room temperature in a 1% SDS solution for 4 days and subsequently washed with 1% Triton-X and PBS solutions for at least 1hr. The dECM was then frozen in OCT and coverslips to obtain 10µm dECM slices. The coverslips with dECM were rinsed in PBS and UV-treated for at least 30 minutes to avoid contaminations. VinTS iPSC-FBs were replated onto dECM coverslips at day 33 in Promocell Fibroblast Growth Medium 3. After 24hrs, the media was switched to the Assay Media (RPMI, 10% FBS, and 50µM ascorbic acid). The VinTS iPSC-FB were cultured on the dECM for a total of 4 days before being fixed with 4% PFA. VinTS iPSC-FB were stained with Phalloidin (Thermo Fisher A22287) and Hoechst to visualize the cells on the matrix.

To measure adhesion force, VinTS iPSC-FB were imaged on a Live-Cell Inverted Widefield/Spinning Disk Confocal at 63x with z-stacks. Images of the donor (Clover), sensitized emission (FRET) and acceptor (mRuby2) were inputted into a MATLAB script adapted from the Hoffman group (*288*) using FRET analysis calculations outlined in Chen et al (*289*). Other inputs required are the donor and acceptor bleedthrough constants and the G constant (ratio of sensitized emission to quenched donor fluorescence). ECM was visualized through autofluorescence in the FRET channel and segmented using an Ilastik pipeline (*285*). To avoid confounding affects from adhesions bound to the hard coverglass, ECM-touching adhesions were segmented and quantified based on whether they overlapped the ECM mask.

3.5 Supplemental Figures

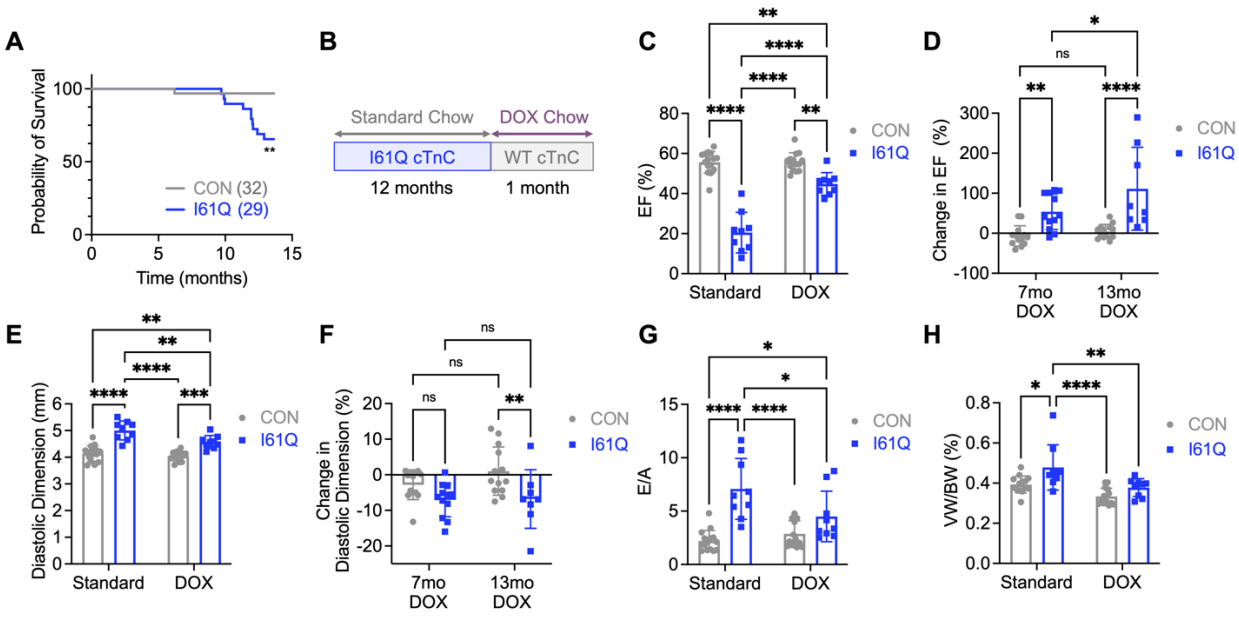

Supplemental Figure 3.1: Mice with end-stage DCM are still capable of recovery. ***A)*** *Survival curve comparing CON and I61Q mice out to 13 months of age. Significance determined using the Gehan-Breslow-Wilcoxon test.* ***B)*** *Schematic of the experimental design, where I61Q mice and their control littermates were aged to 12 months before beginning treatment with DOX chow for one month, replacing I61Q cTnC with WT cTnC.* ***C)*** *Left ventricular ejection fraction (EF) in 12mo mice +/- 1 month of DOX and* ***D)*** *percent change in EF in 1-month treated mice beginning treatment at 6 and 12months.* ***E)*** *Diastolic dimension and* ***F)*** *percent change in diastolic dimension.* ***G)*** *E/A. Bar graphs are mean ± standard deviation (SD) and dots represent biological replicates (CON N=15, I61Q N=9, CON DOX N=14, I61Q DOX N=9).* ***H)*** *Ventricle hypertrophy measured by the ventricle weight (VW) to body weight (BW) ratio (CON N=14, I61Q N=9, CON DOX N=14, I61Q DOX N=9). All bar graphs are mean ± SD, and statistical significance was determined using two-way ANOVA + Tukey post-hoc (*p<0.05, **p<0.01, ***p<0.001, ****p<0.0001).*

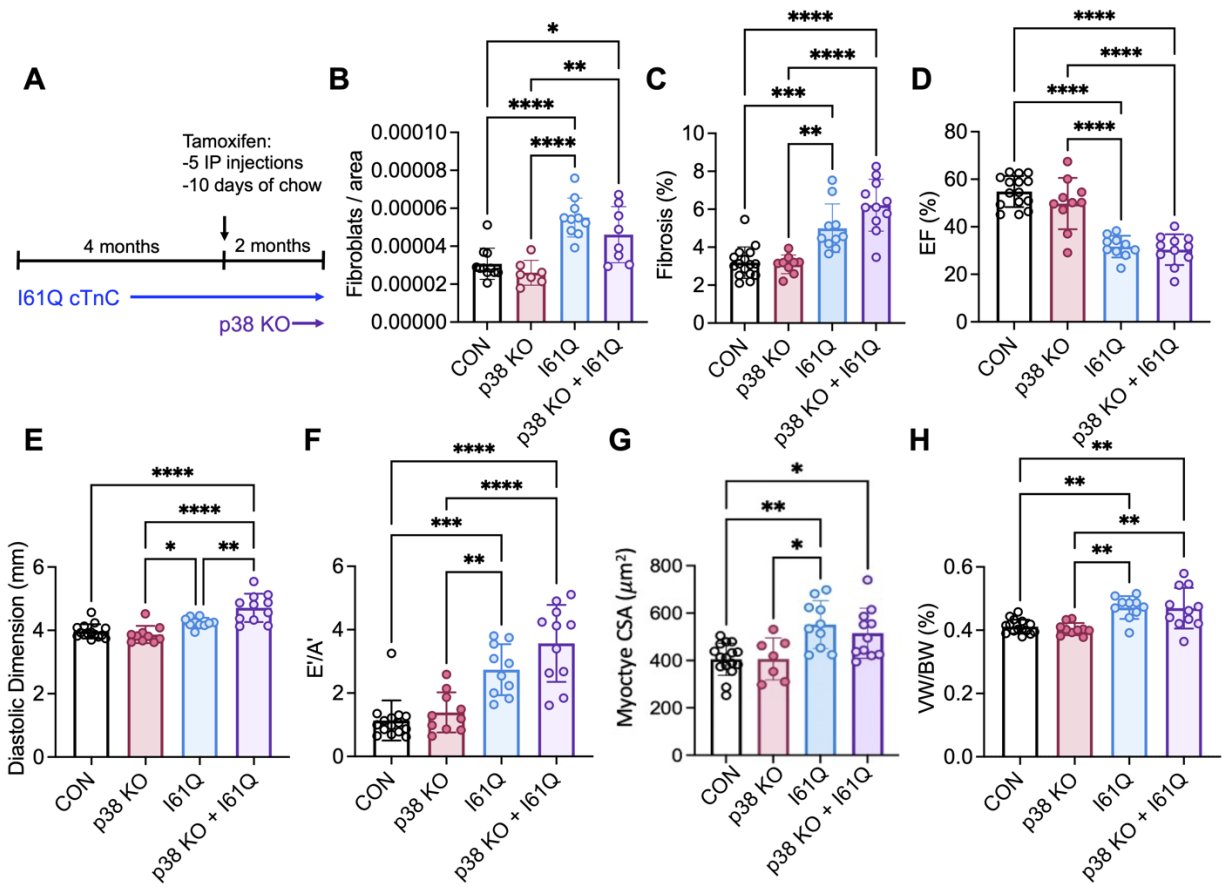

Supplemental Figure 3.2: Late p38 knockdown in fibroblasts fails to reduce fibroblast number or improve function. ***A)*** *Schematic of the experimental design: mice were aged to 3.5 months before receiving 2 weeks of tamoxifen to knock out p38 in Tcf21-expressing fibroblasts, followed by a 2-month incubation period to assess effects on I61Q-induced DCM.* ***B)*** *Quantification of fibroblast number normalized by tissue area, showing p38 KO does not reduce fibroblast numbers in I61Q mice.* ***C)*** *Quantification of fibrosis from PSR/FG-stained slides.* ***D-F)*** *Echocardiographic measurements of left ventricular ejection fraction (EF), E'/A', and diastolic dimension.* ***G)*** *Myocyte cross-sectional area (CSA) from myocardial sections stained with wheat germ agglutinin (WGA).* ***H)*** *Ventricular hypertrophy quantified as ventricle weight (VW) to body weight (BW) ratio. Bar graphs show mean ± standard deviation (SD), with dots representing biological replicates (CON N = 11, p38 KO N = 7, I61Q N = 10,*

*p38 KO + I61Q N = 8 for G–H; CON N = 15, p38 KO N = 10, I61Q N = 10, p38 KO + I61Q N = 11 for D-H). One-way ANOVA + Tukey post-hoc. *p < 0.05, **p < 0.01, ***p < 0.001, ****p < 0.0001.*

Chapter 4: Impact of developmental timing on DCM onset and progression

4.1 Introduction

While the central focus of this dissertation has been to define the reversibility of DCM after the establishment of pathological remodeling, several experiments conducted during my PhD addressed how developmental processes may shape disease onset and progression. Cardiac development is a period of high cellular plasticity, characterized by dynamic changes in cardiomyocyte maturation, fibroblast proliferation, and ECM organization. In particular, postnatal fibroblasts are transiently proliferative and contribute substantially to ECM deposition during myocardial maturation (*46*). Given the central role of fibroblasts and ECM stiffness in limiting recovery in adult DCM, it is reasonable to hypothesize that the timing of disease onset relative to developmental windows of fibroblast activity could influence the severity and trajectory of disease.

4.2 Results

4.2.1 Developmental suppression of DCM mutation delays dysfunction

To determine whether hypocontractility during early postnatal life contributes to DCM progression in adulthood, we transiently suppressed expression of the I61Q cTnC transgene by administering doxycycline chow (DOX) from birth until one month of age. DOX was then withdrawn to allow transgene re-expression during adulthood. Mice were harvested at 1, 2, 3, 4, or 5 months after DOX removal to define the kinetics of transgene return (**Figure 4.1A**). Western blot quantification of mutant-to-total cTnC revealed that expression began to reappear between 2-3 months and reached full expression by 4 months (**Figure 4.1B**). In untreated I61Q

mice maintained on standard chow (STD), contractile dysfunction and LV are detectable by 2 months of age (**Supplemental Figure 2.1B, Figure 2.2D**). Therefore, to assess whether developmental suppression alters this trajectory, we examined control (CON) and I61Q at 6 months, allowing for at least 2 months of full transgene expression. Western blots for cTnC and FLAG confirmed robust transgene expression at this timepoint (**Figure 4.1C**). I61Q mice that were given DOX during development expressed ~35% mutant cTnC, compared in ~45% in untreated I61Q mice, a level that modeling predicts is still sufficient to reduce the tension time integral (*290*) (**Figure 4.1D**). Interestingly, isolated myocytes from developmentally suppressed I61Q mice showed preserved contractile function at 6 months. Fractional shortening, time to baseline relaxation, and cell size (area, length, width) were unchanged (**Figure 4.1E-K**). These cells did display a modest reduction in departure velocity accompanied by a corresponding increase in Ca^{2+} release rate (**Figure 4.1E-I**). Echocardiography similarly demonstrated that DOX-treated I61Q mice did not develop reduced ejection fraction, LV dilation, or ventricular hypertrophy by 6 months (**Figure 4.1M-N**). To determine whether developmental suppression prevented DCM entirely or simply delayed its presentation, we aged these mice further. By 8 months, isolated myocytes displayed reduced fractional shortening (**Figure 4.1P**). By 12 months, DOX-treated I61Q mice exhibited decreased LVEF, increased LV diastolic dimension, and increased ventricular mass, though these changes remained attenuated compared to age-matched I61Q mice on standard chow (**Figure 4.1Q-S**). Together, these findings demonstrate that transient suppression of the I61Q cTnC mutation during early development substantially delays both the onset and severity of DCM. This suggests that key disease-initiating processes active during the postnatal window, potentially including fibroblast expansion or ECM remodeling, predispose the myocardium to more rapid and severe dysfunction in adulthood.

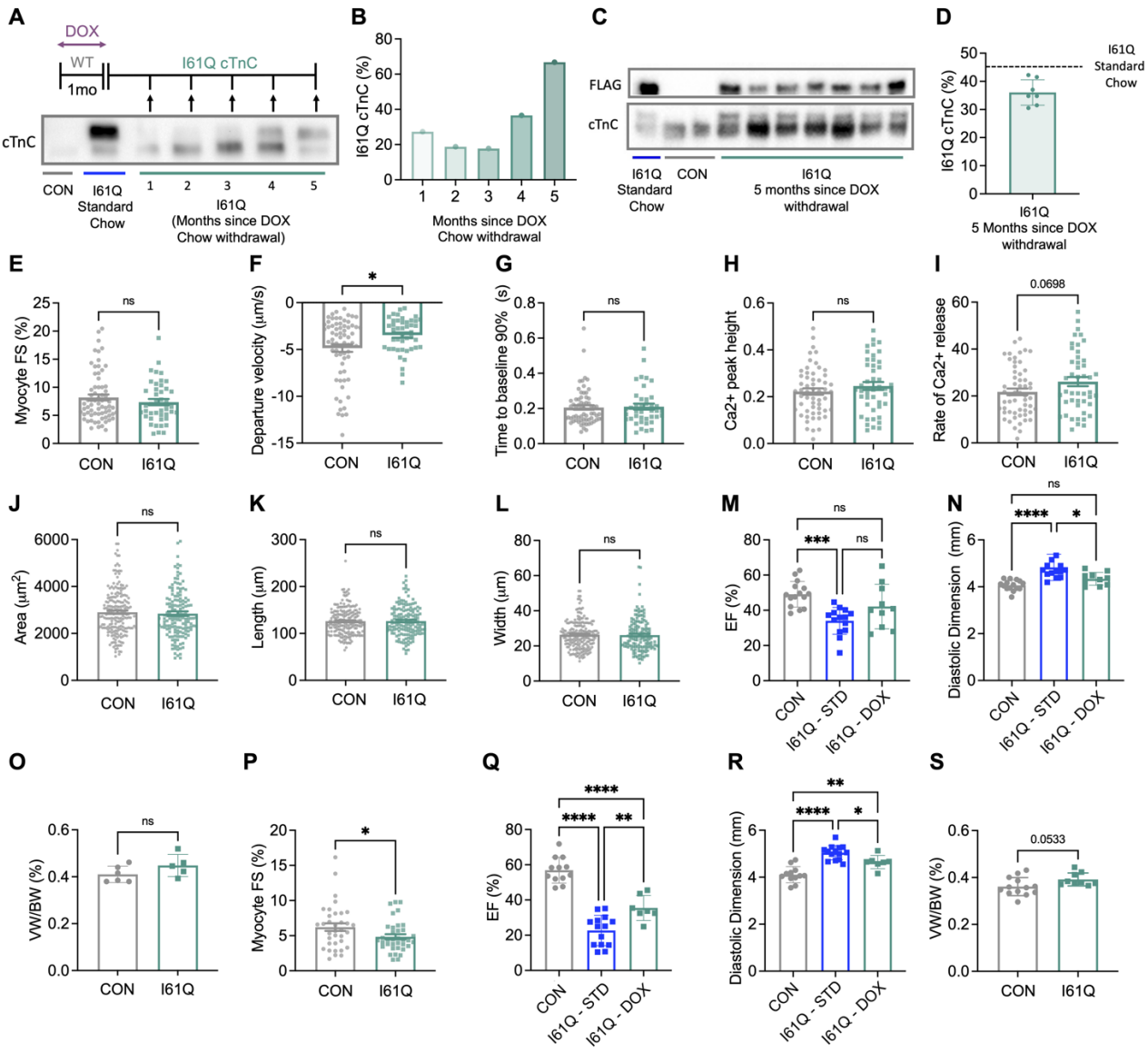

Figure 4.1: Developmental suppression of DCM mutation delays dysfunction. *All mice shown here received doxycycline (DOX) during the first month of life to suppress I61Q cTnC expression, followed by removal from DOX for the indicated durations. In panels M, N, Q, and R, an additional untreated I61Q group on standard chow (STD) is included for comparison (blue).* ***A)*** *Representative western blot and* ***B)*** *quantification showing recovery of I61Q cTnC expression over time after DOX withdrawal.* ***C)*** *Western blots for total cTnC and FLAG, and D) quantification, confirming robust re-expression of I61Q cTnC by 6 months of age (5 months off DOX).* ***E–I)*** *Isolated myocyte measurements from 6-month-old CON and*

I61Q mice: ***E)*** *fractional shortening,* ***F)*** *departure velocity,* ***G)*** *time to 90% baseline,* ***H)*** *Ca^{2+} peak height, and* ***I)*** *rate of Ca^{2+} release (CON N=4, I61Q N=3; CON n=68 myocytes, I61Q n=44; unpaired t-test).* ***J–L)*** *Myocyte morphology:* ***J)*** *area,* ***K)*** *length,* ***L)*** *width (CON n=200 myocytes, I61Q n=150 from the same mice as above; unpaired t-test).* ***M–N)*** *Left ventricular ejection fraction* ***(M)*** *and diastolic dimension* ***(N)*** *at 6 months (CON N=15, I61Q-STD N=14, I61Q-DOX N=10; one-way ANOVA with Tukey post hoc).* ***O)*** *Ventricle weight-to-body weight ratio at 6 months (CON N=6, I61Q N=5; unpaired t-test).* ***P)*** *Myocyte fractional shortening at 8 months (CON n=35, I61Q n=36 myocytes from CON N=2, I61Q N=1; unpaired t-test).* ***Q–R)*** *Left ventricular ejection fraction* ***(Q)*** *and diastolic dimension* ***(R)*** *at 12 months (WT N=12, I61Q-STD N=14, I61Q-STD N=7; one-way ANOVA with Tukey post hoc).* ***S)*** *Ventricle weight-to-body weight ratio at 12 months (CON N=13, I61Q N=9; unpaired t-test).*

4.2.2 Targeting $Postn^+$ fibroblasts during development does not alter DCM onset

Given that a pro-proliferative population $Postn^+$ fibroblasts emerges during postnatal myocardial maturation (*46*) and that I61Q mice show increased Postn protein expression by 2 months of age (**Figure 2.2M**), we hypothesized that this subset of cells may be responsible for the fibroblast expansion observed in our DCM model. As a preliminary test, we stained P14 CON and I61Q heart sections for Postn and PDGFRα (**Figure 4.2A**). $PDGFR\alpha^+$ fibroblasts within $Postn^+$ regions were ~3-fold more abundant in I61Q hearts compared to CON (**Figure 4.2B**), prompting further investigation. To more precisely track $Postn^+$ fibroblast dynamics, we used a lineage tracing approach in Postn-MerCreMer;Rosa26-mTmG mice. Tamoxifen (12.5 mg/kg) was delivered intragastrically at P1, 3, 5, 7, and 9 to cover the proliferative window identified by Hortells et al (**Figure 4.2C**). Mice were aged to P30, stained for PDGFRα, and analyzed for fibroblast subset composition. While total $PDGFR\alpha^+$ fibroblast numbers were higher in I61Q hearts (**Figure 4.2D-E**), the number of Postn-lineage cells were unchanged

(**Figure 4.2F-G**). If anything, the Postn$^+$ fraction trended smaller relative to total fibroblasts (**Figure 4.2H**), suggesting that expansion occurs predominantly in the non-Postn$^+$ fibroblast lineage. This potentially suggests that despite their developmental proliferative capacity, fibroblasts from this Postn$^+$ lineage may have limited proliferative potential later in life.

To determine whether targeting this fibroblast population during development could mitigate disease progression, we genetically deleted p38 MAPK, a pathway previously implicated in regulating fibroblast proliferation (**Figure 2.5**), during the postnatal period (**Figure 4.2J**). At 2 months, I61Q mice lacking p38 in Postn-lineage cells showed no improvement in ejection fraction, ventricular dilation, and diastolic dysfunction (**Figure 4.2K-M**), and ventricular hypertrophy was worsened (**Figure 4.2N**). These results indicate that Postn$^+$ fibroblasts are not the primary drivers of hyperproliferation or disease progression in I61Q mice.

One potential caveat to this data is that although our tamoxifen dose was 25% higher than Hortells et al., subsequent work in our lab suggests that labeling efficiency may be greater at 15-17.5 mg/kg. Thus, incomplete labeling may have limited our ability to detect small changes in this population.

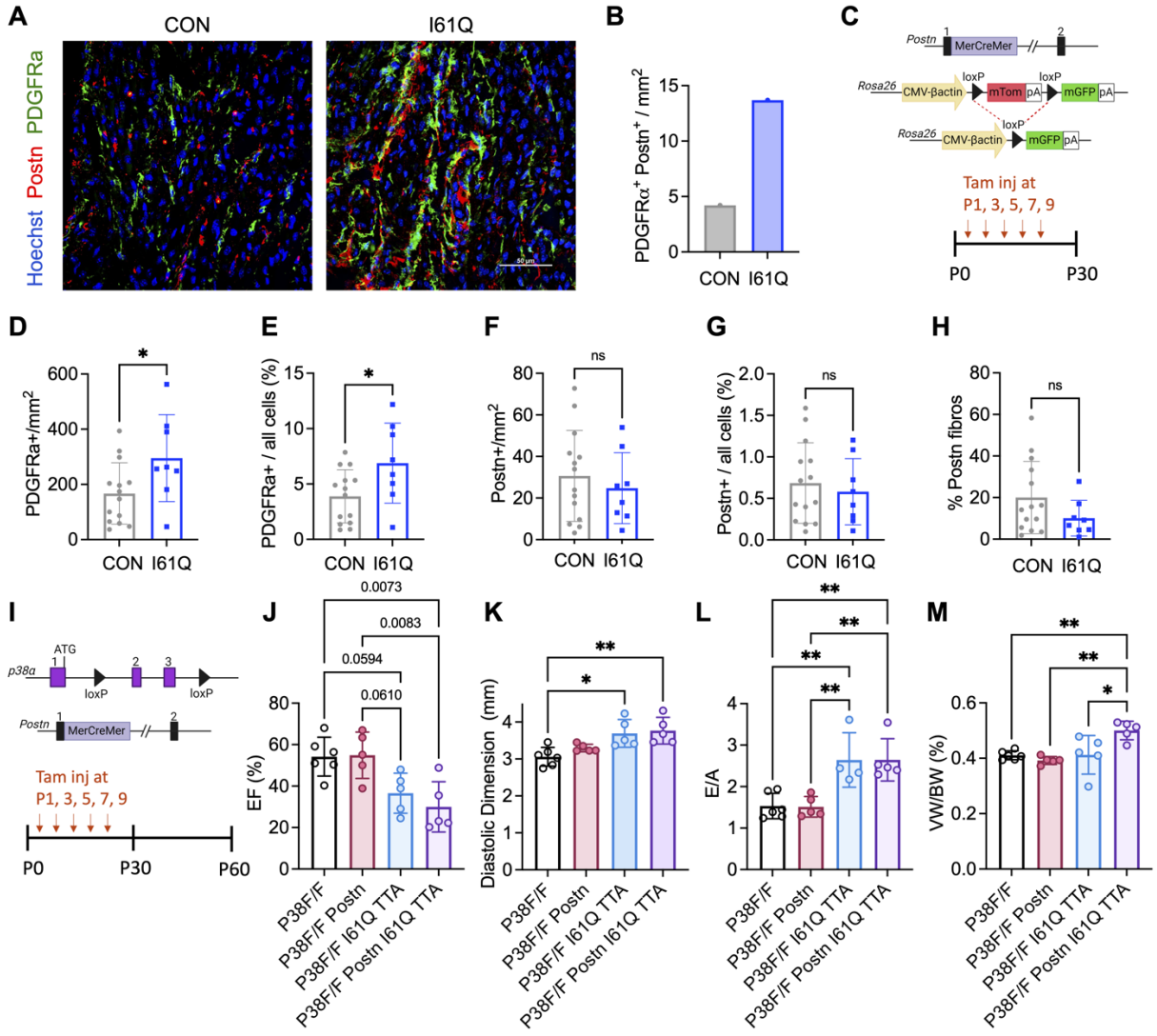

Figure 4.2: Targeting Postn$^+$ fibroblasts during development does not alter DCM onset. A) *Representative images and* ***B)*** *quantification of P14 CON and I61Q heart sections stained for Postn and PDGFRa (N=1 mouse per genotypes).* ***C)*** *Schematic of the Postn-mTmG lineage tracing strategy and tamoxifen dosing regimen.* ***D-G)*** *Quantification of PDGFRA$^+$ and Postn$^+$ lineage-traced fibroblasts, normalized to area (D and F) or total nuclei number (E and G) at 1 month of age.* ***H)*** *Proportion of total fibroblasts derived from the Postn$^+$ lineage. For panels D-H: CON N = 14, I61Q N =8; significance determined by Student's t-test.* ***I)*** *Schematic of p38$^{F/F}$ x Postn-MerCreMer genetic cross and tamoxifen dosing scheme for postnatal knockout.* ***J-L)*** *Echocardiographic measurements at 2months for left*

ventricular ejection fraction (J), diastolic dimension (K), and E/A ratio (L). ***M)*** *Ventricle weight-to-body weight ratio. For panels J-M: $P38^{F/F}$ N = 6, $P38^{F/F}$ Postn N = 5, $P38^{F/F}$ I61Q TTA N=5, $P38^{F/F}$ Postn I61Q TTA N=5; significance determined by one-way ANOVA with Tukey post hoc test.*

4.3 Conclusions and Future Directions

These developmental studies provide new insight into how hypocontraction during the postnatal period shapes the trajectory of dilated cardiomyopathy in adulthood. Transiently suppressing the pathogenic mutation during development substantially delayed the onset of myocyte dysfunction and adverse remodeling. While these mice ultimately developed DCM, the delayed phenotype suggests that pathogenic processes initiated during early myocardial maturation exacerbate disease severity later in life. This finding aligns with the broader conclusion of this dissertation, which is that timing and duration of transgene expression critically influence both the severity of disease and the extent to which the myocardium can recover.

We initially hypothesized that fibroblasts from the $Postn^{+}$ lineage might be a key driver of the early fibroblast expansion in I61Q hearts, and that suppression of the mutant cTnC during development would prevent this expansion and thereby delay disease onset. Preliminary histology appeared consistent with this idea, suggesting increased $PDGFR\alpha^{+}$ fibroblasts in Postn-rich regions. However, lineage tracing revealed that $Postn^{+}$ fibroblasts themselves were not hyperproliferative in DCM. In fact, their proportional contribution to the total fibroblast pool appeared to decline, implying that other fibroblast subsets account for the early expansion. Given that POSTN in the matrix can stimulate fibroblast proliferation (*291*), these findings raise the possibility that fibroblasts proliferate in response to extracellular POSTN deposition rather than arising from a $Postn^{+}$ lineage. Consistent with $Postn^{+}$ cells not being the primary effector

population, development p38 MAPK deletion within this lineage failed to prevent dysfunction, dilation, or hypertrophy. Together, these data indicate that the $Postn^{+}$ developmental fibroblast subset is not the primary driver of early fibroblast expansion or disease initiation in this model, and that inhibiting this pathway during development is not protective.

Overall, these results emphasize that the developmental period is a critical window for shaping long-term cardiac outcomes. However, not all cell populations that are highly active during this window are necessarily culpable in disease initiation, underscoring the need for precise identification of pathogenic drivers before pursuing early-life interventions.

Chapter 5: Appendices

5.1 References

1. Y. Ababio, S. P. Kelly, F. S. Angeli, J. Berghout, K. Huang, K. Liu, S. Burns, C. Senerchia, R. Moccia, G. C. Brooks, Prevalence and Clinical Burden of Idiopathic Dilated Cardiomyopathy in the United States. *Am. J. Med. Open* **10**, 100038 (2023).

2. H.-P. Schultheiss, D. Fairweather, A. L. P. Caforio, F. Escher, R. E. Hershberger, S. E. Lipshultz, P. P. Liu, A. Matsumori, A. Mazzanti, J. McMurray, S. G. Priori, Dilated cardiomyopathy. *Nat. Rev. Dis. Primer* **5**, 1–19 (2019).

3. M. Weigner, J. P. Morgan, "Causes of dilated cardiomyopathy" in *UpToDate*, R. F. Connor, Ed. (Wolters Kluwer, 2024; https://www-uptodate-com.offcampus.lib.washington.edu/contents/causes-of-dilated-cardiomyopathy/print).

4. N. R. | C. E. Hershberger, Dilated cardiomyopathy: the complexity of a diverse genetic architecture. *Nat Rev Cardiol* **10**, 531–547 (2013).

5. E. L. Burkett, R. E. Hershberger, Clinical and genetic issues in familial dilated cardiomyopathy. *J. Am. Coll. Cardiol.* **45**, 969–981 (2005).

6. D. S. Herman, L. Lam, M. R. G. Taylor, L. Wang, P. Teekakirikul, D. Christodoulou, L. Conner, S. R. DePalma, B. McDonough, E. Sparks, D. L. Teodorescu, A. L. Cirino, N. R. Banner, D. J. Pennell, S. Graw, M. Merlo, A. Di Lenarda, G. Sinagra, J. M. Bos, M. J. Ackerman, R. N. Mitchell, C. E. Murry, N. K. Lakdawala, C. Y. Ho, P. J. R. Barton, S. A. Cook, L. Mestroni, J. G. Seidman, C. E. Seidman, Truncations of Titin Causing Dilated Cardiomyopathy. *N. Engl. J. Med.* **366**, 619–628 (2012).

7. E. M. McNally, J. R. Golbus, M. J. Puckelwartz, Genetic mutations and mechanisms in dilated cardiomyopathy. *J. Clin. Invest.* **123**, 19–26 (2013).

8. P. Elliott, C. O'Mahony, P. Syrris, A. Evans, C. Rivera Sorensen, M. N. Sheppard, G. Carr-White, A. Pantazis, W. J. McKenna, Prevalence of desmosomal protein gene mutations in patients with dilated cardiomyopathy. *Circ. Cardiovasc. Genet.* **3**, 314–322 (2010).

9. E. Arbustini, A. Pilotto, A. Repetto, M. Grasso, A. Negri, M. Diegoli, C. Campana, L. Scelsi, E. Baldini, A. Gavazzi, L. Tavazzi, Autosomal dominant dilated cardiomyopathy with atrioventricular block: a lamin A/C defect-related disease. *J. Am. Coll. Cardiol.* **39**, 981–990 (2002).

10. Y. Wang, B. Han, Y. Fan, Y. Yi, J. Lv, J. Wang, X. Yang, D. Jiang, L. Zhao, J. Zhang, H. Yuan, Next-Generation Sequencing Reveals Novel Genetic Variants for Dilated Cardiomyopathy in Pediatric Chinese Patients. *Pediatr. Cardiol.* **43**, 110–120 (2022).

11. Y. Dai, Y. Wang, Y. Fan, B. Han, Genotype-phenotype insights of pediatric dilated cardiomyopathy. *Front. Pediatr.* **13**, 1505830 (2025).

12. C. R. Vissing, K. Espersen, H. L. Mills, E. D. Bartels, R. Jurlander, S. V. Skriver, J. Ghouse, J. J. Thune, A. Axelsson Raja, A. H. Christensen, H. Bundgaard, Family Screening in Dilated Cardiomyopathy. *JACC Heart Fail.* **10**, 792–803 (2022).

13. H.-P. Schultheiss, D. Fairweather, A. L. P. Caforio, F. Escher, R. E. Hershberger, S. E. Lipshultz, P. P. Liu, A. Matsumori, A. Mazzanti, J. McMurray, S. G. Priori, Dilated cardiomyopathy. *Nat. Rev. Dis. Primer* **5**, 1–19 (2019).

14. G. L. Brower, J. D. Gardner, M. F. Forman, D. B. Murray, T. Voloshenyuk, S. P. Levick, J. S. Janicki, The relationship between myocardial extracellular matrix remodeling and ventricular function☆. *Eur. J. Cardiothorac. Surg.* **30**, 604–610 (2006).

15. C. Y. Ho, S. M. Day, S. D. Colan, M. W. Russell, J. Towbin, M. V. Sherrid, C. E. Canter, J. L. Jefferies, A. M. Murphy, A. L. Cirino, T. P. Abraham, M. Taylor, L. Mestroni, D. A. Bluemke, P. Jarolim, L. Shi, L. A. Sleeper, C. E. Seidman, E. J. Orav, The Burden of Early Phenotypes and the Impact of Left Ventricular Wall Thickness on Hypertrophic Cardiomyopathy Sarcomere Mutation Carriers: Findings from the HCMNet Study. *JAMA Cardiol.* **2**, 419–428 (2017).

16. A. E. Deranek, M. M. Klass, J. C. Tardiff, Moving Beyond Simple Answers to Complex Disorders in Sarcomeric Cardiomyopathies: The Role of Integrated Systems. *Pflugers Arch.* **471**, 661–671 (2019).

17. M. J. Greenberg, J. C. Tardiff, Complexity in genetic cardiomyopathies and new approaches for mechanism-based precision medicine. *J. Gen. Physiol.* **153** (2021).

18. J. Davis, L. C. Davis, R. N. Correll, C. A. Makarewich, J. A. Schwanekamp, F. Moussavi-Harami, D. Wang, A. J. York, H. Wu, S. R. Houser, C. E. Seidman, J. G. Seidman, M. Regnier, J. M. Metzger, J. C. Wu, J. D. Molkentin, A Tension-Based Model Distinguishes Hypertrophic versus Dilated Cardiomyopathy. *Cell* **165**, 1147–1159 (2016).

19. H. Ashrafian, C. Redwood, E. Blair, H. Watkins, Hypertrophic cardiomyopathy:a paradigm for myocardial energy depletion. *Trends Genet.* **19**, 263–268 (2003).

20. J. D. Powers, K. B. Kooiker, A. B. Mason, A. E. Teitgen, G. V. Flint, J. C. Tardiff, S. D. Schwartz, A. D. McCulloch, M. Regnier, J. Davis, F. Moussavi-Harami, Modulating the tension-time integral of the cardiac twitch prevents dilated cardiomyopathy in murine hearts. *JCI Insight* **5** (2020).

21. M. Merlo, D. Stolfo, M. Anzini, F. Negri, B. Pinamonti, G. Barbati, F. Ramani, A. D. Lenarda, G. Sinagra, Persistent Recovery of Normal Left Ventricular Function and Dimension in Idiopathic Dilated Cardiomyopathy During Long-Term Follow-up: Does Real Healing Exist? *J. Am. Heart Assoc.* **4**, e001504 (2015).

22. E. Ito, S. Miyagawa, S. Fukushima, Y. Yoshikawa, S. Saito, T. Saito, A. Harada, M. Takeda, N. Kashiyama, Y. Nakamura, M. Shiozaki, K. Toda, Y. Sawa, Histone Modification Is Correlated With Reverse Left Ventricular Remodeling in Nonischemic Dilated Cardiomyopathy. *Ann. Thorac. Surg.* **104**, 1531–1539 (2017).

23. P. G. Rodrigues, A. F. Leite-Moreira, I. Falcão-Pires, Myocardial reverse remodeling: How far can we rewind? *Am. J. Physiol. - Heart Circ. Physiol.* **310**, H1402–H1422 (2016).

24. N. Koitabashi, D. A. Kass, Reverse remodeling in heart failure—mechanisms and therapeutic opportunities. *Nat. Rev. Cardiol. 2012 93* **9**, 147–157 (2011).

25. P. F. Kantor, J. R. Abraham, A. I. Dipchand, L. N. Benson, A. N. Redington, The Impact of Changing Medical Therapy on Transplantation-Free Survival in Pediatric Dilated Cardiomyopathy. *J. Am. Coll. Cardiol.* **55**, 1377–1384 (2010).

26. J. C. Tardiff, L. Carrier, D. M. Bers, C. Poggesi, C. Ferrantini, R. Coppini, L. S. Maier, H. Ashrafian, S. Huke, J. Van Der Velden, Targets for therapy in sarcomeric cardiomyopathies. *Cardiovasc. Res.* **105**, 457–470 (2015).

27. K. Alsulami, S. Marston, Small Molecules Acting on Myofilaments as Treatments for Heart and Skeletal Muscle Diseases. *Int. J. Mol. Sci.* **21**, 1–31 (2020).

28. F. Baudenbacher, T. Schober, J. R. Pinto, V. Y. Sidorov, F. Hilliard, R. J. Solaro, J. D. Potter, B. C. Knollmann, Myofilament Ca^{2+} sensitization causes susceptibility to cardiac arrhythmia in mice. *J. Clin. Invest.* **118**, 3893–3903 (2008).

29. B. P. Morgan, A. Muci, P.-P. Lu, X. Qian, T. Tochimoto, W. W. Smith, M. Garard, E. Kraynack, S. Collibee, I. Suehiro, A. Tomasi, S. C. Valdez, W. Wang, H. Jiang, J. Hartman, H. M. Rodriguez, R. Kawas, S. Sylvester, K. A. Elias, G. Godinez, K. Lee, R. Anderson, S. Sueoka, D. Xu, Z. Wang, N. Djordjevic, F. I. Malik, D. J. Morgans, Discovery of Omecamtiv Mecarbil the First, Selective, Small Molecule Activator of Cardiac Myosin. *ACS Med. Chem. Lett.* **1**, 472–477 (2010).

30. F. I. Malik, B. P. Morgan, Cardiac myosin activation part 1: From concept to clinic. *J. Mol. Cell. Cardiol.* **51**, 454–461 (2011).

31. Y. Liu, H. D. White, B. Belknap, D. A. Winkelmann, E. Forgacs, Omecamtiv Mecarbil Modulates the Kinetic and Motile Properties of Porcine β-Cardiac Myosin. *Biochemistry* **54**, 1963–1975 (2015).

32. J. A. Rohde, D. D. Thomas, J. M. Muretta, Heart failure drug changes the mechanoenzymology of the cardiac myosin powerstroke. *Proc. Natl. Acad. Sci.* **114**, E1796–E1804 (2017).

33. M. S. Woody, M. J. Greenberg, B. Barua, D. A. Winkelmann, Y. E. Goldman, E. M. Ostap, Positive cardiac inotrope omecamtiv mecarbil activates muscle despite suppressing the myosin working stroke. *Nat. Commun.* **9**, 3838 (2018).

34. T. Kampourakis, X. Zhang, Y.-B. Sun, M. Irving, Omecamtiv mercabil and blebbistatin modulate cardiac contractility by perturbing the regulatory state of the myosin filament. *J. Physiol.* **596**, 31–46 (2018).

35. M. S. Utter, D. M. Ryba, B. H. Li, B. M. Wolska, R. J. Solaro, Omecamtiv Mecarbil, a Cardiac Myosin Activator, Increases Ca2+ Sensitivity in Myofilaments With a Dilated Cardiomyopathy Mutant Tropomyosin E54K. *J. Cardiovasc. Pharmacol.* **66**, 347–353 (2015).

36. J. R. Teerlink, G. M. Felker, J. J. V. McMurray, S. D. Solomon, K. F. Adams, J. G. F. Cleland, J. A. Ezekowitz, A. Goudev, P. Macdonald, M. Metra, V. Mitrovic, P. Ponikowski, P. Serpytis, J. Spinar, J. Tomcsányi, H. J. Vandekerckhove, A. A. Voors, M. L. Monsalvo, J. Johnston, F. I. Malik, N. Honarpour, Chronic Oral Study of Myosin Activation to Increase Contractility in Heart

Failure (COSMIC-HF): a phase 2, pharmacokinetic, randomised, placebo-controlled trial. *The Lancet* **388**, 2895–2903 (2016).

37. Teerlink John R., Diaz Rafael, Felker G. Michael, McMurray John J.V., Metra Marco, Solomon Scott D., Adams Kirkwood F., Anand Inder, Arias-Mendoza Alexandra, Biering-Sørensen Tor, Böhm Michael, Bonderman Diana, Cleland John G.F., Corbalan Ramon, Crespo-Leiro Maria G., Dahlström Ulf, Echeverria Luis E., Fang James C., Filippatos Gerasimos, Fonseca Cândida, Goncalvesova Eva, Goudev Assen R., Howlett Jonathan G., Lanfear David E., Li Jing, Lund Mayanna, Macdonald Peter, Mareev Viacheslav, Momomura Shin-ichi, O'Meara Eileen, Parkhomenko Alexander, Ponikowski Piotr, Ramires Felix J.A., Serpytis Pranas, Sliwa Karen, Spinar Jindrich, Suter Thomas M., Tomcsanyi Janos, Vandekerckhove Hans, Vinereanu Dragos, Voors Adriaan A., Yilmaz Mehmet B., Zannad Faiez, Sharpsten Lucie, Legg Jason C., Varin Claire, Honarpour Narimon, Abbasi Siddique A., Malik Fady I., Kurtz Christopher E., Cardiac Myosin Activation with Omecamtiv Mecarbil in Systolic Heart Failure. *N. Engl. J. Med.* **384**, 105–116 (2021).

38. G. M. Felker, S. D. Solomon, B. Claggett, R. Diaz, J. J. V. McMurray, M. Metra, I. Anand, M. G. Crespo-Leiro, U. Dahlström, E. Goncalvesova, J. G. Howlett, P. MacDonald, A. Parkhomenko, J. Tomcsányi, S. A. Abbasi, S. B. Heitner, T. Hucko, S. Kupfer, F. I. Malik, J. R. Teerlink, Assessment of Omecamtiv Mecarbil for the Treatment of Patients With Severe Heart Failure: A Post Hoc Analysis of Data From the GALACTIC-HF Randomized Clinical Trial. *JAMA Cardiol.* **7**, 26–34 (2022).

39. B. S. Wessler, M. McCauley, K. Morine, M. A. Konstam, J. E. Udelson, Relation between therapy-induced changes in natriuretic peptide levels and long-term therapeutic effects on mortality in patients with heart failure and reduced ejection fraction. *Eur. J. Heart Fail.* **21**, 613–620 (2019).

40. M. Vaduganathan, B. Claggett, M. Packer, J. J. V. McMurray, J. L. Rouleau, M. R. Zile, K. Swedberg, S. D. Solomon, Natriuretic Peptides as Biomarkers of Treatment Response in Clinical Trials of Heart Failure. *JACC Heart Fail.* **6**, 564–569 (2018).

41. G. D. Lewis, A. A. Voors, A. Cohen-Solal, M. Metra, D. J. Whellan, J. A. Ezekowitz, M. Böhm, J. R. Teerlink, K. F. Docherty, R. D. Lopes, P. H. Divanji, S. B. Heitner, S. Kupfer, F. I. Malik, L. Meng, A. Wohltman, G. M. Felker, Effect of Omecamtiv Mecarbil on Exercise Capacity in Chronic Heart Failure With Reduced Ejection Fraction: The METEORIC-HF Randomized Clinical Trial. *JAMA* **328**, 259–269 (2022).

42. K. B. Kooiker, S. Mohran, K. L. Turner, W. Ma, A. Martinson, G. Flint, L. Qi, C. Gao, Y. Zheng, T. S. McMillen, C. Mandrycky, M. Mahoney-Schaefer, J. C. Freeman, E. G. Costales Arenas, A.-Y. Tu, T. C. Irving, M. A. Geeves, B. C. W. Tanner, M. Regnier, J. Davis, F. Moussavi-Harami, Danicamtiv Increases Myosin Recruitment and Alters Cross-Bridge Cycling in Cardiac Muscle. *Circ. Res.* **133**, 430–443 (2023).

43. A. A. Voors, J. Tamby, J. G. Cleland, M. Koren, L. B. Forgosh, D. Gupta, L. H. Lund, A. Camacho, R. Karra, H. P. Swart, P. Pellicori, F. Wagner, R. E. Hershberger, N. Prasad, R. Anderson, A. Anto, K. Bell, J. M. Edelberg, L. Fang, M. Henze, C. Kelly, G. Kurio, W. Li, K. Wells, C. Yang, S. L. Teichman, C. L. del Rio, S. D. Solomon, Effects of danicamtiv, a novel cardiac myosin activator, in heart failure with reduced ejection fraction: experimental data and clinical results from a phase 2a trial. *Eur. J. Heart Fail.* **22**, 1649–1658 (2020).

44. Bristol-Myers Squibb, “An Open-Label, Exploratory Study of the Safety and Preliminary Efficacy of Danicamtiv in Stable Ambulatory Participants With Primary Dilated Cardiomyopathy Due to Either MYH7 or TTN Variants or Other Causalities” (Clinical trial registration NCT04572893, clinicaltrials.gov, 2025); https://clinicaltrials.gov/study/NCT04572893.

45. H. He, T. Baka, J. Balschi, A. S. Motani, K. K. Nguyen, Q. Liu, R. Slater, B. Rock, C. Wang, C. Hale, G. Karamanlidis, J. J. Hartman, F. I. Malik, J. D. Reagan, I. Luptak, Novel Small-Molecule Troponin Activator Increases Cardiac Contractile Function Without Negative Impact on Energetics. *Circ. Heart Fail.* **15**, e009195 (2021).

46. L. Hortells, I. Valiente-Alandi, Z. M. Thomas, E. J. Agnew, D. J. Schnell, A. J. York, R. J. Vagnozzi, E. C. Meyer, J. D. Molkentin, K. E. Yutzey, A specialized population of Periostin-expressing cardiac fibroblasts contributes to postnatal cardiomyocyte maturation and innervation. *Proc. Natl. Acad. Sci. U. S. A.* **117**, 21469–21479 (2020).

47. I. M. Reichardt, K. Z. Robeson, M. Regnier, J. Davis, Controlling cardiac fibrosis through fibroblast state space modulation. *Cell. Signal.* **79**, 109888 (2021).

48. N. L. Thompson, F. Bazoberry, E. H. Speir, W. Casscells, V. J. Ferrans, K. C. Flanders, P. Kondaiah, A. G. Geiser, M. B. Sporn, Transforming growth factor beta-1 in acute myocardial infarction in rats. *Growth Factors Chur Switz.* **1**, 91–99 (1988).

49. M. Wünsch, H. S. Sharma, T. Markert, S. Bernotat-Danielowski, R. J. Schott, P. Kremer, N. Bleese, W. Schaper, In situ localization of transforming growth factor beta 1 in porcine heart: enhanced expression after chronic coronary artery constriction. *J. Mol. Cell. Cardiol.* **23**, 1051–1062 (1991).

50. H. Khalil, O. Kanisicak, V. Prasad, R. N. Correll, X. Fu, T. Schips, R. J. Vagnozzi, R. Liu, T. Huynh, S. J. Lee, J. Karch, J. D. Molkentin, Fibroblast-specific TGF-β-Smad2/3 signaling underlies cardiac fibrosis. *J. Clin. Invest.* **127**, 3770–3783 (2017).

51. J. E. Cartledge, C. Kane, P. Dias, M. Tesfom, L. Clarke, B. Mckee, S. Al Ayoubi, A. Chester, M. H. Yacoub, P. Camelliti, C. M. Terracciano, Functional crosstalk between cardiac fibroblasts and adult cardiomyocytes by soluble mediators. *Cardiovasc. Res.* **105**, 260–270 (2015).

52. J. A. Fontes, N. R. Rose, D. Čihák̆ová, The varying faces of IL-6: from cardiac protection to cardiac failure. *Cytokine* **74**, 62–68 (2015).

53. S. Fredj, J. Bescond, C. Louault, A. Delwail, J. Lecron, D. Potreau, Role of interleukin-6 in cardiomyocyte/cardiac fibroblast interactions during myocyte hypertrophy and fibroblast proliferation. *J. Cell. Physiol.* **204**, 428–436 (2005).

54. S. Sanada, D. Hakuno, L. J. Higgins, E. R. Schreiter, A. N. J. McKenzie, R. T. Lee, IL-33 and ST2 comprise a critical biomechanically induced and cardioprotective signaling system. *J. Clin. Invest.* **117**, 1538–1549 (2007).

55. Y. Zhang, E. M. Kanter, J. G. Laing, C. Aprhys, D. C. Johns, E. Kardami, K. A. Yamada, Connexin43 Expression Levels Influence Intercellular Coupling and Cell Proliferation of Native Murine Cardiac Fibroblasts. *Cell Commun. Adhes.* **15**, 289–303 (2008).

56. M. B. Rook, H. J. Jongsma, B. de Jonge, Single channel currents of homo- and heterologous gap junctions between cardiac fibroblasts and myocytes. *Pflüg. Arch.* **414**, 95–98 (1989).

57. P. Camelliti, C. R. Green, I. LeGrice, P. Kohl, Fibroblast Network in Rabbit Sinoatrial Node. *Circ. Res.* **94**, 828–835 (2004).

58. E. Ongstad, P. Kohl, Fibroblast-Myocyte Coupling in the Heart: Potential Relevance for Therapeutic Interventions. *J. Mol. Cell. Cardiol.* **91**, 238–246 (2016).

59. P. Camelliti, G. P. Devlin, K. G. Matthews, P. Kohl, C. R. Green, Spatially and temporally distinct expression of fibroblast connexins after sheep ventricular infarction. *Cardiovasc. Res.* **62**, 415–425 (2004).

60. Y. W. Liu, B. Chen, X. Yang, J. A. Fugate, F. A. Kalucki, A. Futakuchi-Tsuchida, L. Couture, K. W. Vogel, C. A. Astley, A. Baldessari, J. Ogle, C. W. Don, Z. L. Steinberg, S. P. Seslar, S. A. Tuck, H. Tsuchida, A. V. Naumova, S. K. Dupras, M. S. Lyu, J. Lee, D. W. Hailey, H. Reinecke, L. Pabon, B. H. Fryer, W. R. MacLellan, R. S. Thies, C. E. Murry, Human embryonic stem cell-derived cardiomyocytes restore function in infarcted hearts of non-human primates. *Nat. Biotechnol.* **36**, 597–605 (2018).

61. A. J. Engler, C. Carag-Krieger, C. P. Johnson, M. Raab, H.-Y. Tang, D. W. Speicher, J. W. Sanger, J. M. Sanger, D. E. Discher, Embryonic cardiomyocytes beat best on a matrix with heart-like elasticity: scar-like rigidity inhibits beating. *J. Cell Sci.* **121**, 3794–3802 (2008).

62. M. F. Berry, A. J. Engler, Y. J. Woo, T. J. Pirolli, L. T. Bish, V. Jayasankar, K. J. Morine, T. J. Gardner, D. E. Discher, H. L. Sweeney, Mesenchymal stem cell injection after myocardial infarction improves myocardial compliance. *Am. J. Physiol.-Heart Circ. Physiol.* **290**, H2196–H2203 (2006).

63. S. Querceto, R. Santoro, A. Gowran, B. Grandinetti, G. Pompilio, M. Regnier, C. Tesi, C. Poggesi, C. Ferrantini, J. M. Pioner, The harder the climb the better the view: The impact of substrate stiffness on cardiomyocyte fate. *J. Mol. Cell. Cardiol.* **166**, 36–49 (2022).

64. J. Solon, I. Levental, K. Sengupta, P. C. Georges, P. A. Janmey, Fibroblast Adaptation and Stiffness Matching to Soft Elastic Substrates. *Biophys. J.* **93**, 4453–4461 (2007).

65. B. P. Halliday, A. Gulati, A. Ali, K. Guha, S. Newsome, M. Arzanauskaite, V. S. Vassiliou, A. Lota, C. Izgi, U. Tayal, Z. Khalique, C. Stirrat, D. Auger, N. Pareek, T. F. Ismail, S. D. Rosen, A. Vazir, F. Alpendurada, J. Gregson, M. P. Frenneaux, M. R. Cowie, J. G. F. Cleland, S. A. Cook, D. J. Pennell, S. K. Prasad, Association between midwall late gadolinium enhancement and sudden cardiac death in patients with dilated cardiomyopathy and mild and moderate left ventricular systolic dysfunction. *Circulation* **135**, 2106–2115 (2017).

66. M. M. H. Marijianowski, P. Teeling, J. Mann, A. E. Becker, Dilated cardiomyopathy is associated with an increase in the type I/type III collagen ratio: A quantitative assessment. *J. Am. Coll. Cardiol.* **25**, 1263–1272 (1995).

67. J. G. Travers, S. A. Wennersten, B. Peña, R. A. Bagchi, H. E. Smith, R. A. Hirsch, L. A. Vanderlinden, Y. H. Lin, E. Dobrinskikh, K. M. Demos-Davies, M. A. Cavasin, L. Mestroni, C. Steinkühler, C. Y. Lin, S. R. Houser, K. C. Woulfe, M. P. Y. Lam, T. A. McKinsey, HDAC

Inhibition Reverses Preexisting Diastolic Dysfunction and Blocks Covert Extracellular Matrix Remodeling. *Circulation* **143**, 1874–1890 (2021).

68. P. Sivakumar, S. Gupta, S. Sarkar, S. Sen, Upregulation of lysyl oxidase and MMPs during cardiac remodeling in human dilated cardiomyopathy. *Mol. Cell. Biochem.* **307**, 159–167 (2007).

69. N. Verzijl, J. DeGroot, S. R. Thorpe, R. A. Bank, J. N. Shaw, T. J. Lyons, J. W. Bijlsma, F. P. Lafeber, J. W. Baynes, J. M. TeKoppele, Effect of collagen turnover on the accumulation of advanced glycation end products. *J. Biol. Chem.* **275**, 39027–39031 (2000).

70. M. D. Tallquist, J. D. Molkentin, Redefining the identity of cardiac fibroblasts. Nature Publishing Group [Preprint] (2017). https://doi.org/10.1038/nrcardio.2017.57.

71. X. Fu, H. Khalil, O. Kanisicak, J. G. Boyer, R. J. Vagnozzi, B. D. Maliken, M. A. Sargent, V. Prasad, I. Valiente-Alandi, B. C. Blaxall, J. D. Molkentin, Specialized fibroblast differentiated states underlie scar formation in the infarcted mouse heart. *J. Clin. Invest.* **128**, 2127–2143 (2018).

72. N. Farbehi, R. Patrick, A. Dorison, M. Xaymardan, V. Janbandhu, K. Wystub-Lis, J. W. K. Ho, R. E. Nordon, R. P. Harvey, Single-cell expression profiling reveals dynamic flux of cardiac stromal, vascular and immune cells in health and injury. *eLife* **8**, e43882 (2019).

73. M. A. McLellan, D. A. Skelly, M. S. I. Dona, G. T. Squiers, G. E. Farrugia, T. L. Gaynor, C. D. Cohen, R. Pandey, H. Diep, A. Vinh, N. A. Rosenthal, A. R. Pinto, High-Resolution Transcriptomic Profiling of the Heart During Chronic Stress Reveals Cellular Drivers of Cardiac Fibrosis and Hypertrophy. *Circulation*, doi: 10.1161/circulationaha.119.045115 (2020).

74. D. A. Skelly, G. T. Squiers, M. A. McLellan, M. T. Bolisetty, P. Robson, N. A. Rosenthal, A. R. Pinto, Single-Cell Transcriptional Profiling Reveals Cellular Diversity and Intercommunication in the Mouse Heart. *Cell Rep.* **22**, 600–610 (2018).

75. C. H. Waddington, *The Principles of Embryology* (Routledge, 1st Editio., 2017).

76. M. B. Fagan, Waddington redux: Models and explanation in stem cell and systems biology. *Biol. Philos.* **27**, 179–213 (2012).

77. C. Marr, J. X. Zhou, S. Huang, Single-cell gene expression profiling and cell state dynamics: Collecting data, correlating data points and connecting the dots. Elsevier Ltd [Preprint] (2016). https://doi.org/10.1016/j.copbio.2016.04.015.

78. R. Bretherton, D. Bugg, E. Olszewski, J. Davis, Regulators of cardiac fibroblast cell state. *Matrix Biol.*, doi: 10.1016/j.matbio.2020.04.002 (2020).

79. O. Kanisicak, H. Khalil, M. J. Ivey, J. Karch, B. D. Maliken, R. N. Correll, M. J. Brody, S.-C. J. Lin, B. J. Aronow, M. D. Tallquist, J. D. Molkentin, Genetic lineage tracing defines myofibroblast origin and function in the injured heart. *Nat. Commun.* **7**, 12260 (2016).

80. Y. Xiao, M. C. Hill, M. Zhang, T. J. Martin, Y. Morikawa, A. R. Moise, J. D. Wythe, J. F. Martin, Hippo signaling plays an essential role in cell state transitions during cardiac fibroblast development. *Dev. Cell* **45**, 153–169 (2019).

81. D. Bugg, R. C. Bretherton, P. Kim, E. Olszewski, A. Nagle, A. E. Schumacher, N. Chu, J. Gunaje, C. A. DeForest, K. Stevens, D.-H. Kim, J. M. Davis, Infarct Collagen Topography Regulates Fibroblast Fate Via p38-Yap-TEAD Signals. *Circ. Res.*, 1306–1322 (2020).

82. J. D. Molkentin, D. Bugg, N. Ghearing, L. E. Dorn, P. Kim, M. A. Sargent, J. Gunaje, K. Otsu, J. Davis, Fibroblast-specific genetic manipulation of p38 MAPK in vivo reveals its central regulatory role in fibrosis. *Circulation* **136**, 549–561 (2018).

83. Y. Zhou, Z. Liu, J. D. Welch, X. Gao, L. Wang, T. Garbutt, B. Keepers, H. Ma, J. F. Prins, W. Shen, J. Liu, L. Qian, Single-Cell Transcriptomic Analyses of Cell Fate Transitions during Human Cardiac Reprogramming. *Cell Stem Cell* **25**, 149-164.e9 (2019).

84. J. Cao, W. Zhou, F. Steemers, C. Trapnell, J. Shendure, Sci-fate characterizes the dynamics of gene expression in single cells. *Nat. Biotechnol.* **38**, 980–988 (2020).

85. A. Olsson, M. Venkatasubramanian, V. K. Chaudhri, B. J. Aronow, N. Salomonis, H. Singh, H. L. Grimes, Single-cell analysis of mixed-lineage states leading to a binary cell fate choice. *Nature* **537**, 698–702 (2016).

86. M. Mojtahedi, A. Skupin, J. Zhou, I. G. Castaño, R. Y. Y. Leong-Quong, H. Chang, K. Trachana, A. Giuliani, S. Huang, Cell Fate Decision as High-Dimensional Critical State Transition. *PLoS Biol.* **14**, 1–28 (2016).

87. B. Hinz, S. H. Phan, V. J. Thannickal, A. Galli, M. L. Bochaton-Piallat, G. Gabbiani, The myofibroblast: One function, multiple origins. *Am. J. Pathol.* **170**, 1807–1816 (2007).

88. J. R. Crawford, S. B. Haudek, K. A. Cieslik, J. Trial, M. L. Entman, Origin of developmental precursors dictates the pathophysiologic role of cardiac fibroblasts. *J Cardiovasc. Transl. Res.* **5**, 749–759 (2012).

89. S. B. Haudek, J. Cheng, J. Du, Y. Wang, J. Hermosillo-Rodriguez, J. A. Trial, G. E. Taffet, M. L. Entman, Monocytic fibroblast precursors mediate fibrosis in angiotensin-II-induced cardiac hypertrophy. *J. Mol. Cell. Cardiol.* **49**, 499–507 (2010).

90. S. B. Haudek, J. A. Trial, Y. Xia, D. Gupta, D. Pilling, M. L. Entman, Fc receptor engagement mediates differentiation of cardiac fibroblast precursor cells. *Proc. Natl. Acad. Sci. U. S. A.* **105**, 10179–10184 (2008).

91. S. B. Haudek, Y. Xia, P. Huebener, J. M. Lee, S. Carlson, J. R. Crawford, D. Pilling, R. H. Gomer, J. A. Trial, N. G. Frangogiannis, M. L. Entman, Bone marrow-derived fibroblast precursors mediate ischemic cardiomyopathy in mice. *Proc. Natl. Acad. Sci. U. S. A.* **103**, 18284–18289 (2006).

92. A. Moeller, S. E. Gilpin, K. Ask, G. Cox, D. Cook, J. Gauldie, P. J. Margetts, L. Farkas, J. Dobranowski, C. Boylan, P. M. O'Byrne, R. M. Strieter, M. Kolb, Circulating fibrocytes are an indicator of poor prognosis in idiopathic pulmonary fibrosis. *Am. J. Respir. Crit. Care Med.* **179**, 588–594 (2009).

93. A. Acharya, S. T. Baek, G. Huang, B. Eskiocak, S. Goetsch, C. Y. Sung, S. Banfi, M. F. Sauer, G. S. Olsen, J. S. Duffield, E. N. Olson, M. D. Tallquist, The bHLH transcription factor Tcf21 is

required for lineage-specific EMT of cardiac fibroblast progenitors. *Development* **139**, 2139–2149 (2012).

94. T. Moore-Morris, N. Guimarães-Camboa, I. Banerjee, A. C. Zambon, T. Kisseleva, A. Velayoudon, W. B. Stallcup, Y. Gu, N. D. Dalton, M. Cedenilla, R. Gomez-Amaro, B. Zhou, D. A. Brenner, K. L. Peterson, J. Chen, S. M. Evans, Resident fibroblast lineages mediate pressure overload-induced cardiac fibrosis. *J. Clin. Invest.* **124**, 2921–2934 (2014).

95. M. B. Furtado, M. W. Costa, E. A. Pranoto, E. Salimova, A. R. Pinto, N. T. Lam, A. Park, P. Snider, A. Chandran, R. P. Harvey, R. Boyd, S. J. Conway, J. Pearson, D. M. Kaye, N. A. Rosenthal, Cardiogenic genes expressed in cardiac fibroblasts contribute to heart development and repair. *Circ. Res.* **114**, 1422–1434 (2014).

96. S. R. Ali, S. Ranjbarvaziri, M. Talkhabi, P. Zhao, A. Subat, A. Hojjat, P. Kamran, A. M. S. Müller, K. S. Volz, Z. Tang, K. Red-Horse, R. Ardehali, Developmental heterogeneity of cardiac fibroblasts does not predict pathological proliferation and activation. *Circ. Res.* **115**, 625–635 (2014).

97. A. R. Pinto, A. Ilinykh, M. J. Ivey, J. T. Kuwabara, M. L. D'Antoni, R. Debuque, A. Chandran, L. Wang, K. Arora, N. A. Rosenthal, M. D. Tallquist, Revisiting Cardiac Cellular Composition. *Circ. Res.* **118**, 400–409 (2016).

98. H. Kaur, M. Takefuji, C. Y. Ngai, J. Carvalho, J. Bayer, A. Wietelmann, A. Poetsch, S. Hoelper, S. J. Conway, H. Möllmann, M. Looso, C. Troidl, S. Offermanns, N. Wettschureck, Targeted Ablation of Periostin-Expressing Activated Fibroblasts Prevents Adverse Cardiac Remodeling in Mice. *Circ. Res.* **118**, 1906–1917 (2016).

99. J. J. Tomasek, G. Gabbiani, B. Hinz, C. Chaponnier, R. A. Brown, Myofibroblasts and mechano-regulation of connective tissue remodelling. *Nat. Rev. Mol. Cell Biol.* **3**, 349–363 (2002).

100. J. D. Molkentin, D. Bugg, N. Ghearing, L. E. Dorn, P. Kim, M. A. Sargent, J. Gunaje, K. Otsu, J. Davis, Fibroblast-specific genetic manipulation of p38 MAPK in vivo reveals its central regulatory role in fibrosis. *Circulation* **136**, 549–561 (2018).

101. N. Dhanesha, M. R. Chorawala, M. Jain, A. Bhalla, D. Thedens, M. Nayak, P. Doddapattar, A. K. Chauhan, Fn-EDA (Fibronectin Containing Extra Domain A) in the Plasma, but Not Endothelial Cells, Exacerbates Stroke Outcome by Promoting Thrombo-Inflammation. *Stroke* **50**, 1201–1209 (2019).

102. M. J. Ivey, J. T. Kuwabara, K. L. Riggsbee, M. D. Tallquist, Platelet derived growth factor receptor alpha is essential for cardiac fibroblast survival. *Am. J. Physiol.-Heart Circ. Physiol.*, doi: 10.1152/ajpheart.00054.2019 (2019).

103. G. Takemura, M. Ohno, Y. Hayakawa, J. Misao, M. Kanoh, A. Ohno, Y. Uno, S. Minatoguchi, T. Fujiwara, H. Fujiwara, Role of Apoptosis in the Disappearance of Infiltrated and Proliferated Interstitial Cells After Myocardial Infarction. *Circ. Res.* **82**, 1130–1138 (1998).

104. W. Zhao, L. Lu, S. S. Chen, Y. Sun, Temporal and spatial characteristics of apoptosis in the infarcted rat heart. *Biochem. Biophys. Res. Commun.* **325**, 605–611 (2004).

105. J. P. Coppé, P. Y. Desprez, A. Krtolica, J. Campisi, The senescence-associated secretory phenotype: The dark side of tumor suppression. NIH Public Access [Preprint] (2010). https://doi.org/10.1146/annurev-pathol-121808-102144.

106. F. Zhu, Y. Li, J. Zhang, C. Piao, T. Liu, H. H. Li, J. Du, Senescent cardiac fibroblast is critical for cardiac fibrosis after myocardial infarction. *PloS One* **8** (2013).

107. N. G. Frangogiannis, Cardiac fibrosis: Cell biological mechanisms, molecular pathways and therapeutic opportunities. *Mol. Aspects Med.* **65**, 70–99 (2019).

108. E. Bassat, Y. E. Mutlak, A. Genzelinakh, I. Y. Shadrin, K. Baruch Umansky, O. Yifa, D. Kain, D. Rajchman, J. Leach, D. Riabov Bassat, Y. Udi, R. Sarig, I. Sagi, J. F. Martin, N. Bursac, S. Cohen, E. Tzahor, The extracellular matrix protein agrin promotes heart regeneration in mice. *Nature* **547**, 179–184 (2017).

109. P. Pakshir, M. Alizadehgiashi, B. Wong, N. M. Coelho, X. Chen, Z. Gong, V. B. Shenoy, C. McCulloch, B. Hinz, Dynamic fibroblast contractions attract remote macrophages in fibrillar collagen matrix. *Nat. Commun.* **10**, 1850 (2019).

110. F. Perbellini, S. A. Watson, I. Bardi, C. M. Terracciano, Heterocellularity and Cellular Cross-Talk in the Cardiovascular System. *Front. Cardiovasc. Med.* **5** (2018).

111. K. Fountoulaki, N. Dagres, E. K. Iliodromitis, Cellular Communications in the Heart. *Card. Fail. Rev.* **1**, 64–68 (2015).

112. H. Khalil, O. Kanisicak, V. Prasad, R. N. Correll, X. Fu, T. Schips, R. J. Vagnozzi, R. Liu, T. Huynh, S. J. Lee, J. Karch, J. D. Molkentin, "Fibroblast-specific TGF-β-Smad2/3 signaling underlies cardiac fibrosis" in *Journal of Clinical Investigation* (American Society for Clinical Investigation, 2017)vol. 127, pp. 3770–3783.

113. M. Bujak, G. Ren, H. J. Kweon, M. Dobaczewski, A. Reddy, G. Taffet, X. F. Wang, N. G. Frangogiannis, Essential role of Smad3 in infarct healing and in the pathogenesis of cardiac remodeling. *Circulation* **116**, 2127–2138 (2007).

114. P. Kong, A. V. Shinde, Y. Su, I. Russo, B. Chen, A. Saxena, S. J. Conway, J. M. Graff, N. G. Frangogiannis, Opposing actions of fibroblast and cardiomyocyte smad3 signaling in the infarcted myocardium. *Circulation* **137**, 707–724 (2018).

115. V. Divakaran, J. Adrogue, M. Ishiyama, M. L. Entman, S. Haudek, N. Sivasubramanian, D. L. Mann, Adaptive and maladptive effects of SMAD3 signaling in the adult heart after hemodynamic pressure overloading. *Circ. Heart Fail.* **2**, 633–642 (2009).

116. R. A. Bagchi, P. Roche, N. Aroutiounova, L. Espira, B. Abrenica, R. Schweitzer, M. P. Czubryt, The transcription factor scleraxis is a critical regulator of cardiac fibroblast phenotype. *BMC Biol.* **14**, 3–6 (2016).

117. R. A. Bagchi, M. P. Czubryt, Synergistic roles of scleraxis and Smads in the regulation of collagen 1α2 gene expression. *Biochim. Biophys. Acta - Mol. Cell Res.* **1823**, 1936–1944 (2012).

118. N. Koitabashi, T. Danner, A. L. Zaiman, Y. M. Pinto, J. Rowell, J. Mankowski, D. Zhang, T. Nakamura, E. Takimoto, D. A. Kass, Pivotal role of cardiomyocyte TGF-β signaling in the murine pathological response to sustained pressure overload. *J. Clin. Invest.* **121**, 2301–2312 (2011).

119. J. Davis, A. R. Burr, G. F. Davis, L. Birnbaumer, J. D. Molkentin, A TRPC6-Dependent Pathway for Myofibroblast Transdifferentiation and Wound Healing In Vivo. *Dev. Cell* **23**, 705–715 (2012).

120. D. Bugg, R. C. Bretherton, P. Kim, E. Olszewski, A. Nagle, A. E. Schumacher, N. Chu, J. Gunaje, C. A. DeForest, K. Stevens, D.-H. Kim, J. M. Davis, Infarct Collagen Topography Regulates Fibroblast Fate Via p38-Yap-TEAD Signals. *Circ. Res.*, 1306–1322 (2020).

121. W. J. Richardson, J. W. Holmes, Emergence of Collagen Orientation Heterogeneity in Healing Infarcts and an Agent-Based Model. *Biophys. J.* **110**, 2266–2277 (2016).

122. Y. Xiao, M. C. Hill, L. Li, V. Deshmukh, T. J. Martin, J. Wang, J. F. Martin, Hippo pathway deletion in adult resting cardiac fibroblasts initiates a cell state transition with spontaneous and self-sustaining fibrosis. *Genes Dev.* **33**, 1491–1505 (2019).

123. D. Bugg, R. C. Bretherton, P. Kim, E. Olszewski, A. Nagle, A. E. Schumacher, N. Chu, J. Gunaje, C. A. DeForest, K. Stevens, D.-H. Kim, J. M. Davis, Infarct Collagen Topography Regulates Fibroblast Fate Via p38-Yap-TEAD Signals. *Circ. Res.*, 1306–1322 (2020).

124. Z. P. Liu, Z. Wang, H. Yanagisawa, E. N. Olson, Phenotypic modulation of smooth muscle cells through interaction of Foxo4 and Myocardin. *Dev. Cell* **9**, 261–270 (2005).

125. E. M. Small, J. E. Thatcher, L. B. Sutherland, H. Kinoshita, R. D. Gerard, J. A. Richardson, J. M. Dimaio, H. Sadek, K. Kuwahara, E. N. Olson, Myocardin-related transcription factor-a controls myofibroblast activation and fibrosis in response to myocardial infarction. *Circ. Res.* **107**, 294–304 (2010).

126. E. M. Small, The Actin-MRTF-SRF gene regulatory axis and myofibroblast differentiation. *J Cardiovasc. Transl. Res.* **5**, 794–804 (2012).

127. K. Kuwahara, Y. Wang, J. McAnally, J. A. Richardson, R. Bassel-Duby, J. A. Hill, E. N. Olson, TRPC6 fulfills a calcineurin signaling circuit during pathologic cardiac remodeling. *J. Clin. Invest.* **116**, 3114–3126 (2006).

128. J. Francisco, Y. Zhang, J. I. Jeong, W. Mizushima, S. Ikeda, A. Ivessa, S. Oka, P. Zhai, M. D. Tallquist, D. P. Del Re, Blockade of Fibroblast YAP Attenuates Cardiac Fibrosis and Dysfunction Through MRTF-A Inhibition. *JACC Basic Transl. Sci.* **5**, 931–945 (2020).

129. A. R. Perestrelo, A. C. Silva, J. O. La Cruz, F. Martino, V. Horváth, G. Caluori, O. Polanský, V. Vinarský, G. Azzato, D. Marco, V. Žampachová, P. Skládal, S. Pagliari, A. Rainer, P. Pinto-do-, Multiscale Analysis of Extracellular Matrix Remodeling in the Failing Heart. *Circ. Res.*, doi: 10.1161/CIRCRESAHA.120.317685 (2020).

130. D. P. Del Re, Y. Yang, N. Nakano, J. Cho, P. Zhai, T. Yamamoto, N. Zhang, N. Yabuta, H. Nojima, D. Pan, J. Sadoshima, Yes-associated protein isoform 1 (Yapl) promotes cardiomyocyte survival and growth to protect against myocardial ischemic injury. *J. Biol. Chem.* **288**, 3977–3988 (2013).

131. M. Xin, Y. Kim, L. B. Sutherland, M. Murakami, X. Qi, J. McAnally, E. R. Porrello, A. I. Mahmoud, W. Tan, J. M. Shelton, J. A. Richardson, H. A. Sadek, R. Bassel-Duby, E. N. Olson, Hippo pathway effector Yap promotes cardiac regeneration. *Proc. Natl. Acad. Sci. U. S. A.* **110**, 13839–13844 (2013).

132. Z. Liu, L. Wang, J. D. Welch, H. Ma, Y. Zhou, H. R. Vaseghi, S. Yu, J. B. Wall, S. Alimohamadi, M. Zheng, C. Yin, W. Shen, J. F. Prins, J. Liu, L. Qian, Single-cell transcriptomics reconstructs fate conversion from fibroblast to cardiomyocyte. *Nature* **551**, 100–104 (2017).

133. E. B. Schelbert, L. Y. Hsu, S. A. Anderson, B. D. Mohanty, S. M. Karim, P. Kellman, A. H. Aletras, A. E. Arai, Late gadolinium-enhancement cardiac magnetic resonance identifies postinfarction myocardial fibrosis and the border zone at the near cellular level in ex vivo rat heart. *Circ. Cardiovasc. Imaging* **3**, 743–752 (2010).

134. S. Orn, C. Manhenke, I. S. Anand, I. Squire, E. Nagel, T. Edvardsen, K. Dickstein, Effect of Left Ventricular Scar Size, Location, and Transmurality on Left Ventricular Remodeling With Healed Myocardial Infarction. *Am. J. Cardiol.* **99**, 1109–1114 (2007).

135. J. D. Molkentin, D. Bugg, N. Ghearing, L. E. Dorn, P. Kim, M. A. Sargent, J. Gunaje, K. Otsu, J. Davis, Fibroblast-specific genetic manipulation of p38 MAPK in vivo reveals its central regulatory role in fibrosis. *Circulation* **136**, 549–561 (2018).

136. S. Kyoi, H. Otani, S. Matsuhisa, Y. Akita, K. Tatsumi, C. Enoki, H. Fujiwara, H. Imamura, H. Kamihata, T. Iwasaka, Opposing effect of p38 MAP kinase and JNK inhibitors on the development of heart failure in the cardiomyopathic hamster. *Cardiovasc. Res.* **69**, 888–898 (2006).

137. F. See, W. Thomas, K. Way, A. Tzanidis, A. Kompa, D. Lewis, S. Itescu, H. Krum, P38 mitogen-activated protein kinase inhibition improves cardiac function and attenuates left ventricular remodeling following myocardial infarction in the rat. *J. Am. Coll. Cardiol.* **44**, 1679–1689 (2004).

138. K. Yamagami, T. Oka, Q. Wang, T. Ishizu, J.-K. Lee, K. Miwa, H. Akazawa, A. T. Naito, Y. Sakata, I. Komuro, Pirfenidone exhibits cardioprotective effects by regulating myocardial fibrosis and vascular permeability in pressure-overloaded hearts. *Am. J. Physiol.-Heart Circ. Physiol.* **309**, H512–H522 (2015).

139. D. T. Nguyen, C. Ding, E. Wilson, G. M. Marcus, J. E. Olgin, Pirfenidone mitigates left ventricular fibrosis and dysfunction after myocardial infarction and reduces arrhythmias. *Heart Rhythm* **7**, 1438–1445 (2010).

140. Y. Wang, Y. Wu, J. Chen, S. Zhao, H. Li, Pirfenidone attenuates cardiac fibrosis in a mouse model of TAC-induced left ventricular remodeling by suppressing NLRP3 Inflammasome formation. *Cardiol. Switz.* **126**, 1–11 (2013).

141. T. Yamazaki, N. Yamashita, Y. Izumi, Y. Nakamura, M. Shiota, A. Hanatani, K. Shimada, T. Muro, H. Iwao, M. Yoshiyama, The antifibrotic agent pirfenidone inhibits angiotensin II-induced cardiac hypertrophy in mice. *Hypertens. Res.* **35**, 34–40 (2012).

142. L. K. Newby, M. S. Marber, C. Melloni, L. Sarov-Blat, L. H. Aberle, P. E. Aylward, G. Cai, R. J. De Winter, C. W. Hamm, J. F. Heitner, R. Kim, A. Lerman, M. R. Patel, J. F. Tanguay, J. J.

Lepore, H. R. Al-Khalidi, D. L. Sprecher, C. B. I. Granger, Losmapimod, a novel p38 mitogen-activated protein kinase inhibitor, in non-ST-segment elevation myocardial infarction: A randomised phase 2 trial. *The Lancet* **384**, 1187–1195 (2014).

143. M. L. O'Donoghue, R. Glaser, M. A. Cavender, P. E. Aylward, M. P. Bonaca, A. Budaj, R. Y. Davies, M. Dellborg, K. A. A. Fox, J. A. T. Gutierrez, C. Hamm, R. G. Kiss, F. Kovar, J. F. Kuder, K. A. Im, J. J. Lepore, J. L. Lopez-Sendon, T. O. Ophuis, A. Parkhomenko, J. B. Shannon, J. Spinar, J. F. Tanguay, M. Ruda, P. G. Steg, P. Theroux, S. D. Wiviott, I. Laws, M. S. Sabatine, D. A. Morrow, Effect of losmapimod on cardiovascular outcomes in patients hospitalized with acute myocardial infarction: A randomized clinical trial. *JAMA - J. Am. Med. Assoc.* **315**, 1591–1599 (2016).

144. A. Muchir, W. Wu, J. C. Choi, S. Iwata, J. Morrow, S. Homma, H. J. Worman, Abnormal p38α mitogen-activated protein kinase signaling in dilated cardiomyopathy caused by lamin A/C gene mutation. *Hum. Mol. Genet.* **21**, 4325–4333 (2012).

145. P. Garcia-Pavia, J. F. R. Palomares, G. Sinagra, R. Barriales-Villa, N. K. Lakdawala, R. L. Gottlieb, R. I. Goldberg, P. Elliott, P. Lee, H. Li, F. S. Angeli, D. P. Judge, C. A. MacRae, REALM-DCM: A Phase 3, Multinational, Randomized, Placebo-Controlled Trial of ARRY-371797 in Patients With Symptomatic LMNA-Related Dilated Cardiomyopathy. *Circ. Heart Fail.* **17**, e011548 (2024).

146. C. D. K. Nguyen, C. Yi, YAP/TAZ Signaling and Resistance to Cancer Therapy. Cell Press [Preprint] (2019). https://doi.org/10.1016/j.trecan.2019.02.010.

147. M. Liang, M. Yu, R. Xia, K. Song, J. Wang, J. Luo, G. Chen, J. Cheng, Yap/Taz deletion in gli+ cell-derived myofibroblasts attenuates fibrosis. *J. Am. Soc. Nephrol.* **28**, 3278–3290 (2017).

148. S. G. Szeto, M. Narimatsu, M. Lu, X. He, A. M. Sidiqi, M. F. Tolosa, L. Chan, K. De Freitas, J. F. Bialik, S. Majumder, S. Boo, B. Hinz, Q. Dan, A. Advani, R. John, J. L. Wrana, A. Kapus, D. A. Yuen, YAP/TAZ are mechanoregulators of TGF-b-smad signaling and renal fibrogenesis. *J. Am. Soc. Nephrol.* **27**, 3117–3128 (2016).

149. D. M. Santos, L. Pantano, G. Pronzati, P. Grasberger, C. K. Probst, K. E. Black, J. J. Spinney, L. P. Hariri, R. Nichols, Y. Lin, M. Bieler, P. Seither, P. Nicklin, D. Wyatt, A. M. Tager, B. D. Medoff, Screening for YAP inhibitors identifies statins as modulators of fibrosis. *Am. J. Respir. Cell Mol. Biol.* **62**, 479–492 (2020).

150. A. J. Haak, E. Kostallari, D. Sicard, G. Ligresti, K. M. Choi, N. Caporarello, D. L. Jones, Q. Tan, J. Meridew, A. M. D. Espinosa, A. Aravamudhan, J. L. Maiers, R. D. Britt, A. C. Roden, C. M. Pabelick, Y. S. Prakash, S. M. Nouraie, X. Li, Y. Zhang, D. J. Kass, D. Lagares, A. M. Tager, X. Varelas, V. H. Shah, D. J. Tschumperlin, Selective YAP/TAZ inhibition in fibroblasts via dopamine receptor D1 agonism reverses fibrosis. *Sci. Transl. Med.* **11**, 6296 (2019).

151. S. D. Farris, C. Don, D. Helterline, C. Costa, T. Plummer, S. Steffes, C. Mahr, N. A. Mokadam, A. Stempien-Otero, Cell-Specific Pathways Supporting Persistent Fibrosis in Heart Failure. *J. Am. Coll. Cardiol.* **70**, 344–354 (2017).

152. L. S. Neff, Y. Zhang, A. O. Van Laer, C. F. Baicu, M. Karavan, M. R. Zile, A. D. Bradshaw, Mechanisms that limit regression of myocardial fibrosis following removal of left ventricular pressure overload. *Am. J. Physiol.-Heart Circ. Physiol.* **323**, H165–H175 (2022).

153. H. Aghajanian, T. Kimura, J. G. Rurik, A. S. Hancock, M. S. Leibowitz, L. Li, J. Scholler, J. Monslow, A. Lo, W. Han, T. Wang, K. Bedi, M. P. Morley, R. A. Linares Saldana, N. A. Bolar, K. McDaid, C.-A. Assenmacher, C. L. Smith, D. Wirth, C. H. June, K. B. Margulies, R. Jain, E. Puré, S. M. Albelda, J. A. Epstein, Targeting cardiac fibrosis with engineered T cells. *Nature* **573**, 430–433 (2019).

154. J. E. Ballou, R. C. Thompson, Studies of metabolic turnover with tritium as a tracer. V. The predominantly non-dynamic state of body constituents in the rat. *J. Biol. Chem.* **223**, 795–809 (1956).

155. T. Kisseleva, D. Brenner, Molecular and cellular mechanisms of liver fibrosis and its regression. *Nat. Rev. Gastroenterol. Hepatol.* **18**, 151–166 (2021).

156. Z. Rolfs, B. L. Frey, X. Shi, Y. Kawai, L. M. Smith, N. V. Welham, An atlas of protein turnover rates in mouse tissues. *Nat. Commun.* **12**, 6778 (2021).

157. J. Yu, C. Zeng, Y. Wang, Epigenetics in dilated cardiomyopathy. *Curr. Opin. Cardiol.* **34**, 260 (2019).

158. B. Meder, J. Haas, F. Sedaghat-Hamedani, E. Kayvanpour, K. Frese, A. Lai, R. Nietsch, C. Scheiner, S. Mester, D. M. Bordalo, A. Amr, C. Dietrich, D. Pils, D. Siede, H. Hund, A. Bauer, D. B. Holzer, A. Ruhparwar, M. Mueller-Hennessen, D. Weichenhan, C. Plass, T. Weis, J. Backs, M. Wuerstle, A. Keller, H. A. Katus, A. E. Posch, Epigenome-Wide Association Study Identifies Cardiac Gene Patterning and a Novel Class of Biomarkers for Heart Failure. *Circulation* **136**, 1528–1544 (2017).

159. V. K. Topkara, K. T. Chambers, K.-C. Yang, H.-P. Tzeng, S. Evans, C. Weinheimer, A. Kovacs, J. Robbins, P. Barger, D. L. Mann, Functional significance of the discordance between transcriptional profile and left ventricular structure/function during reverse remodeling. *JCI Insight* **1** (2016).

160. C. J. Walker, C. Crocini, D. Ramirez, A. R. Killaars, J. C. Grim, B. A. Aguado, K. Clark, M. A. Allen, R. D. Dowell, L. A. Leinwand, K. S. Anseth, Nuclear mechanosensing drives chromatin remodelling in persistently activated fibroblasts. *Nat. Biomed. Eng. 2021*, 1–15 (2021).

161. A. R. Killaars, J. C. Grim, C. J. Walker, E. A. Hushka, T. E. Brown, K. S. Anseth, Extended Exposure to Stiff Microenvironments Leads to Persistent Chromatin Remodeling in Human Mesenchymal Stem Cells. *Adv. Sci. Weinh. Baden-Wurtt. Ger.* **6**, 670 (2018).

162. C. Yang, M. W. Tibbitt, L. Basta, K. S. Anseth, Mechanical memory and dosing influence stem cell fate. *Nat. Mater. 2014 136* **13**, 645–652 (2014).

163. M. Alexanian, P. F. Przytycki, R. Micheletti, A. Padmanabhan, L. Ye, J. G. Travers, B. Gonzalez-Teran, A. C. Silva, Q. Duan, S. S. Ranade, F. Felix, R. Linares-Saldana, L. Li, C. Y. Lee, N. Sadagopan, A. Pelonero, Y. Huang, G. Andreoletti, R. Jain, T. A. McKinsey, M. G. Rosenfeld, C.

A. Gifford, K. S. Pollard, S. M. Haldar, D. Srivastava, A transcriptional switch governs fibroblast activation in heart disease. *Nat. 2021 5957867* **595**, 438–443 (2021).

164. M. A. McLellan, D. A. Skelly, M. S. I. Dona, G. T. Squiers, G. E. Farrugia, T. L. Gaynor, C. D. Cohen, R. Pandey, H. Diep, A. Vinh, N. A. Rosenthal, A. R. Pinto, High-Resolution Transcriptomic Profiling of the Heart During Chronic Stress Reveals Cellular Drivers of Cardiac Fibrosis and Hypertrophy. *Circulation*, doi: 10.1161/circulationaha.119.045115 (2020).

165. J. J. Saucerman, P. M. Tan, K. S. Buchholz, A. D. McCulloch, J. H. Omens, Mechanical regulation of gene expression in cardiac myocytes and fibroblasts. *Nat. Rev. Cardiol.* **16**, 361–378 (2019).

166. R. Yotti, C. E. Seidman, J. G. Seidman, Advances in the Genetic Basis and Pathogenesis of Sarcomere Cardiomyopathies. *Annu. Rev. Genomics Hum. Genet.* **20**, 129–153 (2019).

167. G. W. Dec, V. Fuster, Idiopathic dilated cardiomyopathy. *N. Engl. J. Med.* **331**, 1564–1575 (1994).

168. S. Saberi, N. Cardim, M. Yamani, J. Schulz-Menger, W. Li, V. Florea, A. J. Sehnert, R. Y. Kwong, M. Jerosch-Herold, A. Masri, A. Owens, N. K. Lakdawala, C. M. Kramer, M. Sherrid, T. Seidler, A. Wang, F. Sedaghat-Hamedani, B. Meder, O. Havakuk, D. Jacoby, Mavacamten Favorably Impacts Cardiac Structure in Obstructive Hypertrophic Cardiomyopathy. *Circulation* **143**, 606–608 (2021).

169. A. Gulati, A. G. Japp, S. Raza, B. P. Halliday, D. A. Jones, S. Newsome, N. A. Ismail, K. Morarji, J. Khwaja, N. Spath, C. Shakespeare, P. R. Kalra, G. Lloyd, A. Mathur, J. G. F. Cleland, M. R. Cowie, R. G. Assomull, D. J. Pennell, T. F. Ismail, S. K. Prasad, Absence of Myocardial Fibrosis Predicts Favorable Long-Term Survival in New-Onset Heart Failure. *Circ. Cardiovasc. Imaging* **11**, e007722 (2018).

170. A. Mandawat, P. Chattranukulchai, A. Mandawat, A. J. Blood, S. Ambati, B. Hayes, W. Rehwald, H. W. Kim, J. F. Heitner, D. J. Shah, I. Klem, Progression of Myocardial Fibrosis in Nonischemic DCM and Association With Mortality and Heart Failure Outcomes. *JACC Cardiovasc. Imaging* **14**, 1338–1350 (2021).

171. O. Kanisicak, H. Khalil, M. J. Ivey, J. Karch, B. D. Maliken, R. N. Correll, M. J. Brody, S. C. J. Lin, B. J. Aronow, M. D. Tallquist, J. D. Molkentin, Genetic lineage tracing defines myofibroblast origin and function in the injured heart. *Nat. Commun.* **7**, 1–14 (2016).

172. T. Moore-Morris, N. Guimarães-Camboa, I. Banerjee, A. C. Zambon, T. Kisseleva, A. Velayoudon, W. B. Stallcup, Y. Gu, N. D. Dalton, M. Cedenilla, R. Gomez-Amaro, B. Zhou, D. A. Brenner, K. L. Peterson, J. Chen, S. M. Evans, Resident fibroblast lineages mediate pressure overload–induced cardiac fibrosis. *J. Clin. Invest.* **124**, 2921–2934 (2014).

173. R. Bretherton, D. Bugg, E. Olsewski, J. Davis, Regulators of Cardiac Fibroblast Cell State. *Matrix Biol. J. Int. Soc. Matrix Biol.* **91–92**, 117–135 (2020).

174. J. D. Humphrey, E. R. Dufresne, M. A. Schwartz, Mechanotransduction and extracellular matrix homeostasis. *Nat. Rev. Mol. Cell Biol.* **15**, 802–812 (2014).

175. K. L. Kreutziger, N. Piroddi, J. T. McMichael, C. Tesi, C. Poggesi, M. Regnier, Calcium binding kinetics of troponin C strongly modulate cooperative activation and tension kinetics in cardiac muscle. *J. Mol. Cell. Cardiol.* **50**, 165–174 (2011).

176. S. B. Tikunova, J. P. Davis, Designing calcium-sensitizing mutations in the regulatory domain of cardiac troponin C. *J. Biol. Chem.* **279**, 35341–35352 (2004).

177. S. M. Haldar, D. Srivastava, Sarcomeres and Cardiac Growth: Tension in the Relationship. *Trends Mol. Med.* **22**, 530–533 (2016).

178. I. Kehat, J. D. Molkentin, Molecular pathways underlying cardiac remodeling during pathophysiologic stimulation. *Circulation* **122**, 10.1161/CIRCULATIONAHA.110.942268 (2010).

179. I. Kehat, J. Davis, M. Tiburcy, F. Accornero, M. K. Saba-El-Leil, M. Maillet, A. J. York, J. N. Lorenz, W. H. Zimmermann, S. Meloche, J. D. Molkentin, Extracellular signal-regulated kinases 1 and 2 regulate the balance between eccentric and concentric cardiac growth. *Circ. Res.* **108**, 176–183 (2011).

180. B. P. Halliday, A. J. Baksi, A. Gulati, A. Ali, S. Newsome, C. Izgi, M. Arzanauskaite, A. Lota, U. Tayal, V. S. Vassiliou, J. Gregson, F. Alpendurada, M. P. Frenneaux, S. A. Cook, J. G. F. Cleland, D. J. Pennell, S. K. Prasad, Outcome in Dilated Cardiomyopathy Related to the Extent, Location, and Pattern of Late Gadolinium Enhancement. *JACC Cardiovasc. Imaging* **12**, 1645–1655 (2019).

181. A. Gulati, A. G. Japp, S. Raza, B. P. Halliday, D. A. Jones, S. Newsome, N. A. Ismail, K. Morarji, J. Khwaja, N. Spath, C. Shakespeare, P. R. Kalra, G. Lloyd, A. Mathur, J. G. F. Cleland, M. R. Cowie, R. G. Assomull, D. J. Pennell, T. F. Ismail, S. K. Prasad, Absence of Myocardial Fibrosis Predicts Favorable Long-Term Survival in New-Onset Heart Failure. *Circ. Cardiovasc. Imaging* **11**, e007722 (2018).

182. C. S. Chung, H. L. Granzier, Contribution of titin and extracellular matrix to passive pressure and measurement of sarcomere length in the mouse left ventricle. *J. Mol. Cell. Cardiol.* **50**, 731–739 (2011).

183. N. Hamdani, M. Herwig, W. A. Linke, Tampering with springs: phosphorylation of titin affecting the mechanical function of cardiomyocytes. *Biophys. Rev.* **9**, 225–237 (2017).

184. M. M. LeWinter, H. L. Granzier, Cardiac titin and heart disease. *J. Cardiovasc. Pharmacol.* **63**, 207–212 (2014).

185. R. O. Hynes, A. Naba, Overview of the Matrisome—An Inventory of Extracellular Matrix Constituents and Functions. *Cold Spring Harb. Perspect. Biol.* **4**, a004903 (2012).

186. M. Cescon, F. Gattazzo, P. Chen, P. Bonaldo, Collagen VI at a glance. *J. Cell Sci.* **128**, 3525–3531 (2015).

187. J. A. Chirinos, L. Zhao, A. L. Reese-Petersen, J. B. Cohen, F. Genovese, A. M. Richards, R. N. Doughty, J. Díez, A. González, R. Querejeta, P. Zamani, J. Nuñez, Z. Wang, C. Ebert, K. Kammerhoff, J. Maranville, M. Basso, C. Qian, D. G. K. Rasmussen, P. H. Schafer, D. SeifFert, M. A. Karsdal, D. A. Gordon, F. Ramirez-Valle, T. P. Cappola, Endotrophin, a Collagen VI Formation-Derived Peptide, in Heart Failure. *NEJM Evid.* **1** (2022).

188. K. L. Herrmann, A. D. McCulloch, J. H. Omens, Glycated collagen cross-linking alters cardiac mechanics in volume-overload hypertrophy. *Am. J. Physiol. Heart Circ. Physiol.* **284**, H1277-1284 (2003).

189. S. Bansode, U. Bashtanova, R. Li, J. Clark, K. H. Müller, A. Puszkarska, I. Goldberga, H. H. Chetwood, D. G. Reid, L. J. Colwell, J. N. Skepper, C. M. Shanahan, G. Schitter, P. Mesquida, M. J. Duer, Glycation changes molecular organization and charge distribution in type I collagen fibrils. *Sci. Rep.* **10**, 3397 (2020).

190. R. Borst, L. Meyaard, M. I. Pascoal Ramos, Understanding the matrix: collagen modifications in tumors and their implications for immunotherapy. *J. Transl. Med.* **22**, 382 (2024).

191. P. Fratzl, "Collagen: Structure and Mechanics, an Introduction" in *Collagen: Structure and Mechanics*, P. Fratzl, Ed. (Springer US, Boston, MA, 2008; https://doi.org/10.1007/978-0-387-73906-9_1), pp. 1–13.

192. G. M. Fomovsky, S. Thomopoulos, J. W. Holmes, Contribution of Extracellular Matrix to the Mechanical Properties of the Heart. *J. Mol. Cell. Cardiol.* **48**, 490–496 (2010).

193. R. P. Wohlgemuth, S. Sriram, K. E. Henricson, D. T. Dinh, S. E. Brashear, L. R. Smith, Strain-dependent dynamic re-alignment of collagen fibers in skeletal muscle extracellular matrix. *Acta Biomater.* **187**, 227–241 (2024).

194. B. A. Roeder, K. Kokini, J. E. Sturgis, J. P. Robinson, S. L. Voytik-Harbin, Tensile mechanical properties of three-dimensional type I collagen extracellular matrices with varied microstructure. *J. Biomech. Eng.* **124**, 214–222 (2002).

195. C. B. Raub, V. Suresh, T. Krasieva, J. Lyubovitsky, J. D. Mih, A. J. Putnam, B. J. Tromberg, S. C. George, Noninvasive assessment of collagen gel microstructure and mechanics using multiphoton microscopy. *Biophys. J.* **92**, 2212–2222 (2007).

196. Y. Izu, H. L. Ansorge, G. Zhang, L. J. Soslowsky, P. Bonaldo, M.-L. Chu, D. E. Birk, Dysfunctional tendon collagen fibrillogenesis in collagen VI null mice. *Matrix Biol. J. Int. Soc. Matrix Biol.* **30**, 53–61 (2011).

197. G. Zhang, Y. Ezura, I. Chervoneva, P. S. Robinson, D. P. Beason, E. T. Carine, L. J. Soslowsky, R. V. Iozzo, D. E. Birk, Decorin regulates assembly of collagen fibrils and acquisition of biomechanical properties during tendon development. *J. Cell. Biochem.* **98**, 1436–1449 (2006).

198. S. P. Reese, C. J. Underwood, J. A. Weiss, Effects of decorin proteoglycan on fibrillogenesis, ultrastructure, and mechanics of type I collagen gels. *Matrix Biol. J. Int. Soc. Matrix Biol.* **32**, 414–423 (2013).

199. D. Bugg, L. R. J. Bailey, R. C. Bretherton, K. E. Beach, I. M. Reichardt, K. Z. Robeson, A. Reese, J. Gunaje, G. Flint, C. A. DeForest, A. Stempien-Otero, J. Davis, MBNL1 drives dynamic transitions between fibroblasts and myofibroblasts in cardiac wound healing. *Cell Stem Cell* **29**, 419-433.e10 (2022).

200. J. Davis, N. Salomonis, N. Ghearing, S. C. J. Lin, J. Q. Kwong, A. Mohan, M. S. Swanson, J. D. Molkentin, MBNL1-mediated regulation of differentiation RNAs promotes myofibroblast transformation and the fibrotic response. *Nat. Commun.* **6**, 1–14 (2015).

201. S. Checa, M. K. Rausch, A. Petersen, E. Kuhl, G. N. Duda, The emergence of extracellular matrix mechanics and cell traction forces as important regulators of cellular self-organization. *Biomech. Model. Mechanobiol.* **14**, 1–13 (2015).

202. K. S. Bielawski, A. Leonard, S. Bhandari, C. E. Murry, N. J. Sniadecki, Real-Time Force and Frequency Analysis of Engineered Human Heart Tissue Derived from Induced Pluripotent Stem Cells Using Magnetic Sensing. *Tissue Eng. Part C Methods* **22**, 932–940 (2016).

203. P. Mulimani, N. A. Mazzawi, A. J. Goldstein, A. M. Obenaus, S. M. Baggett, D. Truong, T. E. Popowics, N. J. Sniadecki, Engineered 3D Periodontal Ligament Model with Magnetic Tensile Loading. *J. Dent. Res.* **103**, 1008–1016 (2024).

204. Y. Xiao, M. C. Hill, L. Li, V. Deshmukh, T. J. Martin, J. Wang, J. F. Martin, Hippo pathway deletion in adult resting cardiac fibroblasts initiates a cell state transition with spontaneous and self-sustaining fibrosis. *Genes Dev.* **33**, 1491–1505 (2019).

205. Y. Xiao, M. C. Hill, M. Zhang, T. J. Martin, Y. Morikawa, S. Wang, A. R. Moise, J. D. Wythe, J. F. Martin, Hippo Signaling Plays an Essential Role in Cell State Transitions during Cardiac Fibroblast Development. *Dev. Cell* **45**, 153-169.e6 (2018).

206. K. C. Lin, H. W. Park, K.-L. Guan, Regulation of the Hippo Pathway Transcription Factor TEAD. *Trends Biochem. Sci.* **42**, 862–872 (2017).

207. J. D. Molkentin, D. Bugg, N. Ghearing, L. E. Dorn, P. Kim, M. A. Sargent, J. Gunaje, K. Otsu, J. Davis, Fibroblast-specific genetic manipulation of p38 MAPK in vivo reveals its central regulatory role in fibrosis. *Circulation* **136**, 549–561 (2018).

208. S. Bhattacharyya, F. Fang, W. Tourtellotte, J. Varga, Egr-1: new conductor for the tissue repair orchestra directs harmony (regeneration) or cacophony (fibrosis). *J. Pathol.* **229**, 286–297 (2013).

209. L. M. Khachigian, Early Growth Response-1, an Integrative Sensor in Cardiovascular and Inflammatory Disease. *J. Am. Heart Assoc.* **10**, e023539 (2021).

210. L. Zhang, J. Elkahal, T. Wang, R. Rimmer, A. Genzelinakh, E. Bassat, J. Wang, D. Perez, D. Kain, D. Lendengolts, R. Winkler, H. Bueno-Levy, K. B. Umansky, D. Mishaly, A. Shakked, S. Miyara, A. Sarusi-Portuguez, N. Goldfinger, A. Prior, D. Morgenstern, Y. Levin, Y. Addadi, B. Li, V. Rotter, U. Katz, E. M. Tanaka, V. Krizhanovsky, R. Sarig, E. Tzahor, Egr1 regulates regenerative senescence and cardiac repair. *Nat. Cardiovasc. Res.* **3**, 915–932 (2024).

211. C. J. Chan, C.-P. Heisenberg, T. Hiiragi, Coordination of Morphogenesis and Cell-Fate Specification in Development. *Curr. Biol. CB* **27**, R1024–R1035 (2017).

212. D. Gilmour, M. Rembold, M. Leptin, From morphogen to morphogenesis and back. *Nature* **541**, 311–320 (2017).

213. C.-P. Heisenberg, Y. Bellaïche, Forces in tissue morphogenesis and patterning. *Cell* **153**, 948–962 (2013).

214. N. I. Petridou, Z. Spiró, C.-P. Heisenberg, Multiscale force sensing in development. *Nat. Cell Biol.* **19**, 581–588 (2017).

215. M. Pesce, G. N. Duda, G. Forte, H. Girao, A. Raya, P. Roca-Cusachs, J. P. G. Sluijter, C. Tschöpe, S. Van Linthout, Cardiac fibroblasts and mechanosensation in heart development, health and disease. *Nat. Rev. Cardiol.* **20**, 309–324 (2023).

216. A. G. Rodriguez, S. J. Han, M. Regnier, N. J. Sniadecki, Substrate stiffness increases twitch power of neonatal cardiomyocytes in correlation with changes in myofibril structure and intracellular calcium. *Biophys. J.* **101**, 2455–2464 (2011).

217. X. Fu, H. Khalil, O. Kanisicak, J. G. Boyer, R. J. Vagnozzi, B. D. Maliken, M. A. Sargent, V. Prasad, I. Valiente-Alandi, B. C. Blaxall, J. D. Molkentin, Specialized fibroblast differentiated states underlie scar formation in the infarcted mouse heart. *J. Clin. Invest.* **128**, 2127–2143 (2018).

218. M. J. Ivey, J. T. Kuwabara, K. L. Riggsbee, M. D. Tallquist, Platelet-derived growth factor receptor- is essential for cardiac fibroblast survival. *Am J Physiol Heart Circ Physiol* **317**, 330–344 (2019).

219. J. T. Kuwabara, A. Hara, S. Bhutada, G. S. Gojanovich, J. Chen, K. Hokutan, V. Shettigar, A. Y. Lee, L. P. DeAngelo, J. R. Heckl, J. R. Jahansooz, D. K. Tacdol, M. T. Ziolo, S. S. Apte, M. D. Tallquist, Consequences of PDGFRα+ fibroblast reduction in adult murine hearts. *eLife* **11**, e69854 (2022).

220. T. R. Eijgenraam, H. H. W. Silljé, R. A. de Boer, Current understanding of fibrosis in genetic cardiomyopathies. *Trends Cardiovasc. Med.* **30**, 353–361 (2020).

221. J. Schindelin, I. Arganda-Carreras, E. Frise, V. Kaynig, M. Longair, T. Pietzsch, S. Preibisch, C. Rueden, S. Saalfeld, B. Schmid, J.-Y. Tinevez, D. J. White, V. Hartenstein, K. Eliceiri, P. Tomancak, A. Cardona, Fiji: an open-source platform for biological-image analysis. *Nat. Methods* **9**, 676–682 (2012).

222. J. S. Bredfeldt, Y. Liu, M. W. Conklin, P. J. Keely, T. R. Mackie, K. W. Eliceiri, Automated quantification of aligned collagen for human breast carcinoma prognosis. *J. Pathol. Inform.* **5**, 28 (2014).

223. Y. Liu, A. Keikhosravi, G. S. Mehta, C. R. Drifka, K. W. Eliceiri, Methods for Quantifying Fibrillar Collagen Alignment. *Methods Mol. Biol. Clifton NJ* **1627**, 429 (2017).

224. M. Pachitariu, M. Rariden, C. Stringer, Cellpose-SAM: superhuman generalization for cellular segmentation. bioRxiv [Preprint] (2025). https://doi.org/10.1101/2025.04.28.651001.

225. F. Pedregosa, G. Varoquaux, A. Gramfort, V. Michel, B. Thirion, O. Grisel, M. Blondel, P. Prettenhofer, R. Weiss, V. Dubourg, J. Vanderplas, A. Passos, D. Cournapeau, M. Brucher, M. Perrot, É. Duchesnay, Scikit-learn: Machine Learning in Python. *J. Mach. Learn. Res.* **12**, 2825–2830 (2011).

226. M. Waskom, O. Botvinnik, M. Gelbart, J. Ostblom, P. Hobson, S. Lukauskas, D. C. Gemperline, T. Augspurger, Y. Halchenko, J. Warmenhoven, J. B. Cole, J. De Ruiter, J. Vanderplas, S. Hoyer, C. Pye, A. Miles, C. Swain, K. Meyer, M. Martin, P. Q. Bachant Eric, G. Kunter, S. Villalba, Brian, C. Fitzgerald, C. G. Evans, M. L. Williams, D. O'Kane, T. Yarkoni, T. Brunner, seaborn: Statistical data visualization. *Astrophys. Source Code Libr.*, ascl:2012.015 (2020).

227. D. Bugg, L. R. J. Bailey, R. C. Bretherton, K. E. Beach, I. M. Reichardt, K. Z. Robeson, A. C. Reese, J. Gunaje, G. Flint, C. A. DeForest, A. Stempien-Otero, J. Davis, MBNL1 drives dynamic transitions between fibroblasts and myofibroblasts in cardiac wound healing. *Cell Stem Cell* **0** (2022).

228. U. N. Lee, J. H. Day, A. J. Haack, R. C. Bretherton, W. Lu, C. A. DeForest, A. B. Theberge, E. Berthier, Layer-by-Layer Fabrication of 3D Hydrogel Structures Using Open Microfluidics. *Lab. Chip* **20**, 525–536 (2020).

229. C. A. DeForest, D. A. Tirrell, A photoreversible protein-patterning approach for guiding stem cell fate in three-dimensional gels. *Nat. Mater.* **14**, 523–531 (2015).

230. A. Dobin, C. A. Davis, F. Schlesinger, J. Drenkow, C. Zaleski, S. Jha, P. Batut, M. Chaisson, T. R. Gingeras, STAR: ultrafast universal RNA-seq aligner. *Bioinforma. Oxf. Engl.* **29**, 15–21 (2013).

231. Y. Liao, G. K. Smyth, W. Shi, featureCounts: an efficient general purpose program for assigning sequence reads to genomic features. *Bioinforma. Oxf. Engl.* **30**, 923–930 (2014).

232. M. I. Love, W. Huber, S. Anders, Moderated estimation of fold change and dispersion for RNA-seq data with DESeq2. *Genome Biol.* **15**, 550 (2014).

233. U. Raudvere, L. Kolberg, I. Kuzmin, T. Arak, P. Adler, H. Peterson, J. Vilo, g:Profiler: a web server for functional enrichment analysis and conversions of gene lists (2019 update). *Nucleic Acids Res.* **47**, W191–W198 (2019).

234. B. K. Martin, C. Qiu, E. Nichols, M. Phung, R. Green-Gladden, S. Srivatsan, R. Blecher-Gonen, B. J. Beliveau, C. Trapnell, J. Cao, J. Shendure, Optimized single nucleus transcriptional profiling by combinatorial indexing. *Nat. Protoc.* **18**, 188–207 (2023).

235. L. R. J. Bailey, D. Bugg, I. M. Reichardt, C. D. Ortaç, A. Nagle, J. Gunaje, A. Martinson, R. Johnson, M. J. MacCoss, T. Sakamoto, D. P. Kelly, M. Regnier, J. Davis, MBNL1 Regulates Programmed Postnatal Switching Between Regenerative and Differentiated Cardiac States. *Circulation*, doi: 10.1161/CIRCULATIONAHA.123.066860 (2024).

236. S. L. Wolock, R. Lopez, A. M. Klein, Scrublet: Computational Identification of Cell Doublets in Single-Cell Transcriptomic Data. *Cell Syst.* **8**, 281-291.e9 (2019).

237. Y. Hao, S. Hao, E. Andersen-Nissen, W. M. Mauck, S. Zheng, A. Butler, M. J. Lee, A. J. Wilk, C. Darby, M. Zager, P. Hoffman, M. Stoeckius, E. Papalexi, E. P. Mimitou, J. Jain, A. Srivastava, T. Stuart, L. M. Fleming, B. Yeung, A. J. Rogers, J. M. McElrath, C. A. Blish, R. Gottardo, P. Smibert, R. Satija, Integrated analysis of multimodal single-cell data. *Cell* **184**, 3573-3587.e29 (2021).

238. A. Butler, P. Hoffman, P. Smibert, E. Papalexi, R. Satija, Integrating single-cell transcriptomic data across different conditions, technologies, and species. *Nat. Biotechnol.* **36**, 411–420 (2018).

239. B. Hegyi, J. M. Borst, L. R. J. Bailey, E. Y. Shen, A. J. Lucena, M. F. Navedo, J. Bossuyt, D. M. Bers, Hyperglycemia regulates cardiac K+ channels via O-GlcNAc-CaMKII and NOX2-ROS-PKC pathways. *Basic Res. Cardiol.* **115**, 1–19 (2020).

240. S. Bremner, A. J. Goldstein, T. Higashi, N. J. Sniadecki, Engineered Heart Tissues for Contractile, Structural, and Transcriptional Assessment of Human Pluripotent Stem Cell-Derived Cardiomyocytes in a Three-Dimensional, Auxotonic Environment. *Methods Mol. Biol. Clifton NJ* **2485**, 87–97 (2022).

241. J. D. Powers, S. A. Malingen, M. Regnier, T. L. Daniel, The Sliding Filament Theory Since Andrew Huxley: Multiscale and Multidisciplinary Muscle Research. doi: 10.1146/annurev-biophys-110320 (2021).

242. R. C. Bretherton, I. M. Reichardt, K. A. Zabrecky, A. Nagle, L. R. J. Bailey, D. Bugg, S. Smolgovsky, A. L. Gifford, T. S. McMillen, A. J. Goldstein, K. B. Kooiker, G. V. Flint, A. Martinson, J. Gunaje, F. Koser, E. Plaster, W. A. Linke, M. Regnier, F. Moussavi-Harami, N. J. Sniadecki, C. A. DeForest, J. Davis, Preventing hypocontractility-induced fibroblast expansion alleviates dilated cardiomyopathy. *Science* **390**, eadv9157 (2025).

243. N. K. Lakdawala, R. E. Hershberger, P. Garcia-Pavia, P. M. Elliott, J. Ginns, B. Meder, S. Solomon, J. W. Cunningham, J. R. Gimeno, R. Barriales-Villa, E. Adler, B. Gerull, N. L. Pereira, B. P. Halliday, W. Li, P. Jarugula, S. Maruyama, S. E. Mohran, M. Papadaki, A. R. Anto, R. L. Anderson, H. M. Rodriguez, C. L. del Rio, J. M. Edelberg, G. Kurio, J. Maya, J. L. Januzzi, Danicamtiv, A Selective Agonist of Cardiac Myosin, for Dilated Cardiomyopathy. *JACC* **0** (2025).

244. M. Merlo, T. Caiffa, M. Gobbo, L. Adamo, G. Sinagra, Reverse remodeling in Dilated Cardiomyopathy: Insights and future perspectives. *IJC Heart Vasc.* **18**, 52–57 (2018).

245. I. Shiojima, K. Sato, Y. Izumiya, S. Schiekofer, M. Ito, R. Liao, W. S. Colucci, K. Walsh, Disruption of coordinated cardiac hypertrophy and angiogenesis contributes to the transition to heart failure. *J. Clin. Invest.* **115**, 2108–2118 (2005).

246. C. J. Weinheimer, A. Kovacs, S. Evans, S. J. Matkovich, P. M. Barger, D. L. Mann, Load-Dependent Changes in Left Ventricular Structure and Function in a Pathophysiologically Relevant Murine Model of Reversible Heart Failure. *Circ. Heart Fail.* **11**, e004351 (2018).

247. N. Glezeva, B. Moran, P. Collier, C. S. Moravec, D. Phelan, E. Donnellan, A. Russell-Hallinan, D. P. O'connor, W. M. Gallagher, J. Gallagher, K. Mcdonald, M. Ledwidge, J. Baugh, S. Das, C. J. Watson, Targeted DNA Methylation Profiling of Human Cardiac Tissue Reveals Novel Epigenetic Traits and Gene Deregulation Across Different Heart Failure Patient Subtypes. *Circ. Heart Fail.* **12** (2019).

248. A. F. Martin, Turnover of cardiac troponin subunits. Kinetic evidence for a precursor pool of troponin-I. *J. Biol. Chem.* **256**, 964–968 (1981).

249. S. Kohli, S. Ahuja, V. Rani, Transcription Factors in Heart: Promising Therapeutic Targets in Cardiac Hypertrophy. *Curr. Cardiol. Rev.* **7**, 262–271 (2011).

250. T. Sakamoto, T. R. Matsuura, S. Wan, D. M. Ryba, J. U. Kim, K. J. Won, L. Lai, C. Petucci, N. Petrenko, K. Musunuru, R. B. Vega, D. P. Kelly, A Critical Role for Estrogen-Related Receptor Signaling in Cardiac Maturation. *Circ. Res.* **126**, 1685–1702 (2020).

251. C. A. Desjardins, F. J. Naya, Antagonistic regulation of cell-cycle and differentiation gene programs in neonatal cardiomyocytes by homologous MEF2 transcription factors. *J. Biol. Chem.* **292**, 10613–10629 (2017).

252. X. Liu, R. M. Burke, anet K. Lighthouse, C. D. Baker, R. A. Dirkx Jr, B. Kang, Y. Chakraborty, D. M. Mickelsen, J. J. Twardowski, S. S. Mello, J. M. Ashton, E. M. Small, p53 Regulates the Extent of Fibroblast Proliferation and Fibrosis in Left Ventricle Pressure Overload. *Circ. Res.* **133**, 2710287 (2023).

253. N. L. Rosin, M. J. Sopel, A. Falkenham, T. D. G. Lee, J.-F. Légaré, Disruption of Collagen Homeostasis Can Reverse Established Age-Related Myocardial Fibrosis. *Am. J. Pathol.* **185**, 631–642 (2015).

254. M. J. Paszek, N. Zahir, K. R. Johnson, J. N. Lakins, G. I. Rozenberg, A. Gefen, C. A. Reinhart-King, S. S. Margulies, M. Dembo, D. Boettiger, D. A. Hammer, V. M. Weaver, Tensional homeostasis and the malignant phenotype. *Cancer Cell* **8**, 241–254 (2005).

255. E. Monaghan-Benson, J. Aureille, C. Guilluy, ECM stiffness regulates lung fibroblast survival through RasGRF1-dependent signaling. *J. Biol. Chem.* **301**, 108161 (2025).

256. C. Uhler, G. V. Shivashankar, Regulation of genome organization and gene expression by nuclear mechanotransduction. *Nat. Rev. Mol. Cell Biol.* **18**, 717–727 (2017).

257. M. P. Grillo, S. Markova, M. Evanchik, M. Trellu, P. Moliner, P. Brun, A. Perreard-Dumaine, P. Vicat, J. P. Driscoll, T. J. Carlson, Preclinical in vitro and in vivo pharmacokinetic properties of danicamtiv, a new targeted myosin activator for the treatment of dilated cardiomyopathy. *Xenobiotica Fate Foreign Compd. Biol. Syst.* **51**, 222–238 (2021).

258. J.-I. Jun, L. F. Lau, The matricellular protein CCN1 induces fibroblast senescence and restricts fibrosis in cutaneous wound healing. *Nat. Cell Biol.* **12**, 676–685 (2010).

259. A. Desmoulière, M. Redard, I. Darby, G. Gabbiani, Apoptosis mediates the decrease in cellularity during the transition between granulation tissue and scar. *Am. J. Pathol.* **146**, 56–66 (1995).

260. V. Krizhanovsky, M. Yon, R. A. Dickins, S. Hearn, J. Simon, C. Miething, H. Yee, L. Zender, S. W. Lowe, Senescence of Activated Stellate Cells Limits Liver Fibrosis. *Cell* **134**, 657–667 (2008).

261. T. Kisseleva, M. Cong, Y. Paik, D. Scholten, C. Jiang, C. Benner, K. Iwaisako, T. Moore-Morris, B. Scott, H. Tsukamoto, S. M. Evans, W. Dillmann, C. K. Glass, D. A. Brenner, Myofibroblasts revert to an inactive phenotype during regression of liver fibrosis. *Proc. Natl. Acad. Sci.* **109**, 9448–9453 (2012).

262. L. Philip, K. Shivakumar, cIAP-2 protects cardiac fibroblasts from oxidative damage: An obligate regulatory role for ERK1/2 MAPK and NF-κB. *J. Mol. Cell. Cardiol.* **62**, 217–226 (2013).

263. A. Beà, J. G. Valero, A. Irazoki, C. Lana, G. López-Lluch, M. Portero-Otín, P. Pérez-Galán, J. Inserte, M. Ruiz-Meana, A. Zorzano, M. Llovera, D. Sanchis, Cardiac fibroblasts display endurance to ischemia, high ROS control and elevated respiration regulated by the JAK2/STAT pathway. *FEBS J.* **289**, 2540–2561 (2022).

264. M. Mayorga, N. Bahi, M. Ballester, J. X. Comella, D. Sanchis, Bcl-2 Is a Key Factor for Cardiac Fibroblast Resistance to Programmed Cell Death*. *J. Biol. Chem.* **279**, 34882–34889 (2004).

265. P. Pandey, F. Khan, T. K. Upadhyay, M. Seungjoon, M. N. Park, B. Kim, New insights about the PDGF/PDGFR signaling pathway as a promising target to develop cancer therapeutic strategies. *Biomed. Pharmacother. Biomedecine Pharmacother.* **161**, 114491 (2023).

266. Y. Sun, L. Yue, P. Xu, W. Hu, An overview of agents and treatments for PDGFRA-mutated gastrointestinal stromal tumors. *Front. Oncol.* **12**, 927587 (2022).

267. M. V. Plikus, X. Wang, S. Sinha, E. Forte, S. M. Thompson, E. L. Herzog, R. R. Driskell, N. Rosenthal, J. Biernaskie, V. Horsley, Fibroblasts: origins, definitions, and functions in health and disease. *Cell* **184**, 3852–3872 (2021).

268. K. Yamagami, T. Oka, Q. Wang, T. Ishizu, J.-K. Lee, K. Miwa, H. Akazawa, A. T. Naito, Y. Sakata, I. Komuro, Pirfenidone exhibits cardioprotective effects by regulating myocardial fibrosis and vascular permeability in pressure-overloaded hearts. *Am. J. Physiol.-Heart Circ. Physiol.* **309**, H512–H522 (2015).

269. A. Muchir, W. Wu, J. C. Choi, S. Iwata, J. Morrow, S. Homma, H. J. Worman, Abnormal p38α mitogen-activated protein kinase signaling in dilated cardiomyopathy caused by lamin A/C gene mutation. *Hum. Mol. Genet.* **21**, 4325–4333 (2012).

270. S. Kyoi, H. Otani, S. Matsuhisa, Y. Akita, K. Tatsumi, C. Enoki, H. Fujiwara, H. Imamura, H. Kamihata, T. Iwasaka, Opposing effect of p38 MAP kinase and JNK inhibitors on the development of heart failure in the cardiomyopathic hamster. *Cardiovasc. Res.* **69**, 888–898 (2006).

271. X. Wang, S. Senapati, A. Akinbote, B. Gnanasambandam, P. S.-H. Park, S. E. Senyo, Microenvironment stiffness requires decellularized cardiac extracellular matrix to promote heart regeneration in the neonatal mouse heart. *Acta Biomater.* **113**, 380–392 (2020).

272. L. S. Eberson, P. A. Sanchez, B. A. Majeed, S. Tawinwung, T. W. Secomb, D. F. Larson, Effect of Lysyl Oxidase Inhibition on Angiotensin II-Induced Arterial Hypertension, Remodeling, and Stiffness. *PLOS ONE* **10**, e0124013 (2015).

273. D. Voehringer, H.-E. Liang, R. M. Locksley, Homeostasis and effector function of lymphopenia-induced 'memory-like' T cells in constitutively T cell-depleted mice. *J. Immunol. Baltim. Md 1950* **180**, 4742–4753 (2008).

274. "Nuclei Isolation from Complex Tissues for Single Cell Multiome ATAC + Gene Expression Sequencing, Rev C" (Demonstrated Protocol CG000375, 10X Genomics, 2022); https://cdn.10xgenomics.com/image/upload/v1660261285/support-documents/CG000375_DemonstratedProtocol_NucleiIsolationComplexSample_ATAC_GEX_Sequencing_Rev_C.pdf.

275. “Chromium Next GEM Single Cell Multiome ATAC + Gene Expression, Rev F” (CG000338, 10X Genomics, 2022); https://cdn.10xgenomics.com/image/upload/v1666737555/support-documents/CG000338_ChromiumNextGEM_Multiome_ATAC_GEX_User_Guide_RevF.pdf.

276. T. Stuart, A. Srivastava, S. Madad, C. A. Lareau, R. Satija, Single-cell chromatin state analysis with Signac. *Nat. Methods* **18**, 1333–1341 (2021).

277. Y. Zhang, T. Liu, C. A. Meyer, J. Eeckhoute, D. S. Johnson, B. E. Bernstein, C. Nusbaum, R. M. Myers, M. Brown, W. Li, X. S. Liu, Model-based analysis of ChIP-Seq (MACS). *Genome Biol.* **9**, R137 (2008).

278. C. S. McGinnis, L. M. Murrow, Z. J. Gartner, DoubletFinder: Doublet Detection in Single-Cell RNA Sequencing Data Using Artificial Nearest Neighbors. *Cell Syst.* **8**, 329-337.e4 (2019).

279. O. Fornes, J. A. Castro-Mondragon, A. Khan, R. van der Lee, X. Zhang, P. A. Richmond, B. P. Modi, S. Correard, M. Gheorghe, D. Baranašić, W. Santana-Garcia, G. Tan, J. Chèneby, B. Ballester, F. Parcy, A. Sandelin, B. Lenhard, W. W. Wasserman, A. Mathelier, JASPAR 2020: update of the open-access database of transcription factor binding profiles. *Nucleic Acids Res.* **48**, D87–D92 (2020).

280. A. N. Schep, B. Wu, J. D. Buenrostro, W. J. Greenleaf, chromVAR: inferring transcription-factor-associated accessibility from single-cell epigenomic data. *Nat. Methods* **14**, 975–978 (2017).

281. I. Korsunsky, A. Nathan, N. Millard, S. Raychaudhuri, Presto scales Wilcoxon and auROC analyses to millions of observations. bioRxiv [Preprint] (2019). https://doi.org/10.1101/653253.

282. Y. Yamada, T. Sadahiro, K. Nakano, S. Honda, Y. Abe, T. Akiyama, R. Fujita, M. Nakamura, T. Maeda, Y. Kuze, M. Onishi, M. Seki, Y. Suzuki, C. Takeuchi, Y. W. Iwasaki, K. Murano, M. Sakata-Yanagimoto, S. Chiba, H. Kato, H. Sakamoto, Y. Hiramatsu, M. Ieda, Cardiac Reprogramming and Gata4 Overexpression Reduce Fibrosis and Improve Diastolic Dysfunction in Heart Failure With Preserved Ejection Fraction. *Circulation* **151**, 379–395 (2025).

283. X. Shao, C. D. Gomez, N. Kapoor, J. M. Considine, C. Grams, Y. (Tom) Gao, A. Naba, MatrisomeDB 2.0: 2023 updates to the ECM-protein knowledge database. *Nucleic Acids Res.* **51**, D1519–D1530 (2023).

284. L. Kolberg, U. Raudvere, I. Kuzmin, J. Vilo, H. Peterson, gprofiler2 -- an R package for gene list functional enrichment analysis and namespace conversion toolset g:Profiler. *F1000Research* **9**, ELIXIR-709 (2020).

285. S. Berg, D. Kutra, T. Kroeger, C. N. Straehle, B. X. Kausler, C. Haubold, M. Schiegg, J. Ales, T. Beier, M. Rudy, K. Eren, J. I. Cervantes, B. Xu, F. Beuttenmueller, A. Wolny, C. Zhang, U. Koethe, F. A. Hamprecht, A. Kreshuk, ilastik: interactive machine learning for (bio)image analysis. *Nat. Methods* **16**, 1226–1232 (2019).

286. E. Karbassi, R. Padgett, A. Bertero, H. Reinecke, J. M. Klaiman, X. Yang, S. D. Hauschka, C. E. Murry, Targeted CRISPR activation is functional in engineered human pluripotent stem cells but undergoes silencing after differentiation into cardiomyocytes and endothelium. *Cell. Mol. Life Sci. CMLS* **81**, 95 (2024).

287. A. J. Whitehead, J. D. Hocker, B. Ren, A. J. Engler, Improved epicardial cardiac fibroblast generation from iPSCs. *J. Mol. Cell. Cardiol.* **164**, 58–68 (2022).

288. A. S. LaCroix, A. D. Lynch, M. E. Berginski, B. D. Hoffman, Tunable molecular tension sensors reveal extension-based control of vinculin loading. *eLife* **7**, 1–36 (2018).

289. H. Chen, H. L. Puhl, S. V. Koushik, S. S. Vogel, S. R. Ikeda, Measurement of FRET Efficiency and Ratio of Donor to Acceptor Concentration in Living Cells. *Biophys. J.* **91**, L39–L41 (2006).

290. S. M. Mijailovich, M. Prodanovic, C. Poggesi, J. D. Powers, J. Davis, M. A. Geeves, M. Regnier, The effect of variable troponin C mutation thin filament incorporation on cardiac muscle twitch contractions. *J. Mol. Cell. Cardiol.*, doi: 10.1016/j.yjmcc.2021.02.009 (2021).

291. J. Crawford, K. Nygard, B. S. Gan, D. B. O'Gorman, Periostin induces fibroblast proliferation and myofibroblast persistence in hypertrophic scarring. *Exp. Dermatol.* **24**, 120–126 (2015).